



HAL
open science

PET molecular imaging of peripheral and central inflammatory processes targeting the TSPO 18 kDa

Nicholas Bernards

► **To cite this version:**

Nicholas Bernards. PET molecular imaging of peripheral and central inflammatory processes targeting the TSPO 18 kDa. Imaging. Université Paris Sud - Paris XI, 2014. English. NNT : 2014PA112211 . tel-01172674

HAL Id: tel-01172674

<https://theses.hal.science/tel-01172674>

Submitted on 7 Jul 2015

HAL is a multi-disciplinary open access archive for the deposit and dissemination of scientific research documents, whether they are published or not. The documents may come from teaching and research institutions in France or abroad, or from public or private research centers.

L'archive ouverte pluridisciplinaire **HAL**, est destinée au dépôt et à la diffusion de documents scientifiques de niveau recherche, publiés ou non, émanant des établissements d'enseignement et de recherche français ou étrangers, des laboratoires publics ou privés.

THÈSE DE DOCTORAT
SCIENCES DE LA VIE ET DE LA SANTÉ

PET MOLECULAR IMAGING OF
PERIPHERAL AND CENTRAL
INFLAMMATORY PROCESSES
TARGETING THE TSPO 18 kDA

Nicholas J. Bernards
nicholas.bernards@gmail.com

Publicly defended the 01/10/2014 before the jury members:

<i>Reviewers</i>	Dr. Hervé Boutin	University of Manchester
	Dr. Sylvie Chalon	Université de Tours
<i>Examiners</i>	Dr. Catherine Chapon	Université Paris Sud XI
	Pr. Viviane Bouilleret	Université Paris Sud XI
<i>Thesis director</i>	Dr. Raphaël Boisgard	Université Paris Sud XI



Thèse réalisée au CEA/DSV/I²BM/Service Hospitalier Frédéric Joliot
Université Paris Sud XI
4, place du Général Leclerc
91401 Orsay
France
Tél : +33 (0) 1 69 86 78 01
Fax : +33 (0) 1 69 86 77 86

Web : <http://www-dsv.cea.fr/dsv/instituts>

Under the supervision of Dr. Raphael Boisgard raphael.boisgard@cea.fr
Financial Sponsor INMiND

Résumé général

L'imagerie moléculaire

L'imagerie moléculaire (MI) est un domaine très diversifié qui présente de nombreuses fonctionnalités. Elle permet de mesurer, de visualiser et de caractériser les divers processus biologiques à différents échelles, allant de l'échelle macroscopique (structures anatomiques) à l'échelle microscopique (cellulaire/moléculaire) [Mankoff 07]. Ce domaine d'étude est en évolution permanente et a pris de l'ampleur depuis son émergence. Initialement, l'imagerie signifiait de regarder simplement un objet ou un échantillon. Cependant, l'observation de l'extérieur ne suffit pas. C'est là que la microscopie a été introduite. Cette invention a permis à l'utilisateur de visualiser les choses invisibles à l'œil nu de mieux comprendre la structure de l'échantillon examiné sous la lentille.

Bien que la microscopie a amélioré l'analyse médicale, en particulier celle des pathologies, il est nécessaire de prélever des échantillons de tissu du patient afin d'émettre un diagnostic. Toutefois, lorsque le tissu entreprend des changements morphologiques, ils subit beaucoup de changement au niveau moléculaire. Les chercheurs ont donc développé différentes modalités d'imagerie : l'imagerie optique (OI), l'échographie par ultrasons (US), l'imagerie par résonance magnétique (IRM), la tomодensitométrie par rayons X (CT), la tomographie d'émission monophotonique (TEMP ou SPECT), et la tomographie par émission de positons (TEP). Chacune de ces modalités présente (ses points forts) des atouts, mais aussi des inconvénients.

L'imagerie nucléaire permet d'appréhender des phénomènes quantitatifs. Il existe deux techniques d'imagerie nucléaire : la tomographie d'émission monophotonique (SPECT) et la tomographie par émission de positons (TEP). Ces deux techniques permettent de réaliser l'imagerie fonctionnelle contrairement à l'imagerie anatomique conventionnelle. Chacune de ces deux techniques d'imagerie présente des avantages attrayants. La résolution d'un appareil de SPECT est de 8-10 mm environ alors que la résolution du TEP est généralement de 1-2 mm dans l'application préclinique et de 3-4mm dans la plupart des machines cliniques. En revanche, les deux modalités ne sont pas identiques et possèdent des propriétés caractéristiques

qui marquent la différence entre les deux dans la pratique. La faible résolution de l'imagerie SPECT rend la TEP plus intéressant, tandis que la première possède une meilleure sensibilité que la seconde.

Les agents de contraste

Les agents de contraste sont des substances qui sont injectés afin d'augmenter le contraste entre les tissus biologiques *in vivo* en leur conférant des propriétés d'imagerie différentes à la région d'intérêt tel qu'une augmentation de l'absorption (applicable au CT) ou une augmentation de la radioactivité locale (PET ou SPECT).

En imagerie nucléaire les agents de contraste sont donc des molécules radioactives capable de mettre en évidence une fonction biologique.

Il existe plusieurs méthodes de marquage des différentes molécules / traceurs, mais également plusieurs isotopes qui peuvent être utilisés. Cependant, des limites chimiques peuvent s'opposer au marquage de certains composés. Aussi, on doit tenir compte de la durée de demi-vie de chaque élément. Le $[^{11}\text{C}]$ a par exemple une durée de demi-vie de 20,3 minutes, celle du $[^{64}\text{Cu}]$ est de 12,7 heures. Un des éléments les plus utilisés est le $[^{18}\text{F}]$ qui a une demi-vie de 109,8 minutes. D'une part, cette durée relativement longue n'exige pas la précipitation de l'utilisateur comme c'est le cas pour $[^{15}\text{O}]$ qui a une demi-vie de seulement 122,24 secondes. D'autre part, la demi-vie du $[^{18}\text{F}]$ d'environ 2 heures assure une exposition limitée du patient / sujet à une substance radioactive. Cela signifie également que l'utilisateur est capable d'effectuer des expériences successives vu que la radioactivité d'un jour donné n'aura plus d'effet le lendemain.

Le $[^{18}\text{F}]\text{FDG}$, un analogue de glucose, est véhiculé dans les cellules par des transporteurs de glucose et y est piégé ensuite après phosphorylation enzymatique par l'hexokinase. L'absorption du glucose est une condition nécessaire pour la survie cellulaire et l'utilisation de $[^{18}\text{F}]\text{FDG}$ est en étroite corrélation avec différentes formes de métabolisme du tissu. Le $[^{18}\text{F}]\text{FDG}$ étant un analogue du glucose, une accumulation naturelle du traceur a lieu dans les tissus qui contiennent des cellules à forte consommation de glucose. De telles cellules se trouvent dans le cerveau, les reins, mais également dans les lésions de type cancéreuse. Comme le $[^{18}\text{F}]$ a remplacé un groupe 2 hydroxyl, une fois que le $[^{18}\text{F}]\text{FDG}$ est absorbé dans la cellule par phosphorylation, il ne subit plus de glycolyse. Cela signifie que dans les zones où il y a une accumulation excessive, une fois peut dire avec certitude qu'il n'y a donc une augmentation augmentée, il n'y a donc une augmentation du niveau de la consommation de glucose qui est susceptible d'être directement lié à un processus pathologique.

L'imagerie TEP offre la possibilité d'utiliser un très grand choix de traceurs. Pourtant, le $[^{18}\text{F}]\text{FDG}$ reste le plus couramment utilisé et présente des avantages.

Comme mentionné plus haut, le [^{18}F]FDG est un analogue du glucose et à ce titre s'accumule dans les cellules qui ont une forte activité métabolique. A l'origine, le [^{18}F]FDG a été utilisé pour la détection de cellules cancéreuses et a prouvé à plusieurs reprises qu'il est efficace pour cette application. Cependant, les cellules cancéreuses ne sont pas les seules à avoir une forte activité métabolique, notamment les cellules impliquées dans des réactions et maladies inflammatoires [Buscombe 03] [Basu 09]. Quoique ce traceur ait longtemps fait ses preuves dans l'exploration de ces pathologies, d'autres traceurs existent et peuvent être mieux adaptés et plus spécifiques à l'inflammation et à l'analyse moléculaire *in vivo* de cette fonction biologique [Wu 13].

En effet certaines cellules saines du tissu (cellules non tumorales) et non liées directement au tissu immunitaire (cellules non inflammatoires) peuvent montrer un taux de consommation de glucose élevé lié à l'environnement cytokinique locale [CORNELIUS 90].

En définitive, même si le [^{18}F]FDG est un bon indicateur pour certaines applications, il est toutefois non spécifique et parfois imprécis dans d'autres.

L'inflammation

L'augmentation de l'activité cellulaire n'est pas le seul phénomène se produisant lors d'une inflammation. Différents stimuli peuvent déclencher une cascade inflammatoire qui commence avec la libération de médiateurs pro-inflammatoires, dont des cytokines, des leucotriènes et des chimiokines. Ces derniers sont initiés par des cellules résidentes inflammatoires et endothéliales. S'en suit l'augmentation de la perméabilité vasculaire qui à son tour permet une infiltration des neutrophiles et des macrophages.

Le principe de l'inflammation n'est pas une découverte récente. Il a d'abord été observé d'un point de vue macroscopique. Par la suite, on était à la recherche de signes différents à l'échelle cellulaire. L'inflammation a été décrite il y a plus de 2000 ans par Celsius et dans sa déclaration («Rubor et Tumor cum Calore et Dolore» qui signifie «rougeur et gonflement avec de la chaleur et de la douleur») décrit les signes cardinaux d'un état inflammatoire. Ces symptômes sont rencontrés par la plupart des individus à un moment ou un autre de leur vie, qu'ils se soient coupé le doigt ou qu'ils aient eu une entorse à la cheville [Rocha e Silva 78] [Benaroyo 94]. Bien que ces quatre symptômes soient remarquables, la conséquence ultime est la perte de la fonction, qui peut arriver si l'inflammation n'est pas détectée et / ou traitée.

Bien que les symptômes énumérés peuvent inhiber le fonctionnement normal dans la vie quotidienne, la réponse inflammatoire est une fonction nécessaire et présente une réponse immunitaire saine. Il faut noter que les symptômes se dissiperont assez rapidement dans une inflammation aiguë et permettent ainsi à la

zone touchée de recouvrer son fonctionnement normal [Mueller 13].

Quand le fonctionnement normal est compromis et que les aspects bénéfiques restent actifs même après avoir atteint leurs objectifs, ceux-ci deviennent pathologique. Cette suite incontrôlée du processus inflammatoire peut alors conduire à la pathogenèse telles que, les maladies métaboliques / le diabète de type 2, les maladies neurodégénératives, les maladies cardiovasculaires entre autres [Mueller 13] [Schwartz 13] [Aguzzi 13].

Historiquement, la seule façon d'examiner la présence des différents aspects ou d'un processus biologique (que ce soit physiologique ou physiopathologique) était de prélever un échantillon de tissu pour l'analyser. Cela implique dans certains cas que les échantillons sont prélevés après la mort du patient comme dans le cas de personnes qui ont succombé à leurs maladies neurodégénératives. Ainsi, l'observation était établie a posteriori et donc trop tard pour aider le patient. Une autre conséquence est les phases pro-inflammatoires demeurent peu connues. Au-delà de cet aspect, il y a une série de mécanismes de régulation et de rétroaction qui sont également impliqués dans le système de rétroaction, mais qui ne sont pas entièrement compris. En définitive, toutes les recherches menées n'ont pas été en mesure d'éclaircir tous les phénomènes qui se produisent pendant l'activation ou le contrôle d'un état inflammatoire [Foley 13].

De nouvelles approches sont nécessaires et c'est là que le domaine de l'imagerie intervient, particulièrement l'imagerie nucléaire. Cet outil a radicalement changé la façon dont les chercheurs et les médecins abordent les problèmes. Ceci est en partie dû au fait que l'imagerie nucléaire permet à l'utilisateur d'observer ce qui se passe au niveau moléculaire *in vivo*.

Une cible récemment explorée est la protéine de translocation (Translocator Protein TSPO) de 18kDa.

Translocator protein 18kDa

La TSPO, anciennement connue sous le nom de peripheral benzodiazepine receptor (PBR), a été découverte en 1977. C'est une protéine transmembranaire de 18kDa qui se trouve principalement dans la membrane mitochondriale externe. Ses fonctions exactes sont encore inconnues, mais elles sont clairement importantes vu que la prolifération cellulaire nécessite beaucoup d'énergie et donc un apport mitochondrial significatif.

La TSPO est omniprésente dans toute les régions périphériques et en moindre quantité dans le cerveau sain. Ce niveau minimal augmente chez les malades d'Alzheimer, de Parkinson ou d'AVC [Scarf 09] [Venneti 08]. Il a été démontré que cette augmentation de la TSPO est liée à l'activation de la microglie [Scarf 09].

Le cas échéant, il y eu un intérêt grandissant pour le développement de radioligands TEP qui ciblent de façon sélective la TSPO tout en ayant une forte affinité.

Cela a alors permis aux chercheurs d'étudier le processus impliqué dans l'activation de la microglie.

L'expression de la TSPO est également été mise en évidence dans dans les macrophages activés en périphérie dans des pathologie de types 'athérosclérose, arthrite rhumatoïde, ainsi que la maladie inflammatoire de l'intestin (inflammatory bowel disease, IBD) [Bird 10] [Pottier 14] [Ostuni 10]. Elle a également été décrite comme étant surexprimés dans divers cancers comme le cancer du sein,, du colon et de la prostate [Batarseh 10]. Tous ceci confirme l'intérêt de disposer de ligands spécifiques de la TSPO pour l'imagerie des processus inflammatoires.

Les radioligands de TSPO

Ces dernières années ont vu le développement rapide de plus de 40 différents radiotraceurs possibles pour cette seule cible [Chauveau 08], validé au niveau pré-cliniques et dont certains ont été jugés plus ou moins prometteurs pour des applications cliniques. Cela peut paraître simple, cependant des obstacles doivent être surmontés. Il faut d'abord prendre en compte la base de comparaison. On ne peut pas comparer des pommes et des oranges, il faut choisir des éléments comparables. Afin de créer éventuellement des applications cliniques, on choisit de travailler avec des modèles animaux qui seraient plus appropriés et mieux adaptés. Par contre, il faut considérer la reproductibilité du modèle animal avec l'espèce sélectionnée. Sachant que les principales applications du ligand de TSPO concernent les pathologies cérébrales, le tissu cérébral paraît une cible logique pour tester les nouveaux radioligands. Quant à l'espèce étudiée, les rongeurs, plus précisément les rats, semblent un choix évident dans le domaine préclinique pour les raisons suivantes : ils sont génétiquement identiques, ils ne nécessitent pas beaucoup d'espace pour être stockés, et ils ont un cerveau de taille suffisamment grande pour permettre de réaliser des études par micro TEP . La TSPO ayant une faible expression à l'état basal, le modèle animal doit également être robuste et idéalement permettre d'induire une inflammation dont le rapport cible sur bruit de fond est élevé [Benavides 83].

L'objectif de la thèse

À ce jour, il est admis que la TSPO joue un rôle important dans le processus inflammatoire, et qu'il est possible de suivre sa présence à l'aide d'une variété de radiotraceurs adaptés. Les impacts de l'inflammation touchent un grand nombre de personnes à travers le monde pour diverses raisons ; c'est pourquoi, quoique le [¹⁸F]DPA-714 est très prometteur, il est nécessaire d'aller plus loin pour explorer ses capacités et ses applications possibles.

L'inflammation a une forte incidence sur différentes maladies, par conséquent,

nous allons étudier différents modèles animaux reproduisant les maladies humaines à impact social élevé (comme la maladie inflammatoire de l'intestin (IBD), la neuroinflammation, et le choc septique). Dans ces modèles nous analyserons et quantifierons les niveaux de d'expression de TSPO 18kDa par imagerie TEP que nous comparerons au niveau exprimé trouvéschez des sujets contrôles. L'objectif étant de déterminer si la TSPO peut constituer une cible biologique d'intérêt pour l'évaluation et la quantification d'un état inflammatoire chez l'individu en utilisant l'imagerie TEP avec le radioligand [^{18}F]DPA-714.

Matériels et méthodes

Les problématiques abordées dans les paragraphes précédents poussent à élaborer des méthodes d'investigation qui soient transférables à l'homme et pour cela, il est nécessaire de mettre en place des expériences adaptées aux problèmes posés.

Afin de mieux reproduire la maladie, et donc les états inflammatoires étudiés, nous avons développé pour chacun des modèles animaux dans le but d'acquérir des images *in vivo* en utilisant l'imagerie TEP et de quantifier les données. Par la suite, les animaux sont sacrifiés et l'organe en question excisé et analysé par différentes méthodes.

L'acquisition des images est effectuée dans une machine Siemens INVEON μ TEP dédiée à l'imagerie du petit animal.

Les images du modèle animal final uniquement sont acquises à l'aide d'une autre machine, la Siemens HRRT afin d'obtenir une image du corps entier de l'animal, alors que l'INVEON ne le permet pas chez les rats.

Un modèle animal précédemment établi par une équipe de chercheurs a révélé la présence de TSPO lorsque l'état inflammatoire augmente à un instant donné. Ce modèle traite particulièrement une inflammation globale dans les intestins et est consacré à la recherche dans le domaine des maladies inflammatoires de l'intestin IBD. Nous avons voulu reproduire ce même phénomène et suivre la présence de TSPO avec le [^{18}F]DPA-714, c'est pourquoi nous avons reproduit le modèle et étudié la capacité du [^{18}F]DPA-714 de visualiser la TSPO.

Nous sommes ensuite passés mis en place un modèle animal d'une inflammation plus locale, puis d'évaluer la capacité du [^{18}F]DPA-714 à quantifier la expression de TSPO à différents instants pour enfin déterminer le signal maximal et ainsi l'inflammation.

Les résultats obtenus avec le radioligand de TSPO ont été comparés aux résultats obtenus avec un traceur le [^{18}F]FDG sur le même animal.

Une fois les images acquises, le tissu d'intérêt est retiré pour faire l'objet d'une analyse par immunohistochimie ainsi que par comptage gamma.

Dans le domaine de la neuro inflamamtion nous avons mis en place et caractérisé par imagerie TEP dynamique un modèle d'inflammation unilatérale chez la rat par

injection intra striatale de lipopolysaccharide bactérien (LPS).

Un autre modèle d'inflammation unilatérale mais induit par injection intrastriatale d'AMPA chez le rat a également été utilisé pour l'évaluation d'un nouveau radioligand de la TSPO.

Enfin le dernier nous avons également mis en place un modèle d'inflammation systémique par injection intraperitonéale de LPS chez le rat.

Aperçu sur le travail de recherche

L'étude entreprise dans cette thèse a fourni des informations conduisant à la conclusion suivante : la TSPO 18kDa peut en effet être utile comme biomarqueur pour l'évaluation d'un état inflammatoire dans plusieurs maladies. Nous avons pu illustrer par l'intermédiaire de deux modèles de la maladie inflammatoire de l'intestin, un modèle de la neuroinflammation et un modèle de choc septique, que la TSPO est un indicateur du niveau de l'inflammation dans la zone affectée. De plus, nous avons pu suivre, mesurer et quantifier l'évolution d'une zone inflammée en fonction du temps.

Bien que le [^{18}F]DPA-714 est le traceur utilisé pour déterminer la présence et le niveau de l'inflammation, d'autres traceurs sont constamment en cours de développement. Cela est démontré par le travail de collaboration effectuée avec l'équipe de radiochimie, dans lequel nous avons illustré le potentiel d'un nouveau radioligand de TSPO, le [^{18}F]DPA-C5yne.

Contributions et perspectives

Ce travail de thèse a permis la validation de la TSPO en tant que biomarqueur de l'inflammation dans différentes maladies comme l'a montré la corrélation des mesures avec l'analyse immunohistochimique. Nous avons mesuré et quantifié les différents niveaux de l'inflammation (en tenant compte des variations inter-individuelles) à l'aide du radioligand [^{18}F]DPA-714. Nous avons également montré que le développement continu de nouveaux radiotraceurs est nécessaire afin d'atteindre un meilleur diagnostic et de meilleurs soins aux patients.

Les prochaines travaux en cour de programmation concerne le passage en clinique. En collaboration avec l'hôpital du Kremlin Bicêtre nous envisageons d'explorer début 2015 l'intérêt du DPA-714 chez des patients atteint de maladies inflammatoires digestives en termes d'outil diagnostique mais également pronostic concernant l'évaluation de thérapie conventionnelles dans un second temps. . En effet il pourrait être envisagé de suivre l'impact d'un traitement administré dans le but de réaliser un véritable soin théranostic du patient.

Quant à la recherche relative à la neuroinflammation, il serait intéressant de comparer les résultats immunohistochimiques à ceux d'autres modèles et d'ana-

lyser les résultats obtenus. Ces résultats pourraient aider à élucider le processus inflammatoire, d'autant que le développement continu et l'amélioration des ligands de TSPO contribueraient à une meilleure précision et donc à une meilleure quantification dans la détection et l'évaluation des maladies.

À ce jour, le choc septique est difficile à mesurer, et il est encore tôt pour dire si les expériences préliminaires menées dans cette thèse montrent l'état inflammatoire. En effet, les résultats actuels ne sont pas suffisants et des recherches supplémentaires approfondies sont nécessaires. Toutefois, l'utilisation de la TSPO comme biomarqueur offre un grand potentiel dans les cas de choc septique. Si les niveaux de TSPO sont révélateurs de la dysfonction d'organes liée à cette pathologie, les médecins pourraient avoir plus d'informations avec pour agir.

L'inflammation est à l'origine de nombreux troubles et maladies, nous devrions la traiter avec ses composants, comme un outil, et non pas comme une menace.

Mots clés : Inflammation, TSPO 18 kDa, Imagerie TEP, [^{18}F]DPA-714, Maladies inflammatoires de l'intestin, Neuroinflammation, choc septique

**PET Molecular Imaging of
Peripheral and Central Inflammatory
Processes Targeting the TSPO
18kDa**

Abstract

Purpose:

The purpose of this study was to determine the *in vivo* potential of the TSPO 18 kDa as a biomarker of inflammation, with the use of its radioligand [^{18}F]DPA-714, to non-invasively quantify the inflammatory state within the scope of various pathologies.

Procedure:

Multiple animal models of various inflammatory diseases, to include: inflammatory bowel disease, neuroinflammation, and septic shock, were developed and put in place by adapted measures. The animals well-being and the subsequent inflammation was evaluated. The inflammatory state was measured using quantitative PET imaging with the TSPO radioligand [^{18}F]DPA-714 and correlated to the expression of conventional inflammatory markers using microscopy.

Results:

Based on the observed data, we were able to distinguish control groups in our animal models of inflammatory bowel disease, neurodegeneration as well as septic shock, when using [^{18}F]DPA-714. This TSPO radioligand permitted us to quantify the inflammatory level and to observe temporal changes in the inflammatory state of the disease in multiple models. The PET results, using the [^{18}F]DPA-714 signal was correlated with an increased TSPO expression at cellular level.

Conclusion:

Results indicate that [^{18}F]DPA-714 is a suitable tracer for studying inflammation in multiple diseases. [^{18}F]DPA-714 could be a good molecular probe to non-invasively evaluate the level and localization of inflammation. Moreover, *in vivo* imaging using this TSPO ligand is potentially a powerful tool to stage and certainly to follow the evolution and therapeutic efficiency at molecular level in inflammatory diseases.

Keywords: Inflammation, TSPO 18 kDa, PET imaging, [¹⁸F]DPA-714, Inflammatory Bowel Diseases, Neuroinflammation, Septic Shock.

Acknowledgements

First and foremost I would like to thank my advisor Raphael Boisgard. It was an honor to be his Ph.D. student. Although my thesis dealt with molecular imaging and the inflammatory process, Raphael taught me more than that. He guided me throughout and always took time to make sure that no question I had left unanswered. Raphael was a good role-model not just as a scientist, but also as a person. He has become a friend who I hope to remain in touch with.

I would like to thank Alexandra Winkeler for her discussions throughout my thesis too. Her input was very valued and appreciated, along with the Feuerzangenbowle. Also thank you to Geraldine. Her presence and laughter in the same office made for a great time and interesting discussions too, not just scientifically. I am sure she will guide the following Ph.D. student well.

The Physics group (Seb, Yoann, Simon, Fabian, Claude, Lionel and Vincent) for their constant help should a machine have an error or an image not reconstruct properly. Thank you also for the radiochemists (Frederic, Bertrand, Annelaure, Stephane) for without them there would not have been any tracers to use and also for their scientific input throughout in papers and posters. Thank you also to Max for his IT help. Without him, it would have proven very difficult to work.

The members and teams of the SHFJ. We crossed paths daily for years and each time it was with a smile and a laugh. Even when things had to be quick or pressing matters were upcoming, there was always enough time to make a peace sign. Thank you for the good times.

Thank you to the riders (Benoit and Yoann). The coffee breaks filled with bike talk were always a nice interruption to the day and lead to some great trips and outings.

Thank you also to the fellow Ph.D. students. The ones preceding (Maya) me I thank for assuring me that things get better. The ones following me (Sylvain, Hayet and Loc) I thank for forcing me to understand some things before teaching them. Good luck to you, and things get better.

I gratefully acknowledge the INMiND consortium for their funding throughout my Ph.D. at the SHFJ. Their research I feel is of great importance and I am fortunate to have been a part of it and able to have contributed to their goal.

Acknowledgements

I would also like to thank my parents for their love and encouragement. For raising me and supporting me in my pursuits. I would also like to thank my in-laws for support and hospitality as I was writing my thesis. And most of all I would like to thank my wife, Alexandra for her patients, encouragement, support, and love during the final stages of this Ph.D.

Contents

Résumé général	i
Abstract	ix
Acknowledgements	xii
Contents	xiv
List of Figures	xviii
List of Abbreviations	xx
Section I	1
1 Introduction	2
1.1 Molecular Imaging	2
1.1.1 Optical Imaging	3
1.1.2 Ultrasound	5
1.1.3 Computerized Tomography	6
1.1.4 Magnetic Resonance Imaging	7
1.1.5 Nuclear Imaging	8
1.1.6 Tracers/Contrast agents	9
1.2 Inflammation	12
1.2.1 Inflammatory targets	17
1.2.2 Inflammatory metabolism	20
1.2.3 Vascular biomarkers of inflammation	20
1.2.4 Other targets	22
1.3 The Translocator Protein 18kDa (TSPO)	22
1.3.1 TSPO radioligands and evaluation	27

CONTENTS

1.4	Issues effecting society	29
1.4.1	Inflammatory bowel disease	29
1.4.2	Neurodegenerative diseases	31
1.4.3	Septic shock	32
1.5	Objective of the thesis	32
2	Materials and methods	34
2.1	Animal models	34
2.1.1	Animal model for a global intestinal inflammation	34
2.1.2	Animal model for a local intestinal inflammation	35
2.1.3	Animal model for neuroinflammation (INMiND)	35
2.1.4	Animal model for tracer evaluation	36
2.1.5	Animal model for septic shock	36
2.2	Imaging	36
2.2.1	PET Radiotracer	36
2.2.2	μ PET image acquisition	37
2.2.3	HRRT image acquisition	37
2.2.4	PET image analysis for the IBD models	38
2.2.5	PET image analysis for the neuroinflammation model	38
2.2.6	PET Image analysis for the septic shock model	38
2.2.7	Statistical analysis	38
2.3	Ex vivo gamma counting	38
2.4	In vitro	39
2.4.1	Autoradiography study for the IBD models	39
2.4.2	Autoradiography study for the tracer validation	39
2.4.3	Immunohistochemistry (IHC) and morphological analysis	39
	Section II	42
3	Evaluation and quantification of TSPO expression in an acute model of global intestinal inflammation	43
3.1	Model validation	43
3.1.1	Imaging specific considerations	44
3.2	Radiotracer choice and comparison	54
3.2.1	Reference glucose analog vs. TSPO ligand	54
3.3	Results	55
3.3.1	Observation of the animals well-being	55
3.3.2	PET results	56
3.3.3	Gamma-count	57
3.3.4	Histo- and immunohistochemistry	58

3.4	Conclusion	60
4	Evaluation and quantification of TSPO expression in an acute model of local intestinal inflammation	61
4.1	Model validation	61
4.1.1	Imaging specific considerations	62
4.2	Results	63
4.2.1	Observation of the animals well-being	63
4.2.2	PET results for evolution experiments	63
4.2.3	PET results for comparison experiments	63
4.2.4	Histo- and immunohistochemistry	65
4.3	Conclusion	66
5	Evaluation and quantification of TSPO expression in an acute model of neuroinflammation	69
5.1	Model validation	69
5.1.1	Imaging specific considerations	70
5.2	Results	70
5.2.1	PET Results	71
5.2.2	Histo- and immunohistochemistry	75
5.3	Conclusion	79
6	Tracer evaluation and validation	80
6.1	Model validation	81
6.1.1	Imaging specific considerations	81
6.1.2	Addressing the problem	83
6.2	Results	84
6.2.1	<i>In vitro</i>	84
6.2.2	<i>In vivo</i>	85
6.2.3	PET results and animal well-being observations	85
6.3	Conclusion	87
7	Evaluation and quantification of TSPO expression in an animal model of septic shock	88
7.1	Model validation	89
7.1.1	Imaging specific considerations	89
7.2	Radiotracer choice	91
7.2.1	TSPO ligand	91
7.3	Results	91
7.3.1	Observation of the animals well-being	91
7.3.2	PET results	92

CONTENTS

7.4 Conclusion	95
Section III	96
8 Discussion	97
8.1 Chapter 3	97
8.2 Chapter 4	99
8.3 Chapter 5	101
8.4 Chapter 6	102
8.5 Chapter 7	104
Conclusion and perspectives	106
Annexes	108
A Published Articles	109
Bibliography	154

List of Figures

1.1.1	Detection Range of Molecular Imaging Modalities	3
1.1.2	<i>In vivo</i> optical image	4
1.1.3	<i>In vivo</i> wavelength extinction coefficient	5
1.1.4	Ultrasound Image	6
1.1.5	CT & MRI images	7
1.1.6	Cerebral MRI image	8
1.1.7	Tracers explained	10
1.1.8	[¹⁸ F]FDG uptake	11
1.2.1	Inflammation	13
1.2.2	Inflammatory response	15
1.2.3	Inflammatory foci	17
1.3.1	TSPO location	23
1.3.2	TSPO implications	25
1.3.3	TSPO ligands	26
1.3.4	TSPO radioligands	28
1.4.1	IBD prevalence	30
3.1.1	Subject positioning	44
3.1.2	Subject positioning with a box	45
3.1.3	Default CT settings	46
3.1.4	CT with CA	47
3.1.5	CT with Klean-Prep	48
3.1.6	CT with negative contrast	49
3.1.7	CT voltage settings	50
3.1.8	CT exposure time settings	51
3.1.9	CT settings of choice	52
3.1.10	PET/CT Misalignment	53
3.1.11	PET/CT Phantom	54
3.1.12	PET VOI	55
3.3.1	PET DSS images	56
3.3.2	PET images	57

LIST OF FIGURES

3.3.3	Gamma count	58
3.3.4	H & E stainings	59
3.3.5	DSS IHC images	59
4.2.1	PET TNBS images	64
4.2.2	Evolution of TSPO expression	65
4.2.3	PET control vs. treated images	66
4.2.4	[¹⁸ F]FDG and [¹⁸ F]DPA-7 ₁₄	67
4.2.5	H & E stainings	68
4.2.6	TNBS IHC images	68
5.2.1	PET LPS images	71
5.2.2	Evolution of TSPO expression (ratio)	72
5.2.3	TACs at each time-point	73
5.2.4	TACs of LPS- and AMPA- models	73
5.2.5	LPS ipsi-lateral significance	74
5.2.6	LPS contra-lateral significance	75
5.2.7	Evans Blue staining	76
5.2.8	H & E staining	77
5.2.9	Cresyl Violet staining, LPS	78
5.2.10	Cresyl Violet staining, AMPA	78
6.1.1	[¹⁸ F]DPA-714 metabolic rate	82
6.1.2	[¹⁸ F]DPA-714 metabolic pathways	83
6.1.3	[¹⁸ F]DPA-C5yne	83
6.2.1	Autoradiography	85
6.2.2	Autoradiography quantification	85
6.2.3	[¹⁸ F]DPA-7 ₁₄ vs. [¹⁸ F]DPA-C5yne	86
6.2.4	TSPO ligand ratios	87
7.1.1	HRRT support	90
7.1.2	HRRT support fit	90
7.3.1	LPS control PET image	92
7.3.2	LPS treated PET image	93
7.3.3	Control vs. treated subjects	94

List of Abbreviations

Symbol	Expansion
[¹¹ C]	Carbon 11
[⁶⁴ Cu]	Copper 64
[¹⁸ F]	Fluorine
[⁶⁸ Ga]	Gallium 68
[¹²³ I]	Iodine
[¹⁵ O]	Oxygen 15
[⁹⁹ Tc]	Technetium
AD	Alzheimer's Disease
AMPA	Alpha-amino-3-hydroxy-5-methyl-4-isoxazole Propionic Acid
CA	Contrast Agents
CAM	Cell Adhesion Molecule
CB2R	Type 2 Cannabinoid Receptor
CCD	Charged Coupled Device
CD	Crohn's Disease
CNS	Central Nervous System
COX	Cyclooxygenase
CT	Computerized Tomography
DPA-714	N,N-diethyl-2-[4-(2-fluoroethoxy)phenyl]-5,7-dimethylpyrazolo[1,5-a]pyrimidine-3-acetamide
DPA-C5yne	N,N-diethyl-2-(2-(4-(3-fluoropent-1-yn-1-yl)phenyl)-5,7-dimethylpyrazolo[1,5-a]pyrimidin-3-yl)acetamide
DSS	Dextran Sodium Sulfate
EB	Evans Blue
FDG	Fluorodeoxyglucose
FET	[¹⁸ F]-O-(2-fluoroethyl)-tyrosine
FMT	Fluorescent Molecular Tomography
FOV	Field of View
FPR	Formyl Peptide Receptor

H & E	Hematoxylin and Eosin
I.P.	Intra-peritoneal
I.V.	Intra-venous
IBD	Inflammatory Bowel Disease
IL-2	Interleukin-2
IL-2R	Interleukin-2 Receptor
INMiND	Imaging of Neuroinflammation in Neurodegenerative Diseases
LPS	Lipopolysaccharide
MI	Molecular Imaging
MMP	Matrix Metalloproteinase
MPTP	Membrane Permeability Transition Pore
MRI	Magnetic Resonance Imaging
NIR	Near Infrared
OI	Optical Imaging
OSEM 2D	Ordered Subset Expectation Maximization 2 Dimensional
PBR	Peripheral Benzodiazepine Receptor
PBS	Phosphate-buffered Saline
PD	Parkinson's Disease
PET	Positron Emission Tomography
ROI	Region of Interest
SPECT	Single Photon Emission Computerized Tomography
SSTR	Somatostatin Receptor
TNBS	2,4,6-Trinitrobenzene Sulfonic Acid
TNF-alpha	Tumor Necrosis Factor Alpha
TSPO	Translocator Protein
UC	Ulcerative Colitis
US	Ultra Sound
VAP-1	Vascular Adhesion Protein
VCAM-1	Vascular Cell Adhesion Molecule
VOI	Volume of Interest

Section I

Chapter 1

Introduction

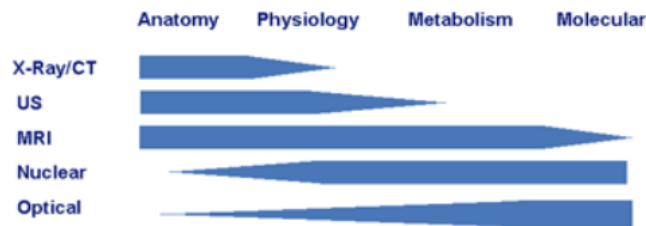
1.1 Molecular Imaging

Molecular imaging (MI) is a very diverse field with many capabilities. Using MI, it is possible to measure, visualize and characterize various biological processes at various levels of size, ranging from the most broad (anatomical structures) to a much more minute target (molecular amount)[Mankoff 07]. This field of study is constantly evolving and has been gaining momentum ever since its emergence. Initially, imaging consisted of simply looking at an object, or specimen. However, it quickly became evident that there is more than meets the eye. This was where the microscope was introduced. This was an invention which allowed the user to see things that the naked eye could not and as such allow for a better understanding of the structure or specimen being observed under the lens.

As much as the microscope had helped increase the understanding of various biological phenomena in the medical world, specifically in pathologies, it still required tissue samples to be excised from a patient in order to diagnose. The drawback being that in order for the tissue may have undertaken morphological and molecular changes. Researchers thus went on to develop various, so called, imaging modalities: Optical Imaging (OI), Ultrasound (US), Magnetic Resonance Imaging (MRI), Computerized Tomography (CT), Single Photon Emission Computerized Tomography (SPECT), and Positron Emission Tomography (PET). Each of these modalities has its advantages, but also its disadvantages as summarized in figure 1.1.1 [Weissleder 99]. X-Rays have a better application for the analysis of anatomical structures due to the high resolution and as such has become the reference for bone imaging. Ultrasound has a much lower resolution than X-Rays do, but does not use radiation for its applications and therefore can be used for physiological imaging, and is used worldwide for echographies of pregnant women. MRI has a much wider range to which it can be applied, making it convenient

for internal medicine. Nuclear imaging has its strengths (such as being functional, non-invasive, and specific) in imaging at a molecular level and has an extremely high sensitivity which in turn enables the user to detect molecules of interest and is inherently quantitative. Optical imaging also has a good sensitivity but is limited when taking tissue depth must be taken into consideration.

Detection Range of Imaging Modalities



Weissleder, *Radiology* 1999; 212: 609–614

Figure 1.1.1: Each modality has its advantages and disadvantages. This illustration reveals the strengths and weaknesses of each imaging modality. Depending on the question at hand, a given modality will most likely be more adapted than another

1.1.1 Optical Imaging

Optical imaging is a molecular imaging modality which describes the behavior of visible, ultraviolet, and infrared light used in medical imaging. It is relatively inexpensive and can provide molecular and functional information, but reveals limited information on a physiological (when organs are deep in the tissue) and anatomical basis. When applying OI, the probe interacts with a biological tissue, and the light then has a resulting photo-physical interactions such as scattering, absorption and emission of light. Each of these interactions can be used in order to obtain information about the various aspects of interest such as biochemical and morphological information about a specific target [Solomon 11]. OI uses light as its medium and often fluorescence is implemented to help view things indirectly that could be seen or 'marked' otherwise. In order to visualize some of these fluorophores, an excitation laser must be used. While near infrared wavelengths are used to avoid light absorption from blood mainly, it still must overcome other as-

pects, such as scattering, attenuation, and energy conversion into heat, to remain visible to the high speed CCD cameras. A non-negligible advantage is the lack of radiation when compared to other modalities. Even though there are numerous advantages to OI, there is one which cannot be disregarded: limited tissue penetration depth which means that a translation into a clinical setting is difficult to carry out at present. Figure 1.1.2 and 1.1.3 illustrate an example of *in vivo* imaging in a mouse and the absorption coefficient, respectively. Figure 1.1.2 was acquired with the help of a contrast agent Angiostamp® which is a near infrared fluorescent probe which targets alpha-v-beta-3 integrin specifically and has been used for the labeling of tumors or angiogenesis studies. This image illustrated the Angiostamp® uptake within the implanted tumors, located behind the head of the mouse. However, due to the path of elimination, one can also see the kidneys. Looking at figure 1.1.3, one can understand why the near infrared (NIR) light is of interest as it is within the optical window for *in vivo* imaging.

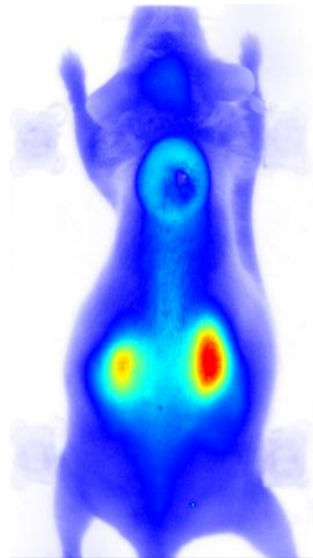


Figure 1.1.2: Optical image obtained using fluorescence molecular tomography (FMT) of a mouse injected with Angiostamp®

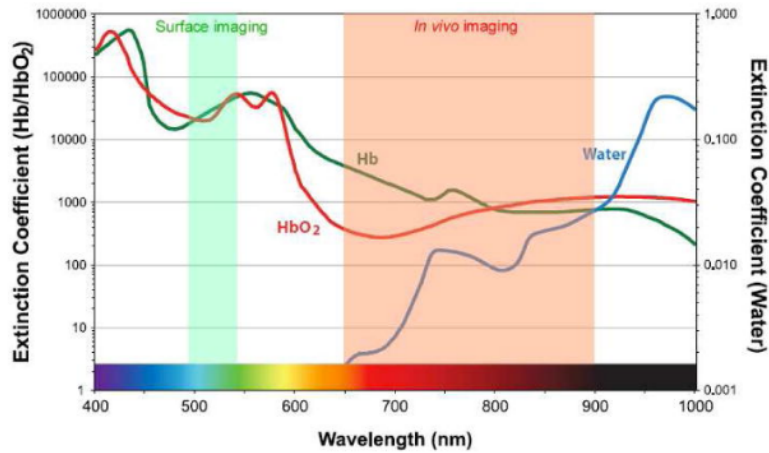


Figure 1.1.3: Depicted here is a graph illustrating the absorption coefficient of the therapeutic window for in vivo imaging in optical imaging.

1.1.2 Ultrasound

Ultrasound (US) is another technique which has very different advantages and disadvantages and is based on oscillating sound pressure wave with a frequency greater than the upper limit above that of human hearing and is used to measure distances for many applications to include the medical imaging field. It allows for the visualization of various structures to include muscles, tendons, and many internal organs, but to also capture their size, structure. US is a widely used diagnostic tool and has been used for the past half a century as it is relatively inexpensive and portable too. US maps the acoustical properties of the tissue to include the density and compressibility [Cobbold 07]. It is commonly used for echographies in a clinical setting and can be an alternative to MRI and CT scans in some cases. As it is relatively inexpensive, it can be widely used and implemented for the diagnosing/staging of various diseases [Fenster 01]. However, the image analysis is very user dependent and can be difficult to interpret if not being looked at by an experienced user as the objects can be distorted due to defraction, attenuation, dispersion and other inhomogeneities [Cobbold 07]. Figure 1.1.4 illustrates a cross section of a moving heart and shows that US can be used for the analysis of a functional organ, contrary to CT scans.

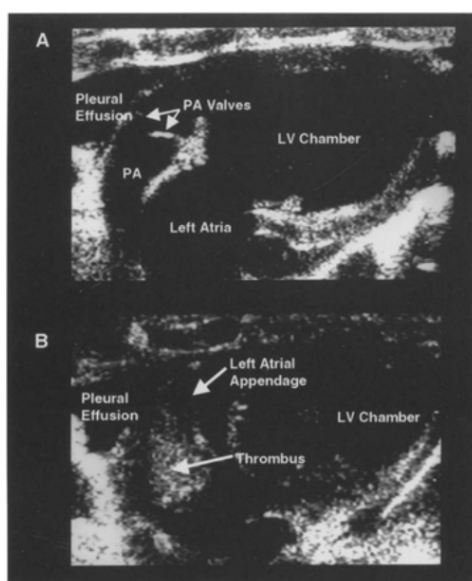


Figure 1.1.4: Cross section of a moving heart

1.1.3 Computerized Tomography

When talking about structural imaging, one must not forget to mention CT scan. CT scans, or X-ray computed tomographies, are generated by X-rays which pass through various tissues. These x-rays are then either absorbed or scattered. The 3D images is acquired by a source which rotates around the subject and on the other end, a detector which measures the difference in received transmitted x-rays. CT's are still the reference modality today when regarding bone imaging. An example of a CT image (figure 1.1.5) shows how clearly one can identify the bone outlines. One advantage of the CT imaging modality is that one can manipulate various parameters of the imaging process to extract different tissue characteristics based on their X-ray absorption. Be this as it may, limitations are still evident when comparing images (A) and (B) in figure 1.1.5. In image (A), the CT image reveals structurally intact bones whereas the MRI (B) using a short T1 inversion recovery image reveals ruptured ligaments where the arrow is located [Fotiadou 11].

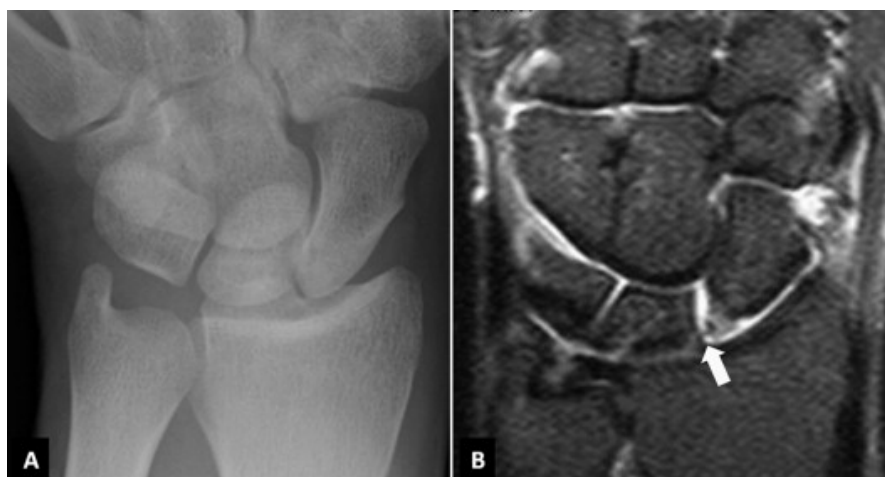


Figure 1.1.5: CT (A) & MRI images (B)

1.1.4 Magnetic Resonance Imaging

As can be seen, there are advantages of each modality, and another imaging modality which has gained much attention and has been translated into a clinical setting quite quickly is magnetic resonance imaging (MRI). This is a medical imaging modality which records changes in magnetic fields and depending on the pulse sequence allows for different kinds of images. Figure 1.1.6 illustrates examples of two different sequences, among others, that are possible with MRI (T1 on the left and T2 on the right). MRI can be used for a wide range of applications ranging from neuroimaging to cardiovascular imaging, musculoskeletal, oncological and also functional applications. Beyond that, a distinct advantage of MRI is that there is no use of ionizing radiation. Each sequence allows the user to extract different kinds of information which in turn will assist in the diagnosis.

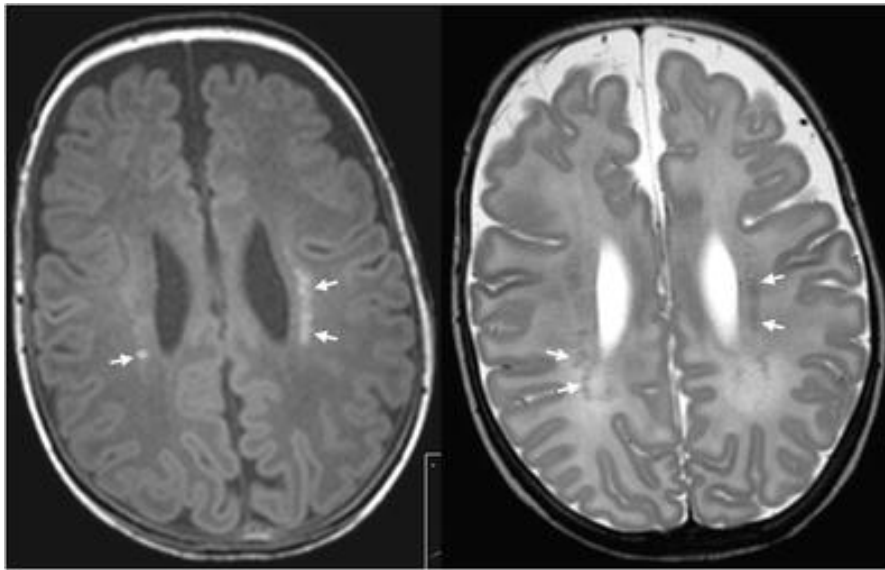


Figure 1.1.6: MRI with T1 (left) and T2 (right)
[Leijser 10]

MRI is used much of the time for brain scans but is also routinely used for whole body image acquisitions. As MRI has exceptional soft tissue contrast properties, the user may be able to determine soft tissue diseases based on an image [Fotiadou 11]. The ability to apply an MRI to various kinds of medical questions shows its wide usage. Beyond this however, there are two more strong argument for this modality; the high resolution and the lack of radiation for the patient.

While it is true that other modalities have a advantages such as not being dependent on a radioactive element, they (OI, US) have depth limitation which become a large obstacle when looking at a living system. MRI, as mentioned previously, is not dependent either on radioactivity, nor is there a depth limitation. All things taken into account, nuclear imaging techniques are able to detect the tracers on a molecular level as depicted in figure 1.1.1. This along with the lack of depth limitation make it of great interest for many applications. The ability to acquire specific information at a molecular level is of great interest in many diseases.

1.1.5 Nuclear Imaging

There are two nuclear imaging modalities to look at. The first being single photon emission computed tomography (SPECT) and the second being positron emission tomography (PET). SPECT and PET are imaging techniques which allow for functional imaging, as oppose to anatomical imaging. In these modalities, there

are advantages which are very desirable, such as being able to obtain functional information at a molecular level while not being limited to the depth at which the functions are taking place. The resolution of a SPECT device is at about 8-10 mm in a clinical setting, but can have competitive resolutions with PET in a preclinical setting. PET resolution is generally anywhere between 1-2 mm in the preclinical field and at 3-4mm in most clinical machines.

The two modalities however are not identical and have, again, different characteristics which make a difference in practice. The resolution disadvantage of SPECT imaging makes PET very interesting. Beyond that though, there is the higher sensitivity of PET.

This increased sensitivity is non-negligible as it increased by two to three orders of magnitude[Rahmim 08]. Both PET and SPECT however have different limitations when talking about the spatial resolution. SPECT is limited by technology at the moment due to the design of collimators. PET on the other hand is limited by physics. Due to the non-collinearity of the photons. Much of this can however be corrected by reconstruction modeling[Reader 07]. The other aspect that one should take into account, when dealing with nuclear imaging, is the temporal resolution. Each modality is able to exploit dynamic information which in many cases is of great importance. The possible alteration in bio-distribution of the radiotracers/radiopharmaceuticals within a subject, may yield pertinent physiological or pathophysiological information which could not otherwise be observed.

A distinct advantage of SPECT is that the user is able to carry out an acquisition of two different parameters if using two different isotopes, each with their own distinct energy. This is of great interest, especially in a clinical setting as it allows both, the hospital/doctor as well as the patient to gain time as well as supplementary information, if required.

While, dual tracer acquisitions are currently not being carried out in PET, it could one day be possible. Using the knowledge of the different half-life durations, it has been shown that this simultaneous acquisition of two different tracers, emitting the same energy, and separation of the two signals is indeed possible [Kadmas 05] [Rust 06].

1.1.6 Tracers/Contrast agents

Contrast agents, or tracers, are substances which are injected and used to increase the contrast of fluids or structures during an imaging process.

When speaking about the ability to detect something (in regard to PET imaging), one must understand the principle behind this. There are multiple ways in which a tracer can detect and or interact with its target. Haberkorn et al [Haberkorn 11] displayed this nicely in figure 1.1.7.

In the image below one can observe that (1) [^{18}F]FDG (fluorodeoxyglucose) is taken up into cells by glucose transporters and subsequently trapped after enzymatic phosphorylation by hexokinase; (2) radioactive isotopes of iodide are taken up by the sodium iodide symporter on thyroid or breast cancer tissues; (3) the amino acid [^{18}F]-O-(2-fluoroethyl)-tyrosine (FET) is taken up into cells by the L-type amino-acid transporter system; (4) radiolabeled antibodies such as Zevalin bind to antigens specifically expressed on the surface of tumor cells.

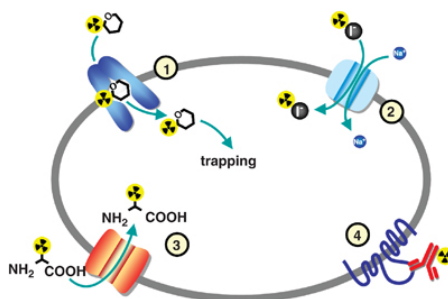


Figure 1.1.7: Multiple ways for a radiotracer to be taken up and provide contrast [Haber Korn 11] [Damont 08]

Figure 1.1.7 illustrated the multiple ways in which various molecules/tracers can be marked, not only in terms of methodology, but also in terms of which isotope is used. There are of course chemical limitations as to which element can be used to mark a given molecule too. This aside though, one should also take into account that each element has a certain half-life. [^{11}C] for example has a half-life duration of 20.3 minutes where the half-life of [^{64}Cu] lasts 12.7 hours. One of the most used elements is [^{18}F] however, which has a half-life of 109.8 minutes. This amount of time is practical as it allows the user to not have to rush as is the case for [^{15}O] which is very brief and has a half-life of a mere 122.24 seconds, but the half-life of about 2 hours also ensures that the patients/subject will not be exposed to a radioactive substance for a prolonged time period either. Beyond this, it also means that the user would be able to carry out successive experiments as the radioactivity of a given day would be decayed by the following day.

As mentioned previously, [^{18}F]FDG is taken up into cells by glucose transporters and subsequently trapped after enzymatic phosphorylation by hexokinase. Glucose uptake is a necessary for cellular survival and the use of [^{18}F]FDG is closely correlated with various types of tissue metabolism. As [^{18}F]FDG is an analog of glucose, there will be a natural accumulation of the tracer in tissues which contain high-glucose consuming cells. Such cells can be found in the brain, the kidneys, but also in cancer cells. As the [^{18}F] has replaces a 2'hydroxyl group, once the [^{18}F]FDG has been included into the cell via phosphorylation, it cannot undergo further glycolysis. This means that in areas where there is an excess accumulation,

once can say with certainty that there is therefore an increased level of glucose consumption which is likely to be pathologically related. Figure 1.1.8 exemplifies a whole-body scan in which one can observe the accumulation of $[^{18}\text{F}]\text{FDG}$. Here one can observe in image (A) that with the help of a PET scan, a spotty or focal accumulation which is more intense than the liver uptake (arrow). (B) reveals a focal accumulation in the area of the lower abdomen (arrow). (C) PET scan demonstrates no definite accumulation of FDG in the stomach. (D) PET scan demonstrates diffuse accumulation (normal physiological accumulation) of FDG in the stomach (arrow).

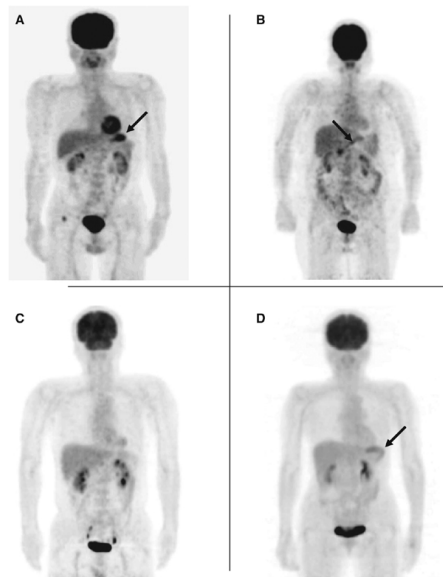


Figure 1.1.8: Whole-body scan of $[^{18}\text{F}]\text{FDG}$ accumulation
[Shoda 07]

PET imaging has the fortune of having a very large selection of tracers to choose from. Yet $[^{18}\text{F}]\text{FDG}$ remains the most commonly used. $[^{18}\text{F}]\text{FDG}$ does have its advantages however. As previously mentioned, $[^{18}\text{F}]\text{FDG}$ is a glucose analog and as such accumulates in cells which have an increased activity. Originally, $[^{18}\text{F}]\text{FDG}$ was used for the detection of cancerous cells and has proven time and time again to be very effective in this application. However, as cancerous cells are not the only ones which have an increased activity, $[^{18}\text{F}]\text{FDG}$ has thus also been used for other applications in which there are malfunctioning cells and as such has been used to a great extent in evaluation of various inflammatory diseases [Buscombe 03] [Basu 09] As this tracer has served the medical world well for a very long time in many different applications, one can use better tracers which are better adapted to targets specific to inflammation. The reason for this statement is that increased

glucose metabolism, as previously mentioned, and the subsequent [^{18}F]FDG accumulation are not phenomena which are unique to malignant cells [Wu 13]

Benign processes, as can be found in inflammatory pathologies, will also accumulate [^{18}F]FDG and as a result yield false positive results for tumor detection [Rosenbaum 06]. This is also due to the fact that certain indicators and factors in an inflammatory response require glucose at an elevated rate when compared to the healthy cells in the surrounding tissue (non-inflammatory foci). This in turn explains why [^{18}F]FDG was of interest initially.

As good as [^{18}F]FDG is and as much as it can tell the user about a given subject, [^{18}F]FDG is also non-specific and as such can be imprecise by definition. However, it should not be confused with the non-specificity of the cellular process.

Increased cellular activity is not the only phenomenon occurring in an inflammatory state however. There various stimuli which are triggered, initiate the inflammatory cascade which starts with the release of a variety of pro-inflammatory mediators, to include cytokines, leukotrienes, chemokines. All these are initiated by resident inflammatory and endothelial cells. Once this has occurred, the vascular permeability is increase which in turn allowed for an infiltration on both neutrophils and macrophages. In an activated environment the [^{18}F]FDG uptake is increased in many types of cells and is not specific to one population or a single type of molecular event. It has, for example, been shown that fibroblasts increase their metabolic glucose activity when in a stressful environment [CORNELIUS 90]. The fact that [^{18}F]FDG has a nonspecific uptake is inconvenient when investigating molecular processes related to inflammation.

1.2 Inflammation

The principle of inflammation is not a new discovery. It was just looked at from a more macroscopic stand-point. At the time, one was looking for different signs, other than a cellular level. The tell-tale signs of inflammation have been described over 2000 years ago by Celsius and in his statement ('Rubor et Tumor cum Calore et Dolore' meaning 'redness and swelling with heat and pain') described the cardinal signs of an inflammatory state. These symptoms are things that most individuals have come across at one point or another in their life when they have either been cut or had a sprained ankle [Rocha e Silva 78] [Benaroyo 94]. While these four symptoms are remarkable, the ultimate consequence is the loss of function, which can certainly be a possibility if left undetected and/or untreated.

As much as the these above listed phenomena may inhibit normal functionality in daily life, the inflammatory response is a necessary function and exhibits a healthy immune response. One should note that the symptoms will dissipate relatively quickly in an acute inflammation and thus enable the affected area to

resume a normal functioning state [Mueller 13].

Functionality is compromised if the beneficial aspects have all served their purpose, but have not halted their activity, then, what once was of aid to the healthy state, becomes pathological and this uncontrolled continuity of the inflammatory process can then lead to pathogenesis such as, but not limited to, metabolic diseases / type 2 diabetes, neurodegenerative diseases, and cardiovascular diseases among others [Mueller 13] [Schwartz 13] [Aguzzi 13]. Figure 1.2.1 illustrates some of the health areas which are concerned and can be affected by inflammation and some which can be a consequence of an inflammation which goes uncontrolled, thus developing a pathological state. Inflammation plays a central role as can be seen in this illustration. The upper 3rd (above the inflammation bubble) lists possible origins for an inflammatory reaction while the lower 3rd (below the inflammation bubble) illustrates possible consequences of a pathological inflammatory state.

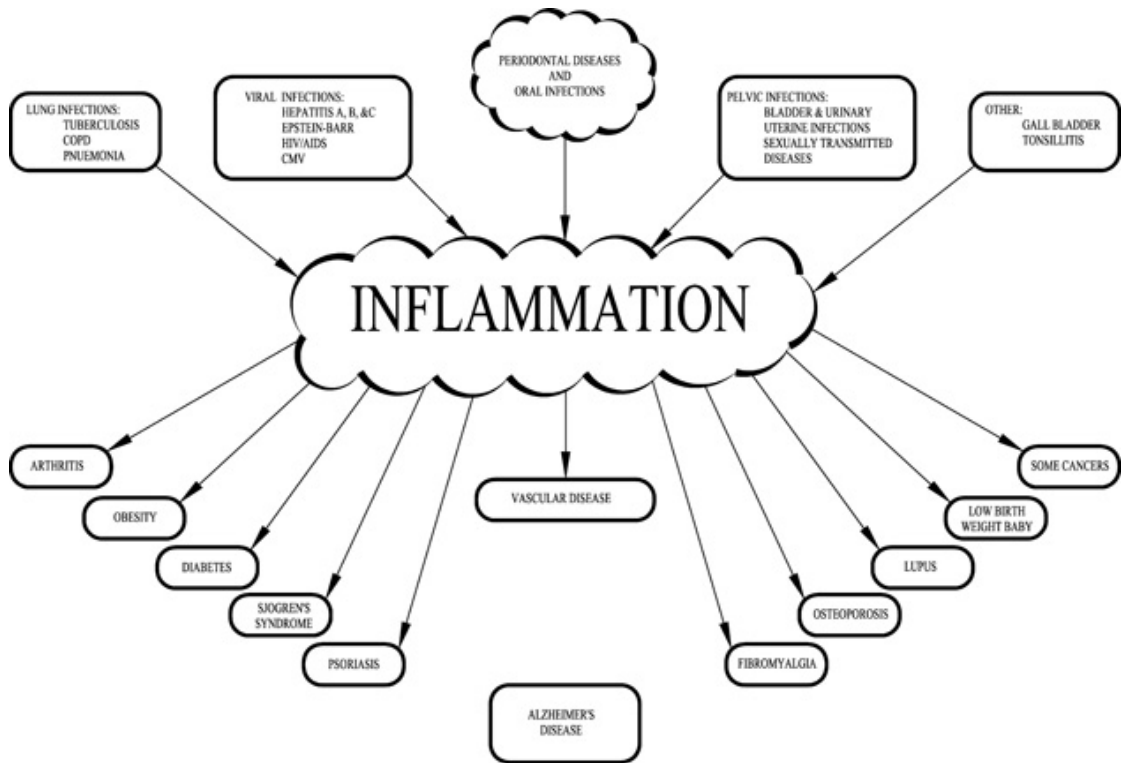


Figure 1.2.1: Inflammation plays a central role in pathologies and disorders

Figure ?? by Tabas et al. [Tabas 13] illustrate the principle behind the pathological state and how this state becomes a health problem. In an acute inflammatory response (image A) there is a suppression of the pathogen, which in turn brings the stimulus to an arrest. Some reversible tissue damage will also occur which will be

repaired and ultimately bring the damaged tissue to a homeostatic state. In image B, the chronic response, one can observe some of the classical responses, and thus features, of a chronic inflammatory disease. This, non-immune, pathophysiological process triggers a sterile inflammatory response. This is most likely initiated by the production of damage-associated molecular patterns. This response then is amplified by various factors such as chemokines and cytokines. Due to the fact that the initial response is not stopped as would be the case in a physiological situation, it continues and a chronic inflammation takes place.

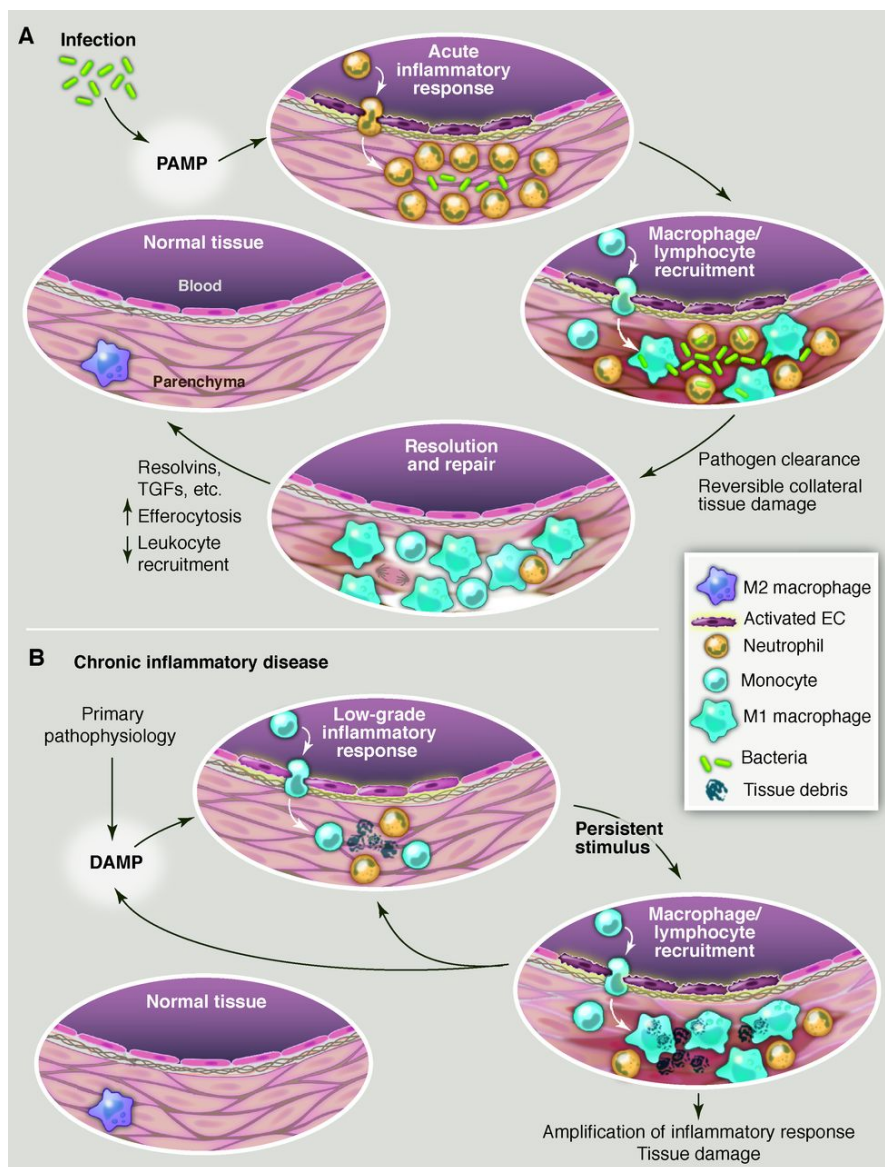


Figure 1.2.2: Acute inflammatory response (image A) and chronic inflammatory disease

[Tabas 13]

The previous illustration remains vague but allows for a global view of what can go wrong when inflammation is present. It also shows that inflammation is of great importance in various pathologies and that this phenomenon is of utmost importance and as such could be a significant factor in disease development to observe and evaluate.

Inflammation in itself is a double edged sword; on the one hand it removes the

harmful pathogens, while on the other it is also necessary for the repair of damaged tissue [Foley 13]. The consequences are rather dire as can be seen in some of the better known diseases, such as the inflammatory bowel diseases (be it Crohn's diseases or Ulcerative Colitis), neurodegenerative diseases such as Alzheimer's-, Parkinson's-, and Huntington's disease, or Sepsis. As much as we feel we 'know' about the previously mentioned diseases, there is still much work that needs to be done in the future in order to properly understand them.

It is a start to know that there is a problem present and that it is possible to follow the various diseases by various methods. But it is not enough. In order to bring help those suffering, one must be able to do better than just admit that there is a problem. There is a need for precise prognosis, which can be made by a precise diagnosis, which ultimately leads to the global desire for personalized medicine.

Traditionally, the only way to really observe the presence of various aspects or any biological (be it physiological or pathophysiological) process, one was obliged to extract a tissue sample and then analyze it. This meant that in some cases, the patient had to already have been deceased in order to obtain the samples, such as in individuals who ultimately succumb to their neurodegenerative diseases. Thus, the observation was retrospective and too late for the patient. This has another consequence, that there is not much known about the exact nature of the pro-inflammatory stages. Beyond this aspect, there are also a list of regulatory and feedback mechanisms which are also involved in the feedback system, but are not fully understood either. Alas, all that has been researched, has not been able to fully bring to light all the involved phenomena that occur while an inflammatory state is being activated or controlled [Foley 13].

New approaches were needed and this is where the field of imaging comes in; specifically nuclear imaging. This tool has drastically changed the way that researchers and medical doctors approach problems. This is in part due to the fact that nuclear imaging enables the user to observe what is happening on a molecular level while *in vivo*. Figure 1.2.3 illustrates a list of biomarkers, along with their foci, implicated in inflammation [Wu 13].

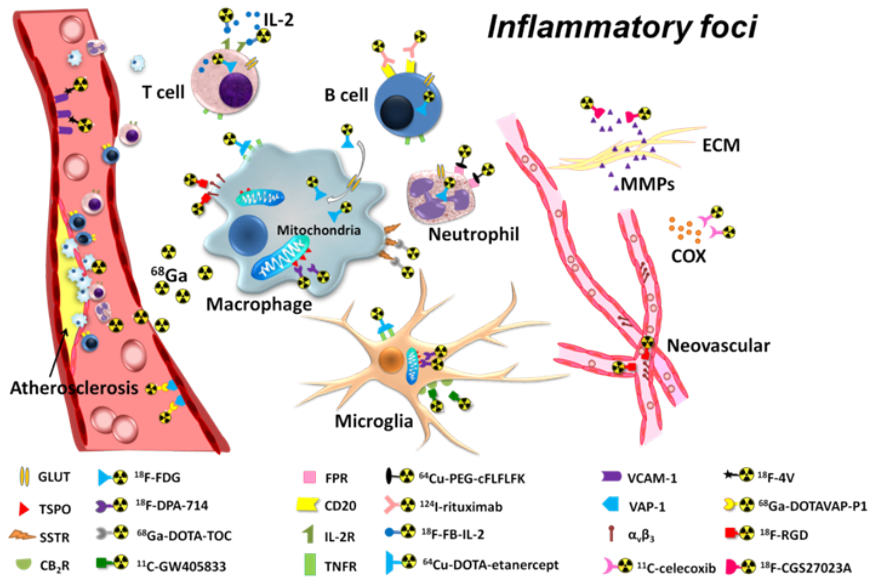


Figure 1.2.3: PET-radiotracers for inflammatory phenomena with corresponding targets

[Wu 13]

A wide range of studies have been carried out by numerous groups in an effort to better understand inflammation. The first steps were to analyze which aspects were able to be traced with the ultimate goal to one day be able to effectively diagnose and thus prognose an inflammation, no matter what the origin or state.

Some of the targets have been inflammatory cytokines, choline metabolism, inflammatory related vessels, and membrane markers.

1.2.1 Inflammatory targets

As inflammation induces a whole cascade of events, one can imagine that there are various participants that could serve as targets which in turn might be able to indicate the level of inflammation currently taking place.

Among the participants are MMP's (matrix metalloproteinase), inflammatory cytokines, and COX (cyclooxygenase). Each has a different function and is of interest for various reasons.

MMP's are zinc-dependant endopeptidases and were originally thought to be exclusively implicated in matrix degradation but have been proven to be able to modify cytokines (such as TNF-alpha, IL-6) and chemokines (CXCL-8 or CCL2 for example), which are found in inflammatory states and as such is now thought to be of importance for inflammatory conditions [Ryu 12]. This would mean that the imaging of the MMP's in itself would be of interest, and as such has been

investigated by Zhu et al. [Zhu 11] among others who have also mainly used SPECT as their modality of choice [Hermann 12] [Schäfers 04] [Kuge 10]. The areas in which these radiolabeled tracers have been used was largely in the cancer detection field, but also in vascular inflammation too.

PET has also been used to investigate MMP expression in the field of tumor imaging using [^{18}F]CGS27023A and [^{11}C]CGS27023A (same compound, marked with a different radioisotope) while ^{124}I -MIP (both are MMP inhibitors) to target vascular lesions [Wagner 9] [Zheng 02] [Hartung 07]. Initial investigations using [^{11}C]CGS27023A has led the researchers to continue the development of the tracer as it has a very high lipophilicity and as such yields characteristics which they deem possible to improve upon. Its counter part (the ^{18}F marked compound) has also shown to be of interest while also having a strong inhibitory effectiveness on MMP-1 in comparison with the parent compound CGS27023A. One should also note the half-life of ^{11}C (20.33 minutes) and take into consideration the impact that this time constraint has on clinical applications. ^{124}I -HO-MIP (half-life of 4.8 days) has also been tested and as might be expected, has the disadvantage of the relatively long half-life. The half-life is something to take into consideration, yet the potential impact does need to be weighed out as to whether or not a patient can benefit from a diagnosis using such a tracer with a long half-life isotope. Yet, MMP's are maybe not the most advantageous target all inflammatory diseases. There are various MMP's, some of which promote, and others inhibit the inflammatory process and as such are modulators. This means that the existing MMP radioligands to date are imprecise and as such yield poor specificity.

Inflammatory Cytokines are loosely defined as a group of immunoregulatory proteins (such as growth factors, interleukins and other lymphocytes) which are small in size, yet important in cell signaling.

There are a few cytokines which have been targeted in the past. Among them are IL-2 (interleukin-2), and the TNF-alpha (tumor necrosis factor alpha). Each has their role within the inflammatory process and as such were targeted for imaging purposes.

The presence of **IL-2** is augmented by activated T lymphocytes which are observed in multiple types of inflammatory pathologies ranging from tumor inflammation to organ specific autoimmune diseases [Kintscher 08]. These activated T lymphocytes (Th1 CD8^+ and CD4^+ in large part) not only synthesize the IL-2, but also express an IL-2 receptor to which the IL-2 bind with a high affinity. This shows the interest of using a marked (radiolabeled) IL-2 as the user is also able to differentiate between activated and non activated T lymphocytes. There have been some SPECT tracers which have been used in the past, but also PET tracers ($^{99\text{m}}\text{Tc}$ and ^{123}I labeled IL-2 for SPECT usage and [^{18}F]SFB to also label IL-2 to create the tracer [^{18}F]FB-IL-2 for PET acquisitions) [Di Gialleonardo 12]. The tracer

did prove useful and was able to assist the user in detecting areas of inflammation in an *in vivo* situation. The authors state that the tracer was indeed useful for the detection and quantification of lymphocyte infiltration. However, as imaging is a field in which many areas of science work together, one cannot just look at the final result. There are many difficulties that may be overlooked. Here for example, one must also consider the work that is done when preparing the radiotracer itself too. Even though, the tracer may be of interest, much needs to be done to facilitate the production as the radiolabeled IL-2 tracer is tedious to produce as there is a poor solubility and stability problems [Signore 02].

TNF-alpha is another cytokine that is implicated in the inflammatory phenomenon which is produced by monocytes and macrophages. There are two distinct actions that the presence of TNF-alpha causes. The first being physiological in that it increases the transport of white blood cells to the inflamed area. The second is pathological. There is a delayed inflamed state in which the presence of TNF-alpha leads to organ dysfunction and cellular apoptosis [Mäki-Petäjä 06]. Some of the tracers used in past *ex vivo* studies has been ^{64}Cu -DOTA-etanercept among others. ^{64}Cu -DOTA-etanercept for example was able to detect the TNF-alpha cytokines, but only in the early stages and was not of use for chronic inflammation as TNF-alpha is not significantly over-expressed outside of an acute inflammation.

The Cyclooxygenases (**COX,-1 and -2**) family are important enzymes for the conversion of arachidonic acid to prostaglandins along with other lipid mediators. As COX can be induced by inflammatory stimuli, COX-2 has been classically considered as the most appropriate target for anti-inflammatory drugs. The inhibition leads to pain relief [Hawkey 99]. It has been found that the cyclooxygenases are implicated in neuroinflammatory related instances such as cancers, Alzheimer's Disease, Parkinson's Disease, and various ischemias [Katori 00] [Minghetti 04].

As this is yet another aspect of the inflammatory process which could possibly be of interest for the imaging in community, multiple tracers have been developed and implemented in a range of studies. Some of the tracers (each a COX-inhibitor) produced are: ^{18}F desbromo-Dup-697, ^{18}F SC58125 as well as ^{11}C tagged celecoxib, and rofecoxib [de Vries 03] [McCarthy 02] [Prabhakaran 05] [de Vries 08]. The studies performed tried to address inflammation in the fields of neuroinflammation and tumors [de Vries 08] [Shukuri 11] [Gao 11] [Uddin 11]. The results of the previously mentioned studies revealed that the tracers were not of great value to imaging due to undesired *in vivo* and *ex vivo* characteristics such as low binding affinity and unspecific binding.

1.2.2 Inflammatory metabolism

In this area, there are two aspects to take into account. The first being glucose metabolism, which has been addressed in the Tracers/Contrast Agents section, and choline metabolism being the second.

Glucose metabolism, as previously mentioned, has its interests as an imaging target and is currently the most used radiotracer used for nuclear imaging purpose as it is very versatile. However, as it is 'versatile', [^{18}F]FDG is non-specific and often leads to a false positive diagnoses [Rosenbaum 06].

Choline is an amino alcohol found in the synthesis of two types of phospholipids; sphingomylin and phosphatidylcholine. The biosynthesis pathway of these phospholipids can be imaged using radiolabeled choline as choline is associated with the phosphorycholine, which is an intermediary step which is involved with the phospholipid synthesis. The choline, which is radiolabeled to with ^{11}C and ^{18}F , has been applied to image prostate cancers, but also inflammatory diseases such as atherosclerosis, by targeting the macrophages and monocytes [Schwarzenböck 12] [Matter 06]. ^{18}F labels choline is more interesting as the half-life is easier to handle in an clinical environment. The experiments carried out until now have shown that the ^{18}F labeled choline did not have other marked advantages, but could however create a point to consider as the kidney have a high choline retention along the nephrons, which must be considered when taking the radiation-dose into account [Witney 12].

In comparison to FDG, tagged choline has an advantage over FDG in that it has much less uptake within the heart and as such would be better adapted for detecting coronary plaques [Roivainen 06]. It is not only in the myocardium that [^{18}F]choline may have an advantage over the popular [^{18}F]FDG. [^{18}F]choline has been shown to have a better sensitivity for the detection and characterization of atherosclerotic plaques too [Matter 06].

1.2.3 Vascular biomarkers of inflammation

Another aspect of inflammation related to vessels is the permeability. In a physiological situation, the vessels are of the utmost importance in regulating a homeostatic state for the internal environment. This means that the structural integrity can be altered, situation dependent. Upon stimulation, the vessels can become more or less permeable. If an inflammatory state triggering various factors (such as cytokines, chemokines or leukotrienes) to be released by the local inflammatory cells, then the permeability is vastly increased in order to allow for the arrival and infiltration of macrophages or neutrophils, among other immune cells, at the inflamed site [Tsan 85]. This means that one would not have to distinguish between an infectious inflammation or a sterile one to be able to use a tracer for vessel per-

meability to target the inflamed area. The tracers developed (^{68}Ga -citrate among others) have been applied in animal models of atherosclerotic inflammation but also in models of bone defects [Mäkinen 05] [Silvola 11].

Swelling, or an edema, is one of the hallmarks used to characterize and describe inflammation. The change that occurs, from the non-swollen state to the swollen one, is due to alterations of the blood vessel permeability, their density as well as the vessel permeability.

Within this subject there are also multiple targets which can be of interest for investigatory purposes. Notably the vascular adhesion protein (VAP-1), Integrin receptor (integrin alpha-v-beta-3), vascular cell adhesion molecule (VCAM-1).

Once the VAP-1 is stimulated, which is located within the intracellular granules within endothelial cells, it relocates to the luminal area of the endothelial cells, which in turn causes leukocytes to migrate to the site of inflammation [Salmi 01]. This aspect alone would therefore be promising as a target of inflammation, thus enabling imaging of an inflammatory related occurrence. A few radioligands have been developed (^{68}Ga -DOTAVAP-P1 and ^{68}Ga -DOTA-Siglec-9 for example) as such and have been tested to see whether or not the VAP-1 expression could be evaluated [Autio 11] [Aalto 11]. The developed ligands were then compared to the tracer of reference (^{18}F FDG), and found that ^{18}F FDG could not tell the difference between the inflamed areas and a tumor. ^{68}Ga -DOTAVAP-P1 on the other hand had low uptake in Bx PC3 tumors which meant that there was perhaps the ability of the tracer to be able to detect a difference that was not possible using ^{18}F FDG, for inflammation [Ujula 09]. The findings then lead to seeing whether or not the ^{68}Ga -DOTAVAP-P1 VAP-1 ligand could then be used for applications investigating osteomyelitic bones [Lankinen 08].

Integrin alpha-v-beta-3 is a cell adhesion molecule (CAM) that becomes over-expressed in many situations ranging from neovessels post angiogenesis, cancer cell presence and in inflammatory cells such as macrophages [Hodivala-Dilke 08] [Desgrosellier 10] [Antonov 11].

Alpha-v-beta-3 has also been shown to be involved in some chronic inflammatory diseases such as inflammatory bowel disease (IBD) as well as rheumatoid arthritis [Danese 06] [Wilder 02]. RGD (Arg-Gly-Asp) peptides are alpha-v-beta-3 specific ligands, as has been shown over the past decades, which led to radiolabeled RGD peptides. The radiolabeled RGD peptides were then used as a complimentary aspect of inflammation to be compared to the conventional ^{18}F FDG [Gaertner 12]. The ligands however were only able to detect the chronic inflammation and failed to highlight the acute stages [Pichler 05].

VCAM-1, another CAM and is a membrane protein of the immunoglobulin superfamily endothelial adhesion molecules and is important throughout the stages of atherosclerotic plaque [Ley 01]. Its expression is augmented once it is activated

and as such was targeted with the tracer $[^{18}\text{F}]4\text{V}$ to observe its expression in an inflammatory state. Nahrendorf et al. were able to demonstrate that they were able to detect VCAM-1 expression non-invasively and correlate their PET quantification with the gene expression they analyzed (with VCAM-1). Beyond that, they propose that $[^{18}\text{F}]4\text{V}$ could possibly be implemented in situations that might involve VCAM-1-mediated monocyte recruitment [Nahrendorf 09]. The tracer has been since used for applications in myocardial applications as it does not share the same characteristic issues that $[^{18}\text{F}]4\text{V}$ does.

1.2.4 Other targets

There are multiple membrane markers on inflammatory cells for many different modalities. Formyl peptide receptor (FPR) is expressed on neutrophils and causes leukocyte migration when inflammation is present and is able to be used for multiple imaging modalities such as OI, MRI, SPECT and even PET imaging [Xiao 10] [Stasiuk 13] [Zhang 10] [Locke 09]. The ligand cFLFLFK is what is used to bind to FPR and is marked with ^{64}Cu to create cFLFLFK-PEG- ^{64}Cu for applications in PET. The team of Locke et al. were able to show a significant tracer accumulation in the lungs of mice when compared to the control group [Locke 09].

The two main targets however are type 2 Cannabinoid Receptor (CB_2R) and the Translocator protein (TSPO).

As the name CB_2R suggests, there are more than one Cannabinoid Receptor in the endocannabinoid system. CB_1R is expressed in the Central Nervous System (CNS), and is implicated in the immune response. CB_2R however is expressed at a much lower level than its CB_1R counterpart. This means that there is a lower background signal level when looking at an acquired image using PET. Thus, CB_2R is advantageous as it also is up-regulated in immune-responses and can be found in microglia, the resident immune cells within the CNS [Cabral 08]. Many studies have been carried out to evaluate whether or not the target could be of interest for PET imaging and are still currently underway as preliminary results from the groups of Vandeputte et al., Even et al., and Horti et al. have all shown promising results [Vandeputte 11] [Evens 12] [Evens 11] [Horti 10]. Alas, it is still not known the role of CB_2R within the CNS, thus demanding more research for this target. The other membrane marker is the translocator protein 18kDa.

1.3 The Translocator Protein 18kDa (TSPO)

TSPO, which was previously known as the peripheral benzodiazepine receptor (PBR), was originally discovered in 1977. It is an 18kDa transmembrane protein which is mainly found, and thus located, in the outer mitochondrial membrane.

A topological model of human TSPO through the outer mitochondrial membrane. There are 5 alpha-helical transmembrane domains as depicted in figure 1.3.1. (A) is a perpendicular view of the to membrane plane of the TpsO dimer with alpha-helices fitted into density. Yellow and blue a-helices represent individual monomers of TspO, and they are labeled arbitrarily a–e and a9–e9. (C) View perpendicular to membrane plane [Korkhov 10].

It is thought that TSPO forms a complex with other proteins of the mitochondrial membrane and plays an important role in the membrane permeability transition pore (MPTP), which is key player for the regulation of both apoptotic and necrotic cell death during injury [Papadopoulos 06].

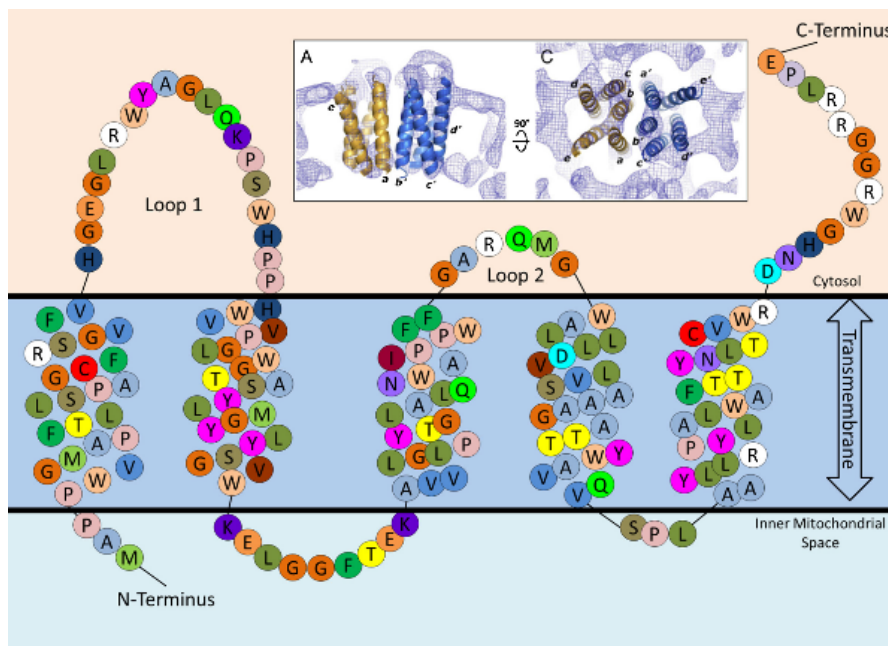


Figure 1.3.1: Topological model of human TSPO through the outer mitochondrial membrane

[Korkhov 10]

The exact functions are still illusive, but it is clear that TSPO is important as cellular proliferation requires much energy which requires significant mitochondrial input [Austin 13]. Other roles in which TSPO is of importance are Ca^{2+} regulation as well as mitochondrial respiration and oxidation. Ca^{2+} is stored within the mitochondria for signaling functions. If TSPO is activated by a ligand, this will also induce an alteration of the intracellular Ca^{2+} via the MPTP, and this in turn initiates transepithelial Cl^- secretion. This may be involved in the modulation of cell apoptosis [Ostuni 07]. A final implication of TSPO is with the mitochondrial respiration and oxidation. As mitochondria generate ATP, the electron transport needs

to be maintained by a phenomenon called mitochondrial respiratory control. Studies using PK11195 and Ro5-4864 demonstrated that the mitochondrial respiration can be altered and is dose dependent, meaning that there is not an on-off switch per se but can be modulates [Hirsch 89]. While the structural make-up of TSPO is starting to be better understood, thanks to NMR spectroscopy, its functionality has been put into questions. The main function is to regulate cholesterol translocation (hence the name) via the mitochondrial membrane. This in itself important as it is what determines the rate at which biosynthesis occurs [Veenman 07]. It is after this step that the cholesterol is converted to pregnenolone by cleavage of its oxidative side chain by P450_{SCC} [Scarf 09]. As such it is critical for the homeostatic state of the cell. TSPO is located at the MPTP, as previously stated and as such is important in the regulation of cellular apoptosis [Papadopoulos 06]. Beyond this, TSPO is also important for the transport of porphyrins and heme biosynthesis. The iron levels in mitochondria are elevated, as it is the site of heme biosynthesis, to be able to support future biosynthesis for various molecule, such as heme [Verma 87]. TSPO is also implicated in the protein importation and cellular proliferation within the mitochondria.

Figure 1.3.2 is an illustration which exemplifies all the previously mentioned implications of TSPO. (A) Forms part of the mitochondrial permeability transition pore (with other protein constituents), the TSPO helps to regulate the release of apoptotic and necrotic factors into the cytosol. (B) TSPO is responsible for binding and transporting cholesterol into the mitochondria for bioprocessing into steroids. (C) TSPO translocates porphyrin molecules (including protoporphyrin IX) into mitochondria for iron incorporation and heme synthesis. (D) TSPO transports mitochondrial pre-proteins into the organelle for maturation – this is an important stage in cell proliferation. (E) Small molecule ligands bind and alter TSPO function (e.g.affecting Ca²⁺ concentration or mitochondrial respiration)[Austin 13].

While some of the functional roles have been able to be determined, there is yet another aspect of the TSPO 18 kDa that still remains unknown: the binding sites. Previous research has shown that there are perhaps multiple binding sites even. While this finding in itself is an accomplishment, it is still not clear what the nature of them is. In order to better understand this protein, various ligands have been used to try and better understand the functionality of the binding sites, namely benzodiazepine Ro 5-4864 and the isoquinoline carboxamide PK11195. Each (depicted in figure 1.3.3) of the ligands has a nano-molar binding affinity and are both TSPO selective [Scarf 11].

TSPO is expressed ubiquitously throughout the periphery (kidneys, heart and other steroid producing organs), and only to a small extent within the healthy brain. This minimal level is increased in diseased states such as found in AD, PD, or stroke subjects [Scarf 09] [Venneti 08]. The increase has also been shown to

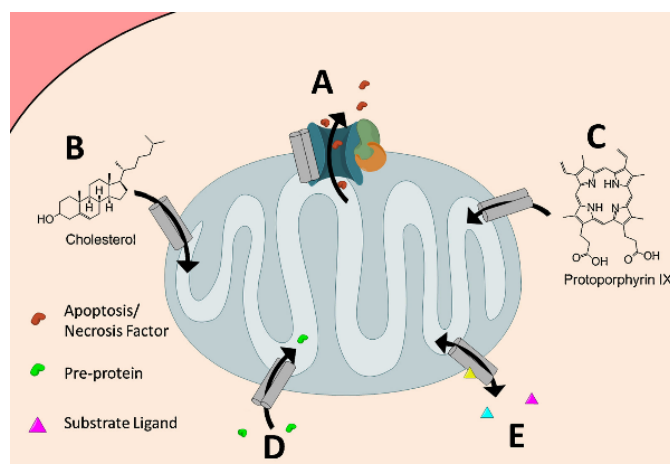


Figure 1.3.2: TSPO implications

have a correlation with microglial activation as well [Scarf 09].

With this being the case, interest was sparked and developments have been made to create PET radioligands which target TSPO selectively while having a high affinity. This then has enabled researchers to investigate the process which is implicated for microglial activation.

The expression of TSPO has also been evidenced in Schwann cells in the peripheral nervous system (PNS) as well as in macrophages, to include detection for atherosclerosis and rheumatoid arthritis, as well as inflammatory bowel diseases (IBD) [Bird 10] [Pottier 14] [Ostuni 10]. As mentioned previously, TSPO is also expressed in the periphery, where it has also been over-expressed in various cancers to include, breast, colon, and prostate cancers [Batarseh 10]. All this evidence only supported the initial theory that TSPO could be of great value as a target for imaging the inflammatory process.

Both PK-11195 and Ro-4864 have proven to be very promising in the preclinical studies that have been carried out on human glioma and breast cancer models [Buck 11] [Wyatt 10].

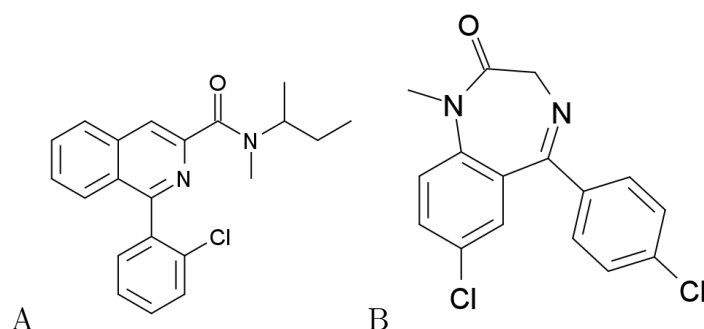


Figure 1.3.3: Molecular structures of the TSPO ligands PK11195 (A) and Ro 5-4864 (B)

The two ligands, PK11195 and Ro 5-4864 are able to displace one another and are each able to saturate a binding site. This is good, however, the results which have been obtained have varied from one species to another [Scarf 09]. Some other studies were contradictory in showing that PK11195 was able to bind to multiple sites and the research of Sakai et al. was able to find that there are two separate binding sites [Sakai 10]. This is not all though; yet other studies, using other ligands have revealed there are even differences in binding site affinities from one patient to another [Kreisl 10]. It turns out that the first radioligand used, ^3H -PK11195, had a stable uptake throughout the subjects tested, along with brain tissue. ^3H -PBR 28 on the other hand revealed different uptake from one patient to another [Owen 10]. Saturation studies revealed that ^3H -PBR 28 bound to three separate binding sites for TSPO, a low-affinity binding sites, a high affinity binding site, and a mixed affinity binding site [Owen 10]. PK11195 has since been tagged with ^{11}C to be adapted for PET imaging and has been applied in cases dealing with atherosclerosis, vascular inflammation, acute subcortical stroke, neuroinflammation in AD patients, just to name a few [Gaemperli 12] [Pugliese 10] [Thiel 10] [Edison 08]. . ^{11}C PK11195 has been useful, but has certain aspects which still leave something to be desired, be it a higher affinity or better specificity. As microglia has come under the magnifying glass, so to speak, and become a target of interest for PET imaging, it became clear that there was a need for improved radiotracers for this protein. ^{11}C PBR 28 was also synthesized to be adapted to PET imaging initially and applied in to studies involving primates and rats for applications addressing the effect of systemic inflammation on microglia and neuronal inflammation involving early epileptogenesis respectively [Hannestad 12] [Dedeurwaerdere 12].

^{11}C PK11195 has thus far been the reference by which other tracers have been judged. Yet, ^{11}C PK11195 has weaknesses which cause it to be insufficient in regard to its pharmacokinetic properties. Beyond this, there is a poor bioavailability

for the brain tissue and the high non-specific binding [Venneti 06]. Of course, one should always consider that half-life of ^{11}C (20.4minutes) which in itself is an aspect which limits the geographic delivery range to which the tracer could be brought to from a production center. This brings us back to the ^{18}F (109.8 minute half-life duration) labeled tracers, in terms of practicality purposes. These limitations inspired some groups to carry out their investigations into the possibilities of creating an improved tracer [James 06].

There are still many questions remaining unanswered regarding the relationship between the structure of the protein and the metabolic activity of TSPO as becomes clear when looking at the studies performed by the group of Owen et al in which they bring to light that there are polymorphisms (as previously mentioned) of the TSPO which lead to a variation in affinity to the radioligand PBR28 [Owen 11]. As TSPO is transmembrane protein, it has proven very difficult to study. These difficulties are multifaceted and are not limited to complications with purifying and stabilizing the protein. The obstacles hinder the x-ray crystal analysis for the structural studies [Scarf 11]. As such, other groups have attempted to reveal the structure by means of immunodetection, thermodynamic simulations, the use of the bacterial homolog TspO (tryptophan rich sensory protein) from *Rhodobacter spheroides* as well as nuclear magnetic resonance. This last method has yielded interesting results and was able to bring to light a 3D structures seen in figure 1.3.1A [Korkhov 10]. Korkhov and his colleagues suggest therefore that there are 2 binding sites per dimer which in turn would permit a cooperation between the transportation of substrates and as such possibly have an enable allosteric modulation [Korkhov 10].

1.3.1 TSPO radioligands and evaluation

As this topic sparked a rapid development of over 40 different potential radiotracers for this one target [Chauveau 08]. As these were all experimental, some were deemed more or less promising. However straight forward as this may seem, there are always obstacles which need to be overcome. one major point to take into consideration is the basis of comparison. One cannot compare apples and oranges so to speak, one must make a comparison just. As the ultimate goal is to create clinical applications, it was decided that animal models would be the most fitting and best suited. Yet, one must then consider the reproducibility of the animal model along with the species of choice too. As the primary applications of the TSPO ligand seem to be directed towards cerebral pathologies, brain tissue would be a logical target to test the novel radioligands on. As for a species; rodents, rats more specifically, are an obvious choice in the preclinical field, as they are genetically identical, easy to keep without taking too much space, yet have a brain which is still large enough to carry out PET studies on. As TSPO

has a low expression at a basal state, the animal model also needs to be robust and should ideally induce an inflammation for which a high target to background ratio can be acquired from [Benavides 83]. The animal model of choice was an unilateral intra-striatal injection of AMPA ((RS)-alpha-amino-3-hydroxy-5-methyl-4-isoxazolepropionic acid hydrobromide) for which the methodology will be explained in detail in the materials and methods section.

Once the model was decided upon and developed to a point at which it was reproducible, the tracers could then be tested *in vivo*.

One of the first novel tracers which reached preclinical trial stages was [^{11}C]DPA-713, which was tagged with ^{11}C to create [^{11}C]DPA-713.

Some of the characteristics of this tracer offered advantages over the reference [^{11}C]PK11195. [^{11}C]DPA-713 demonstrated a higher, and therefore better, signal to noise ratio than its competitor [Boutin 07a]. The authors suggest that this difference is due to a lower non-specific binding, meaning that there is less non-specific binding of the [^{11}C]DPA-713 compared to [^{11}C]PK11195, which in turn means that there are better conditions for quantification. Beyond this fortunate finding, [^{11}C]DPA-713 also displayed a slower pharmacokinetics (accumulation occurred over a time period of 20-40 minutes) than [^{11}C]PK11195 (which accumulated much faster at 1-15 minutes post injection) [Chauveau 08]. It was supposed by the authors that this could possibly be the case if [^{11}C]DPA-713 had a lower lipophilicity, this meaning that the number of free ligands is also reduced when compared to [^{11}C]PK11195 [Boutin 07a]. Seeing that [^{11}C]DPA-713 is labeled with ^{11}C , and knowing the restrictions or disadvantages that this brings along with it, it was a logical step to attempt to mark the DPA-713 with ^{18}F .

This was then carried out which then led to the comparison between the radioligand of reference; [^{11}C]PK11195 and its new competition [^{18}F]DPA-714, but also then compare this novel tracer with its predecessor [^{11}C]DPA-713 (all of which are depicted in figure 1.3.4).

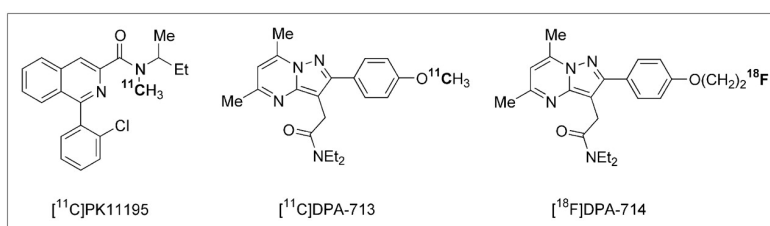


Figure 1.3.4: Chemical structures of [^{11}C]PK11195; [^{11}C]DPA-713; and [^{18}F]DPA-714

This comparison led to a publication by Chauveau et al. in 2009 [Chauveau 09]. Here they also used the AMPA animal model which was previously mentioned

and used by the same group and considered to be an efficient neuroimaging model [Boutin 07a] [Boutin 07b] [Chauveau 08]. The idea behind this study was to observe whether the ^{18}F tagged TSPO ligand would be of interest for further studies considering its preferred isotope.

Initial findings did reveal that their model did indeed create a difference in neuroinflammation from one hemisphere to another, meaning that not only did the AMPA do what it was intended to, but also that the contralateral side served as a convenient control tissue from the same subject.

Each of the novel tracers was able to be displaced by the reference compound PK11195 and the cold compounds as well (DPA-713 and DPA-714 respectively), proving the specificity. Interestingly the ^{18}F marked DPA-714 was more displaced than the ^{11}C DPA-713, and was thought to perhaps be caused by a difference in non-specific binding levels of the two molecules, ^{11}C DPA-713 and ^{18}F DPA-714 [Chauveau 09].

The study also yielded results indicating that ^{18}F DPA-714 performed the best when looking at the signal ratio ipsi-lateral vs contra-lateral. This suggesting a higher bioavailability within the tissue.

While these results were promising in a predictive animal model, it has underlined the interest of pursuing further studies in which ^{18}F DPA-714 can be used for the study of other inflammatory issues.

1.4 Issues effecting society

1.4.1 Inflammatory bowel disease

The previous section included remarks about some of diseases which are affected by the inflammatory process. As one can tell, there is a vast number of pathologies which are implicated and there might be many others which have not yet been studied and thus escaped realization of its inclusion into the phenomenon. Just reading about a study however does not give an idea of the grandeur of the impact, especially when looking at a single disease or disease family. Inflammatory bowel disease for example is not a single disease, but rather a family in which Crohn's Disease and Ulcerative Colitis also belong. IBD is a disease which society does not talk about as it makes most individuals uncomfortable and due to this one does not come face to face with the pathology.

Beyond the fact that it is a sensitive subject for patients to discuss, medical doctors also have difficulty classifying each IBD pathology. This leads to methodological differences in their analysis and thus diagnosis which in turn impacts how a regional prevalence is evaluated [Gismera 08]. Nonetheless, when looking at all the various retrospective, and the few prospective, reviews, the data seems to indicate

a rise in IBD presence throughout. In particular in the industrialized countries. Figure 1.4.1 from Molodecky et al. illustrates the increased incidence in both CD and UC diseases. Worldwide CD (Left column) and UC (Right column) incidence rates and/or prevalence for countries reporting data (A) before 1960, (B) from 1960 to 1979, and (C) after 1980. Incidence and prevalence values were ranked into quintiles representing low (dark and light blue) to intermediate (green) to high (yellow and red) occurrence of disease

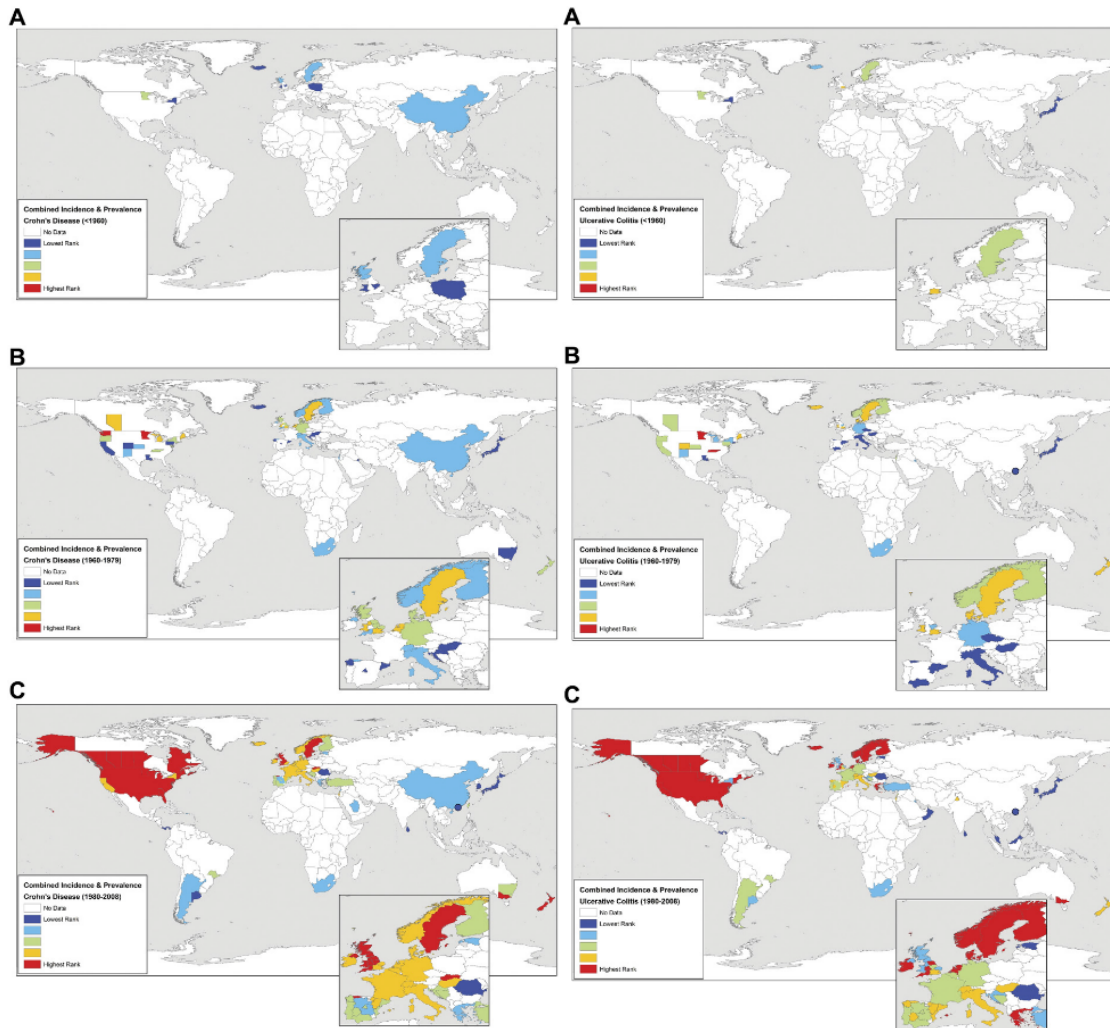


Figure 1.4.1: Worldwide IBD prevalence
[Ostuni 10]

As the seriousness of the disease becomes evident (even when considering how much of the world still lacks data) when looking at only the rise in incidence, one would hope that the topic has been addressed. There has been much research

that has gone into all aspects of IBD, ranging from the understanding of the basic biology of the diseases, to the treatment, prognosis, but also the diagnosis and detection of the various diseases within this family.

As described initially, molecular imaging, PET specifically, is a tool with great potential if used correctly. This implies using the correct tracer for an adapted target for the problematic at hand. Lacapere et al. found that there was a presence of TSPO 18 kDa in individuals suffering from IBD. This would then mean that one would be able to detect this protein using the radioligand [^{18}F]DPA-714 to detect its presence and thus, theoretically be able to tell a difference between IBD sufferers and those who are not and perhaps even help with the diagnosis seeing as that one would then also be able to visualize the exact location of the inflamed area [Ostuni 10].

The potential benefit is enormous when considering that the treatments could then reach the personalized level.

Inflammation within the bowel is however not the only burden that patients suffer from. Another field which was touched on earlier in the text was neurodegenerative diseases. The following subsection will elaborate on that topic.

1.4.2 Neurodegenerative diseases

In order to better understand the magnitude of the issue, one must perhaps see number to start to have a grasp on just how many individuals are currently and will be affected one day by one or more of the neurodegenerative disease that are known to date. Among the most well known, not necessarily understood, are Alzheimer's Disease, Parkinson's Disease, Huntington's Disease, Amyotrophic Lateral Sclerosis and prion diseases. These diseases are not only causing suffering to the individuals who have one or more of the listed diseases, but their families and even society are also impacted. In 2010, Alzheimer's Disease International estimated that there were 35.6 million individuals suffering from dementia alone and that this number would increase to 65.7 million by the year 2030. By 2050, an estimated 115.4 million people will be effected by dementia [Wimo 10].

To put some numbers in terms of economic costs to the disease: annually, it is estimated that \$604 billion are spent on dementia. The socioeconomic impact is high to say the least. And if dementia were a country, it would rank 21st in the world in terms of largest economy [Wimo 10].

Although, as a society we tend to only see the aftermath, one must not forget that to alter the effects, it is necessary to act ahead of time. The best way to act in time then, is to detect and thus prevent any advancement of the pathology in question.

As previously demonstrated, inflammation is at the core of the issue. This is a process which is complex and tries to balance the equilibrium between preservation

and restoration. This is paradoxical as it (the physiological response to various stimuli) increases the damage as well as the disease state under pathophysiological conditions [Jacobs 12]. With this taken into account, one should also understand that this response will thus determine the final outcome.

It is due to all this, that nuclear imaging is so important. It allows for an early detection, a spatial detection, and a quantifiable, and thus specific, detection in many different pathologies, yet could allow for a benefit throughout the medical field in regard to the possible diagnosis of other diseases.

But what if the problematic is not so clear-cut. What if the symptoms are due to a problematic or a pathophysiological state which is more complex than if it were due to just one single/local inflammation. What if there is multiple organ failure..?

1.4.3 Septic shock

Sepsis is a difficult and challenging subject to try and decipher. All systems are under shock and create a systemic inflammation which affects even the brain. Hannestad et al. demonstrated that they were able to detect an increased level of TSPO, with the use of [^{11}C]PBR28, within the brain of nonhuman-primates after inducing a systemic inflammation with the use of *E. coli* lipopolysaccharide (LPS) [Hannestad 12].

This begs to ask other questions then; would it be possible to quantify a systemic inflammation? Would it be possible to reliably detect the difference in TSPO presence within each organ?

Each of the previously mentioned topics left us with questions about whether or not TSPO could possibly be a good target for the detection and quantification of an inflammatory state. Would it be possible to measure this difference? To do this we had to develop various animal models in which an inflammation would be induced, be it global, local, systemic, acute or chronic. In the following section there will be a description of the materials and methods used to try and answer the posed questions.

1.5 Objective of the thesis

To date it is accepted that TSPO is of importance for the inflammatory process, and we now know that it is possible to trace its presence with a variety of adapted radiotracers. [^{18}F]DPA-714 is very promising, but it is necessary to push the envelope to find out its capabilities and possible applications as inflammation impacts a large number of people across the world for various reasons as previously evidenced.

Here we will look into various animal models which replicate human diseases of high social impact, and analyze and quantify the levels of TSPO 18kDa found in each of the subjects to determine whether or not TSPO can be used as a target for the evaluation of an inflammatory state within a single individual using PET imaging with the radioligand [¹⁸F]DPA-714.

Chapter 2

Materials and methods

As seen in the preceding section, there are questions that need to be addressed and in order to better do so, and in a fashion which could then be transferred to humans as soon as possible, there is a need for experiments which are adapted to the question at hand.

In order to best replicate the disease, and thus inflammatory states, in question we developed animal models for each of the diseases in order to acquire *in vivo* images using PET imaging in order to quantify the data. Once this was done, the animals were sacrificed and the organ in question was excised and analyzed by various methods as described below.

2.1 Animal models

The animals chosen were male Wistar rats (Centre d'Élevage René Janvier, France) with a weight of $250\text{g} \pm 20\text{g}$. The subjects were kept in an adapted environment in which the temperature and humidity are regulated. The lights are on a 12h cycle on and then off. The experiments were carried out in accordance with French guidelines.

Two different animal models of acute bowel inflammation were developed and implemented in the study

2.1.1 Animal model for a global intestinal inflammation

The first being a Dextran Sodium Sulfate (DSS) (Sigma-Aldrich, France; MW40,000), induced model, which leads to haematochezia, and also to weight loss along with a shortening of the intestine among other consequences leading to a colitis rat model [Okayasu 90]. DSS induces *in vivo* intestinal inflammation and is simple, affordable, and also has a high degree of uniformity and reproducibility of most

lesions in the distal colon. In this model we added DSS at 5% (v:v) into the drinking water of the animals from which they had ad libitum access throughout the duration of the experiments. [^{18}F]FDG images were acquired after 7 days of treatment whereas [^{18}F]DPA-714 images were acquired after 8 days of treatment. The treatment has been used successfully with rats in previous tests [Gaudio 99]. Non-treated rats were given plain water in their bottles and all the animals were weighed daily and their feces state was also observed on a daily schedule. The DSS solution was exchanged for a new one on days 3 and 5 in the treated groups and the non-treated groups also had their water exchanged for a new bottle containing plain water at the same time points.

2.1.2 Animal model for a local intestinal inflammation

The second model was carried out on the same species as well as the same weights and was chemically induced by instilling Trinitrobenzenesulfonic acid (TNBS) (Sigma-Aldrich) as described by Seibel et al. [Seibel 09]. Some slight alterations were made in order to adapt this model to the PET modality. Here, inflammation was induced into male Wistar rats by administering 100 μL of 50% ethanol-water solution (to help bypass the mucosal layer of the intestine) containing TNBS (100g/L, corresponding to 40mg/kg body weight) 4 cm into the rectum from the anus [Hibi 02]. During this administration, the rats were under anesthesia using 2.5% isoflurane in 100% O_2 . This anesthesia was maintained for an extra 10 minutes post instillation in order to reduce displacement and possible leakage of the chemical. Non-treated animals were injected with 100 μL of ethanol and water (1/1, v:v). The animals were then placed into individual cages and their weights were measured on a daily basis and their feces state was also observed. Inflammation was evaluated with PET imaging on day 7 using [^{18}F]FDG and on day 8 using [^{18}F]DPA-714 after TNBS administration.

2.1.3 Animal model for neuroinflammation (INMiND)

This model is very similar to that previously used by Chauveau et al. (also Wistar rats at about 250 grams) and was used such as to observe and analyze the neuroinflammation induced by lipopolysaccharide LPS (Sigma-Aldrich, lipopolysaccharide from E. Coli 055:B55) [Chauveau 09].

The striatal injections were carried out while the rats were under 5% isoflurane anesthesia and maintained by 2.0%2.5% isoflurane in 70%/30% NO_2/O_2 . 1 microliter of LPS (1 μg ram/ μl iter in phosphate-buffered saline) was stereotactically injected in the right striatum (the bregma: +1 mm rostral-caudal; -3 mm medial-lateral and -4 mm dorsal-ventral) using a 1-mL micro-syringe. The Hamilton needle is left in place 5 for minutes before injecting the LPS with a micro-pump

at an injection rate of 0.5 $\mu\text{L}/\text{min}$. (UltraMicroPump II and Micro4 Controller; WPI Inc.). The animals were maintained normothermic using a heating blanket (Homeothermic Blanket Control Unit; Harvard Apparatus Limited). Once the injection was completed, the needle was left in the injection site for a further 10 minutes in order to allow absorption of the LPS. The needle was then removed slowly to avoid an ejection of the LPS as well.

The site of incision was then cleaned, and sutured using 4.0 braided silk before being disinfected.

The animals were then placed into a warming box in which they awoke on their own before being placed back into their cages.

2.1.4 Animal model for tracer evaluation

The animal implemented here was identical to that of the INMiND LPS model (Wistar rats at about 250 grams) with the exception of the injection coordinates and injected product. These were as follows, again using the bregma as a reference point: the bregma: +0,7 mm rostral-caudal; -2,7 mm medial-lateral and -5,4 mm dorsal-ventral into the striatum. The injected product was alpha-amino-3- hydroxy-5-methyl-4-isoxazole propionic acid (AMPA) ([AMPA] 15 mM in phosphate-buffered saline [PBS] buffer; Sigma) and injected at a rate and volume of 0.5 $\mu\text{L}/\text{min}$ and 0,5 μL respectively.

2.1.5 Animal model for septic shock

Here we also used Wistar rats at a weight of about 250 grams each. The LPS was from the same batch as same as previously mentioned in the INMiND neuroinflammation section. We dissolved the LPS in physiological solution at 5mg/kg. The solution was then injected *i.p.* while under anesthesia at a concentration of 2-3%. The animals were returned to their cages for 24 hours before image acquisition.

2.2 Imaging

2.2.1 PET Radiotracer

[^{18}F]FDG was purchased from the commercially available source Cyclopharma S.A. (Clermont-Limagne, France). [^{18}F]DPA-714 was produced on site according to slight modifications of procedures already reported [Damont 08], and using a commercially available GE TRACERLab FX-FN synthesizer [Kuhnast 12]. Ready-to-inject, >99% radiochemically pure [^{18}F]DPA-714 (formulated in physiological

saline containing less than 10% of ethanol) was obtained with 15-20% non-decay-corrected yields and specific radioactivities at the end of the radiosynthesis ranging from 37 to 111 GBq/ μ mol.

2.2.2 μ PET image acquisition

The PET and PET/CT images were acquired using two separate machines. The first one is a Siemens INVEON PET and the second a Siemens INVEON PET/CT, both being dedicated small animal scanners with a resolution of 1.4 mm. Each animal had its images acquired in the same machine each day. The animals were kept normothermic with the help of a heating carpet. Rats had a catheter placed into one of the lateral tail veins after having been anesthetized at 4% Isoflurane. The anesthesia was then adjusted as needed while keeping the animals sedated throughout the acquisition. Images were acquired dynamically during a time span of 60 minutes, beginning at the same time as the injection. The [^{18}F]DPA-714 dynamic images were acquired with the same protocol. Each animal was injected with 37 ± 2 MBq (1.0 mCi \pm 0.054 mCi). Both the [^{18}F]FDG acquisitions and the [^{18}F]DPA-714 images were sorted into 16 frames. Frames 1-5 each lasted 1 minute, frames 6-10 lasted 2 minutes, frames 11-13 each lasted 5 minutes, and the remaining frames (14-16) lasted for 10 minutes each. The energy discrimination was set at 350 KeV and 650 KeV. The list-mode acquisition was as described previously and the data files were histogrammed into 3 dimensional sinograms with a maximum difference of 47 and a span of 3 [Damont 08].

The attenuation correction of the Siemens INVEON PET was measured with the help of a Cobalt-57 point source. The Siemens INVEON PET/CT carried out the attenuation correction measurement with the use of its CT imaging capabilities and settings, which are implemented directly by the manufacturer. In order to obtain the best resolution possible within the intestines, we implemented a Fourier rebinning and an OSEM 2D reconstruction method.

2.2.3 HRRT image acquisition

Rats were anesthetized (isoflurane with oxygen, 4% for induction and 2.5% thereafter) and the tail vein was catheterized. Rats were imaged using an HRRT scanner (Siemens-Healthcare, Knoxville, TS, USA), a dedicated human brain PET scanner with an isotropic spatial resolution of 2.5 mm. Rats were placed in an especially designed bed in which it is possible to image four rats simultaneously. This device is adapted to the HRRT gantry and ensures suitable anesthetic supply to each animal. PET acquisition started at the time of the injection and lasted for 60 minutes. A dynamic series of 16 images were reconstructed, with a temporal frame duration ranging from 15 s at the beginning to 120 s at the end of the scan.

2.2.4 PET image analysis for the IBD models

The reconstructions of the PET images were carried out using OSEM 2D. The image analysis and quantification of the radioactivity uptake in the regions and volumes of interest (ROI's & VOI's) were carried out with the use of Brain-Visa/Anatomist Version 4.3.0. Delineation of the ROI's and VOI's was selected by means of manual segmentation and always carried out by the same user. The selected region of the intestine was 5 x 3 x 2 voxels, or a 3.6 mm³ volume placed on the intestinal wall.

2.2.5 PET image analysis for the neuroinflammation model

The analysis of the images was carried out with the same tools as mentioned above, however the selecting of the ROI was done manually for both hemispheres. The contralateral side serves as the control and a VOI of a spherical size of 4 was systematically used in order to be able to compare all the subjects to each other. A muscle section was also chosen as it was in the other models, again to be able to compare all the subjects.

2.2.6 PET Image analysis for the septic shock model

As the septic shock induced a systemic inflammation, it is not easy to distinguish one tissue from another as a user. However, using the methodology developed by Maroy et al. [Maroy 08], it was possible to obtain the different VOI's and evaluate the level of inflammation found in each one.

2.2.7 Statistical analysis

Statistical analyses were conducted using Microsoft Excel software and GraphPad Prism software. A significant difference between treated and control groups was determined at each point by the one-tailed Student's t-test.

2.3 Ex vivo gamma counting

The intestines were excised once the subject had been euthanized via an *i.v.* injection of pentobarbital and divided into 3 sections. The sections were then placed into individual tubes, which were then inserted into a Perkin Elmer Cobra II Auto-Gamma Gamma-ray counter.

2.4 In vitro

2.4.1 Autoradiography study for the IBD models

We created a solution of Trizma[®]Base 50mM (Sigma Aldrich, primary standard buffer at equal or higher than 99.9% titration) and NaCl 120 mM (Sigma-Aldrich, France, ACS reagent at equal or higher than 99.0% purity) which was introduced into MilliQ (Millipore, France) filtered water and mixed until both powders were dissolved. Once this was done, the pH was measured (using a HANNA pH21 pH/mV meter) and adjusted to 7.4 pH using HCl (Fischer Scientific, Analytical Reagent). The solution was then stored at 4°C over-night.

The following day, the solution is filled into 4 baths of 200mL each which are themselves placed onto a chilled work bench.

The radiotracer is then added into the top bath along with the 200mL solution. The slide, which were kept in the cold as long as possible, were then submerged and left in the initial bath, containing the solution + radioactive tracer, for 20minutes. Then the slides are rinsed in 3 more successive baths for 2 minutes, 2 minutes and 5 seconds respectively. Once the slides have been removed from the final bath, they are then left to dry on a heated plate for about 5 minutes. Once the slides are dry, they are then places in an autoradio-cassette containing a phosphor-imaging screen and left for 10 half-lives.

Once this time period is done, the screen is taken out of the cassette and scanned using a Storm 860 scanner (Molecular Dynamics).

When the scan is completed, the image is then analyzed using the free software Image J.

2.4.2 Autoradiography study for the tracer validation

The solution was prepared as previously described. Once the tracer was ready along with the competitive cold compounds, the brain slices were incubated with [¹⁸F] DPA-C5yne ([¹⁸F]-1, 7.4 nM) alone, and also co-incubated with non-labelled DPA-C5yne (1, 20µM), or PK11195 (20 µM, the TSPO ligand of reference) in order to confirm the selectivity and specificity of the binding.

2.4.3 Immunohistochemistry (IHC) and morphological analysis

Post mortem tissue samples were excised, once the [¹⁸F]DPA-714 images had been acquired, and fixed with 4% paraformaldehyde (PFA, Sigma-Aldrich) in Phosphate-buffered saline (PBS, pH 7.4 Sigma-Aldrich, France) for 2 h followed by cryopreservation by incubation in PBS, pH 7.4 containing 20%-sucrose for 24 h.

The intestines were then cut into thirds (ascending, transverse, and descending sections), immersed in embedding tissue (Shandon M-1 Embedding Matrix, Thermo, USA) and frozen rapidly in liquid nitrogen. Immunohistochemistry was then carried out on the specimen from which slices of 5 μm thickness were cut. Anti-TSPO marker (NP-155, kind gift of Dr. Makoto Higuchi, The National Institute of Radiological Sciences, Chiba, Japan) was used on individual slices. Non-specific binding were blocked with 5% BSA and 0.5% Tween 20 in PBS (5 min, room temperature (RT)) and incubated (1 h, RT) with primary antibodies as follows: Rabbit anti-TSPO antibody (NP155, 1:500) diluted in 5% BSA and 0.5% Tween 20 in PBS, and, after PBS washes (three times), sections were incubated (30 min, RT) with Alexa Fluor-488 goat anti-rabbit (A11034, 1:1000; Invitrogen, France), diluted in 5% BSA and 0.5% Tween 20 in PBS.

Hematoxylin and eosin

The frozen slides containing slices of the intestines were placed into fresh PBS for rehydration 5 min before being placed into deionized water for one minute. The slides were then introduced for 5 min into Hematoxylin solution ready to use (Sigma-Aldrich, France). Once this was carried out, the slides were placed into tap water for 5 mins before being placed into a series of 5 mins-baths of deionized water, followed by Eosin-Y solution (LABOnord, Templemars, France), 90% ethanol in water, 100% ethanol and finally toluene for 15 minutes. Once this was done, the slides were individually mounted with the Eukitt quick-hardening mounting medium (Sigma-Aldrich, France), by placing a few drops onto the slide and then laying a cover slip over them.

Nissle staining

Frozen brain slices were rehydrated in successive baths, for 1 minute each, containing ethanol at concentrations of 100%, 95%, 70%, and then finally 50%. The slides were then rinsed for 1 minute in tap water. Then the slides were placed into Cresyl Violet (acc. Moore, DiaPath, Microstain Division, Italy) for 5 minutes. The slides were then dipped in tap water a few times before incubating them in ethanol for 10 seconds, 10 seconds, 90 seconds, 1 minutes and 1 minute in 50%, 70%, 95%, 100% and 100% respectively. Once that was done, the slides were incubated in 2 separate Toluene (Toluene Pure, Carlo Erba Reagents, France) baths for 5 minutes each. Then the slides were mounted with Eukitt quick-hardening mounting medium (Sigma-Aldrich, France) and let dry.

Evans blue

A 2% solution of Evans Blue in normal saline (4 ml/kg of body weight) was injected into one of the lateral tail veins of the subjects while they were anesthetized with isoflurane between 2 and 3%. Once injected, the stain was allowed to circulate for 10 minutes. At this point the subjects were sacrificed and the brain was removed quickly and submerged into isopentane which was already cold enough to freeze the brain without letting it explode (about -40°C). Once hardened, the isopentane is removed and the brains are then placed into liquid nitrogen and stored at - 80 °C for later analysis.

Section II

Chapter 3

Evaluation and quantification of TSPO expression in an acute model of global intestinal inflammation

Objective: To determine if TSPO 18kDa can be used as a precise -, specific -, and quantifiable target for the evaluation of the inflammatory process in an animal model presenting a global intestinal inflammation, using the radioligand [^{18}F]DPA-714.

Summary:

This chapter explores the potential of TSPO 18kDa to serve as a precise-, specific-, as well as measurable parameter of inflammation using the radioligand [^{18}F]DPA-714 for its evaluation. Beyond this, we will also compare the obtained results of the TSPO radioligand to those obtained with the most commonly used radiotracer for IBD imaging, [^{18}F]FDG, which was used in the same subjects.

3.1 Model validation

As animal models can be a challenge to put into place, some research had to be carried out in order to see whether or not something regarding this topic had already been done. As it turns out, not only had an animal model of a global inflammation been mentioned in literature, but another author had also found the presence of the target of choice, the translocator protein 18 kDa, too [Ostuni 10]. This was of particular interest as the same group had reported findings of TSPO in human biopsies of patients suffering from Crohn's disease (CD), Ulcerative Colitis (UC) as well as colon cancer.

We were able to use the animal model described by Lacapere and as such attempted to reproduce it, as described in the materials and methods section. The protocol had worked for us as indicated and was verified by evaluating feces state and weight loss of each subject on a day to day basis.

However, the lab in which the group of Dr. Lacapere was implementing this model had different objectives and tools than we did. This meant that we had to make some considerations to obtain the most accurate information possible.

3.1.1 Imaging specific considerations

When looking at a physiological system, one must also look at all organs which could possibly be impacted or impacting upon the area of interest. Seeing as that we were looking at the intestines, the lower intestine specifically, we had to consider various factors.

Gravitational factors

The first factor we considered was the effect that gravity would have on the animals. Normally this is not such an issue, but as we had planned to acquire images over the course of a whole hour, it was important to take the flattening of the animal into account. This is important as the animal then spreads out over the body support. The reason for this is that we wanted to be certain that there was no movement or displacement over time.

Some instances would allow for simple taping (as seen in figure 3.1.1) of the subject to the bed. This can work just fine for many applications. In our case however, we wanted to avoid taping the animals to the support as it would compress the organs of the animal, thus possibly rendering the tissue of interest difficult to analyze.



Figure 3.1.1: Animals can be simply taped to the support in some instances

To address the obstacle, we used a simple box (as seen in figure 3.1.2) which was cut to size to fit the animal and provide support along the sides of the subject.

The box was cut such that the tail could protrude, allowing access to a vein, while still fitting into the FOV of the scanner as well. Also, we left the box slightly wide, laterally, and used rolled cotton pads to insert between the walls of the box and the animals flanks. This was done in order to obtain a rounder shape of the animal and this a less squished organization of the internal organs.

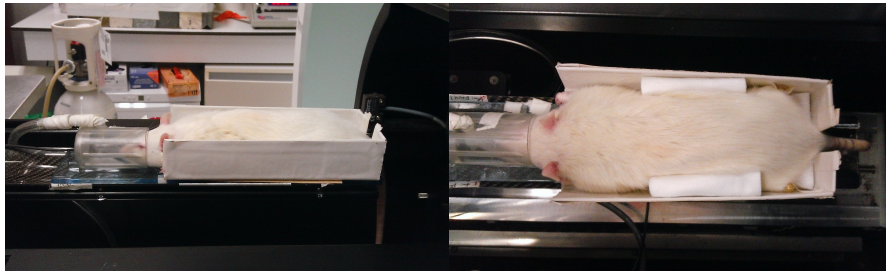


Figure 3.1.2: The box helped maintain the positioning of the animal without the use of tape and the subsequent compression of the internal organs.

VOI definition

Initially we acquired the first images as described in the materials and methods chapter. One of the machines at the institute is a Siemens μ PET/CT machine which uses the CT image for the attenuation correction, meaning that we were obliged to use the CT in any case and following this, we decided to attempt to apply it for the selection of the volume of interest and then apply the VOI from the CT to the PET image to then extract the data for the quantification.

The CT settings however were optimized for speed of acquisition, and not contrast, leading us to attempt to improve on this aspect. The default settings yielded the image depicted in figure 3.1.3.

Contrast improvements

The first ideas were to naturally adjust the look up table (LUT) and alter the color scale. This did not work as desired which led us to trying to introduce a contrast agent (CA).

Barium sulfate

The first one to be tried was barium sulfate as this is the contrast agent which is commonly used for the investigation of the bowel in humans.

Adding barium sulfate to the drinking water was not successful as the animals did not like the taste and the barium sulfate also separated from the water quickly,



Figure 3.1.3: CT images acquired with the default settings. These settings are optimized for speed of acquisition, and not soft tissue contrast.

leaving a sedimentation along the base of the bottle, which is inserted into the cage at a 45° angle.

The next attempt was to administer the barium sulfate by gavage. The administration was successful using a small metal pipe, which had a smooth plastic cover on the end being inserted as to avoid damaging the esophagus of the subject. The animals did not take well to this and caused discomfort, keeping the animals awake at this stage helped the injection of the CA as their reaction was to ingest.

The following unknown was the time that it would take for the barium sulfate to reach the lower intestine. This led us to then acquire multiple CT images of the same subject at different time point in an attempt to determine at when the CA should be administered to be able to best define the VOI based on the CT image.

The results however were very diverse and varied from subject to subject, rendering this method of little use. However, the barium sulfate did yield a decent contrast, as expected. This meant that we could perhaps still obtain a contrasted image if we changed the method of administration.

Following this observation, we began to administer the CA rectally, just prior to the image acquisition (both CT and PET), in hopes that we could extract better contrast for the VOI determination. The reason for the administration prior to the acquisition is that we wanted to avoid altering the position of the lower intestine in regard to the PET image, thus defeating the purpose.

The adding of the CA was fairly straight forward. However, the images acquired were not of much help as the Barium was not coating the entire lower intestine and we had to roll the subject to assure covering the whole lumen of the intestine. Certain tests revealed a sedimentation of Barium along the lower section, in regard to the bed (ventral). Other images revealed the creation of artifacts as can be seen

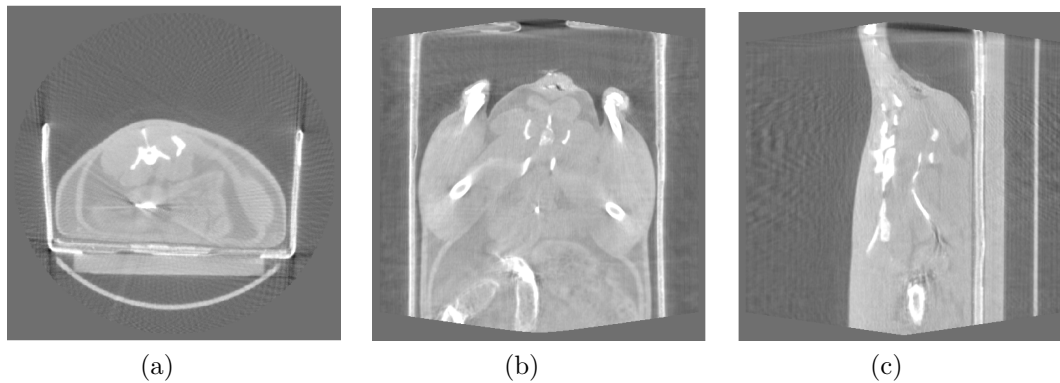


Figure 3.1.4: The first image (a) illustrates the displacement of the Barium. One can observe (in each of the views coronal (b) and sagittal (c)) that the delineation of the lumen is difficult with the artifact that was created.

in the first image of the figure 3.1.4. We did notice that the presence of feces was also playing a role in the artifacts in that the Barium could not bypass the feces in all cases due to human error, but also, the feces seemed to absorb the CA to an extent. This phenomenon can be seen in the second image of the same figure. The third image of the same figure illustrates that the spread of Barium was also uneven, thus not allowing for confidence in its use for this application.

Bowel cleaning with Klean-prep

As the presence of feces was potentially causing an obstacle for the application of Barium for the aid in contrast, we administered Klean-Prep. This product is commonly used for the preparation of the colon prior to a colonoscopy or X-ray and is considered to be an important procedure to undergo before a diagnostic examination.

The application of this product was less helpful than hoped. Not only could we still find a sedimentation of Barium along the ventral section of the lower intestine (still causing artifacts), but it also obstructed another parameter we wanted to observe; the feces state. As the Klean-Prep aids in emptying the intestines, we could no longer be sure if the feces state was due to the initial DSS 5% administration, or if it was due to the Klean-Prep (figure 3.1.5).

Negative contrast

Barium sulfate, being a positive contrast, was not of much use in our application as we determined. But we still had hope to create contrast, just by other means.



Figure 3.1.5: These subjects were given Klean-Prep prior to imaging in order to empty the bowel.

The next idea was to use negative contrast. The thought was to introduce a liquid into the rectum which had a density lower than water, but was more viscous to avoid leakage which would alter the volume within the colon.

We decided on using corn oil as this had been used by other teams in the past too [Pickhardt 05].

The oil was introduced rectally with a gavage needle, again to avoid damage to the intestinal walls. As the oil is still rather non viscous, there was still leakage found. This problem was resolved after multiple attempts ranging from taping cotton to the orifice to 'plugging' with an obturator. The latter solution worked best, but in the end was still not of much help as the wall thickness seemed compressed. Beyond this however, the oil was lining the colon, which in turn could cause a potential problem for the tissue treatment that was to follow. Had the study been solely for the contrast, the oil maybe have been of great interest. However, this was not the case. We were creating more problems than solutions. This was amplified as we would have to introduce the oil prior to the PET image as the anatomical location would have to be kept the same to avoid misalignments between the modalities for the drawing of the VOI. Figure 3.1.6 illustrates the resulting images.

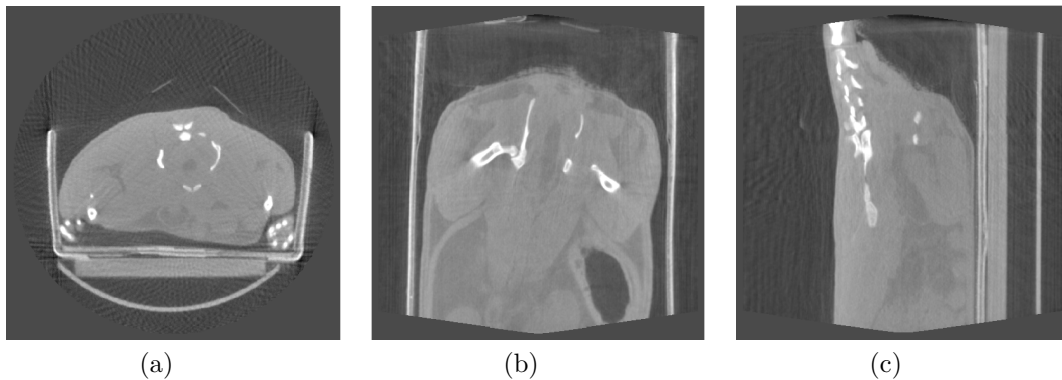


Figure 3.1.6: This figure illustrates 3 slices (axial (a), coronal (b), and sagittal (c)) of an animal in which Corn Oil was used to attempt to use a negative contrast for an improved visibility of the intestinal lumen.

CT parameters

As each of attempts for improved contrast (both positive and negative agents) were of little help, we turned to the CT settings. It was clear that we would have to forfeit speed for contrast as the original settings for the attenuation correction for time optimized for time.

As there were multiple parameters to change, we made a side study in which we were able to determine the best settings for a good contrast for the soft tissues within a Wistar rat at about 250g.

Initially we looked at the parameters at hand and altered them one by one. The parameters we were able to alter were the voltage settings (kV), time of exposure (ms), the number of projections (to increase the number of projections over a 360° radius), and current settings (μA).

We had to be methodological and so we stepped through each parameter, one by one. The first parameter was the voltage that we looked at.

The minimum was 40kV, while the maximum was at 80 kV. So, we tried both as well as the median voltage of 60 kV. Each of the settings revealed the corresponding images depicted in figure 3.1.7.

As we lowered the voltage however, we were obliged to increase the exposure time in order to optimize the caption of the x-rays. This would mean that the animal would be obliged to remain under anesthesia longer than with the default settings.

The next parameter we looked into was the exposure time. This was our next choice as we thought that the voltage settings made a difference and wanted to shorten the time that the acquisition would take. The figure 3.1.8 illustrated the

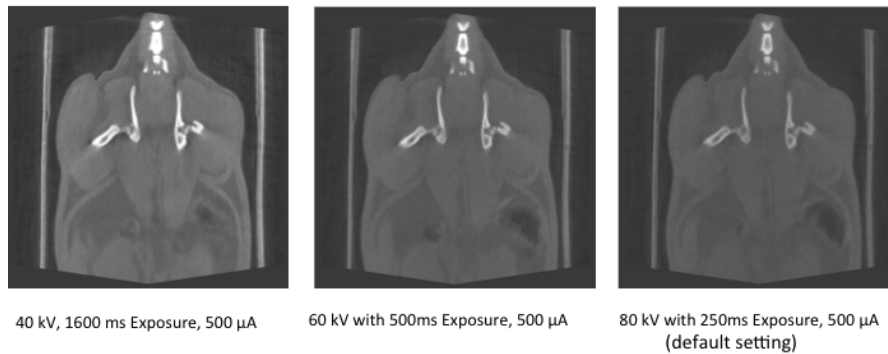


Figure 3.1.7: Here one can see that the altered voltage settings had an impact on the contrast and varied from the default settings found on the image on the right.

images corresponding to the various exposure time settings.

Having analyzed each of the images, we decided to make a compromise as is often the case in imaging. We decided upon 1000ms exposure in order to gain in contrast, but thought that exposing for a 1600ms was too long and would potentially cause undesired effects on the animal, namely premature death, possibly leading to a loss of PET data.

Once we had decided on that, we still had another 2 parameters to look into.

The default settings have a projection occurring every 2° over a 220° circumference. The thought was to then increase this number by simply taking out the 2° steps and project at each degree over the original 220° degrees and then testing the whole 360° .

This alteration was quickly chosen against as the acquisition time was going to take about 40 minutes before taking the second bed position into account. This is a step that would be necessary for the PET study as the PET FOV is slightly larger than a single CT FOV.

The final parameter was the current (μ A). The default setting is at 500 μ A and the minimum at 100 μ A. So we acquired images at 100 μ A, 300 μ A, and 500 μ A All while having steps every 2° over a 220° range around the animal.

The two images acquired at 100 μ A and 300 μ A were more grainy and did not allow any gain in time. It is for these reasons that we then decided to go forward with the settings with an energy of 40kV, exposure times of 100ms and a current of 500 μ A. All while having steps every 2° over a 220° range around the animal. This was a decent alteration from the original settings which were determined to be quickest, yet solely for the attenuation correction, and not for any gain in anatomical information. The chosen settings yield the above image shown in figure 3.1.9.

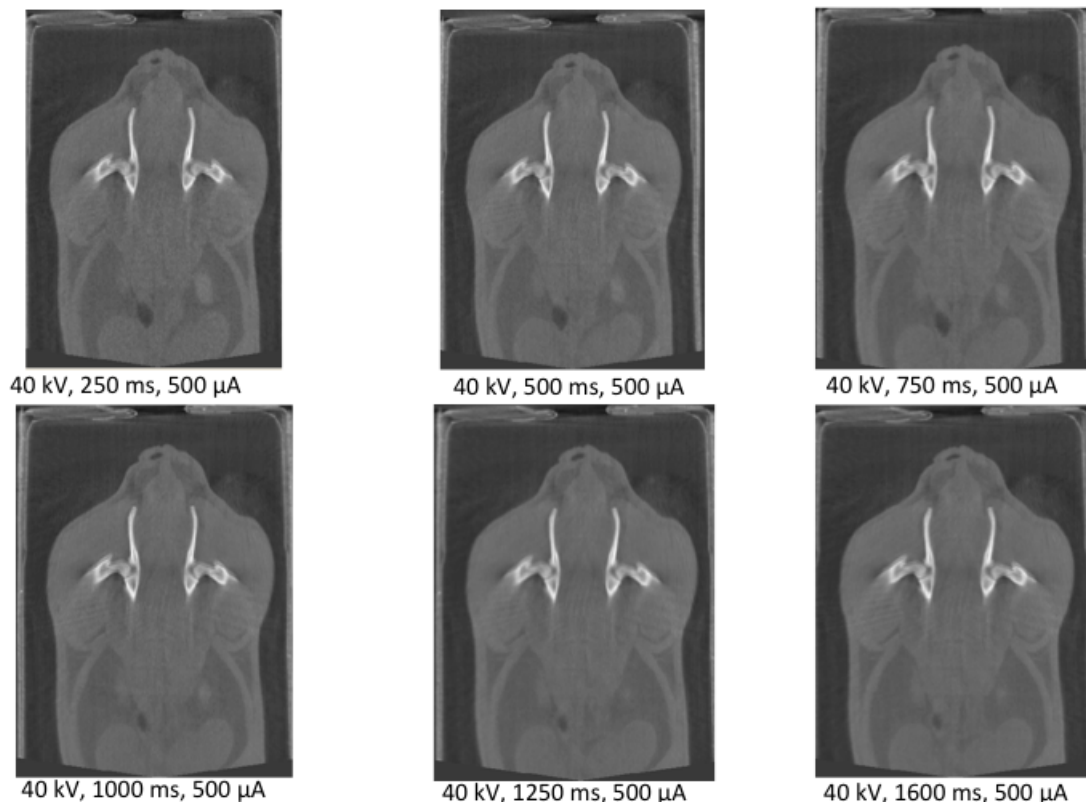


Figure 3.1.8: In this figure one can observe the impact that the alteration of exposure time had on the resulting image.

Co-registration

As we were now content with the CT settings and assured that there was no bowel movement that we should be worried about, we carried out an exam and found that the images from each modality (CT and PET) were not aligned as can be seen in the following *in vivo* image 3.1.10.

To assure ourselves that this was due solely to the machine and not an external factor, we carried out another experiment with a phantom depicted in figure 3.1.11.

The bad alignment did indeed come from the machine and not due to an external factor such as an anesthesia tube tugging on the bed, thus causing a displacement.

This mismatch however was not devastating as we were then able to create a co-registration in Anatomist which corrected the misalignment. As this problem came from the machine, it was a constant and the co-registration was applicable to all images already acquired.

Reconstruction after co-registration with both images corrected this.

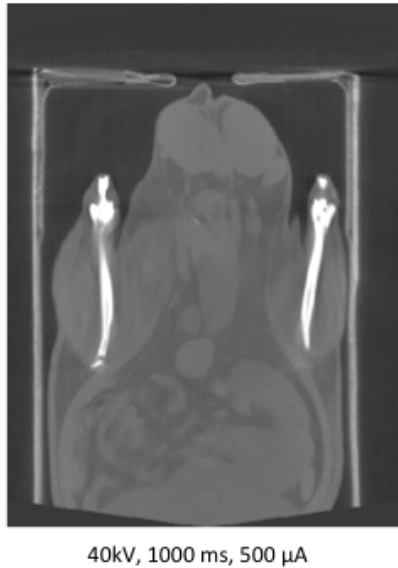


Figure 3.1.9: The settings of choice were determined at an energy of 40kV, exposure times of 100ms and a current of 500 μ A.

Quantification method

Initial attempts to quantify the inflamed area were difficult as we were obtaining values in the inflamed animal which were lower than the control animals. This was odd as we were able to see on the images that there was a higher signal in the DSS 5% treated animals once the images had been calibrated.

However, as inflammation can occur in living beings who are healthy, there will also be areas which are affected, thus leading to a signal. As this signal may be very local, but relatively high, the VOI selected will not have the same area in each of the cases. Beyond this, inflamed colons increase in surface size and it turned out that due to the fact that we were designing the VOI around the entire colon, we were artificially lowering the signal when compared to the control animals. It is also possible that this difference in signal was due to an alteration of the wall thickness. A wall thinning, due to the DSS 5%, would then increase the partial volume effect, thus decreasing the quantified signal.

This means that we had to devise a way in which we were able to select the VOI in a manner which would not impact the quantification.

The solution we came up with was to apply the same region, to each of the animals, around the area of highest intensity. The volume selected was chosen as 5x2x3 voxels. This was the mean volume typically found around the area of highest signal. Figure 3.1.12 illustrates the means by which the VOI was defined.

Result of the Fusion:

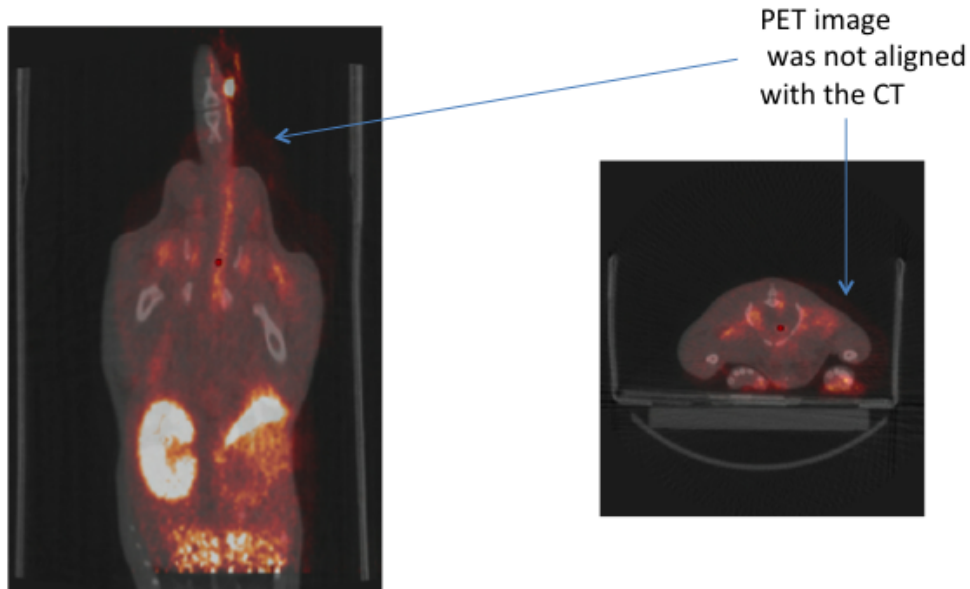


Figure 3.1.10: Misalignment of the CT and PET images

Beside being able to avoid surface area impact on the quantification, we were also able to avoid any impact that the presence of feces might have had on the selection process.

Applying this method allowed, to the PET image, for an accurate quantification, but it also meant that we would not be applying the CT settings we had selected for the anatomical information. The optimized settings were good for the differentiation of various tissues, but the acquisition took 4 times longer than the default settings which were adapted for the speed. As we wanted to avoid leaving the animal in the machines longer than necessary, we opted for the more efficient settings. This choice was not all bad though as it would also allow us to use both of the μ PET machines. One of which uses a point source for the attenuation correction instead of a CT scan. The ability to use two machines, doubled the throughput ability which not only was an advantage to the number of subjects we were able to acquire images of, but it also allowed us to use twice as much of the tracer from the same synthesis as we had less decay constraints.

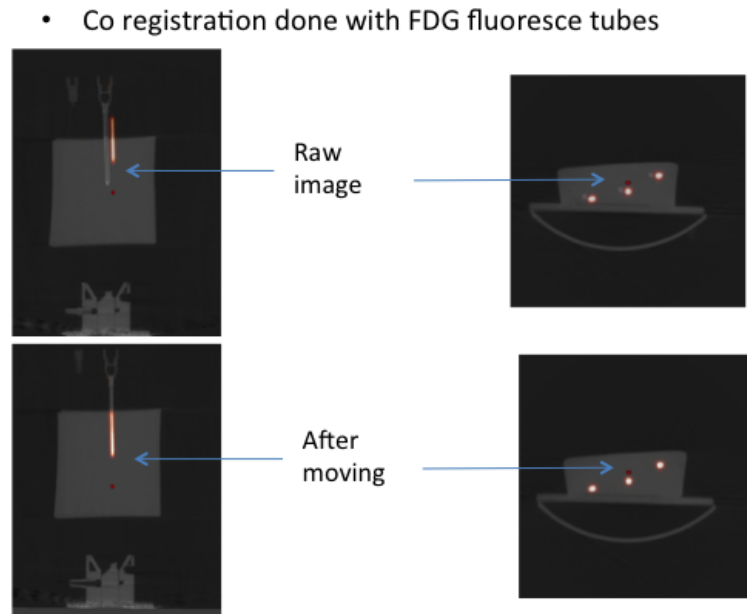


Figure 3.1.11: Phantom experiment indicating that the co-registration issue stemmed from the machine.

3.2 Radiotracer choice and comparison

3.2.1 Reference glucose analog vs. TSPO ligand

To date there is one radio tracer which dominates in the clinical field, the glucose analog $[^{18}\text{F}]\text{FDG}$ which will indicate an increase in glucose metabolic activity. This is helpful for many applications, yet, it is non-specific of inflammation. This means that there is no indication about the origin of the increased metabolic activity it. It is not always necessary to distinguish what the causes are. There are however cases in which it is of great interest. IBD related diseases are such instances in which it can be of diagnostic value to be able to differentiate between a metabolic increase, and an inflamed area, for example. Hence the application of this model of a global inflammation, and two radiotracers. The first one being the reference glucose analog $[^{18}\text{F}]\text{FDG}$, and the second one being the $[^{18}\text{F}]\text{DPA-714}$, which targets TSPO, as described in detail the introductory section.

In order to compare the two tracers, we found it best to do compare the two tracers using the same groups. To do this, we administered the DSS 5% to the subjects and acquired images of the animals using $[^{18}\text{F}]\text{FDG}$ 7 days later. The animals were then put back into their cages and images again the following day using $[^{18}\text{F}]\text{DPA-714}$, as the $[^{18}\text{F}]$ from the FDG was then completely decayed and

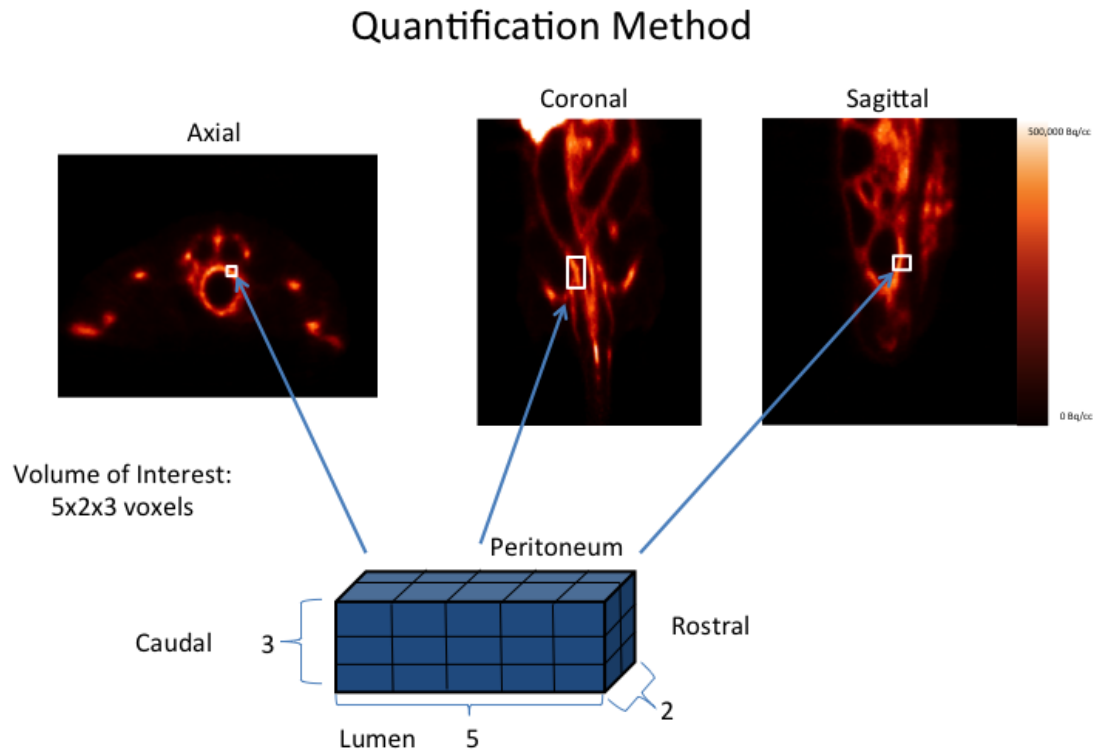


Figure 3.1.12: The VOI was selected as a 5x2x3 voxel volume in order to prevent an impact on the quantification due to a difference in surface area.

did not interfere with the tracer signal.

3.3 Results

3.3.1 Observation of the animals well-being

Initially, the treated animals did not drink as much as the control animals did. This is possibly due to the taste of the DSS 5%. Once ingested however, the treated animals drank more than the control group. Food consumption was not altered in either group.

The treated animals showed some weight loss, and also revealed an alteration in their feces state ranging from normal, to loose feces with some associated bleeding.

3.3.2 PET results

As we were able to replicate the animal model as previously described by Lacapere, we also knew at which time point we would have the highest level of inflammation. It is based on this that we chose the previously mentioned time points for image acquisitions. Using the methods described in the materials and methods chapter, we obtained the following images (figure 3.3.1) and results (figure 3.3.2).

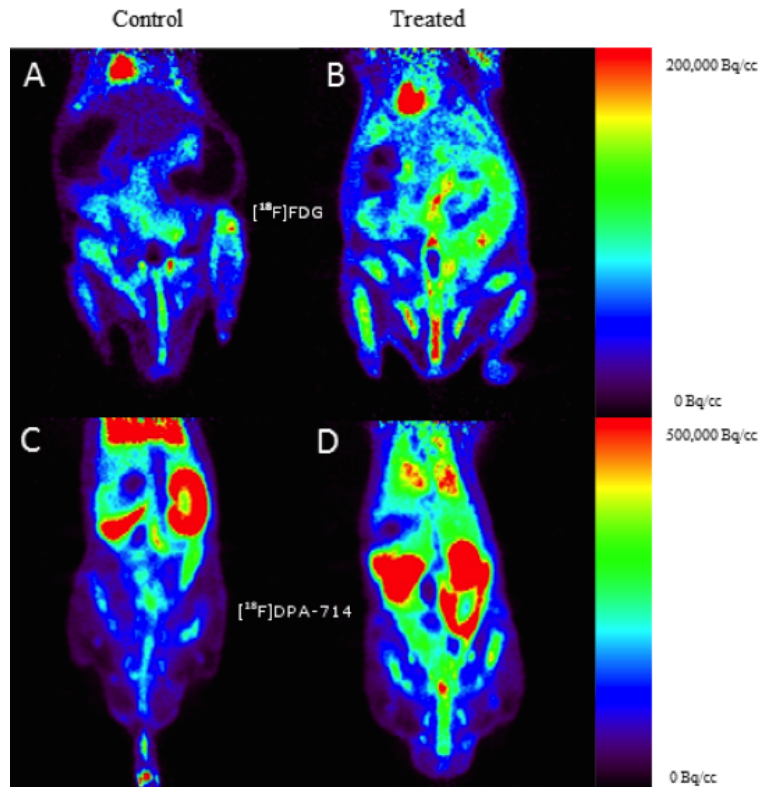


Figure 3.3.1: The above images are of two control animals (labelled A & C), and two treated (labelled B & C). The top row are of animals injected with [¹⁸F]FDG while the lower row were injected with [¹⁸F]DPA-714. One can observe a difference in uptake between the non-treated and treated animals in both cases.

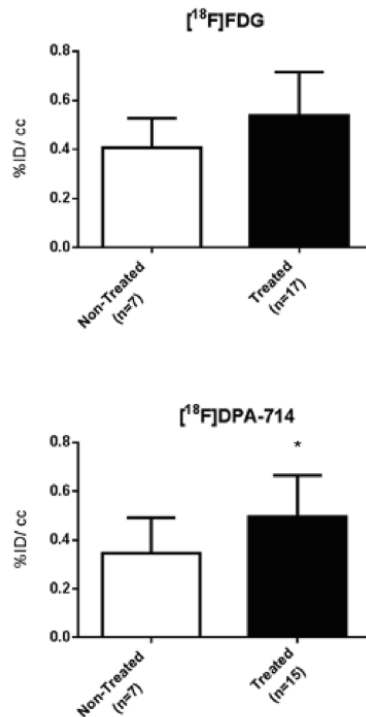


Figure 3.3.2: $[^{18}\text{F}]\text{FDG}$ did not reveal any significant differences between the two groups while $[^{18}\text{F}]\text{DPA-714}$ did show a significant difference between the treated and control groups ($p < 0.05$)

Both tracers showed an increased uptake within the colon of treated animals in comparison to non-treated animals. The image quantification of the radioactivity uptake after 60 min of acquisition revealed that for $[^{18}\text{F}]\text{FDG}$ the mean glucose consumption in the colon increased from 0.40 ± 0.11 %ID/cc to 0.54 ± 0.17 %ID/cc as illustrated previously. This increase identifies the inflammatory processes but it is not sufficiently high to provide a significant difference between the two groups of rats ($P = 0.053$). Similarly, quantification of $[^{18}\text{F}]\text{DPA-714}$ within the colon of non-treated and treated animals revealed a significant increase in uptake level from 0.35 ± 0.15 %ID/cc to 0.50 ± 0.17 %ID/cc ($P = 0.040$).

3.3.3 Gamma-count

To assure ourselves that we were indeed able to differentiate the two groups (non-treated and treated) using the radio tracer $[^{18}\text{F}]\text{DPA-714}$ we verified the PET obtained results with a gamma counter.

In the graph (figure 3.3.3) containing the gamma count quantification, one can

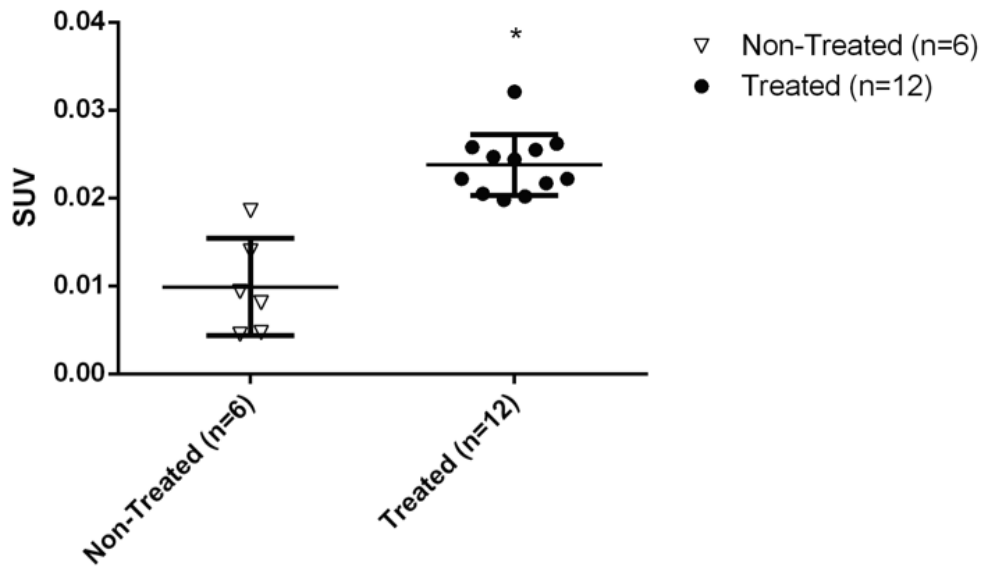


Figure 3.3.3: Weight corrected gamma-count results

observe that the PET data, and the subsequent analysis, were verified and subsequently validated with the gamma counting using a Perkin Elmer Cobra II Auto-Gamma counter. Here we also observed a significant difference between the treated and control groups where $p < 0.0001$.

3.3.4 Histo- and immunohistochemistry

Tissue analysis is still the reference and as such we also excised tissue samples, not only for the gamma-count, but also for an histo- and immunohistochemical analysis. The histological analysis we carried out using H&E staining methods depicted in figure 3.3.4.

Microscopic observations on the different sections of the colon (ascending, transverse, and descending) of treated animals revealed erosion along the entire colon. The control animals revealed intact crypts and villi. These features corresponded with what the group of Lacapere had found in which their group also determined difference between control and treated groups. The control groups revealed intact structures which were dense. The intestinal mucosa had tightly packed microvilli which protruded into the lumen in an organized fashion. The duodenal gland

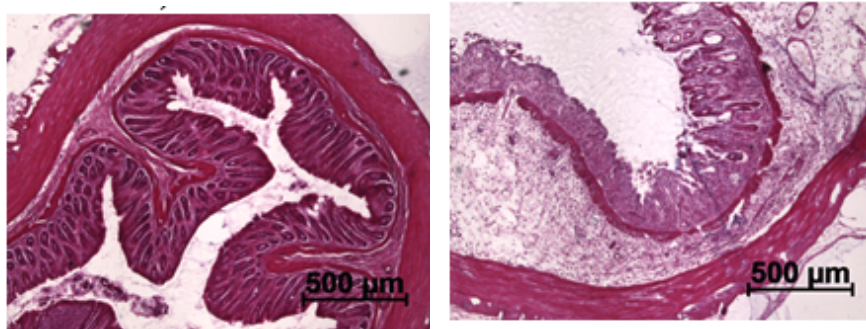


Figure 3.3.4: Hematoxylin & Eosin staining revealed marked difference between the structural integrity when comparing tissue samples obtained from control animals (image A) and treated animals (image B).

within this mucosa was also rather thin and also relatively dense and homogenous. Also, the muscularis mucosa was continuous within the control animals.

The treated animals on the other hand revealed a muscularis mucosa which was interrupted. One was able to observe gaps which allowed the villi to come in direct contact with the duodenal gland. The duodenal gland also revealed a large increase in size. The microvilli were also destroyed and partially, if not completely eroded.

We then investigated the TSPO expression on adjacent tissue samples using the TSPO antibody NP-155.

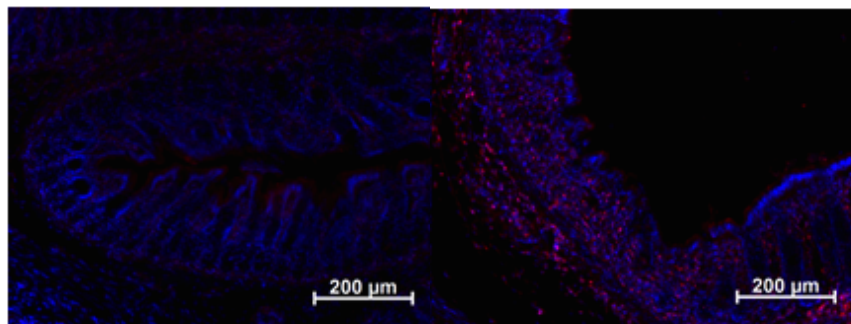


Figure 3.3.5: Immunohistochemical analysis using DAPI (blue) and the TSPO antibody NP-155 (red)

In figure 3.3.5 one can clearly observe the increased presence of TSPO in the colon of treated animals with high infiltration in the entire eroded lamina propria and high density at the base of the intestinal wall (lamina muscularis/mucosa). In

comparison to non-treated animals, TSPO positive cells were mainly found at a lower density within the lamina propria.

3.4 Conclusion

We demonstrate here that with the use of an adapted tracer [^{18}F]DPA-714, we are able to detect, visualize, and quantify a difference between the non-treated animals and the ones that underwent the treatments in order to induce IBD symptoms for a global inflammation. This indicates that the target TSPO may be of great interest in the application for this type of disease.

Seeing as that we were able to detect a significant difference in a global inflammation, we then wanted to investigate as to whether or not one would be able to determine a difference in an IBD model of local inflammation.

Chapter 4

Evaluation and quantification of TSPO expression in an acute model of local intestinal inflammation

Objective: To determine if TSPO 18kDa can be used as a precise-, specific-, and quantifiable target for the evaluation of the inflammatory process in an animal model presenting a local intestinal inflammation, using the radioligand [^{18}F]DPA-714.

Summary:

This chapter aims to evaluate the potential of TSPO 18kDa as a precise-, specific-, as well as measurable parameter of inflammation using the radioligand [^{18}F]DPA-714 for its evaluation. As in the previous chapter, we will also be comparing the results obtained with the [^{18}F]DPA-714 to those obtained using reference tracer [^{18}F]FDG. These comparisons will be made at the peak inflammation, which we will also be determining.

4.1 Model validation

Here we were also quite fortunate in that we were given a starting point from a group who had put an animal model in place for a local inflammation. Although, as in the model of global inflammation, here too we needed to make some adjustments to adapt this model of local inflammation to the tools of molecular imaging for the inflammatory process.

4.1.1 Imaging specific considerations

The starting point we had was based on the animal used by the group of Dr. Seibel. His group was also instilling an intestinal inflammation which was designed to have local effects in which he introduced the TNBS at a depth of 8cm from the rectum.

Pharmacokinetics

As in the preceding chapter, here too we were obliged to make slight adjustments to the animal model in order to adapt it to the imaging tools. The animal model described by Seibel et al. was adapted to our study, but would require slight alterations [Seibel 09].

Based on previous experience from the model of global inflammation, 8 cm seemed extremely invasive and even obstructing for our applications.

A depth of 8 cm would have ended within the small intestine, and based on the previous model, we knew that there was an accumulation within this area of DPA-714. Due to this, it became clear that we should aim at inducing the inflammation within the large colon.

Beyond looking at the image, we also knew that in DPA-714 is eliminated gastrointestinally [Arlicot 12].

This information, combined with the past experience helped us to decide on introducing the TNBS at a depth of 4 cm. We carried the induction out while keeping the animal anesthesia for an added 15 minutes to ensure effectiveness of the TNBS in a local area.

Comparison time point

For the model of global inflammation, we had a time point given at which the highest level of inflammation was taking place. This however was not the case for this model of local inflammation.

To determine at which point we should compare the two radiotracers, we needed first determine the time at which the highest level of inflammation would be present.

The way in which we decided to proceed was to acquire images of subjects prior to the introduction of the TNBS. This was decided upon in order to obtain a baseline reading to which we could then compare, with confidence, various levels of inflammation that we hoped to observe.

Once we had the baseline images acquired, we induced the local inflammation and then acquired images at various time points post induction. This methodology allowed us to follow the inflammation and revealed that we had the highest signal on day 8 post induction. Coincidentally, this was the same time point at this

the model of global inflammation also showed the highest levels of inflammation according to Lacapere et al.

4.2 Results

4.2.1 Observation of the animals well-being

We did not observe any difference between the two groups in regard to their feeding habits throughout the whole experiment. Their weight did not reveal any differentiation between the two groups either. The only difference that we believed to see was that the treated group had possibly produced less feces possibly.

4.2.2 PET results for evolution experiments

As we did not have the same advantage as in the model of global inflammation, we were obliged to find the time point at which the highest level of inflammation would present itself. Previously it was stated that we therefore had to acquire images at various time points post TNBS induction. The time points selected were at days 2,4,8,10, and 22 days post induction. Initially we had also aimed at obtaining information on days 12 and 14, but were hindered by the fact that the radiosynthesis was not successful. However, as we were not sure yet at which point the highest level was at, we still continued and acquired a final image at 22 days post induction. The following images (figure 4.2.1) are what was observed.

As much as one might be able to extract visually, one must still quantify each image in order to be sure of what is being observed. We applied the same methodology for the quantification on this model of a local inflammation as we did for the global inflammation.

This set of experiments allowed us to observe at which time point we would be able to have the highest level of inflammation. The graph in figure 4.2.2 revealed that the results of the quantification indicated that the highest level of inflammation was to be observed at 8 days post injection.

Now that this was resolved, we were able to go forward with the initial question; to determine whether or not TSPO 18kDa could serve as a precise-, specific-, as well as measurable parameter of inflammation using the radioligand [¹⁸F]DPA-714 for the evaluation of a local inflammation found in an animal model of IBD.

4.2.3 PET results for comparison experiments

Now that the highest level of inflammation had been determined at day 8, we again induced a local inflammation into groups of animals. then we acquired images using

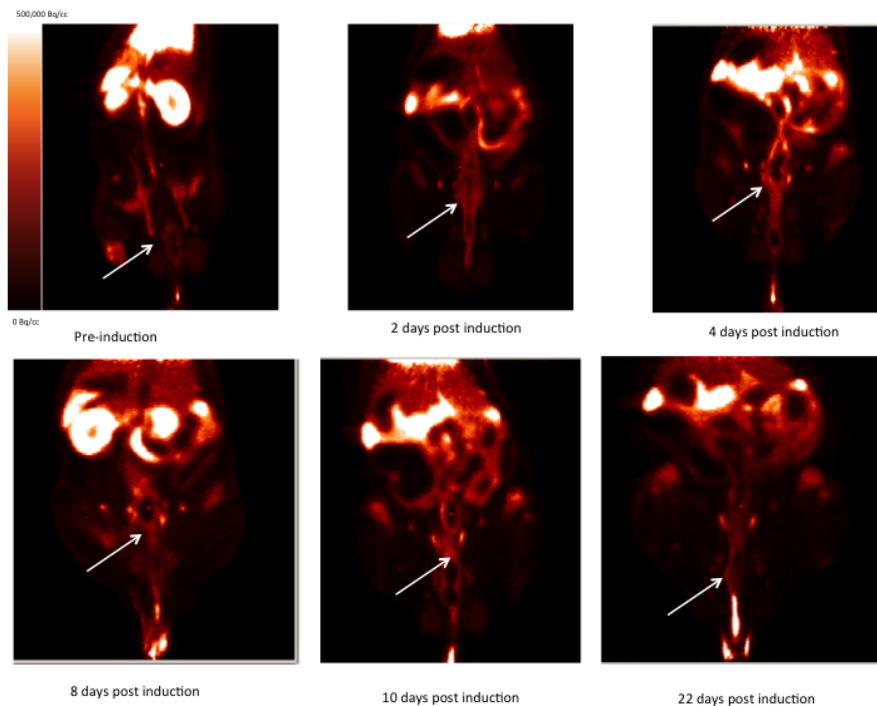


Figure 4.2.1: Evolution of $[^{18}\text{F}]\text{DPA}-7_{14}$ uptake in a local model of IBD.

both the tracer of reference for this kind of disease in humans, $[^{18}\text{F}]\text{FDG}$, and the radioligand, $[^{18}\text{F}]\text{DPA}-714$, to see whether or not TSPO could possibly serve as a better biomarker for the evaluation of a local inflammation within the intestines.

The images we obtained were representative of those in figure 4.2.3.

In both cases (with each tracer) one can observe a higher signal in the treated animals, found on the right (images B & D), when compared to the control animals on the left (images A & C). As for the quantification, the following graphs (figure 4.2.4) reveals equally interesting results.

The image quantification yielded results showing that both tracers were able to detect a significant difference when compared to the control groups. However, contrary to those obtained with the global inflammation, here we obtained a more significant difference with the $[^{18}\text{F}]\text{FDG}$ as well as with the $[^{18}\text{F}]\text{DPA}-714$ tracer. The differences found were at 0.43 ± 0.18 % ID/cc to 1.20 ± 0.56 % ID/cc for $[^{18}\text{F}]\text{FDG}$ and 0.46 ± 0.23 to 1.30 ± 0.62 for $[^{18}\text{F}]\text{DPA}-714$ ($p < 0.0006$ for $[^{18}\text{F}]\text{FDG}$ and $p < 0.0058$ for $[^{18}\text{F}]\text{DPA}-714$).

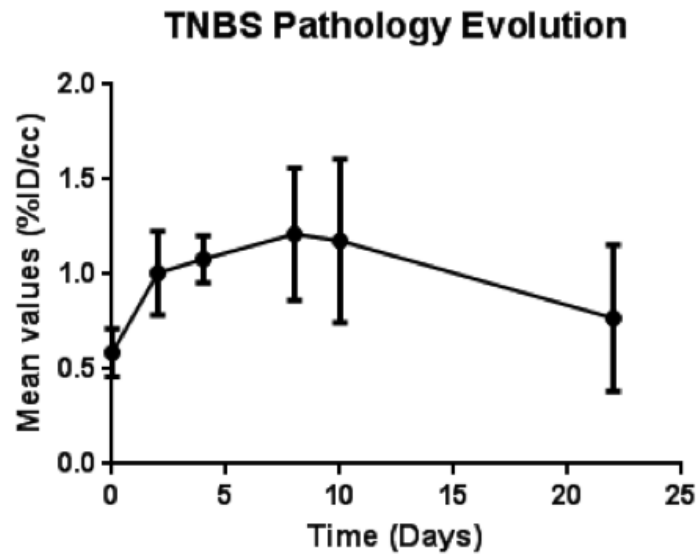


Figure 4.2.2: [^{18}F]DPA-7₁₄ in an acute local model of IBD

4.2.4 Histo- and immunohistochemistry

As tissue samples remain the reference for determining the presence or absence of a given tissue structure or cell type, we also carried out a histochemical as well as an immunohistochemical analysis of tissue samples obtained from both groups.

The tissue samples had then been stained the same way as the previous animal model and we also found here that there was indeed a structural difference to be found between the two groups. The control groups revealed refined crypt and villi structures that were not to be found in the area of inflammation within the animals who underwent the locally induced inflammation. As found in the model of global inflammation, here too we were able to observe a deformation within the entire lamina propria. Figure 4.2.5 illustrates examples of the obtained images.

The next step was to look at the presence of TSPO on adjacent slices. The aim here was to determine whether or not the structural damage correlated with an increased presence of TSPO 18kDa.

Immunohistochemical analyses revealed a marked difference between the two groups when marking for TSPO with the antibody NP-155 within the area in which the TNBS had been introduced. The control group revealed very low levels of TSPO whereas the treated groups did show much higher levels of TSPO. The contrast between the two groups can be seen in figure 4.2.6.

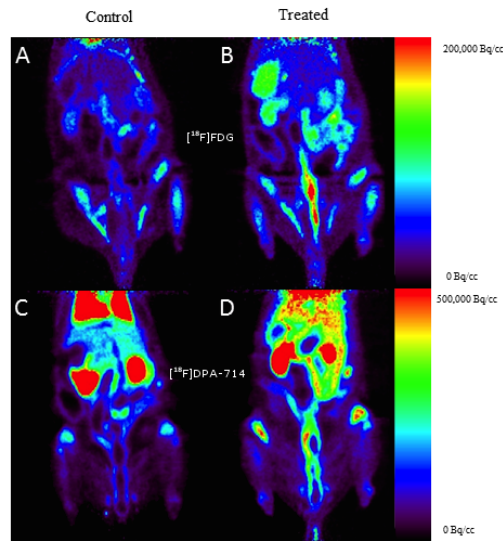


Figure 4.2.3: These images are representative of those usually observed for analysis.

4.3 Conclusion

Here we were able to demonstrate that TSPO 18kDa a valid biomarker for the evaluation of the inflammatory state within an animal model in IBD presenting a local inflammation. With the help of its radioligand $[^{18}\text{F}]\text{DPA-714}$, we were also able to follow the evolution of the disease in a dynamic fashion and quantify the level of inflammation throughout the disease progression or regression.

This ability to follow a progression could be of great interest for the diagnoses and prognoses that could potentially follow and thus lead to theranostic treatments.

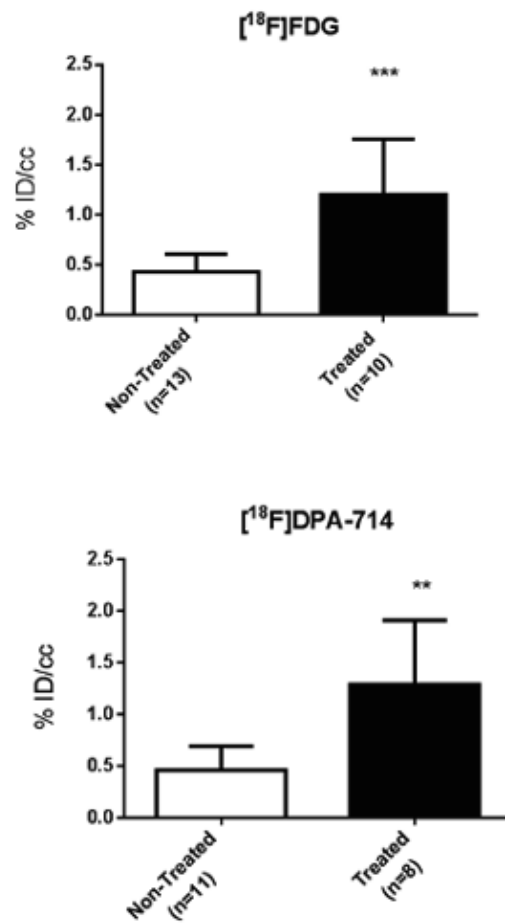


Figure 4.2.4: This graph illustrated the difference found between the non-treated and treated groups as well as the differences found between the two tracers ($[^{18}\text{F}]\text{FDG}$ and $[^{18}\text{F}]\text{DPA-714}$)

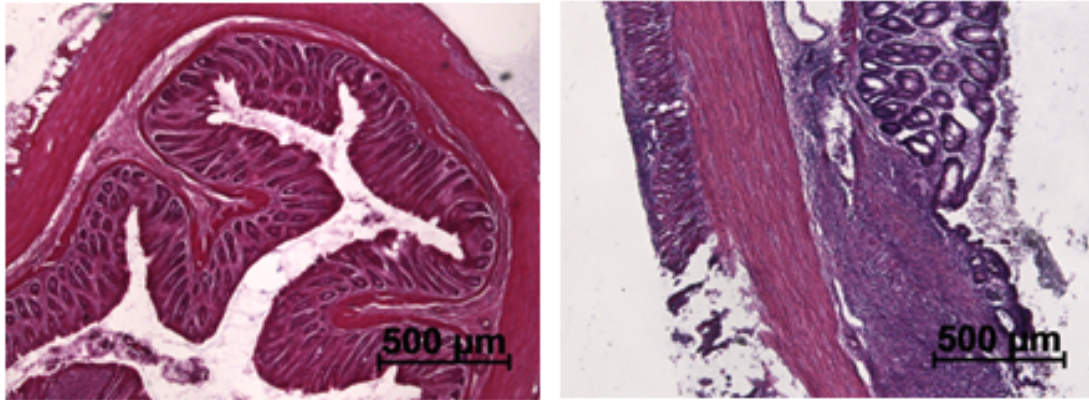


Figure 4.2.5: Using hematoxylin and Eosin staining, we were able to determine a difference between the two groups as we had been able to in the model of global inflammation.

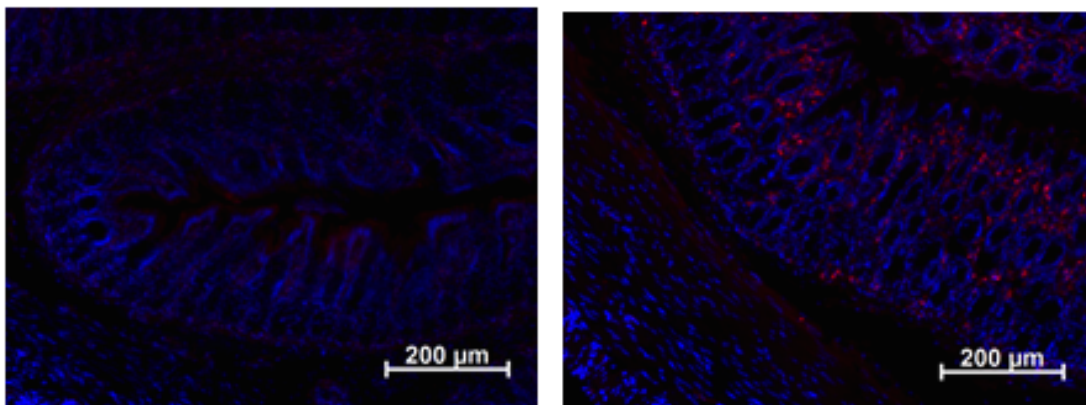


Figure 4.2.6: Immunohistochemical analysis using DAPI (blue) and the TSPO antibody NP-155 (red)

Chapter 5

Evaluation and quantification of TSPO expression in an acute model of neuroinflammation

Objective: To investigate the inflammatory process along with the expression of TSPO in an animal of neuroinflammation.

Summary:

Imaging of Neuroinflammation in Neurodegenerative Diseases (INMiND) is a consortium composed of multiple international laboratories. The consortium is focused on the understanding of neuroinflammation. As neuroinflammation plays a central role in various neuropathologies leading to neurodegeneration, it is of the utmost importance to comprehend its process. Here we will look at the steps taken in order to develop an animal model of neuroinflammation. The consortium called for a model in which Lipopolysaccharides (LPS) was the means of induction. The inflammatory process was then evaluated, especially TSPO, using the radioligand [^{18}F]DPA-714. The purpose of this vast international collaboration was to put a common model in place. This common, replicable model would enable the sharing of data across the various laboratories. Each lab would be able to re-create the model and carry out the kind of analysis that each member is specialized in.

5.1 Model validation

As neuroinflammation is an area of intense research, there have been some animal models which have already been put in place. Our lab is one of the labs which has used rodents for research in this domain and as such we had a decent starting point [Chauveau 09]. The SHFJ uses a model which calls for the injection

of alpha-amino-3-hydroxy-5-methylisoxazol-4-propionate (AMPA). This particular chemical is an excitotoxin which induces neuronal death directly and leads to a subsequent neuroinflammation with a peak at a week post injection [Boutin 07b] [Citraro 06]. The AMPA model has been used for the study of novel radiotracers as it is very reproducible.

This is fundamentally different from LPS which acts indirectly by activating the microglia. The microglia then release a host of factors, to include TLR4 and NK-kB, which lead to an M1 phenotype [Bronstein 95] [Pålsson-McDermott 04]. The LPS model has been used by other teams for research into the neurodegenerative field as well. In particular this latter model has been used for research regarding Parkinson's and Alzheimer's Disease, among other neurodegenerative diseases to help the understanding of the underlying molecular events of the disease progression [Bronstein 95, Pålsson-McDermott 04]. This illustrates that the model could indeed be of interest for this consortium.

The method of induction is described in the materials and methods section.

5.1.1 Imaging specific considerations

As with many other models, there are things that must be taken into consideration when using imaging as the tool of choice. Here too is the case.

Radiotracer choice and quantification method

As it was TSPO that we were looking into, we opted to use its radioligand [¹⁸F]DPA-714. [¹⁸F]FDG would not be of interest for two reasons, one it is non specific as previously discussed, but there is also a very high background signal in the brain as this is an organ that uses a high level of glucose.

As this model differs from those previously described, we used a different method of quantification. Here a single user selected the VOIs for each of the animals. Regions were selected in both hemispheres, both ipsi-lateral and contra-lateral, in regard to the site of injection. Beyond this, another region was selected in the muscle as an intra subject reference to be able to observe any abnormal uptake.

The CT image was not used for the drawing of the VOI and only used for the attenuation correction.

5.2 Results

Compared to the AMPA model, we did not know how the inflammatory response would react to the LPS injection. We did not even know when we would be able to find the time point at which we would observe the inflammatory peak in

this model. It has been documented that AMPA injected animals revealed a peak inflammation 7 days post injection [Boutin 07b]. We were not aware of any similar results for the LPS model.

To address this fundamental question, we carried out PET acquisitions at various time-points. We were hoping to have something comparable to the data observed in the AMPA model.

5.2.1 PET Results

We observed the animals well-being post intra-striatal LPS injection and did not note any behavioral differences in the subjects. The animals did not loose weight over time and their eating habits continued normally.

PET acquisitions, however, did reveal differences over time.

Acquiring images at different time points is of interest as it allows the researcher to observe alterations in a single subject and obtain information about each state. Here, we hoped to be able to determine a time point at which one could observe a peak in inflammation, thus demonstrating the ability to follow the inflammatory progression that can be present in many diseases.

Once we had the images treated and quantified we obtained the following images.

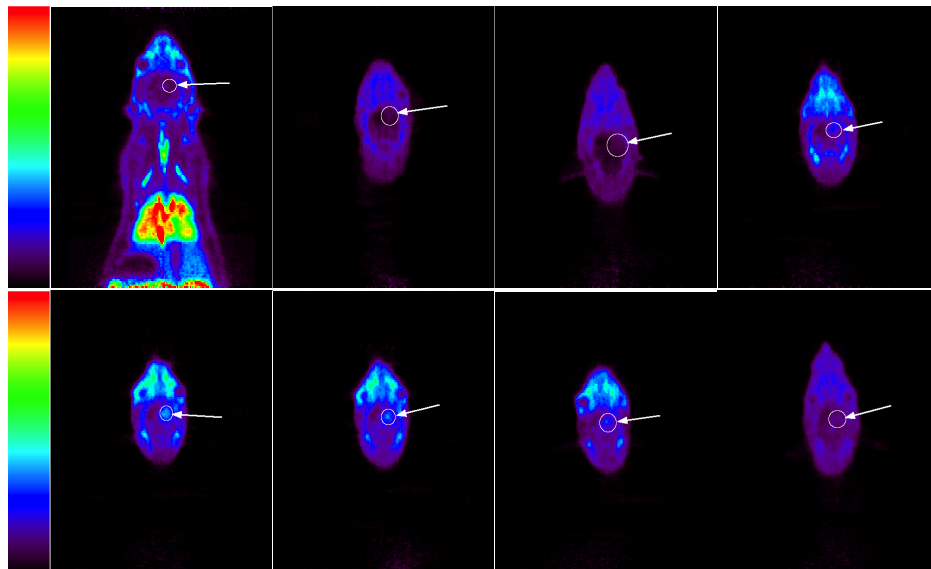


Figure 5.2.1: Intra-subject inflammatory evolution (LUT boundaries are 0-200kBq/cc)

The images (figure 5.2.1) acquired using the INVEON μ PET (or the INVEON μ PET/CT) allowed us to visualize the various levels of inflammation we were able to detect using the radioligand [^{18}F]DPA-714 for the detection of TSPO. The arrow indicated the site of injection, located in the right hemisphere of the rat. The illustrated images acquired at days 1,2,3, and 4 were all of the same subject and show that intra-subject variations were detectable.

However, the images were not the only interesting aspect, the quantification was equally compelling.

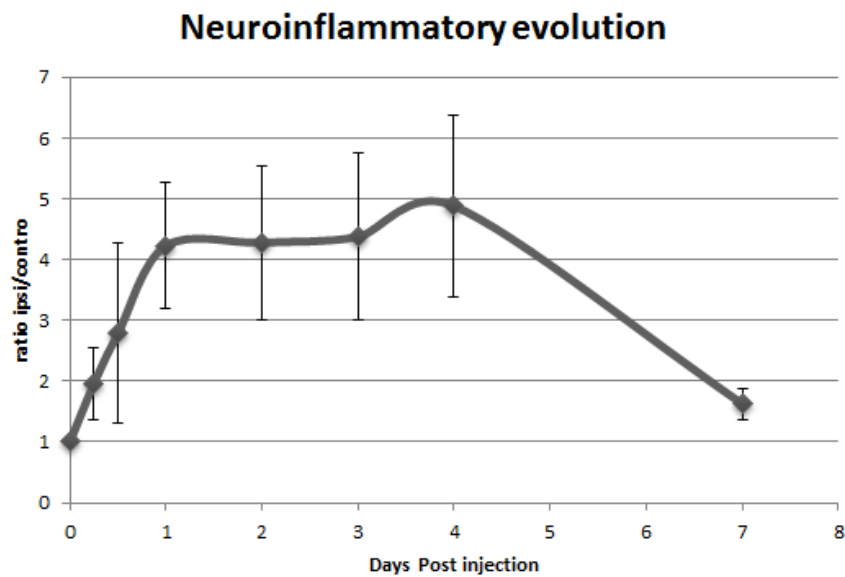


Figure 5.2.2: Evolution of TSPO expression over time post LPS injection

The complimentary graph (figure 5.2.2) also reveals the quantifiable differences (expressed as a ratio ipsilateral/contralateral) in TSPO presence between the acquisitions time-points. One can already observe an increase of inflammation at only 6 hours after injection of the LPS. This rapid rise continued until day 1 post injection and then plateaued until 4 days post injection. Once the peak was reached, the levels of TSPO decreased until nearly reaching a near basal level at 7 days post injection. This was a strong contrast to the inflammatory level observed in the AMPA model. The level of inflammation slowly increased until reaching its peak level at 7 days post injection, at which point it began to diminish until day 7 post injection. We then had a closer look at the time-activity curves (TAC) of the VOI within the ipsilateral hemisphere to inspect the behavior. The time points with the highest levels (1, 2, 3, and 4 days post intra-striatal injection) revealed a faster uptake while maintaining a similar excretion of the radioligand than the

other time points.

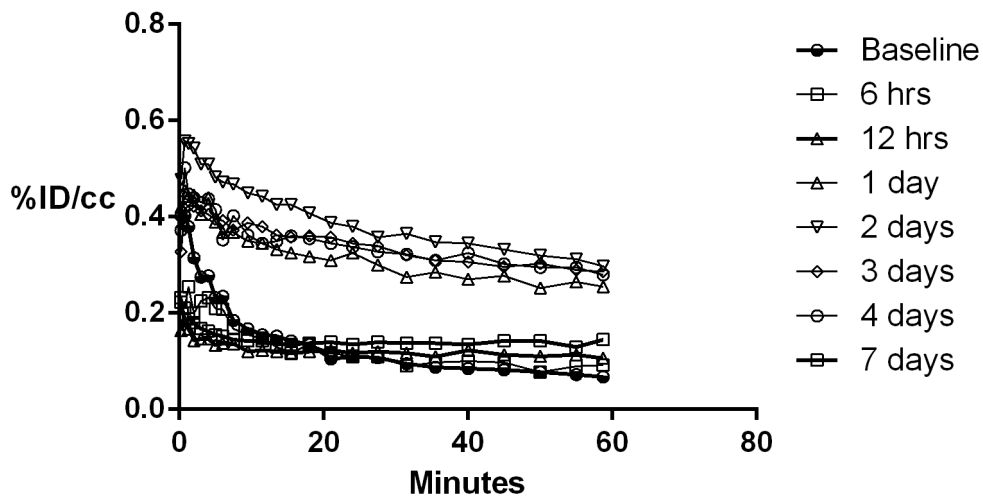


Figure 5.2.3: TAC of LPS injected subjects

It is also noteworthy to observe the differences between each time-points seen in the graph (figure 5.2.3). Seeing as that there was a difference in inflammatory kinetics when comparing the AMPA model and the LPS model, it seemed interesting to also compare the TACs of each model while at their max values.

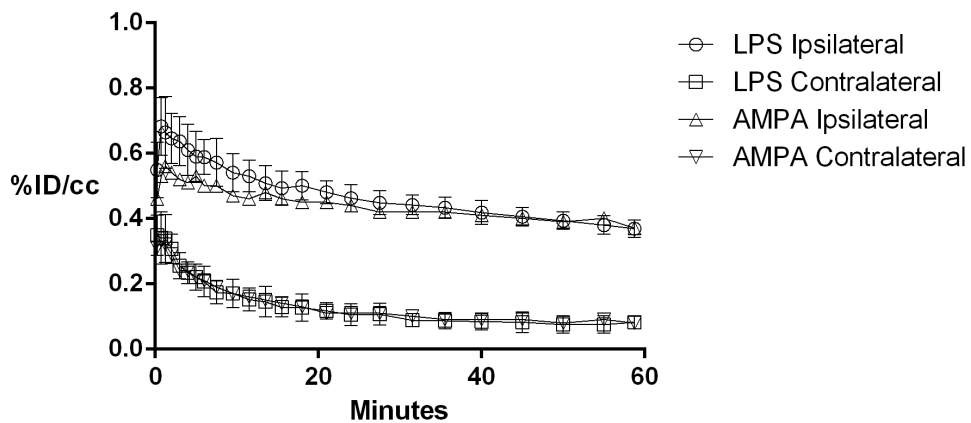


Figure 5.2.4: TACs of both AMPA and LPS models at maximum values

The resulting data (figure 5.2.4) revealed that the two models, although very different in nature, had very similar TAC behavior. While the LPS model had

a slightly higher initial uptake, the excretion brought the final activity to nearly identical values of the inflamed VOI of the AMPA model.

This initial difference in uptake was not to be found in the contra-lateral hemispheres of either model. These values were in turn comparable to those of a non injected animal, validating the use of the contra-lateral hemisphere as an intra-subject control region.

As it is the baseline, or physiological state, to which we wish to compare the level of inflammation expressed in the ipsi-lateral side too, we then analyzed the differences found between the healthy hemisphere to those in which an inflammatory response was induced. We found marked differences for each comparison that can be found in the following figure.

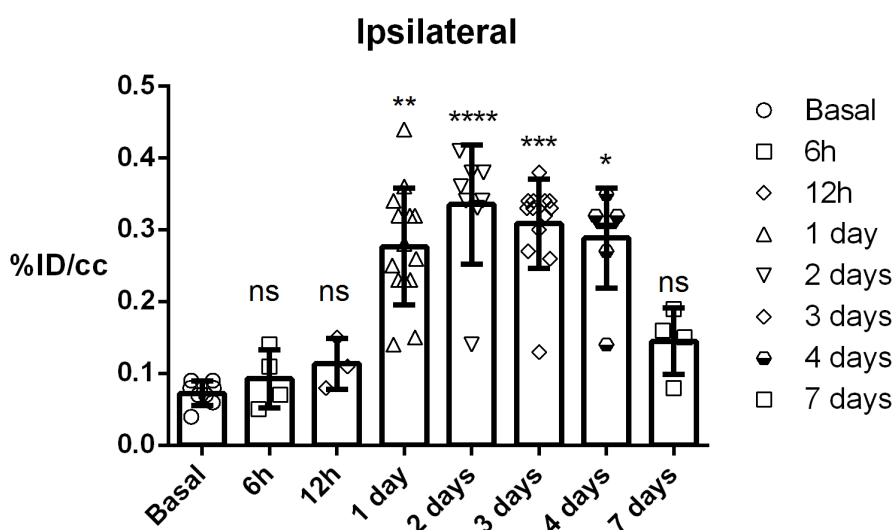


Figure 5.2.5: Relative ipsi-lateral statistical significance

In this graph (figure 5.2.5) we can observe that the difference in [¹⁸F]DPA-714 uptake between the baseline, 6, and 12 hours post injection no significant difference was determined. However, the measurements between baseline and days 1, 2, 3, and 4 post injections were all significantly different. It is interesting to also note that the observed inflammation at 7 days post injection have again receded to a non-significant difference between it and the baseline measurement. (p<0,0001)

The large standard deviation can most likely be described by differences found between subjects.

Contrary to the ipsi-lateral hemisphere, the contra-lateral hemisphere (figure

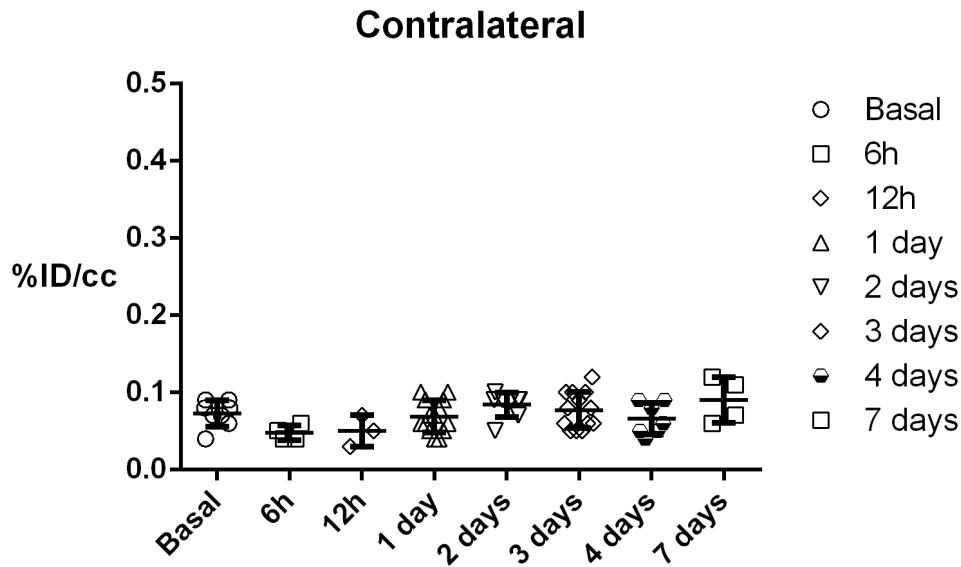


Figure 5.2.6: Relative contra-lateral statistical significance

5.2.6) yielded no significant difference at all. The TSPO level remained stable throughout, for each subject.

5.2.2 Histo- and immunohistochemistry

In order to better understand what was happening on a molecular level, we extracted brains at each time point for further analysis and to observe alterations which may have occurred at the different stages of inflammation.

Initially we were concerned about the impact that the needle might have had on the integrity of the blood brain barrier upon injection. The concern was that foreign factors could perhaps cause an immune response. As such, we wanted to assure ourselves that we were not allowing exterior factors to impact the reaction of the inflammatory process at the injection site and that we were observing only the reaction to the LPS, and not an external impact.

As such we carried out an experiment in which we injected Evans Blue to see if there had been any significant rupture.

Evans Blue is often used for testing the integrity of the blood brain barrier (BBB) as it binds with a high affinity to serum albumin. Serum albumin does not cross the BBB in a physiological state. As such, one would expect to observe the presence of Evans Blue if the BBB had been ruptured. The injection was carried



Figure 5.2.7: Evans Blue images of the site of intra-striatal LPS injections

out on two subjects via a slow i.v. injection and were assured that the injection was successful as the whole animal turned blue. We did not observe any presence of Evans Blue within the injection sites on subjects at 6 (left slide), or 12 (right slide) hours post intra-striatal injections (figure 5.2.7).

The images indicate that there was no impacting rupture as we were not able to find a presence of Evans Blue inside of the brain.

Hematoxylin and Eosin staining is considered as a gold standard by many for the recognition of tissue types and morphological alterations. We had thought that the LPS injection would reveal a difference in staining between the two hemispheres as the LPS would ideally alter the protein concentrations in the ipsi-lateral hemisphere.

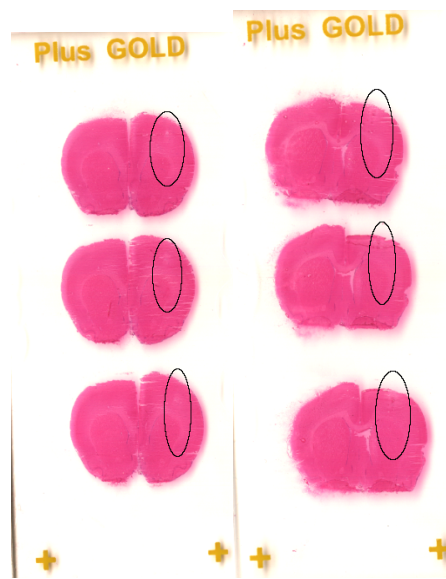


Figure 5.2.8: H & E stained images of the site of intra-striatal LPS injections

The results however did not reveal any alterations at the site of injection at either time point (figure 5.2.8, time-points 6hrs, and 24 hrs post injection respectively).

Since we had not observed any modifications with the H&E staining, nor had we seen a breaching of the BBB with the Evans Blue protocol we thought of other aspects to look for such as Nissle staining.

As we wanted to know more about the impact that the injection of LPS might have had on the neuron density to further investigate this we carried out Nissle staining. For this we used Cresyl Violet.



Figure 5.2.9: Cresyl violet stained brain slices of the site of intra-striatal LPS injection

Here (figure 5.2.9) too, we were not able to detect a large difference as one might expect. This indicated that there was not a large impact of the LPS on the neuronal density when compared to that observed in the AMPA model samples of peak inflammation at 7 days post injection (figure 5.2.10).

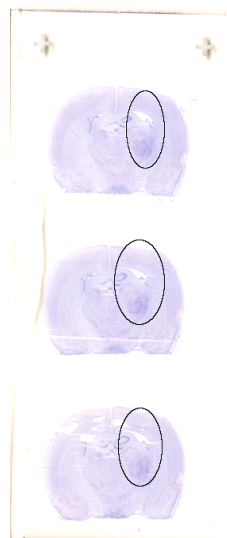


Figure 5.2.10: Cresyl violet stained brain slices of the site of intra-striatal AMPA injection

Contrary to the observation in the LPS model, we were able to identify the

modification of neuronal density in the AMPA model relatively easily.

5.3 Conclusion

Although we were able to determine that the BBB integrity was not compromised at 6 and 24 hours post intra-striatal injection, that the morphological alterations were negligible, and that the neuronal density was minimally impacted, if at all; much still remains to be uncovered. Further investigation is needed into pro-inflammatory factors, especially in comparison to the AMPA model. Especially when taking into account that the radiotracer were very similar even though the time points were different (2 days post injection for the LPS model and 7 days post injection for the AMPA model).

This is of great interest especially when looking at the information acquired using PET imaging. It will be fascinating to be able to correlate the TSPO expression (due to PET imaging) with the expression of other aspects such as macrophages, Iba-1 for example. The fact that this evolution of the inflammatory process changes over time, could indicate an adaptation.

Be this as it may, the above experiments and results indicate that [^{18}F]DPA-714 is a tracer with which we are able to detect a difference in TSPO presence and that it may indeed be a very powerful tool which is adapted for the evaluation of the inflammatory process. This is of great interest as it would possibly allow for disease staging one day and ultimately lead to early treatment.

Chapter 6

Tracer evaluation and validation

Objective: To test and evaluate a novel metabolically stable radioligand for the targeting of TSPO 18kDa.

Summary:

In this chapter we will explore the processes and experiments that are undertaken to further develop imaging tracers. We will look at the characteristics of the novel radioligand [^{18}F]DPA-C5yne applied to an animal model of neuroinflammation.

Reasoning:

Imaging is a domain which is multidisciplinary. Many fields must come together in order to make this research domain possible. A problem, or an inexactitude in one field will leave an impact on the final results. This is also the case for the tracers. Precise quantification is a major hurdle for PET imaging and it is difficult to determine the level of target- or process expression *in vivo*. The metabolism of a xenobiotic radioligand presents complications as the metabolic alteration of the radioligand creates many byproducts which may or may not contain a radioisotope. If the metabolite maintains the affinity, then the target remains occupied, but not tagged, thus interfering and impacting the specific radioactivity.

A similar case could be presented if the the metabolic consequence were to create a metabolite which could perhaps maintain an affinity for its destined target, but alter the kinetics of the binding. This also introduces convolutions which make the *in vivo* quantification a challenge.

Another factor that needs to be addressed when discussing metabolites, are the radiolabeled metabolites that stem from the initial molecule, but do not have an affinity for its target anymore. As this radio-metabolite is free, it can be found in the blood throughout the entire body. It is possible to analyze and characterize this kind of metabolite through blood samples. However, it is not possible to

measure the amount of the radio-metabolite found within the biological target to which the original intact tracer had an affinity for.

Peyronneau et al characterized the *in vivo* metabolic pathways for the TSPO radioligand [^{18}F]DPA-714. Their analysis included the loss of the lateral fluorine chain that leads to the free radio-metabolite which is able to diffuse throughout the subjects entire system, including the brain [Peyronneau 13].

In order to address this free radio-metabolite issue, the team of radiochemists at the labs of the SHFJ developed a more stable [^{18}F]DPA-714 derivative named [^{18}F]DPA-C5yne.

6.1 Model validation

To evaluate this novel tracer, we implemented the AMPA animal model, which was described in the previous chapter briefly. This model is reproducible and as such allows for comparable conditions when testing novel tracers.

6.1.1 Imaging specific considerations

As imaging is a field which was created thanks to the input of many different fields of research ranging from physics, to biology, chemistry and back, each of these field has their own importance and role. Sometimes it is the improvement of one of the players, which can render the results more reliable.

Signal to noise ratio

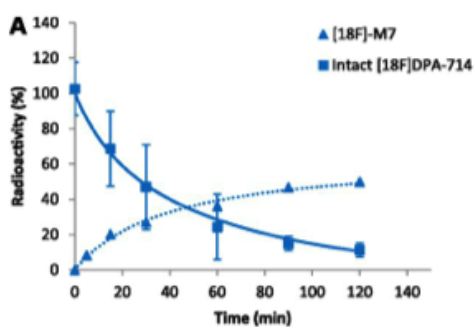
The signal to noise ratio is an important parameter. Ideally, a tracer will have very little background noise (or low non-specific binding) and thus be able to give a clearer signal of where the tracer accumulation took place. However, a specific target may also be implicated in multiple phenomena, thus revealing more than one process. This is not always a bad thing, but it may not always be an advantage, as we saw in chapters 3 and 4 when exploring whether or not the TSPO radioligand [^{18}F]DPA-714 was able to detect different levels of inflammation within two different animal models of IBD. In these cases it became evident that [^{18}F]FDG, the reference tracer, would perhaps be at a disadvantage when looking for the level of inflammation alone, and wanting to be able to be sure that there was no signal coming from a muscle movement.

Metabolism

An aspect that can easily be overlooked if not in the field is the metabolism of the radiotracers, or any tracer for that matter. Here however we are dealing with

radiotracers which, as the name implies has a radioactive element to it.

Recent studies have brought to light that there are some characteristics of the radioligand being used ($[^{18}\text{F}]\text{DPA-714}$), that could be improved upon [Peyronneau 13]. There has been an in-house study that was carried out by the group working with Dr. Valette which demonstrated that there is an extensive metabolism of $[^{18}\text{F}]\text{DPA-714}$ in both rodents as well as in primates blood plasma.



Peyronneau et al Drug Metab Dispos. 2013

Figure 6.1.1: Here one can see the metabolic rate that $[^{18}\text{F}]\text{DPA-714}$ undergoes over time.

As stated previously, the metabolism of a compound is something that should not be neglected as the free radio-metabolite reaches a higher level than that of the intact compound. The rate of metabolism of $[^{18}\text{F}]\text{DPA-714}$ is depicted in graph 6.1.1.

Among the various pathways (figure 6.1.2), there is one in particular which has been shown to occur *in vitro* and thought to also occur *in vivo*. They looked at the metabolism which occurs due to O-dealkylation. This metabolism leads to free ^{18}F small metabolites, such as $[^{18}\text{F}]$ fluoroacetaldehyde, or its oxidation product $[^{18}\text{F}]$ fluoroacetic acid [Peyronneau 13].

The reason that this is a potential problem is that the free $[^{18}\text{F}]$ metabolites are able to cross the blood brain barrier. The avid binding of the $[^{18}\text{F}]$ to bones is a problem as it could impact the quantification due to a partial volume effect.

This means that there is potentially an increased background signal which would impact the ratio between the area of interest and the tissue which is in a healthy state. Ultimately, this could lead to a false negative diagnosis as an increased background due to metabolism would likely lead to a loss of signal.

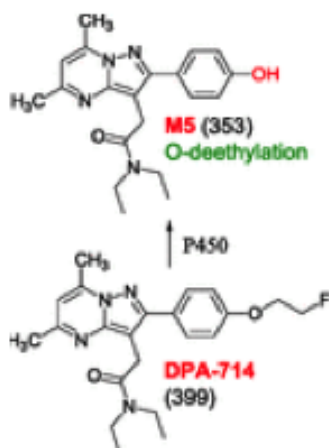


Figure 6.1.2: Illustrations of various metabolic pathways can be seen in this figure in grey. Here we can see the metabolic pathway discussed with the white background.

6.1.2 Addressing the problem

This aspect has been addressed by another student has been working on the development of novel tracers. Here he, along with the team of chemists have worked to improve on the tracers in creating an analog of the [^{18}F]DPA-714 to create [^{18}F]DPA-C5yne.

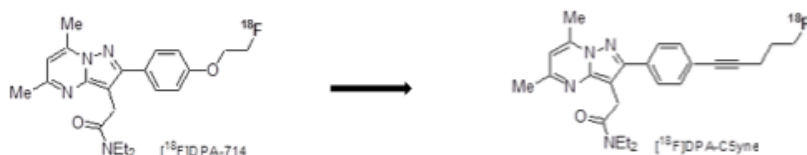


Figure 6.1.3: Modifications to create the [^{18}F]DPA-714 analog

In the preceding image (figure 6.1.3), one can observe that the the group altered the structure of the DPA-714 chemotype. This was carried out to avoid the O-dealkylation which in turn would address the issue of the free [^{18}F]. They group decided to work off of the DPA-714 structure and to replace the oxygen atom with a carbon atom.

There were many DPA-714 analogues, but among them, it was DPA-C5yne that revealed the highest affinity to TSPO [Médran-Navarrete 14]. Thus, it was decided

to tag the DPA-C5yne with ^{18}F using a TRACERLab FX N Pro module to create [^{18}F]DPA-C5yne.

Once the molecule had been created, tagged and evaluated for chemistry and radiochemistry feasibility, the molecule was ready to be evaluated in the preclinical domain.

6.2 Results

6.2.1 *In vitro*

As the compound had proven to be of interest by the chemistry group, they then passed the tracer on to us in the preclinical group to evaluate the novel TSPO 18kDa ligand [^{18}F]DPA-C5yne.

The first experiment was carried out *in vitro* on brain sliced obtained from AMPA injected animal. This AMPA model is the animal model used for the evaluation of novel tracers here in the institute of the CEA at Orsay, France. This model is robust and very reproducible and as such is well adapted for comparative evaluations.

As [^{18}F]DPA-C5yne is a novel compound, it needs to outperform the predecessors in order to be deemed better. To test this, we carried out an Autoradiography.

This experiment tests the affinity of a compound and can be used to test the competition between two different compounds and evaluate the displacement that one compound imposes upon another. This means that if the slides are emerged into a solution in which there is a presence of compound A, and then compound B is introduced, the occupation of the target will be divided between compounds A and B if both compounds target the same molecule.

As even [^{18}F]DPA-714 has not yet been translated into routine exams, we compared the novel compound [^{18}F]DPA-C5yne with its own cold compound and the current reference radioligand for TSPO, namely PK11195.

The resulting image of the autoradiography (figure 6.2.1) allows for a signal comparison between the two hemispheres as only one of the two hemispheres underwent the AMPA injection. The signal ratio between the two may also be evaluated and used to compare to the ratios obtained from other tracer developments and subsequent evaluations.

As can be see in the image, [^{18}F]DPA-C5yne was able to be displaced by its own cold compound, but also by the reference tracer PK11195. This displacement reveals the specificity of the tracer for TSPO.

The next step is to quantify of signal over noise signal.

As can be seen in the graph illustrating the results obtained from the autoradiographies (figure 6.2.2), there was of interest to further investigate the novel

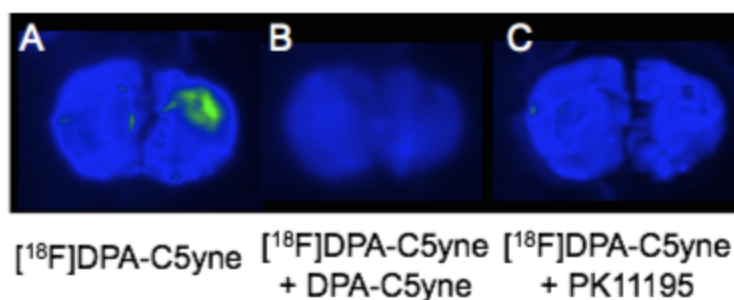


Figure 6.2.1: Autoradiography of: [¹⁸F]DPA–C₅yne alone (A), co-incubated with DPA-C₅yne (B), and PK11195

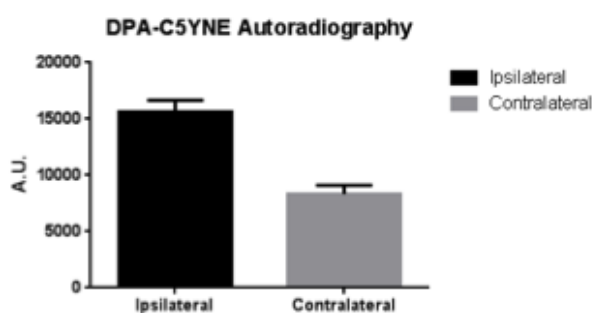


Figure 6.2.2: Quantified autoradiographic results

compound. The study was performed on slices of AMPA lesioned rat brains which showed a high target-to-background ratio of 1.9 ± 0.3 . [¹⁸F]DPA-C₅yne has proven in this experiment to have a low background noise, thus increasing the signal to noise ratio in the ipsi-lateral (AMPA injection site) vs contra-lateral hemispheres.

6.2.2 *In vivo*

6.2.3 PET results and animal well-being observations

In the AMPA model we did not observe any odd behavior. All animals continued eating and drinking as normally and did not show any loss in weight.

Once we had the autoradiography results which showed that the novel tracer could be of interest, we took the next step and carried out an *in vivo* experiment using the animal model used conventionally for novel TSPO tracer screening. Fur-

ther details to the animal model can be found in the Materials and Methods chapter in Section I.

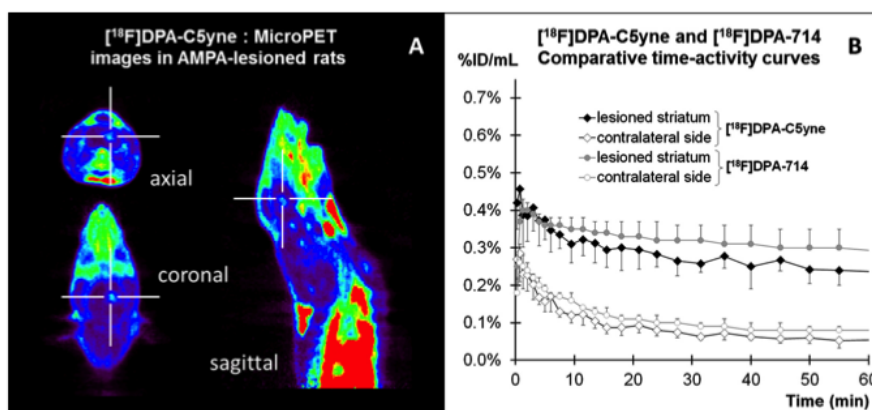


Figure 6.2.3: [¹⁸F]DPA-C5yne injected AMPA rat with corresponding graph compared to values obtained using [¹⁸F]DPA-714

The above images of the AMPA animal model, with the injection side found between the crosshairs, clearly show the novel tracer uptake in the lesioned area (figure 6.2.3).

The graph illustrated the time-activity curves of the novel tracer, [¹⁸F]DPA-C5yne, and its parent compound [¹⁸F]DPA-714. The signal level obtained using [¹⁸F]DPA-C5yne was not as high as that of the [¹⁸F]DPA-714 in the inflamed or the contra-lateral hemisphere. This however needs to be looked at further as higher signal is not always better.

When we compared the two regions and looked at the ratios of signal over background, one can see that it is indeed the novel tracer which has the higher ratio.

[¹⁸F]DPA-C5yne ratio is around 4.62 while the value for [¹¹C]PK11195 were merely 1.65, and at 3.71 for [¹⁸F]DPA-714 [Pålsson-McDermott 04].

This graph (figure 6.2.4), along with the PET images and the autoradiography, all illustrate the interest that this tracer could possibly have in a clinical setting.

Beyond moving the current tracer forward to another setting, this experiment also shows the interest of further developing tracers. A reference tracer, may be improved upon. Imaging is a complex field which leans on many fields, each with their own importance. This experiment and the development of other tracers brings this to light.

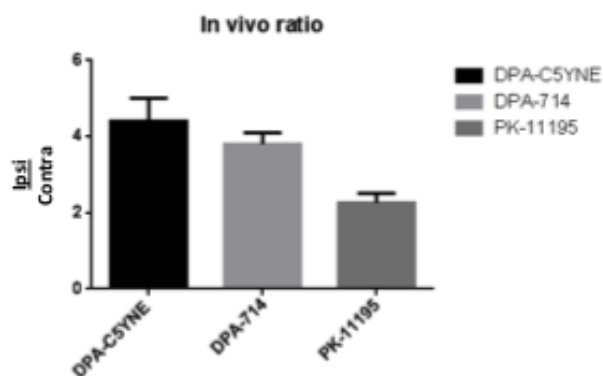


Figure 6.2.4: Ratio comparison between the ipsi-lateral- and contra-lateral areas for each listed tracer

6.3 Conclusion

Improving a tracer's stability is a complex task. Maintaining the tracer's affinity and selectivity while improving its background signal while *in vivo* represents an important objective. If one were to succeed in maintaining each of the three aspects, stability, affinity, and selectivity, the ratio between a specific signal and a background signal would improve. This improvement would be observed as a better contrast when using the same amount of radiotracer. The importance of this could be perhaps better illustrated in a clinical setting. There a clinician, who sees many patients on a daily basis, would be able to use data which is more concise. A clear visual contrast between an area with signal and one without, would greatly help with an interpretation, ultimately benefiting the patient.

Chapter 7

Evaluation and quantification of TSPO expression in an animal model of septic shock

Objective: To recreate an animal model of septic shock and to then determine whether or not TSPO could be a target of interest for the evaluation of a global inflammation in individual organs using radioligand [¹⁸F]DPA-714.

Summary:

Here will explore multiple questions. The first being whether or not we are able to re-create an animal model of a systemic inflammation. The next thing we were aiming to do was to determine whether or not TSPO could be used as a biomarker for a systemic inflammation. The idea behind this was to then also evaluate whether or not we could possibly quantify this increase in inflammation using the already proven radioligand [¹⁸F]DPA-714.

Reasoning:

Septic shock is a medical condition which is representative of the final stage of a severe infection and sepsis which is encountered in various bacterial pathologies. This clinical stage corresponds to a propagation of an infectious agent or their components throughout the entire body. This causes a severe response from the immune system. This «burst» often induces a severe multiple organ dysfunction syndrome and can lead to death. The mechanisms of progression from tissue infections to organ dysfunction and death remain poorly understood. So, the mortality from septic shock remains extremely high and may reach 60% even. This is despite the implementation of international guidelines, constant medical progress

and billions in treatment spent each year. Here will be explore the possibility as to whether or not the TSPO ligand could provide quantitative information about the inflammation induced by an aseptic aggression. This is important as death due to septic shock is associate with organ dysfunction which is linked to the aggression induced by the excessively high immune system activity.

7.1 Model validation

The model in itself was pretty straight forward. We had obtained preliminary LPS dosage suggestions from collaborators. This allowed us to be able to base our first experiments on something other than bibliographical references. We later found out that the dosage we administered was also used by other labs and as such knew that we were being coherent.

7.1.1 Imaging specific considerations

Until now we had been confronted with various difficulties which have obliged us to adapt our experimental processes in order to obtain the data in ways which did not bias out results. Here too we had to make some adjustments in order to be certain that we were obtaining all the data possible, and then be able to sort it out too.

FOV

In all of the previous PET imaging experiments, we used the two μ PET machines. The machines each have a axial FOV of 12.7 cm and is enough for using on whole body imaging on mice. When acquiring whole body images or rats however, a larger FOV is required.

To address this research question, we decided to use another PET than the previously use μ PET machines. Our lab has a HRRT scanner which is dedicated to human brain scans and which has a spatial resolution of 2.3mm. This scanner also has a FOV of 25.2 cm. This is just under twice that of the INVEON μ PET. This extra size allowed us to be able to scan the whole body of a Wistar rat weighing about 250 grams.

Another advantage of the larger FOV, which had a circumference of 31.2 cm, is that we were able to scan multiple subjects simultaneously.

This was possible because our lab also has a home-made support that can be placed into the bore of the HRRT PET scanner. This support (figure 7.1.1) has 2 levels, meaning that there is space to support 4 rats total. This is a distinct advantage.

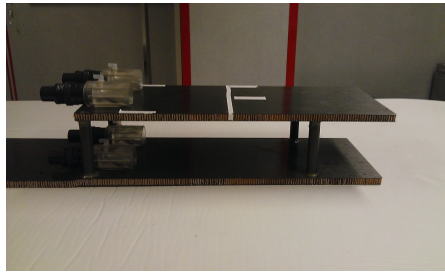


Figure 7.1.1: The support is made of carbon in order to have negligible gamma ray attenuation

The support is designed to fit flush into the bore of the HRRT camera (figure 7.1.2).

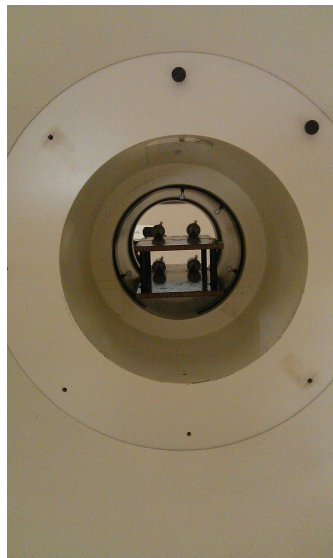


Figure 7.1.2: The support fits into the center of the bore

It is important to have a bed or support that can be placed into the FOV in a replicable manner. This assures a comparable way to image subjects while avoiding false placement.

VOI definition

As previously mentioned, the animal was one of a systemic inflammation. As such it was not easy to manually draw the regions of interest. This being the case, we decided to use an in house developed method of ROI delineation for an auto-segmentation.

This methodology is robust and very reproducible as it is not user dependent. It is based on the time activity curves (TAC) which allows for a differentiation between voxel content based on the kinetics of the radioactivity present.

There are 5 steps that the segmentation method must undergo. The first step extracts the subject from the noisy background with the help of histogram-based algorithms. The second step then uses points inside organs which are then extracted. Thirdly the local mean TACS and global noise properties are computed in the direct vicinity of the extracted points. The image is then segmented into regions which correspond to the extracted points in step four. The final step (5), merges the similar TACs within using a hierarchical linkage algorithm.

This will allow the user, when applying this tool, to be able to distinguish the heart from the lungs for example. The delineation of organs, by a user, based solely on contrast using TSPO ligands would otherwise be more than difficult.

7.2 Radiotracer choice

7.2.1 TSPO ligand

As has become clear throughout the manuscript, there are many tracer options when looking to target the translocator protein 18kDa. Not only are there already many choice, but the choices keep increasing, as was seen in the previous chapter in which we investigated and evaluated the feasibility of another novel tracer (^{18}F]DPA-C5yne).

In this particular animal model of a systemic inflammation, we decided to stay with the TSPO radioligand that we had initially started with (^{18}F]DPA-714). There are a few reasons for this. The first being that the recently tested novel tracer, ^{18}F]DPA-C5yne, has not yet been tested for peripheral applications. The novel tracer would be of interest if the animal model was less complicated and had a local inflammation perhaps. Beyond this, the tracer (^{18}F]DPA-C5yne) is new and more difficult to have access too as well which has an impact on the practical aspects of the experimentation. This leads us to the second reason for the continuity of the ^{18}F]DPA-714. As it is a radiotracer which has been applied to a few clinical exams and is used continuously in the lab, it is easier to obtain.

7.3 Results

7.3.1 Observation of the animals well-being

The acquisitions were carried out at 24 hours post i.p. LPS injection. At this time point, the animals were displaying marked signs of suffering. Their activity was

diminished and the volume in the water bottle had not changed from the previous day.

7.3.2 PET results

Putting the animal model into place was much easier in this case than it was in the previous models. As previously mentioned, we were even able to observe the impact of the LPS at 24 hours post injection.

The PET acquisitions, which were carried out 24 hours post injection, revealed a difference between the control animals and the treated ones.

The images we obtained did not allow us to discern the organs easily. Thus we used the automatic segmentation as we had thought necessary from the beginning.

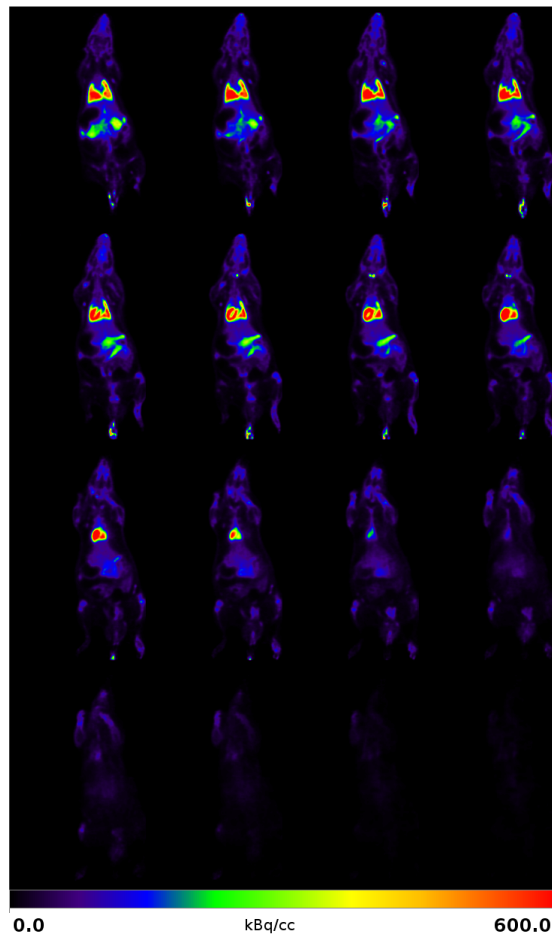


Figure 7.3.1: This figure illustrates various slices of a control rat

The above (figure7.3.1) image allows us to traverse the control subject dorsal

to ventral giving the user an idea of the inflammation present. The center of the organs are somewhat distinguishable, but hard to differentiate when looking at the bordering areas.

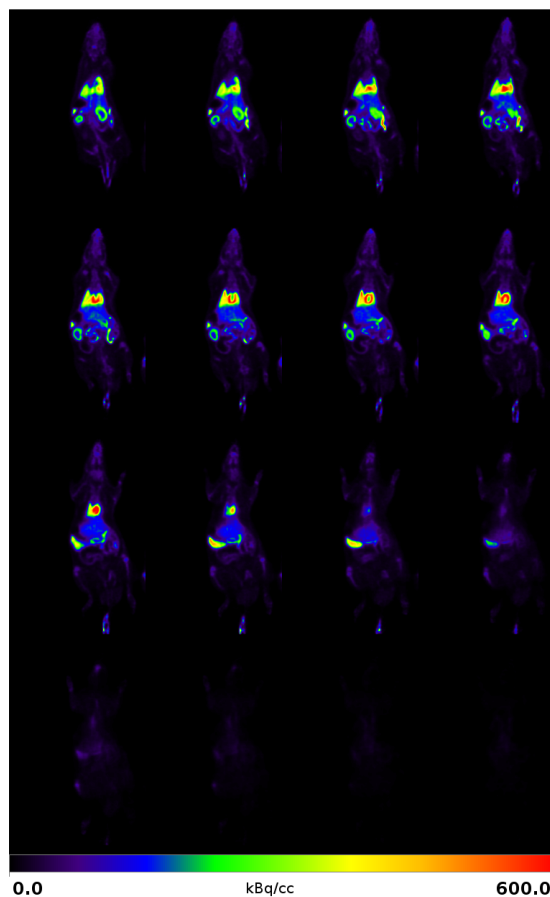


Figure 7.3.2: Images traversing a treated animal i.p. injected with LPS

The images in the figure 7.3.2 again allows the user to observe the treated subject while traversing it dorsal to ventral. Even-though it is merely representative one can observe an increased level of signal when comparing the two image sets on the same planes.

The visual depiction is helpful for an initial idea, but using the automatic segmentation as previously described, we were able to quantify the the levels of TSPO expressed in each of the organs.

The following graph (figure 7.3.3) is indicative of the level of inflammation determines in each of the listed organs.

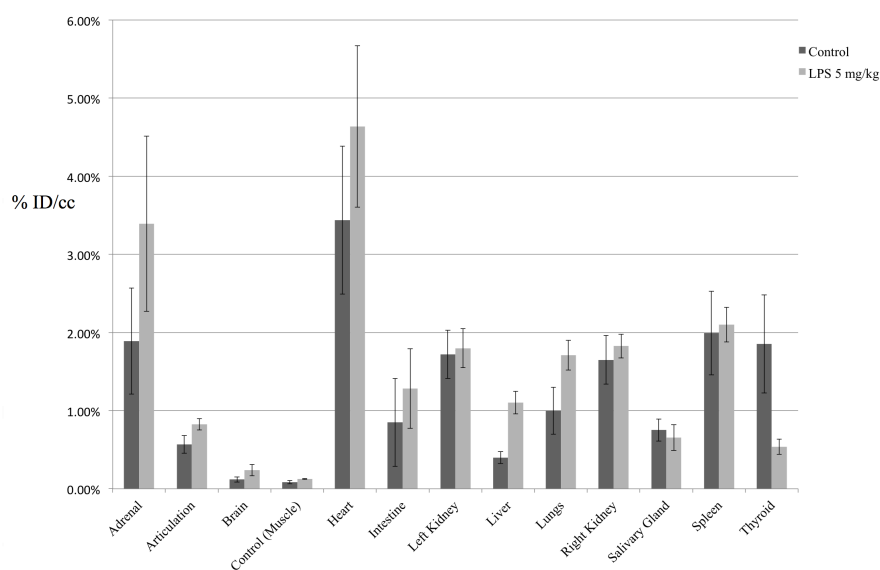


Figure 7.3.3: Control vs. treated animals groups

This study was a pilot study.

Systemic inflammatory states are detrimental to the human health. The systemic inflammation can lead to coronary artery disease, hypertension, kidney disease and many more.

Each individual disease however, is most likely currently looked at using [^{18}F]FDG. The limitations of this glucose analogue have already been covered and the reasons for which the TSPO is of interest as a target also. What we have been looking at thus far however are specific diseases.

The systemic induction is not only a wide spectrum to look at, but it may also serve as a probe to test which areas disease or organs may benefit from TSPO targeting for the evaluation of the inflammatory state.

The results of the exploratory experiment are promising in that each and every organ, that we were able to detect using the segmentation had an increased level of inflammation with the exception of the Thyroid and the spleen.

We know that TSPO is found throughout all organs in a human in varying levels, so it is no surprise that we were able to detect levels in each distinguishable organ. Yet, it is interesting that so many of them were increase. This could possibly be an indication which organs it might be of interest to apply a TSPO radioligand in the case of a clinical exam. This would then of course allow for the exclusion of false positives as can happen with [^{18}F]FDG.

More experiments are needed though at varying doses to investigate all possibilities.

7.4 Conclusion

This set of experiments was different than the others in many way. We set out to see what we could do. This is meant in a global view. Preceding experiments and models were chosen for a specific reason.

This model allowed us to see what else could be possible. Not only for the imaging field, but for other fields too who are investigating inflammation and TSPO specifically. This set of experiments has shown that there are increases to be observed in nearly all organs, and that the auto-segmentation is of great use as the manual delineation would have been heavily user dependent. We verified the volumes however and determined that the volume of a given organ was comparable to that of another subject. Weight was not accounted for on an organ-to-organ basis. The subjects however were of similar weight.

These results do need to be re-tested and compared to other subjects who have been submitted to i.p. injections of LPS at other concentrations. Concretely however, TSPO is of interest in an animal model of septic shock and possibly for the evaluation of the inflammatory levels in various organs throughout other species.

Section III

Chapter 8

Discussion

8.1 Chapter 3

There are many methods one can use in order to investigate a question at hand. Molecular imaging, as a field, offers various tools alone. Among these tools, positron emission tomography has the ability to image targets of choice without depth restriction, while maintaining a sensitivity which reaches a molecular level.

As a field of research, inflammation has many way in which it can be either estimated or targeted. TSPO, while seemingly a good target, is still rather under-investigated and needs to be further researched.

Researchers are aware that it (TSPO) is important for the inflammatory process and that it may also be a biomarker with which the level of inflammation could be gauged. The understanding of this protein is quickly increasing and questions are being raised about its implication in various disease. It is for this that we investigated various animal models of human diseases. IBD is currently evaluated by measuring various parameters to give the most information possible to the physician.

In chapter three we looked into the implications of TSPO in an animal model of inflammatory bowel disease suffering from a global intestinal inflammation.

While the group of Lacapere looked into the presence of TSPO in such an animal model [Ostuni 07], no group had yet investigated the possibility of evaluating the levels of TSPO in regard to a disease state.

The initial evaluations were more difficult than thought. Given that PET is quantitative by definition, it would lead one to believe that the evaluation of control animals versus treated ones would be straightforward. This was not the case (due to multiple factors such as not being able to use an anatomical image in our instance, and the size and spatial conformation of structures of interest)

as was seen in chapter three (Evaluation and quantification of TSPO expression in an acute model of global intestinal inflammation). The use of contrast agents was promising, but did not prove to be of help in our case. It might be of interest however to combine the two, PET/CT, with contrast agent for the anatomical reference image when diagnosing in humans. In such a case the affected areas are larger and as such might yield helpful supplementary data for the physician. Barium is currently being used, but is not without risk. Some deaths have been reportedly linked to Barium poisoning in rare cases. Even though it has been rare, a negative contrast (using water or air for example) might be able to avoid it completely for this kind of exam.

CT setting adjustments for better contrast of various tissues, or so-called 'windows settings', can also be of interest.

The side study that we carried out for the CT parameter settings did indeed help with the contrast improvements. We were able to distinguish various organs fairly easily. However, one should not forget the radiation dose that each subject is exposed to.

It is due to this side study that we realized a misalignment between the CT and PET images being reconstructed from the same machine. The initial worry was that we would be receiving false PET data as the attenuation correction in this machine is corrected by the CT data. This would mean that in areas where a higher density was, PET data would then be over corrected, thus yielding false positive information. To address the misalignment, we corrected the positioning of the CT in reference to the PET by applying a transformation matrix on Anatomist. This transformation matrix is a command, which the user defines. One can adjust the location of one image in respect to its fused image. Once aligned, one can then save the transformation matrix and then use it on any other image of choice.

This was just one of the steps that we had been concerned about while putting the animal model into place and were not yet concerned with disease evaluation. Also as soft tissue attenuates very little, as oppose to bone, it did not have much impact on our quantifications in our model.

The VOI determination was a necessary step and allowed us to have a just comparison between the two groups.

Human application may be similar. Experiments have been carried out in which the researchers used the CT as a means to determining the VOI. This anatomically determined VOI was then placed onto the PET image of that same subject [Bettenworth 13]. While the methodology seems logical (to place the VOI of the CT onto the PET image), it would require a structural alteration for it to be visible in the CT. This means that there is no early detection method as could be possible using PET. The study did indeed show that when using the CT to delineate the damaged VOI, one could be detect a difference between sick and healthy

subjects. The interest of this kind of procedure is questionable as the structural alteration would already be indicative of IBD. One would not require the PET exam in addition. As such, it would be nonsensical as the structural proof would already be present, thus contradicting the radiological dose guideline and negate the necessity of the PET exam. Also, the interest of PET imaging would be to enable detection of a lower level of inflammation (in this case) and avoid the late detection at which point a structural alteration could lead to further complications

A predetermined VOI would then be useful in IBD cases as is currently done in clinical settings for cancer evaluations for SUV determination.

The obtained data indicated that the treatment worked. This became evident when evaluating the PET data and also when observing the histo- and immunohistochemical data. We were able to see an increase in signal from TSPO markers in both PET and microscopical analysis. PET imaging with [^{18}F]FDG did however, not yield a significant difference between the control and treated groups. It is possible that a simple bowel movement could have increased the signal in the control groups, thus leaving false positive signals. The increased control levels then would diminish the difference of signal between the two groups. In a clinical setting, it could lead to a misdiagnosis leaving a patient suffering from IBD without treatment, or a treatment where not needed. [^{18}F]DPA-714 proved otherwise and may be a valid radiotracer for the evaluation of an inflammatory state in IBD disease.

The model however was one with an acute inflammation. It would be of interest to carry out an investigation into a model, maybe the same one, in which a chronic inflammation would be induced. Beyond this, one could then also carry out multiple image acquisitions which ultimately would, perhaps, give information about the evolution of the disease. Should that be the case, one could then imagine a clinical applications in which a physician would be able to follow the impact of a prescribed medication on the disease at hand. Theranostics in a word. The following experimental chapter touched on this question.

8.2 Chapter 4

The third chapter gave us some insight about the possibility of using TSPO as a biomarker in diseases of the periphery. It also permitted us to image other possibilities by leaving us with more questions. The fourth chapter was concentrated around IBD, but this time on a local acute inflammation as oppose to the global acute inflammation investigated in the third chapter.

Other groups had implemented a model which described what we were looking for. However, as their goals were different, some of the procedures had to be adjusted to accommodate our needs.

One factor in particular was the depth at which the TNBS was instilled at.

We decided to instill at 4 cm from the rectum, whereas others had instilled at 8 cm. This would not have been to our advantage as [^{18}F]DPA-714 eliminated via the hepatobiliary system. This would have most likely caused mixed signals, meaning that we would not be able to distinguish the signal due to the physiological elimination from that of the inflamed area.

One might then think that we should have instilled as rectally as possible. This would also have been a problem as we wanted to compare the TSPO radiotracer [^{18}F]DPA-714 to the radiotracer of reference, [^{18}F]FDG. [^{18}F]FDG eliminates via the urinary system. This causes a collection of [^{18}F]FDG in the bladder, which is located near the rectum. The resulting signal could also cause analytical difficulties.

These factors led us to the choice of an instillation depth at 4 cm from the rectum.

Another disadvantage we had was that we did not know at which time point the level of inflammation would be at its highest, as oppose to the previous model. To figure this out, we had to image the same animals at various time points. This not only gave us the time point at which we would have the highest level of inflammation, thus being able to compare the [^{18}F]DPA-714 to the [^{18}F]FDG as done previously, but it also yielded information about the disease evolution. We were able to observe that there was a fast increase of TSPO presence which then slowly decreased over time. This indicates that, if a medication were to be effective, then one could then use [^{18}F]DPA-714 to see the effects that the medication had on the disease. This might also then be of interest for drug resistance. The level of inflammation would increase as the drug resistance comes into affect. This would then be indicative of a need to change medications for an individual.

The other benefit of this experiment was that we were able to determine the time point at which the level of inflammation was at its highest. As it turned out, it was also the same time point as for the previous model.

Once this became known, we carried out comparative exams between the reference tracer and the TSPO ligand. We had expected to have similar findings as those in the model of global inflammation, in which the TSPO ligand revealed a more marked difference between the control and treated groups. This was not the case.

Using [^{18}F]FDG, we observed a larger contrast between the control and treated groups than we were able to with the [^{18}F]DPA-714 radioligand.

This is not too surprising when taking into account that [^{18}F]FDG is a glucose analogue. this means that the [^{18}F]FDG could have been taken up for one of many reasons, ranging from an inflammation, ulcer, to a simply bowel movement. On the other hand, it might be necessary for a higher level of inflammation to be present in order to observe a difference using [^{18}F]FDG, meaning that [^{18}F]DPA-714 could

perhaps be able to reveal more subtle levels of the inflammatory process. Either way, we were still able to determine a difference between the control and treated groups with the radioligand [^{18}F]DPA-714.

However, once again, this was a model of acute inflammation, it would be interesting to induce a chronic inflammation and then follow the disease evolution. The following step would then be to attempt to treat the disease and acquire PET images of the impact that the medication would have on the inflammation.

Diseases within the periphery affect millions of individuals throughout the world. We had decided to concentrate on one disease family (IBD) in order to determine whether or not TSPO could potentially be of interest for early detection of an inflammatory status when using PET imaging. Chapters III & IV went into detail about the potential benefits of the target TSPO in subjects suffering from a form of IBD. In the next chapter (V), we will explore the neuroinflammation using an adapted animal model for CNS.

8.3 Chapter 5

Neuroinflammation is a topic which deserves much attention. It is also the center of concentration for the INMiND consortium, to which our lab belongs too. The consortium is focused on the understanding of neuroinflammation and our lab has a history in the investigation of neuroinflammation and as such had an animal model which has been implemented for testing of novel radiotracers. The INMiND consortium wanted to put a common animal model in place which would be reproducible and common to all members. The purpose of this was to be able to evaluate, characterize, and compare novel ligands and quantification methods which were based on the same model of neuroinflammation on the The SHFJ happened to have developed a very similar model that has and is still used for the radiotracer testing. As such, tools to develop the model were readily available.

The idea behind this study was to develop and evaluate the new model for the investigation into the inflammatory process. We were able to put the model into place relatively quickly as there were only few differences between the protocols of the lab and those proposed by INMiND. The sole difference were the coordinates, which are very important actually. However, the different coordinates still had the user inject within the striatum (as was done for the AMPA model), a brain region which is very homogenous (structurally speaking) and as such favors reproducibility, which is important in any protocol.

The injection was carried out and PET images were acquired at various time points in order to observe the evolution, as we had proven to be possible in the previous chapter (chapter IV). The maximum signal was found to be at 48 hours post injection. This was interesting as it was very quick in comparison to the other

models thus far. Beyond this, it was also interesting to note that the peak was reached much faster than in the AMPA model (which is the model used at the SHFJ for the study of novel radiotracers).

As this inflammatory level increase arose quickly, we were concerned about the structural integrity of the blood brain barrier (BBB).

To be sure however, we carried out the Evans Blue (EB) test.

The EB test did not reveal any coloration/leakage at 2 hours post injection. This could mean that, there was no damage induced, that the point of injection healed after 2 hours, or that the EB is a molecule which is too big, and as such was unable to bypass the BBB itself and would mean that it is poorly adapted to our investigation. As this cannot be ruled out, the integrity should be further investigated by other means, such as MRI perhaps. This would allow for the visualization of a difference in tissue and be able to reveal any leakage or tissue density differences if present.

Another group uses capillary needles for the injection, which could also be an option for this lab, however, the means by which LPS solution is injected, leaves one with some questions about the precision of the volume being introduced.

Even though we have learned a lot from the PET data, further investigation is needed into this topic however, on all fields. IHC analysis is needed to correlate the PET data with tissue analysis. This goes for both models of neuroinflammation, LPS and AMPA. Especially when looking at the results of the TACs which revealed similar [^{18}F]DPA-714 uptake at the peak tracer accumulation. Then of course it would be of value to compare the samples of the two along with the staining and IHC results. It would be interesting to multi-mark brain slices of the LPS and AMPA injected area at each time point and observe which parameter was most present at which time point. This would be in order to better characterize the inflammatory process based on the expression of various biomarkers such as CD68, Iba-1 and TSPO for example and would bring to light the order in which each process occurs and also permit us to determine the kinetics of TSPO expression.

It would be beneficial to know where TSPO has its highest over-expression within the inflammatory process. Physicians could then be able to better diagnose. The diagnosis would then not only be based on an image, but also on knowledge of the inflammatory process.

Evolution is what research aims to bring. To do this, one must also improve the things at hand. This was the seventh chapter aimed to bring to light.

8.4 Chapter 6

In chapter VI we carried out experiments for the evaluation of a novel TSPO radioligand [^{18}F]DPA-C5yne, which is a novel ligand conceived by the radiochemistry

group of the SHFJ. The purpose was to evaluate the potentially better stability of this novel radiotracer in a biological environment in comparison to its predecessor, [^{18}F]DPA-714.

We then used the [^{18}F]DPA-C5yne tracer to evaluate the level of inflammation in the reference model used here in the lab.

Before being able to justify an *in vivo* experiment, we had to carry out the *in vitro* experiment. This is an important step when observing the 3 R's of animal experimentation, replacement, reduction and refinement.

Autoradiographic image analysis revealed a lower background noise in this novel ligand than found with [^{18}F]DPA-714, which is already an improvement to the reference tracer for TSPO, [^{11}C]PK-11195.

The *in vivo* interest of the new tracer, as shown in figure 6.2.3, revealed a significant uptake of [^{18}F]DPA-C5yne in the lesion when compared to the control side. The target-to-background ratio was calculated to be around 4.62 ± 0.4 compared to the [^{18}F]DPA-714 ratio of around 3.71 ± 0.4 . An initial analysis concerning *in vitro* metabolism seemed promising but needs to be further investigated *in vivo*.

The fact of having an animal model dedicated to this kind of evaluation is pinnacle for comparison. This particular model is reproducible. As even the localization is determined with a precision based on a tool, there is little margin for human error.

This kind of evolution is important as it would ideally allow the physician so be able to use tools which are more accurate and as a result be able to give a more informed and hopefully a more precise diagnosis.

This not only shows that there is always room for improvement and development, but that there could also be an interest to test this novel tracer in other disease models.

Research is not just about trying to find something. It is also about evolution. Just because something exists that works, does not mean that it is ideal. This study shows that while there can be a target of interest, there might be a way in which the targeting process could be improved. It became evident that an increased signal is not the only answer, but that a decrease in unspecific signal can be just as beneficial.

This evolution is constant and had already been addressed in previous studies such as that by Boutin et al. with the [^{11}C] marked DPA-713 [Boutin 07a]. While that compound was interesting, a clinical setting would benefit from the longer half-life of an [^{18}F] tagged molecule for convenience purposes too. As such, another TSPO radioligand was created, [^{18}F]DPA-714. However, as previously explained, there was still room for improvement regarding the metabolism of this compound, hence the research into the development of [^{18}F]DPA-C5yne.

So far we have seen that TSPO is of interest as a target for the evaluation of

the inflammatory state. The application was evidenced in animal models designed to replicate a specific disease such as various inflammatory bowel diseases as well as in a model of neuroinflammation. Beyond this we have seen that there can be improvements to the tracers.

8.5 Chapter 7

It became clear that TSPO was a decent biomarker for diseases which were relatively localized thus far. The imaging TSPO was possible throughout the body thus far and able to distinguish inflamed areas from non-inflamed areas. Better than the reference tracer (^{18}F FDG) even in one case.

However, inflammation is not only present in local situations. Septic shock is a prime example of a systemic inflammation before leading to an organ failure. Before testing the novel TSPO ligand, ^{18}F DPA-C5yne, we wanted to see whether or not the relatively novel TSPO tracer, ^{18}F DPA-714 would be able to distinguish basal levels of inflammation from a treated subject.

As we were going to carry out a whole body acquisition and evaluation, we were obliged to use a different PET machine, the HRRT. Even though it is a prototype with a very good resolution for human application, its spatial resolution is half that of the INVEON μ PET that we used for the all previous models.

The advantage of using a larger bore however, is that we were able to have a higher throughput due to a custom made bed which was able to support 4 rats per scan.

The acquired images were not easy to define VOIs on as the whole body, and thus each organ, was inflamed. Human error would have been non-negligible in VOI selection. The delineation between lungs and heart for example were not to be seen by the naked eye.

This problem however had previously been addressed by a member of the lab. The way in which the individual had addressed the question was to see the image as pure activity as oppose to a tissue in which activity was being acquired.

He created a program which differentiates the organs based on their TACs. Each organ has a different pharmacokinetics from its neighboring organ. A voxels TAC is altered based on the pharmacokinetics of the organ on which the voxel is located. This means that due to a difference in TACs, the program is able to distinguish one organ from another, such as the lungs from the heart.

Applying this method of VOI delineation allowed us to have confidence in the analysis as it is a very robust method and was not user dependent.

With its help, we were able to compare TSPO expression in a group of control animal to a group of treated animals. The dose that we chose to inject the animals with was one of the lower doses we found in the literature. This was a conscious

choice as we found that the higher the dosage, the more deaths were reported at 24 hours post injection.

The levels of inflammation, and thus TSPO, were increased in each and every organ, with exception of the thyroid and the salivary gland. This is possibly explained by a disease called the sick euthyroid syndrome. The disease was also induced with LPS as we had done for the model of septic shock. We did not foresee this correlation initially.

It turns out that this lowering of signal could be due to direct thyroidal inhibition which is caused by an extra-thyroidal inhibition of IL-alpha.

It seems as if this lowering of the inflammatory state is also time dependent. This could possibly mean that the level septic shock could be estimated based on the tracer uptake, but that the stage could possibly be estimated based on the signal, or lack of signal, collected in the thyroid, and perhaps the salivary glands. Ultimately, this would mean that looking for both, the presence of TSPO but also its absence, could be indicative of a disease as well as the stage.

Conclusion and perspectives

Reminder of the objectives

During the course of this thesis, we set out to determine whether or not TSPO 18kDa could be a measurable biomarker for the evaluation of various inflammatory diseases, both inside and outside of the central nervous system. To test this, we put multiple animal models in place which were designed to replicate symptoms found in human inflammatory diseases. The level of inflammation was measured and quantified with PET imaging and the TSPO 18kDa radioligand [^{18}F]DPA-714. Each of these results were correlated with a microscopic characterization of either the TSPO directly or other inflammatory markers expressed on a cellular level.

Overview of the research

The research yielded information leading to the conclusion that the TSPO 18kDa could indeed be useful as a biomarker for the evaluation of an inflammatory state for various diseases. We were able to illustrate in two models of IBD, one model of neuroinflammation, and one model of septic shock that TSPO was an indicator of the level of inflammation found within the affected area. Beyond this, we were also able to follow, measure, and quantify the evolution of an inflamed area over time.

Even though [^{18}F]DPA-714 was the tracer used to determine the presence, and level of inflammation, other tracers are constantly being developed. This was illustrated in the collaborative work carried out with another group in which we were able to highlight the potential for tested novel TSPO radioligand ([^{18}F]DPA-C5yne).

Contributions and perspectives

This work validated TSPO as a biomarker of inflammation for the implication in various diseases and that these measurements correlated with IHC analysis. We were able to measure and quantify the varying levels of inflammation (to include inter-individual variations) with the help of the radioligand [^{18}F]DPA-714. We

were also able to illustrate that the continual development of novel radiotracers is needed as this will ultimately lead to a better diagnosis and better patient care.

The next steps would be to attempt clinical PET trials for the IBD related diseases with the use of a TSPO radioligand. Once validated, it would be of interest to follow the inflammatory levels in an individual. One could then also imagine being able to follow the impact of an administered treatment. A real theranostic patient care.

As for the neuroinflammatory research, it would be interesting to compare the IHC results of the LPS (INMiND) model to those of other neuroinflammation models (AMPA in our case) and evaluate the findings. It would be of interest to determine whether each induction method yields a similar inflammatory response or not. These future findings may help elucidate the inflammatory process. This along with the continual development and improvement of TSPO ligands will help in the increased precision and the subsequent quantification of disease detection and evaluation.

To date, septic shock has been difficult to measure, and it is too early to say whether or not the very preliminary experiments carried out in this manuscript will be indicative of the inflammatory state or not. It is noteworthy however that with the current findings, further research is needed to get to the bottom. There is much potential for the use of TSPO as a biomarker in cases of septic shock. If, the levels of TSPO are indicative of the septic state, then physicians would be able to have more information with which to act.

Inflammation is at the origin of many diseases and disorders, we should be treating it, and its components, as a tool, not only a threat.

Annexes

Annexe A
Published Articles

In vivo Evaluation of Inflammatory Bowel Disease with the Aid of μ PET and the Translocator Protein 18 kDa Radioligand [18 F]DPA-714

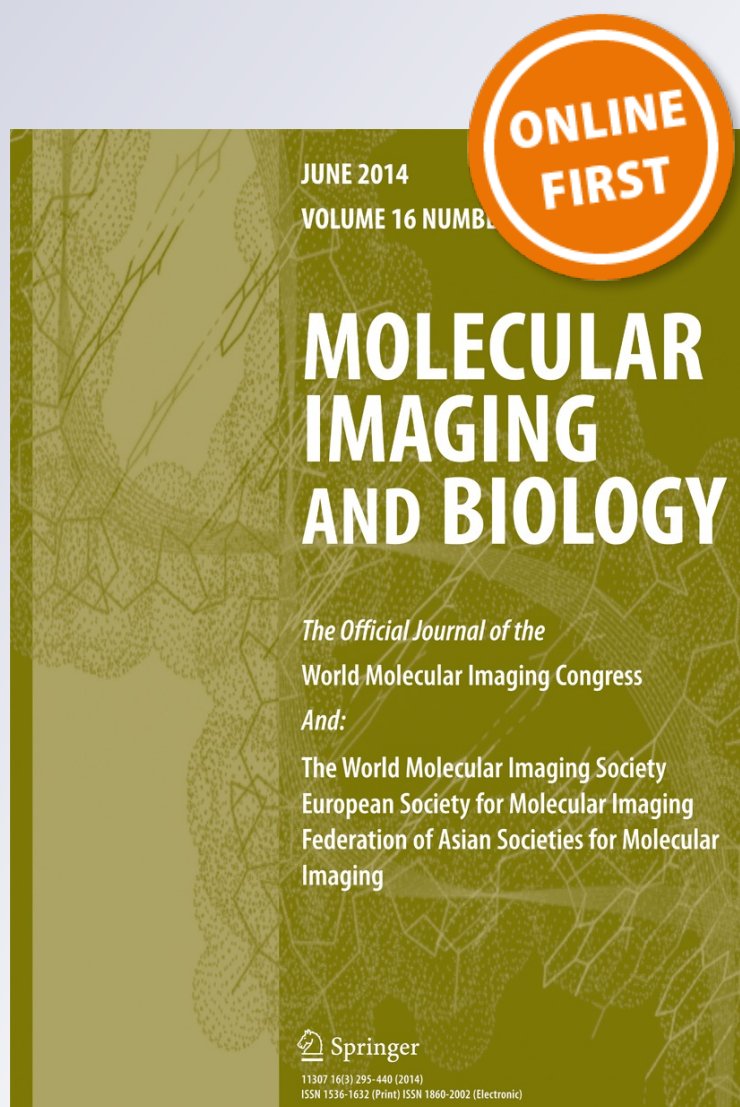
**Nicholas Bernards, Géraldine Pottier,
Benoit Thézé, Frédéric Dollé & Raphael
Boisgard**

Molecular Imaging and Biology

ISSN 1536-1632

Mol Imaging Biol

DOI 10.1007/s11307-014-0765-9



Your article is published under the Creative Commons Attribution license which allows users to read, copy, distribute and make derivative works, as long as the author of the original work is cited. You may self-archive this article on your own website, an institutional repository or funder's repository and make it publicly available immediately.

RESEARCH ARTICLE

In vivo Evaluation of Inflammatory Bowel Disease with the Aid of μ PET and the Translocator Protein 18 kDa Radioligand [^{18}F]DPA-714

Nicholas Bernards,^{1,2} Géraldine Pottier,^{1,2} Benoit Thézé,^{1,2} Frédéric Dollé,² Raphael Boisgard^{1,2}

¹Inserm, Unité 1023, Université Paris Sud, 91400, Orsay, France

²Commissariat à l'Energie Atomique et aux Energies Alternatives, Direction des Sciences du Vivant, Institut d'Imagerie Biomedicale, Service Hospitalier Frédéric Joliot, 4, place du Général Leclerc, 91400, Orsay, France

Abstract

Purpose: The purpose of the study was to validate [^{18}F]DPA-714, a translocator protein (TSPO) 18 kDa radioligand, as a probe to non-invasively quantify the inflammatory state in inflammatory bowel disease (IBD) animal models.

Procedures: Quantitative positron emission tomography (PET) imaging of intestinal inflammation was conducted with 2-deoxy-2-[^{18}F]fluoro-D-glucose ([^{18}F]FDG) a glucose metabolism surrogate marker and [^{18}F]DPA-714 a ligand of the 18 kDa TSPO, on two IBD models. The first model was induced using dextran sodium sulfate (DSS), creating global inflammation in the colon. The second model was induced by rectally administering trinitrobenzenesulfonic acid (TNBS), creating local and acute inflammation.

Results: The level of inflammation was analyzed using PET imaging on days 7 and 8. The analysis obtained with [^{18}F]DPA-714, yielded a significant difference between the DSS treated ($0.50 \pm 0.17\% \text{ID/cc}$) and non-treated rats ($0.35 \pm 0.15\% \text{ID/cc}$). [^{18}F]FDG on the other hand did not yield a significant difference. We did observe a mean glucose consumption in the colon increase from $0.40 \pm 0.11\% \text{ID/cc}$ to $0.54 \pm 0.17\% \text{ID/cc}$. In the TNBS model, the uptake level of [^{18}F]DPA-714 increased significantly from $0.46 \pm 0.23\% \text{ID/cc}$ for the non-treated group, to $1.30 \pm 0.62\% \text{ID/cc}$ for those treated. PET signal was correlated with increased TSPO expression at cellular level.

Conclusions: Results indicate that [^{18}F]DPA-714 is suitable for studying inflammation in IBD models. [^{18}F]DPA-714 could be a good molecular probe to non-invasively evaluate the level and localization of inflammation. Moreover, *in vivo* imaging using this TSPO ligand is potentially a powerful tool to stage and certainly to follow the evolution and therapeutic efficiency at molecular level within this disease family.

Key words: Inflammation, TSPO, DPA-714, Inflammatory Bowel Diseases, PET imaging

Introduction

Inflammatory bowel disease (IBD) is a disease family that has not been getting the attention that it warrants. The incidence has been slowly rising throughout much of the

industrialized world, and is not limited to adults, but also affects children [1].

IBD is comprised of multiple diseases, including Crohn's disease (CD) and ulcerative colitis (UC), which all have aspects of inflammatory responses, ranging from acute to chronic stages, and in many cases include both. The whole gastrointestinal tract can be affected from CD while UC is limited to the cecum, colon, and rectum [2]. Precise

Correspondence to: Raphael Boisgard; e-mail: raphael.boisgard@cea.fr

localization of the inflamed sites is one criteria permitting differential diagnosis between different types of diseases.

The fact that this disease family can have such large variations, and yet present itself with similar if not identical symptoms, makes it very difficult to diagnose and to differentiate. The origins of the diseases are unknown, but there seems to be a tendency for the disease to be more prevalent in the Western world, and in particular, within urban areas; this is not to say that the levels or the incidence outside of the urban Western world are lower, but rather that the methods of detection and definition of what constitutes IBD are similar in these areas [3]. There may be multiple factors which contribute to the development of the diseases ranging from genetic pre-dispositions to lifestyle and stress exposure [4].

Inflammation is only the beginning of medical concerns associated with IBD. If IBD is left untreated, it can lead to cancer of the intestine. Even if this does not happen, there is still a detrimental impact on daily lifestyle. It is not completely clear how to avoid suffering from IBD, but early detection would allow early treatment and thus represent a way by which suffering could be minimized. Moreover, the disease progression and evaluation of the therapeutic efficiency also lack pertinent criteria.

Currently, the clinical evaluation consists of various exams and exam types ranging from physical symptoms, such as bloody diarrhea (a cardinal symptom), to serology, endoscopic exploration, radiological analysis, and nuclear medical investigations [5]. Preclinical investigations often-times use rodents which have had IBD symptoms induced by various means. The general assessment of IBD *in vivo* is commonly carried out by observing bloody diarrhea and by scoring body weight changes. *Post mortem* analyses include measurements of the colon length, cytokine and chemokine concentrations along with histological scoring [6]. These last years, only few articles illustrate the interest of *in vivo* imaging using a non-specific radiotracer, which is based on the increase of glucose metabolism, for the evaluation of IBD in both human and preclinical models [7, 8].

In vivo molecular imaging represents an attractive means to characterize these types of pathologies, especially as it is non-invasive. Of these methods, positron emission tomography (PET) is a powerful technique allowing the clinician to access molecular information *in vivo*. PET imaging has been present in clinical applications since the 1970s and is now routinely used for diagnosis, prognosis, and theranostics. Due to the fact that it is a quantitative, specific, and sensitive imaging modality, this non-invasive *in vivo* technique is well adapted for early detection of various diseases. PET is, however, based on the use of dedicated radiotracers, the most well-known being 2-deoxy-2- ^{18}F fluoro-D-glucose (^{18}F FDG), a surrogate marker for glucose metabolism. Recently, Lapp, but also Shyn and Ostuni and collaborators have shown that PET could indeed be used for the detection of an IBD related disease with the use of ^{18}F FDG [9–11].

^{18}F DPA-714 is a recently developed radioligand of the translocator protein 18 kDa (TSPO) with improved signal to noise ratios as compared to previously used radiotracers and especially ^{11}C PK11195 [12, 13]. TSPO, formerly known as peripheral benzodiazepine receptor (PBR), located on the outer membrane of the mitochondria, is overexpressed in activated macrophages and microglia. This molecular event has been used widely to investigate inflammation inside the central nervous system. TSPO increase in microglia is now presented as a hallmark of brain inflammation and our laboratories have been instrumental in the characterization and validation of this radiotracer in various preclinical models of neuroinflammation [14, 15]. However, when looking at peripheral activation of macrophages and links to the inflammatory processes, little data are currently available. TSPO expression was recently described in tissue samples of human colon suffering from IBD (CD and UC) [11]. Additionally, expression has also been characterized in a rat model of IBD using autoradiography and immunohistochemistry [11].

The use of the TSPO ligand ^{18}F DPA-714 has opened doors to exploration into inflammation within the periphery, and thus also into the domain of inflammatory bowel diseases. It allows the quantification of the inflammation found in a given area within the bowel. To confirm this capability, we implemented two animal models of IBD, one using dextran sodium sulfate (DSS) inducing high diffuse inflammation in the colon, and the other using trinitrobenzenesulfonic acid solution (TNBS) inducing inflammation mainly restricted in the area of instillation [16, 17], and demonstrated the potential of ^{18}F DPA-714 to image IBD with PET.

Materials and Methods

Animal Models

The animals chosen were male Wistar rats (Centre d'Élevage René Janvier, France) with a weight of 250 g±20 g. The subjects were kept in an adapted environment in which the temperature and humidity are regulated. The lights are on a 12-h cycle on and then off. The experiments were carried out in accordance with French guidelines.

Two different animal models of acute bowel inflammation were developed and implemented in the study. The first being a DSS (Sigma-Aldrich, France; MW40,000) induced model, which leads to haematochezia, and also to weight loss along with a shortening of the intestine among other consequences associated with a colitis rat model [16]. DSS induces *in vivo* intestinal inflammation and is simple, affordable, and also has a high degree of uniformity and reproducibility of most lesions in the distal colon. In this model, we added DSS at 5 % (v:v) into the drinking water of the animals from which they had *ad libitum* access throughout the duration of the experiments. ^{18}F FDG images were acquired after 7 days of treatment whereas ^{18}F DPA-714 images were acquired after 8 days of treatment. The treatment has been used successfully with rats in previous tests [18]. Non-treated rats were given plain water in their bottles and all the animals were weighed daily, and their feces state

was also observed on a daily schedule. The DSS solution was exchanged on days 3 and 5 in the treated group and the non-treated group also had their water exchanged for a new bottle containing plain water at the same time points.

The second model was chemically induced by instilling trinitrobenzenesulfonic acid (TNBS) (Sigma-Aldrich) as described by the group of Seibel *et al.* [19]. Some slight alterations were made in order to adapt this model to the PET modality. Here, inflammation was induced into male Wistar rats by administering 100 μ l of 50 % ethanol-water solution (to help bypass the mucosal layer of the intestine) containing TNBS (100 g/l, corresponding to 40 mg/kg body weight) 4 cm into the rectum from the anus [17]. During this administration, the rats were under anesthesia using 2.5 % isoflurane in 100 % O₂. This anesthesia was maintained for an extra 10 min post instillation in order to reduce displacement and possible leakage of the chemical. Non-treated animals were injected with 100 μ l of ethanol and water (1/1, v:v).

The animals were then placed into individual cages and their weights were measured on a daily basis and their feces state was recorded. Inflammation was evaluated with PET imaging on day 7 using [¹⁸F]FDG and on day 8 using [¹⁸F]DPA-714 after TNBS administration.

PET Radiotracer

[¹⁸F]FDG was purchased from the commercially available source Cyclopharma S.A. (Clermont-Limagne, France). [¹⁸F]DPA-714 was produced on site according to slight modifications of procedures already reported [20] and using a commercially available GE TRACERLab FX-FN synthesizer [21]. Ready-to-inject, >99 % radiochemical pure [¹⁸F]DPA-714 (formulated in physiological saline containing less than 10 % of ethanol) was obtained with 15–20 % non-decay-corrected yields and specific radioactivity level at the end of the radiosynthesis ranging from 37 to 111 GBq/ μ mol.

Image Acquisition

The PET and PET/CT images were acquired using two separate machines. The first one is a Siemens INVEON PET and the second a Siemens INVEON PET/CT, both being dedicated small animal scanners. Each animal had its images acquired in the same machine each day. The animals were kept normothermic with the help of a heating carpet. Rats were anesthetized using 3 % isoflurane in pure oxygen and kept sedated throughout the acquisition. For [¹⁸F]DPA-714, images were acquired dynamically during a time span of 60 min, beginning at the same time as the injection. Each animal was injected with 37 ± 2 MBq (1.0 mCi \pm 0.054 mCi). The [¹⁸F]FDG acquisitions (30 min) were sorted into three frames of 10 min each and the [¹⁸F]DPA-714 images were sorted into 16 frames. Frames 1–5 each lasted 1 min, frames 6–10 lasted 2 min, frames 11–13 each lasted 5 min, and the remaining frames (14–16) lasted for 10 min each. The energy discrimination was set at 350 and 650 KeV. The list-mode acquisition was as described previously and the data files were histogrammed into three-dimensional sinograms with a maximum difference of 47 and a span of 3 [20].

The attenuation correction of the Siemens INVEON PET was measured with the help of a Cobalt-57 point source. The Siemens INVEON PET/CT carried out the attenuation correction

measurement with the use of its CT imaging capabilities and settings, which are implemented directly by the manufacturer. In order to obtain the best resolution possible within the intestines, we implemented a Fourier rebinning and an OSEM 2D reconstruction method.

Image Analysis

The reconstructions of the PET images were carried out using ASIPro VM (CTI Concorde Microsystem Analysis Tools and System Setup/Diagnostic Tool). The image analysis and quantification of the radioactivity uptake in the regions and volumes of interest (ROI's and VOI's) were carried out with the use of BrainVisa/Anatomist Version 4.3.0 [22].

Delineation of the ROI's and VOI's was selected by means of manual segmentation and always carried out by the same user. The selected region of the intestine was $5 \times 3 \times 2$ voxels, or a 3.6-mm³ volume placed on the intestinal wall.

Gamma Counting

The ascending colon was excised once the subject had been euthanized *via* an *i.v.* injection of pentobarbital and divided into three sections. Each sample was weighed before being placed into individual tubes, which were then inserted into a Perkin Elmer Cobra II Auto-Gamma Gamma-ray counter. The results were decay-corrected and standardized for the percent injected dose, sample weight, and the body weight of each animal, which corresponds to the standardized uptake value (SUV).

Immunohistochemistry and Morphological Analysis

Post mortem tissue samples were excised, once the [¹⁸F]DPA-714 images had been acquired, and fixed with 4 % paraformaldehyde (PFA, Sigma-Aldrich) in Phosphate-buffered saline (PBS, pH 7.4 Sigma-Aldrich, France) for 2 h followed by cryopreservation by incubation in PBS, pH 7.4 containing 20 % sucrose for 24 h. The intestines were then cut into thirds (ascending, transverse, and descending sections), immersed in embedding tissue medium (Shandon M-1 Embedding Matrix, Thermo, USA), and frozen rapidly in liquid nitrogen. Immunohistochemistry (IHC) was then carried out on slices of 5 μ m thickness taken from the specimen. Anti-TSPO marker (NP-155, a kind gift of Dr. Makoto Higuchi, The National Institute of Radiological Sciences, Chiba, Japan) was used on individual slices.

Non-specific binding were blocked with 5 % BSA and 0.5 % Tween 20 in PBS (5 min, room temperature (RT)) and incubated (1 h, RT) with primary antibodies as follows: Rabbit anti-TSPO antibody (NP155, 1:500) diluted in 5 % BSA and 0.5 % Tween 20 in PBS, and, after PBS washes (three times), sections were incubated (30 min, RT) with Alexa Fluor-488 goat anti-rabbit (A11034, 1:1000; Invitrogen, France), diluted in 5 % BSA and 0.5 % Tween 20 in PBS.

Hematoxylin and Eosin Staining

The frozen slides containing slices of the intestines were placed into fresh PBS for rehydration 5 min before being placed into deionized water for 1 min. The slides were then introduced for 5 min into a Hematoxylin solution ready to use (Sigma-Aldrich, France). Once this was carried out, the slides were placed into tap water for 5 min before being placed into a series of 5-min-baths of deionized water, followed by Eosin-Y solution (LABOnord, Templemars, France), 90 % ethanol in water, 100 % ethanol, and finally toluene for 15 min. Once this was done, the slides were individually mounted with the Eukitt quick-hardening mounting medium (Sigma-Aldrich, France), by placing a few drops onto the slide and then laying a cover slip over them.

Results

As illustrated by the group of Lacapere, there is an overexpression of TSPO in the rat colon of the DSS-induced IBD animal model after 7 days of treatment [11]. To evaluate the possibility to both visualize and quantify the expression of TSPO in IBD, we reproduced the inflammatory model in our laboratories. In the DSS rat model, large alterations to the structure of the colon can be observed when compared with samples of non-treated animals, as illustrated in Fig 1. Microscopic observations on the different sections of the colon (ascending, transverse, and descending) of treated animals revealed erosion along the entire colon. This alteration was also associated with rectal bleeding and a loss of weight in treated animals (data not shown). The non-treated animals showed no such signs and have intact crypts as illustrated on Fig. 1a. TSPO expression was investigated on adjacent tissue samples. Representative images (Fig. 1e, f) clearly show the increased presence of TSPO in the colon of treated animals with high infiltration in the eroded *lamina propria* and high density at the base of the intestinal wall (*lamina muscularis/mucosae*). In comparison to non-treated animals, TSPO positive cells were mainly found at a lower density within the *lamina propria* (Fig. 1d).

In the TNBS model, due to the direct local administration of the inflammatory agent, the phenotype was different with the inflammation localized mainly in the upper part of the ascending colon (around 4 cm from the anus), as opposed to the global inflammation found in the first (DSS) model. In this second model, the H&E staining presented in Fig. 1a, c indicates a morphological difference between a treated animal and a healthy animal, as indicated by an alteration of the microvilli architecture of the colon in the area of instillation. TSPO staining revealed an accumulation of TSPO positive cells at the base (*lamina mucosae*) and at the extremity of the microvilli (Fig. 1f).

In order to investigate the utility of [¹⁸F]DPA-714 to provide information concerning the inflammatory processes *in vivo*, we performed PET imaging on non-treated and treated rats and compared the uptake of this TSPO

radioligand with [¹⁸F]FDG, a radiotracer used previously to visualize IBD in humans. A PET imaging session was carried out on day 7 post treatment induction, using [¹⁸F]FDG, and on day 8 with [¹⁸F]DPA-714 on the same animals.

Figure 2 illustrates representative images of non-treated (2a, c) and DSS treated animals (2b, d) using [¹⁸F]FDG (2a, b) and [¹⁸F]DPA-714 (2c, d) at 7 and 8 days, respectively, along with the corresponding graphs (Figure 2 e, f, respectively). For both tracers, an increased uptake in the colon of treated animals in comparison to non-treated animals was observed. The regions of interest were manually drawn with identical sizes for all images on the colon wall in the area with the highest signal. Quantification of the radioactivity uptake after 60 min of acquisition revealed that for [¹⁸F]FDG, the mean glucose consumption in the colon increased from 0.40 ± 0.11 %ID/cc to 0.54 ± 0.17 %ID/cc (Fig. 2). This increase identified the inflammatory processes but was not sufficiently high to provide a significant difference between the two groups of rats ($P=0.053$). Similarly, quantification of [¹⁸F]DPA-714 in the colon of control and treated animals revealed a significant increase in uptake level from 0.35 ± 0.15 %ID/cc to 0.50 ± 0.17 %ID/cc ($P=0.040$, Fig. 2). This increased significance correlates to the overexpression of TSPO in colon tissue samples as illustrated on the Fig. 1e.

In Fig. 3, one can observe that the PET images and the subsequent analysis, were verified/validated with the gamma counting. Here, we also observed a significant difference between the treated and control groups where $p < 0.0001$.

In the TNBS model, in contrast to the DSS model, the inflammation is localized mainly in the area of administration of the immunogenic stimulating agent. PET image analysis clearly illustrated that [¹⁸F]DPA-714 was able to highlight a difference in inflammatory status between the non-treated and the treated animals. Figure 4 illustrates the increased uptake for both tracers (images a–d and graphs e and f), [¹⁸F]FDG and [¹⁸F]DPA-714. Treated animals (Fig. 4b, d) show a more localized area of inflammation when compared to the distribution of the tracers in the DSS model (Fig. 2b, d). For both tracers, the area of increasing signal is larger than the theoretical area of instillation due to either a diffusion of the TNBS during experimental procedure or to a propagation of inflammation to a large portion of this organ.

For both [¹⁸F]FDG and [¹⁸F]DPA-714, the inflammation induced a significant increase of tracer accumulation from 0.43 ± 0.18 to 1.20 ± 0.56 %ID/cc for [¹⁸F]FDG and 0.46 ± 0.23 to 1.30 ± 0.62 %ID/cc for [¹⁸F]DPA-714 ($p < 0.0006$ for [¹⁸F]FDG and $p < 0.0058$ for [¹⁸F]DPA-714, Fig. 4).

The objective of molecular *in vivo* imaging is to visualize the process of interest, in our case inflammation in an IBD model, but mainly to enable analysis and quantification of a dynamic process. In order to evaluate

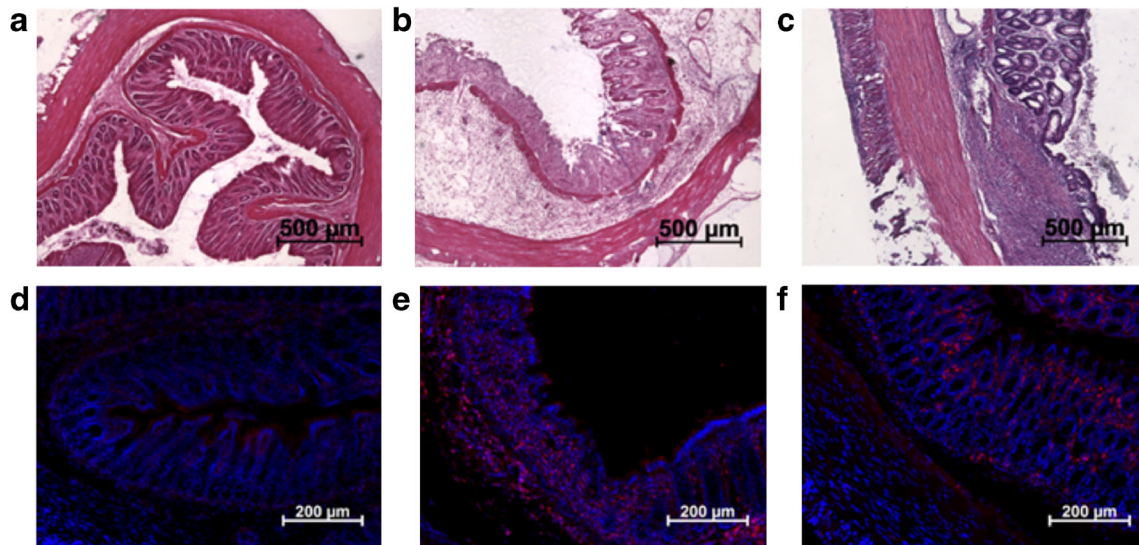


Fig. 1. H&E staining and immunohistochemical observations using TSPO antibody (NP155, red, DAPI in blue). In non-treated rat: **a** H&E staining and **d** NP155; in rat receiving DSS in water during 7 days: **b** H&E staining and **e** NP155; and, in TNBS instilled rats: **c** H&E staining and **f** NP155.

the potential of [^{18}F]DPA-714 to achieve this goal, we followed the inflammation over a period of 22 days in a group of six animals. The first images were acquired on each rat 1 day before the instillation of the TNBS to measure the basal value of [^{18}F]DPA-714 uptake in the middle of the colon for each rat. After induction, the animals were imaged at different days (1, 2, 4, 8, 10,

and 22) as represented in Fig. 5. This figure indicates an increase of [^{18}F]DPA-714 uptake until day 8/10 after which the mean signal decreased slowly to reach basal value at 22 days post induction. A large standard deviation was observed for the mean values at days 8, 10, and 22, illustrating the highly variable inter-individual evolution of the disease.

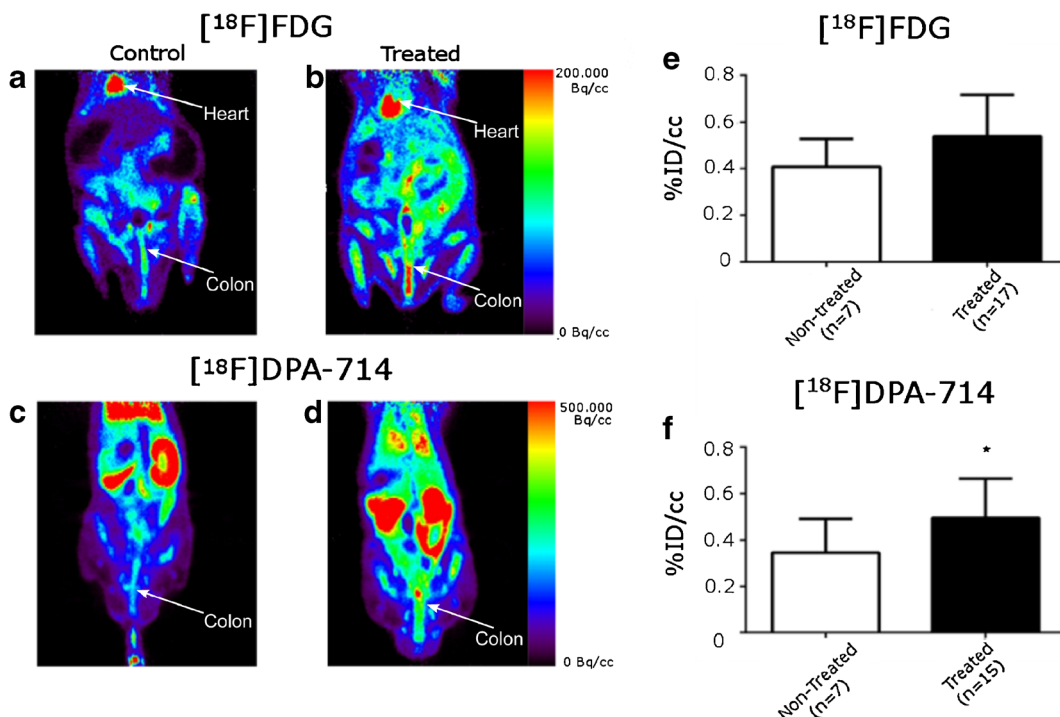


Fig. 2. Whole body PET images on control and DSS treated animals. [^{18}F]FDG in **a** control and **b** treated animals; [^{18}F]DPA-714 in **c** control and **d** treated animals. *Color scales* are different ranging from 0 to 200 MBq/cc for [^{18}F]FDG and to 500 MBq/cc for [^{18}F]DPA-714 images. Quantification of **e** [^{18}F]FDG and **f** [^{18}F]DPA-714 measured on PET images in area with highest uptake within the colon on control and DSS treated rats.

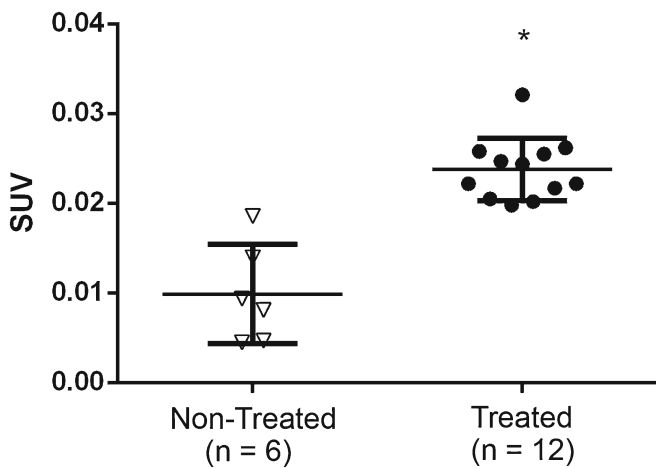


Fig. 3. Gamma counting of the excised sections of intestines revealed a difference of $[^{18}\text{F}]\text{DPA-714}$ presence between the two groups. (*= p value <0.0001) Results are expressed in SUV.

Discussion

IBD is a serious health issue, which appears to be increasing throughout the Western world. It is a disease which does not discriminate between ages, although it does tend to be present in higher numbers among the weaker of society, namely the young and aged groups. IBD, as a family of

diseases, including Crohn's disease and UC, can in many instances turn chronic, at which point there is no treatment for the disease itself, only its symptoms. This in itself will degrade the quality of life and result in additional medical expenses, which could possibly be avoided by early detection or improved diagnostics to evaluate the inflammatory component of the disease. PET imaging, using an appropriate radiotracer, offers this opportunity. It allows the researcher/medical doctor to observe a difference at a molecular level, which could aid in early diagnosis. This diagnosis, however, is only as good as the tools that are used. Thus far, the tools have not been focused on a specific aspect of inflammation, but rather on a symptom of the inflammation. Thus, they currently lack specific techniques for imaging and detection of IBD. We are now capable of producing improved tools and using them more effectively. In this study, we investigated two IBD models reflecting both local and diffuse inflammation of the digestive tract using PET imaging. We demonstrate that with the use of an adapted tracer $[^{18}\text{F}]\text{DPA-714}$, we are able to detect, visualize, and quantify a difference between the non-treated animals and those that underwent the treatments in order to induce IBD symptoms (as seen in Fig. 2 and 4).

The interest of this study was multifaceted. First, we wanted to establish two different (reproducible) models of inflammatory bowel disease, with different origins. Second,

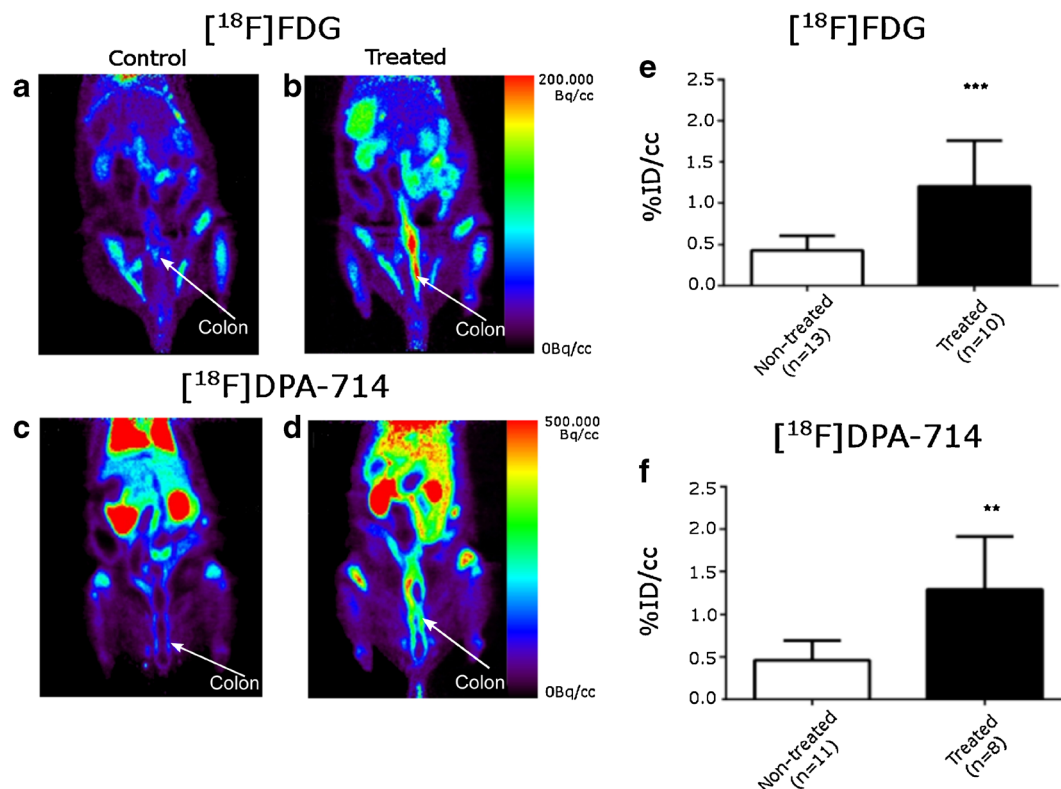


Fig. 4. Whole body PET images on control and TNBS treated animals using $[^{18}\text{F}]\text{FDG}$ in **a** control and **b** treated animals; $[^{18}\text{F}]\text{DPA-714}$ in **c** control and **d** treated animals. Color scales are different ranging from 0 to 200 MBq/cc for $[^{18}\text{F}]\text{FDG}$ and to 500 MBq/cc for $[^{18}\text{F}]\text{DPA-714}$ images. Quantification of **e** $[^{18}\text{F}]\text{FDG}$ and **f** $[^{18}\text{F}]\text{DPA-714}$ measured on PET images in area with highest uptake within the colon on control and TNBS treated rats. (*= p <0.0006 for $[^{18}\text{F}]\text{FDG}$ and p <0.0058 for $[^{18}\text{F}]\text{DPA-714}$).

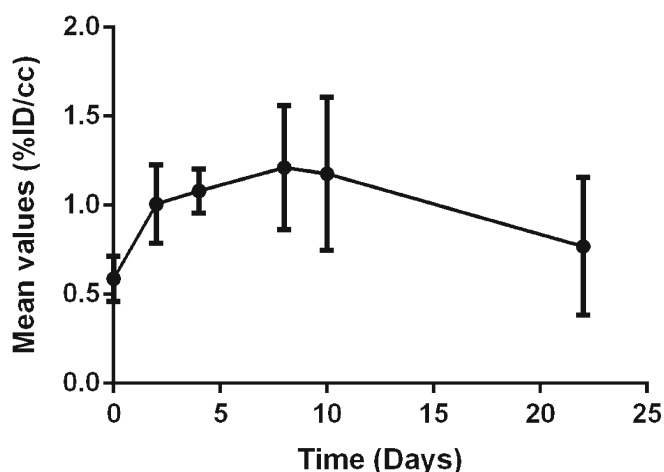


Fig. 5. Characterization of the TSPO expression over time in a rat model of local inflammation within the colon (TNBS rat model).

we wanted to prove the relationship between tissular expression of TSPO and the specific uptake of $[^{18}\text{F}]\text{DPA-714}$ obtained *via* molecular imaging. Third, to show that imaging can provide a quantifiable difference between sick and healthy subjects. Fourth and foremost, we wanted to validate $[^{18}\text{F}]\text{DPA-714}$ as a probe for peripheral inflammation, which has to date been used mainly for neuroinflammation.

In addition to this list of objectives, we examined another aspect of molecular imaging, specifically for PET, which allows the user to follow the advancement and characterize of a disease or any other molecular process of choice. This approach was illustrated by the dynamic description of the inflammatory status using $[^{18}\text{F}]\text{DPA-714}$ in the TNBS model (Fig. 5). Following the uptake of the radioligand in the instillation area, we were able to demonstrate the ability to detect varying levels of inflammation of the disease for each individual animal.

Our first objective had been to reproduce the models used by the groups of Dr. Ostuni and Dr Seibel [11, 19]. This was accomplished and used to detect inflammation in each induced animal and subsequently verified with HE staining, and also by labeling with Iba1 (macrophages) and NP-155 (TSPO 18kDa). In each case, we observed a marked structural difference between the two groups as well as an increase in signal on the treated animals from the markers. The differences can be seen in images on Fig. 1d–f.

This invasive evaluation of inflammatory status (using biopsies) can certainly be characterized using PET as a quantifiable imaging tool. Side effects of these intestinal treatments (diarrhea and reduced gut motility) were found in both DSS and TNBS models, respectively. These two symptoms have a drastic impact on the size of the gut, the first one reducing the thickness making it difficult to visualize the intestine wall (often empty with a collapsed lumen) and the second one with an increase of the diameter due to the accumulation of feces. In the case of preclinical imaging on small animals, the access to conventional CT

anatomical reference images is not possible due to the lack of soft tissue contrast. The other limit in small animal imaging is the spatial resolution of the PET camera in regard to the thickness of the intestinal wall in rodents. This resolution, coupled with the size of the structure impacts the quantitative approach due to a high partial volume effect artificially decreasing the uptake value observed in comparison to the result expected in larger animal model or in humans. To accurately compare data among different animals, with different pathological models and different tracers, we choose to define a small volume ($5 \times 3 \times 2$ voxels) that we placed on the areas of highest uptake of each animal, and then compared this volume between the groups.

Once we quantified the images, we found a difference between the results of the two tracers on the same group. The results on Figs. 2 and 5 revealed different levels of signal when comparing the healthy groups to each other. This means that the healthy group of the DSS $[^{18}\text{F}]\text{FDG}$ animals yielded slightly different results than the same group did with the $[^{18}\text{F}]\text{DPA-714}$ radiotracer. This is understandable and explainable when looking at what each tracer is actually targeting. $[^{18}\text{F}]\text{FDG}$ is a glucose analog which indicates an increase of glucose consumption, which in itself can be indicative of other on-going processes such as cancer, cell regeneration, or muscle contraction as seen in peristalsis [23, 24]. Fibroblasts also have an increase of glucose consumption when they are exposed to inflammatory mediators such as tumor necrosis factors (TNF) [25]. This tracer has been described as a good marker of inflammatory processes but it reflects global impact on different cell populations and biological processes.

On the other hand, $[^{18}\text{F}]\text{DPA-714}$ has not yet been shown to be increased in different cell populations except in immune white cells. This TSPO ligand has been presented as a tracer with high affinity and good specificity. Image quantification of $[^{18}\text{F}]\text{DPA-714}$ uptake correlated with the amount of TSPO, as published previously and provides indirect information about white blood cell activation in the tissue of interest [15, 26]. In the TNBS model, the uptake at 7 days of $[^{18}\text{F}]\text{FDG}$ and on day 8 of $[^{18}\text{F}]\text{DPA-714}$ is higher than in DSS model (Fig. 4). These differences illustrate a higher level of local inflammation in this second model.

Another difficulty we faced in one of the preclinical models was the localization of induced inflammation. Here, in the second model, we had to choose a distance at which the TNBS should be induced. We had to avoid the upper digestive tract as this is the region in which the $[^{18}\text{F}]\text{DPA-714}$ is eliminated by, thus inhibiting us from distinguishing the potential region of inflammation and the regular elimination. Inducing the TNBS too close to the anus on the other hand was also disadvantageous as the bladder is located in the vicinity. This poses a problem as it is the renal pathway by which $[^{18}\text{F}]\text{FDG}$ is eliminated, also obstructing the image quantification. Due to these constraints, we decided to introduce the syringe at a depth of 4 cm from the anus. In larger animals or human, these problems would

not be significant due to the fact that in human, [¹⁸F]DPA-714 is also largely eliminated by the hepatic pathway but with high gall bladder accumulation limiting the radioactivity signal in the intestine. In rats, the lack of gall bladder prevents molecular imaging of the upper part of the intestine.

Beyond this, we used [¹⁸F]DPA-714 to determine the point at which the level of TSPO was at its highest in the TNBS model in order to characterize the dynamic inflammatory processes in this model. This was done by acquiring images at various time points post TNBS induction, illustrating the possibility to repeat image acquisitions and the possibility to follow the evolution of the disease in an individual patient. While the data revealed the time point at which one can observe the highest level of inflammation, one can also observe heterogeneity, post peak, which revealed a large standard deviation. The origin of the heterogeneity is most likely linked to the disease severity. However, a direct correlation between the uptake of [¹⁸F]DPA-714 and a clinical score of the disease was not possible in this study due to the limited number of animals used for the dynamic evaluation ($n=6$). This proof of principle can of course be extrapolated to humans with a protocol dedicated to the evaluation of therapeutic efficiency or disease progression.

Conclusion

In this study, we report for the first time, the ability to distinguish a difference between IBD affected and healthy animals using PET imaging and gamma counting with the use of the TSPO radioligand [¹⁸F]DPA-714 in two separate models. [¹⁸F]FDG also provided a positive contrast in the intestine of sick animals. However, the statistical significance was less than that of the [¹⁸F]DPA-714. Beyond this, we also demonstrated the ability to follow a disease evolution over time with the use of [¹⁸F]DPA-714. Studies such as these demonstrate the potential applications of this TSPO ligand [¹⁸F]DPA-714 which may improve the clinical diagnosis for inflammatory bowel disease patients.

Acknowledgments. We would like to thank Prof. Higuchi (The National Institute of Radiological Sciences, Chiba, Japan) for providing the rabbit polyclonal anti-TSPO antibody.

This work was supported by the European Union's Seventh Framework Programme [FP7/2007-2013] INMiND (Grant agreement no. 278850).

Conflict of Interest. The authors declare that they have no conflict of interest.

Open Access This article is distributed under the terms of the Creative Commons Attribution License which permits any use, distribution, and reproduction in any medium, provided the original author(s) and the source are credited.

References

- Baumgart DC, Bernstein CN, Abbas Z et al (2011) IBD around the world: comparing the epidemiology, diagnosis, and treatment: proceedings of the World Digestive Health Day 2010 inflammatory bowel disease task force meeting. *Inflamm Bowel Dis* 17:639–644
- McCombie AM, Mulder RT, Gearry RB (2013) How IBD patients cope with IBD: A systematic review. *J Crohn's Colitis* 7:89–106
- Shivananda S, Lennard-Jones J, Logan R et al (1996) Incidence of inflammatory bowel disease across Europe: is there a difference between north and south? Results of the European Collaborative Study on Inflammatory Bowel Disease (ECIBD). *Gut* 39:690–697
- Gismera CS, Aladrén BS (2008) Inflammatory bowel diseases: a disease(s) of modern times? Is incidence still increasing? *World J Gastroenterol* 14:5491–5498
- Dambha F, Tanner J, Carroll N (2014) Diagnostic imaging in Crohn's disease: what is the new gold standard? *Best Pract Res Clin Gastroenterol* 28:421–436
- Ito R, Kita M, Shin-Ya M et al (2008) Involvement of IL-17A in the pathogenesis of DSS-induced colitis in mice. *Biochem Biophys Res Commun* 1:12–16
- Bettenworth D, Reuter S, Hermann S et al (2013) Translational 18 F-PET/CT imaging to monitor lesion activity in intestinal inflammation. *J Nucl Med* 54:748–55
- Hindryckx P, Staelens S, Devisscher L et al (2011) Longitudinal quantification of inflammation in the murine dextran sodium sulfate induced colitis model using μ PET/CT. *Inflamm Bowel Dis* 17:2058–64
- Lapp RT, Spier BJ, Perlman SB et al (2010) Clinical utility of positron emission tomography/computed tomography in inflammatory bowel disease. *Mol Imaging Biol* 13:573–576
- Shyn PB (2012) F-18-FDG positron emission tomography: potential utility in the assessment of Crohn's disease. *Abdom Imaging* 37:377–386
- Ostuni MA, Issop L, Péranzi G et al (2010) Overexpression of translocator protein in inflammatory bowel disease: potential diagnostic and treatment value. *Inflamm Bowel Dis* 16:1476–1487
- James ML, Fulton RR, Vercoullie J et al (2008) DPA-714, a new translocator protein-specific ligand: synthesis, radiofluorination, and pharmacologic characterization. *J Nucl Med* 49:814–822
- Chauveau F, Van Camp N, Dollé F et al (2009) Comparative evaluation of the translocator protein radioligands ¹¹C-DPA-713, ¹⁸F-DPA-714, and ¹¹C-PK11195 in a rat model of acute neuroinflammation. *J Nucl Med* 50(3):468–76
- Martin A, Boisgard R, Thézé B et al (2010) Evaluation of the PBR/TSPO radioligand [¹⁸F]DPA-714 in a rat model of focal cerebral ischemia. *J Cereb Blood Flow Metab* 30:230–241
- Abourbeh G, Thézé B, Maroy R et al (2012) Imaging microglial/macrophage activation in spinal cords of experimental autoimmune encephalomyelitis rats by positron emission tomography using the mitochondrial 18 kDa translocator protein radioligand [¹⁸F]DPA-714. *J Neurosci* 32(17):5728–5736
- Okayasu I, Hatakeyama S, Yamada M et al (1990) A novel method in the induction of reliable experimental acute and chronic ulcerative colitis in mice. *Gastroenterology* 98:694–702
- Hibi T, Ogata H, Sakuraba A (2002) Animal models of inflammatory bowel disease. *J Gastroenterol* 37:409–417
- Gaudio E, Taddei G, Vetuschì A et al (2009) Dextran sulfate sodium (DSS) colitis in rats—clinical, structural, and ultrastructural aspects. *Dig Dis Sci* 44:1458–1475
- Seibel J, Molzberger AF, Hertrampf T et al (2009) Oral treatment with genistein reduces the expression of molecular and biochemical markers of inflammation in a rat model of chronic TNBS-induced colitis. *Eur J Nutr* 48:213–220
- Damont A, Hinnen F, Kuhnast B et al (2008) Radiosynthesis of [¹⁸F]DPA-714, a selective radioligand for imaging the translocator protein (18 kDa) with PET. *J Label Compd Radiopharm* 51:286–292
- Kuhnast B, Damont A, Hinnen F et al (2012) [¹⁸F]DPA-714, [¹⁸F]PBR111 and [¹⁸F]FEDAA1106-selective radioligands for imaging TSPO 18 kDa with PET: automated radiosynthesis on a TRACERLab FX-FN synthesizer and quality controls. *Appl Radiat Isot* 70:489–497
- Denghien D et al (2011) Anatomist: a python framework for interactive 3D visualization of neuroimaging data. In *Python in Neuroscience workshop*

N. Bernards et al.: *In vivo* evaluation of inflammatory bowel disease

23. Wu Y, Li P, Zhang H et al (2013) Diagnostic value of fluorine 18 fluorodeoxyglucose positron emission tomography/computed tomography for the detection of metastases in non-small-cell lung cancer patients. *Int J Cancer* 132:e37–e47
24. Lobert P, Brown RKJ, Dvorak RA et al (2013) Spectrum of physiological and pathological cardiac and pericardial uptake of FDG in oncology PET-CT. *Clin Radiol* 68(1):e59–e71
25. Cornelius P, Marlowe M, Pekala PH (1990) Regulation of glucose transport by tumor necrosis factor-alpha in cultured murine 3 T3-L1 fibroblasts. *J Trauma* 30(12):15–20
26. Pottier G, Bernards N, Dollé F, Boisgard R (2014) [¹⁸F]DPA-714 as a biomarker for positron emission tomography imaging of rheumatoid arthritis in an animal model. *Arthritis Res Ther* 16:R69

[¹⁸F]DPA-C5yne, a novel fluorine-18-labelled analogue of DPA-714: radiosynthesis and preliminary evaluation as a radiotracer for imaging neuroinflammation with PET

Vincent Médran-Navarrete,^a† Nicholas Bernards,^{a,b}† Bertrand Kuhnast,^a Annelaure Damont,^a Géraldine Pottier,^{a,b} Marie-Anne Peyronneau,^a Michael Kassiou,^{c,d} Frank Marguet,^e Frédéric Puech,^e Raphaël Boisgard,^{a,b} and Frédéric Dollé^{a*}

DPA-C5yne, the lead compound of a novel series of DPA-714 derivatives in which the fluoroethoxy chain linked to the phenylpyrazolopyrimidine scaffold has been replaced by a fluoroalkyn-1-yl moiety, is a high affinity (K_d : 0.35 nM) and selective ligand targeting the translocator protein 18 kDa. In the present work, DPA-C5yne was labelled with no-carrier-added [¹⁸F] fluoride based on a one-step tosyloxy-for-fluorine nucleophilic substitution reaction, purified by cartridge and HPLC, and formulated as an *i.v.* injectable solution using a TRACERLab FX N Pro synthesizer. Typically, 4.3–5.2 GBq of [¹⁸F]DPA-C5yne, ready-to-use, chemically and radiochemically pure (> 95%), was obtained with specific radioactivities ranging from 55 to 110 GBq/μmol within 50–60 min, starting from a 30 GBq [¹⁸F]fluoride batch (14–17%). LogP and LogD of [¹⁸F]DPA-C5yne were measured using the shake-flask method and values of 2.39 and 2.51 were found, respectively. Autoradiography studies performed on slices of ((R,S)-α-amino-3-hydroxy-5-methyl-4-isoxazolopropionique (AMPA)-lesioned rat brains showed a high target-to-background ratio (1.9 ± 0.3). Selectivity and specificity of the binding for the translocator protein was demonstrated using DPA-C5yne (unlabelled), PK11195 and Flumazenil (central benzodiazepine receptor ligand) as competitors. Furthermore, DPA-C5yne proved to be stable in plasma at 37°C for at least 90 min.

Keywords: fluorine-18; radiosynthesis; DPA-C5yne; DPA-714; TSPO 18 kDa; PBR

Introduction

Overexpression of the translocator protein (TSPO) 18 kDa (formerly known as the peripheral benzodiazepine receptor (PBR)¹) in the brain, during microglial cell activation in response to cerebral insults, has attracted considerable attention for the development of positron emission tomography (PET) radioligands as imaging markers of neuroinflammation.^{2,3}

While several radioligands are still underdevelopment,^{4–9} the pyrazolo[1,5-*a*]pyrimidine-acetamide [¹⁸F]DPA-714^{10–12} is currently considered as a major challenger^{13–23} of the reference ligand, the isoquinoline-carboxamide [¹¹C]PK11195,^{24,25} together with the phenoxy-pyridin-3-yl-acetamide [¹¹C]PBR28^{26–32} and its closely related fluorinated analogue [¹⁸F]FEPPA.^{33,34} However, the use of radioligands belonging to the latter class faces difficulties today in human PET imaging because of differences between individuals linked to the variable expression of two binding sites (a low and a high affinity) for the TSPO, encoded by a single polymorphism (rs6971) at the gene level.^{35–37} Subjects may thus be classified as high-affinity binders or low-affinity binders (when one single binding site for the TSPO is expressed with either high or low affinity, but may also be classified as mixed affinity binders when both sites are expressed

approximately equally. Differences in affinity are higher for [¹¹C]PBR28 (50-fold), whereas pyrazolo[1,5-*a*]pyrimidine-acetamides show lower differences (only fourfold for [¹¹C]DPA-713).³⁶

On the other hand, recent in-house studies have demonstrated that [¹⁸F]DPA-714 is extensively metabolized *in vivo* in both rodents and non-human primates.³⁸ One metabolic pathway, which was demonstrated *in vitro* and was also suggested to occur *in vivo*, results from *O*-dealkylation that leads to the formation of fluorine-18-labelled small metabolites such as [¹⁸F]fluoroacetaldehyde, or its oxidation product [¹⁸F]fluoroacetic acid.

^aCEA, I²BM, Service Hospitalier, Frédéric Joliot, Orsay, France

^bInserm, U1023, Université Paris Sud, Orsay, France

^cSchool of Chemistry, University of Sydney, Sydney, Australia

^dDiscipline of Medical Radiation Sciences, University of Sydney, Sydney, Australia

^eExploratory Unit, Sanofi, Paris, France

*Correspondence to: Dr Frédéric Dollé, Service hospitalier Frédéric Joliot, Institut d'imagerie biomédicale, CEA, 4 place du Général Leclerc, F-91406 Orsay, France. E-mail: frederic.dolle@cea.fr

† These two authors equally contributed to the work.

The main issue is that [^{18}F]fluoroacetate is known to cross the blood brain barrier at a certain level^{39–41} and may thus confound the brain PET signal. Moreover, [^{18}F]fluoroacetate may be converted to [^{18}F]fluoride ion,^{42–44} which bind avidly to the bones, including the skull.⁴⁵ This accumulation of radioactivity in the skull is also problematic as far as brain imaging is concerned because it interferes with the quantification of the radiotracer due to the partial volume effect.⁴⁵

Consequently, structural modifications of the DPA-714/DPA-713 chemotype that could prevent *O*-dealkylation and thus avoid the formation of [^{18}F]fluoroacetate and [^{18}F]fluoride ions were explored. While keeping the scaffold of DPA-714, new analogues have recently been synthesized, in which the oxygen atom bridging the phenyl ring and the fluoroalkyl chain is replaced with a carbon atom. Of particular interest is a novel subclass of compounds featuring an alkyne bond and a short alkane spacer linking the phenylpyrazolopyrimidine scaffold and the fluorine atom.⁴⁶ This series includes four analogues of DPA-714 with a side-chain length ranging from three to six carbon atoms, which all exhibit high affinity and selectivity towards the TSPO. Within this series, DPA-C5yne (**1**, Figure 1) exhibited the highest affinity for the TSPO with a K_i value of 0.35 nM (as reference, the K_i measured for DPA-714 in the same assay was 0.91 nM). No affinity for the central benzodiazepine receptor (CBR) was observed ($K_i > 1 \mu\text{M}$).⁴⁶ Furthermore, preliminary *in vitro* metabolism evaluation of this series using rat microsomal incubations and liquid chromatography–mass spectrometry (LC–MS) analyses showed the absence of defluorinated metabolites.⁴⁶

Based on these data, DPA-C5yne (**1**) was selected for labelling with the short-lived positron-emitter fluorine-18 ($T_{1/2}$: 109.8 min). The present manuscript briefly describes the preparation of the tosylate derivative as precursor for labelling and then focuses on the radiolabelling with fluorine-18 of **1** on a TRACERLab FX N Pro module, the measurement of its lipophilicity (LogP/LogD) based on the shake-flask method and its preliminary evaluation by autoradiography on brain slices of our in-house-developed rat model of acute local neuroinflammation.

Results and discussion

Chemistry

The preparation of DPA-C5yne (**1**, *N,N*-diethyl-2-(2-(4-(3-fluoropent-1-yn-1-yl)phenyl)-5,7-dimethylpyrazolo[1,5-*a*]pyrimidin-3-yl)acetamide) as reference compound and the tosylate **2** (6-(4-(3-(2-

(diethylamino)-2-oxoethyl)-5,7-dimethylpyrazolo[1,5-*a*]pyrimidin-2-yl)phenyl)pent-4-yn-1-yl) 4-methylbenzenesulfonate) as precursor for labelling with fluorine-18 is illustrated in Scheme 1. Briefly, both compounds were synthesized in a single step from the alkynol **3**, the latter being prepared in five chemical steps from commercially available methyl 4-iodobenzoate.⁴⁶ Then, fluorodeoxygenation of **3** was performed using Deoxofluor[®] (Sigma-Aldrich, Saint-Quentin Fallavier, France) in dichloromethane at room temperature for 3 days and afforded the corresponding fluorinated compound, DPA-C5yne (**1**), in 24% yield. The tosylate **2** was also prepared from the alkynol **3**, by treatment with 4-toluenesulfonic anhydride in dichloromethane at room temperature for 2–3 days, and obtained in 54% yield.

Radiochemistry

DPA-C5yne (**1**) was labelled with fluorine-18 from the tosyloxy derivative **2**, purified by HPLC and formulated as an *i.v.* injectable solution by implementing the one-step radiochemical process outlined in Scheme 2. The whole procedure was performed using a commercially available TRACERLab FX N Pro synthesizer (GE Medical Systems, Germany). The positioning of all reagents, solvents and consumables dedicated to the preparation of [^{18}F]DPA-C5yne ([^{18}F]-**1**) on the TRACERLab FX N Pro is illustrated on the control screen copy displayed in Figure 2. Further details are given in the Experimental Section.

No-carrier-added $\text{K}[^{18}\text{F}]\text{F-Kryptofix}^{\text{®}}222$ (Sigma-Aldrich, Saint-Quentin Fallavier, France) complex^{47,48} was prepared from cyclotron-produced [^{18}F]fluoride, K_2CO_3 , Kryptofix[®]222, acetonitrile and water using a step-by-step sequence (time list) developed by GEMS and implemented on the synthesizer at its reception on site. The sequence includes the trapping of [^{18}F]fluoride anions on a dedicated QMA cartridge, their release using a $\text{H}_2\text{O}/\text{CH}_3\text{CN}$ solution containing both K_2CO_3 and Kryptofix[®]222 and a two-step concentration-to-dryness process in a vessel (reactor) made from glassy carbon. $\text{K}[^{18}\text{F}]\text{F-Kryptofix}^{\text{®}}222$ was obtained in 18 min and used without any additional drying sequence.

Radiofluorination was then performed by dilution of the aforementioned reagent using a DMSO solution (700 μL) containing 7.0–8.7 μmoles (4.0–5.0 mg) of the tosylate **2**, followed by stirring and heating. Initially, the conditions used were those optimized for the preparation of [^{18}F]DPA-714, for example, 165°C for 5 min.¹² Using the latter, [^{18}F]DPA-C5yne ([^{18}F]-**1**) was formed and could be isolated after cartridge/HPLC purifications (see in the succeeding texts). However, overall

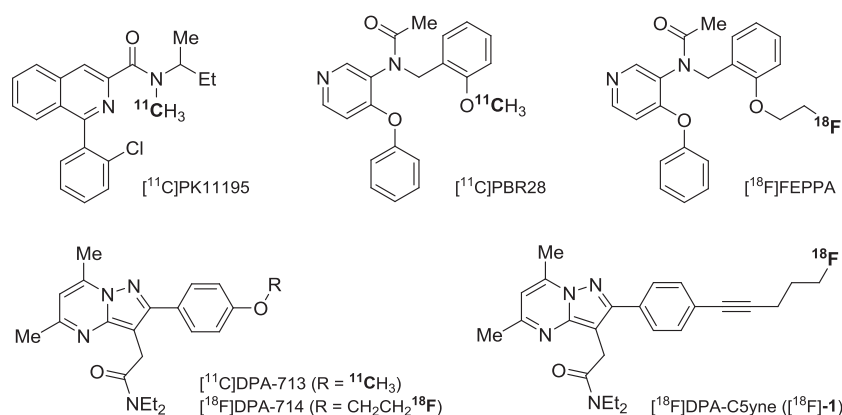
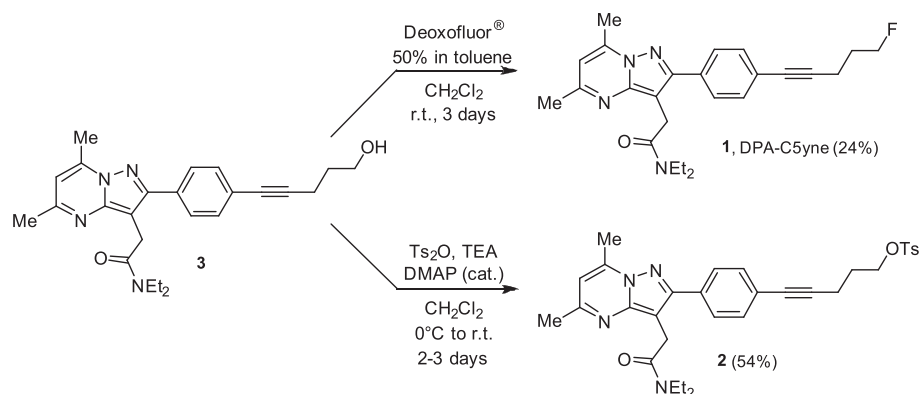
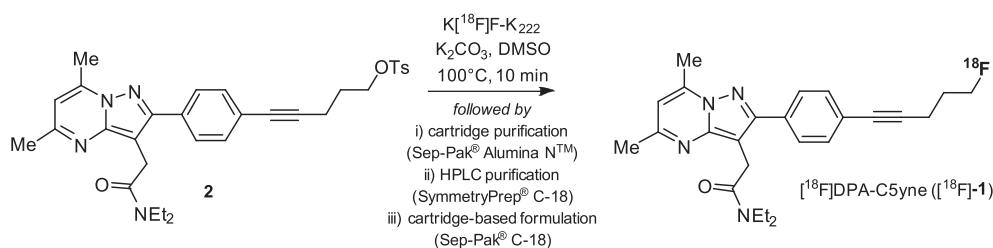


Figure 1. The TSPO radioligands [^{11}C]PK11195, [^{11}C]PBR28, [^{18}F]FEPPA, [^{11}C]DPA-713, [^{18}F]DPA-714 and [^{18}F]DPA-C5yne ([^{18}F]-**1**, present work).



Scheme 1. Synthesis of DPA-C5yne (**1**, reference compound) and its tosylated analogue (**2**) as labelling precursor.



Scheme 2. One-step radiosynthesis, purification and formulation of [¹⁸F]DPA-C5yne ([¹⁸F]-1).

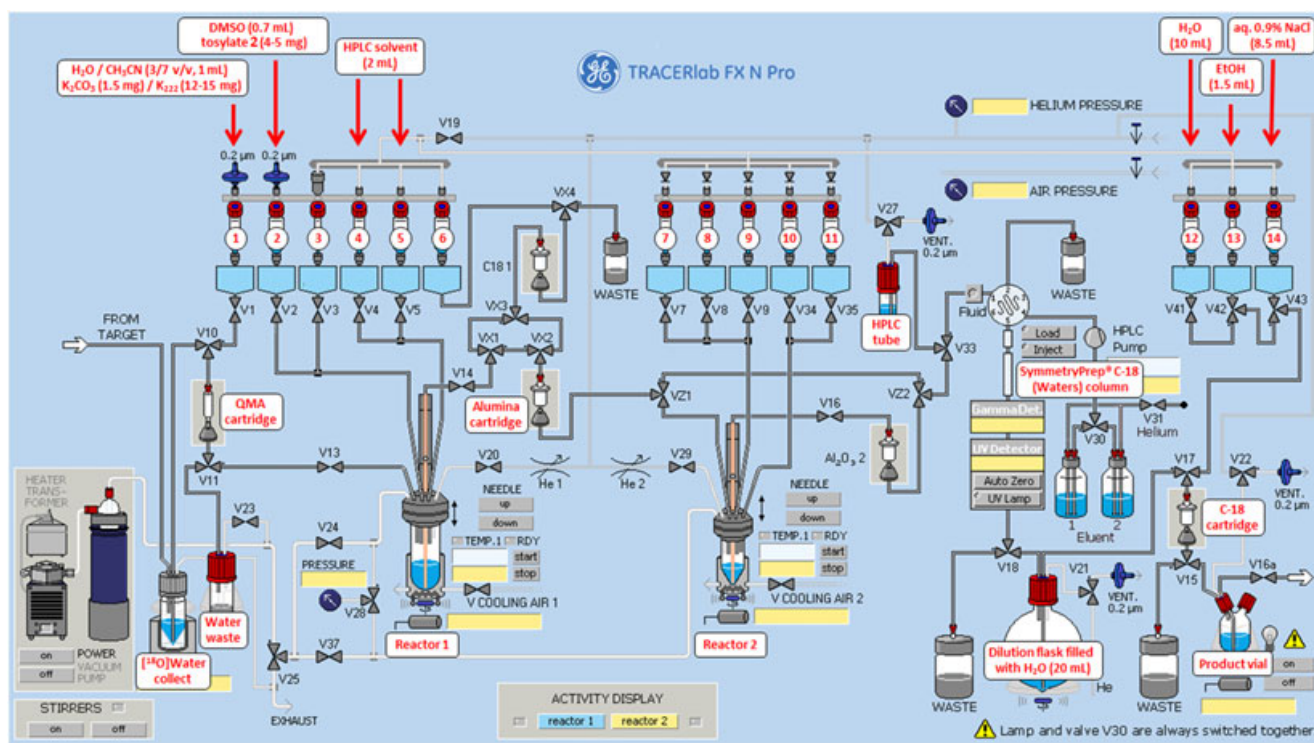


Figure 2. Description of the TRACERlab FX N Pro synthesizer used for the preparation of [¹⁸F]DPA-C5yne ([¹⁸F]-1) and positioning of all required reagents, solvents and consumables.

yields were rather low and not reproducible. Moreover, high chemical and radiochemical purities were not systematically reached based on Quality Control (QC) analysis. These behaviours were not observed during the preparation of [¹⁸F]DPA-714. Decreasing the reaction temperature together with

slightly extending the reaction time (100°C/10 min) provided [¹⁸F]DPA-C5yne ([¹⁸F]-1) in higher and more reproducible yields without any QC issues.

The crude reaction mixture was then cooled down to 50°C before being diluted with the HPLC solvent used for the

purification and then passed through an Al₂O₃ cartridge (Sep-Pak® Alumina N™ cartridge, Waters (Guyancourt, France)) in order to remove (trap) unreacted [¹⁸F]fluoride. The left-over activity in the reactor was then rinsed once with a second portion of HPLC-solvent and passed through the cartridge too. The combined fractions were then purified by HPLC on a semipreparative SymmetryPrep® C-18 column (Waters), using a mixture of CH₃CN, H₂O and Trifluoroacetic acid (TFA) as the eluent (HPLC D, see Experimental Section). Using the latter conditions, [¹⁸F]-**1** (*t_R*: 9–10 min) could be obtained with a > 95% chemical and radiochemical purity and was completely separated from the remaining tosylate **2** (*t_R*: 15–17 min). Removal of the HPLC solvents and formulation of [¹⁸F]DPA-C5yne ([¹⁸F]-**1**) as an *i.v.* injectable solution (0.9% aq NaCl containing EtOH) were performed using a reverse phase cartridge (Sep-Pak® Plus C18 cartridge). The whole process, including radiofluorination, cartridge and HPLC purifications, as well as formulation, lasted between 37 and 42 min.

Typically, 4.3–5.2 GBq of [¹⁸F]DPA-C5yne ([¹⁸F]-**1**) ready-to-use was obtained with specific radioactivities ranging from 55 to 110 GBq/μmol within 50–60 min (HPLC purification and Sep-Pak®-based formulation included), starting from a 30 GBq [¹⁸F]fluoride batch. Overall, non-decay corrected, isolated yields were 14–17% (20–25% decay corrected).

Quality controls of [¹⁸F]DPA-C5yne ([¹⁸F]-**1**) were performed on an aliquot of the ready for *i.v.* injection batch. The prepared radiotracer solution was clear and colourless with a pH between 6 and 7. As demonstrated by analytical-HPLC control (HPLC E, see Experimental Section), the radiotracer preparation was found to be >95% chemically and radiochemically pure (**1**, *t_R*: 2.20 min). The preparation was also shown to be free of the non-radioactive precursor, the tosylate **2** (*t_R*: 3.51 min), and was chemically and radiochemically stable for at least 120 min.

Lipophilicities

LogP (*n*-octanol/water partition coefficient) and LogD (*n*-octanol/buffer pH 7.4 partition coefficient) of [¹⁸F]DPA-C5yne ([¹⁸F]-**1**) were measured using the shake-flask method, and values of 2.39 and 2.51 were found, respectively. The calculated LogP (cLogP) was determined using CHEMBIODRAW ULTRA SOFTWARE, and a value of 4.28 was found. These values were all slightly higher than the ones previously obtained for [¹⁸F]DPA-714 (LogP: 1.66, LogD: 1.74 and cLogP: 3.33) but remained in the recommended range for a radiotracer dedicated to brain imaging (1 < LogP/LogD < 3). As with DPA-714, cLogP value was much higher than LogP and LogD measurements.

In vitro stability in rat plasma

Stability of DPA-C5yne (**1**) was checked *in vitro* in rat spiked plasma at 37°C by LC-MS. Analyses of acetonitrile plasma extracts at different incubation time points (0, 5, 15, 60 and 90 min) showed only one single peak with a retention time (*t_R*: 12.9 min) and UV-spectrum (λ_{max} = 270 nm) identical to those of authentic DPA-C5yne. The variability in the peak area measurement as a function of time was less than 2%. Furthermore, for each time point, MS exhibited one molecular ion, at *m/z* 421 [M+H⁺], with a mass spectrum and a fragmentation profile also identical to those of authentic DPA-C5yne. Thus, DPA-C5yne (**1**) proved to be stable in plasma at 37°C for at least 90 min because no decomposition product could be observed.

Autoradiography studies

Autoradiography studies were performed on slices of our in-house-developed rat model of acute local neuroinflammation. This model is based on an excitotoxic AMPA-mediated brain lesion in the right striatum of Wistar rats. It has already been validated for TSPO expression by immunohistochemical analyses^{49–51} and used for the evaluation of several TSPO radioligands, such as [¹¹C]PK11195,^{49,50} [¹¹C]CLINME,^{50,52} [¹¹C]DPA-713,^{49,51} [¹⁸F]PBR111,⁵² [¹⁸F]DPA-714⁵¹ and more recently [¹¹C]SSR180575.⁵³ Briefly, brain slices were incubated with [¹⁸F]DPA-C5yne ([¹⁸F]-**1**, 7.4 nM) alone, and also coincubated with non-labelled DPA-C5yne (**1**, 20 μM), or PK11195 (20 μM, the TSPO ligand of reference) or Flumazenil (20 μM, a CBR ligand of reference), respectively, in order to confirm the selectivity and specificity of the binding. As shown in Figure 3(A), a significantly increased binding of [¹⁸F]DPA-C5yne ([¹⁸F]-**1**) was detected in the lesion when compared to the control side. The target-to-background ratio (TBR), calculated as the bound tracer in the lesion versus the bound tracer in the contralateral side, was relatively high, 1.9 ± 0.3 (*p* < 0.0001). Addition of an excess of unlabelled DPA-C5yne or PK11195 (20 μM, 2700-fold mass excess compared to [¹⁸F]DPA-C5yne) fully inhibited the binding (Figure 3(B) and 3(C)) in the lesioned area (TBR = 1.0 ± 0.1 for both ligands), proving a high specificity of the binding and selectivity for the TSPO. However, the addition of a similar excess of Flumazenil did not affect the binding of [¹⁸F]DPA-C5yne (Figure 3(D)), yielding a calculated TBR of 1.9 ± 0.1, a value identical to the one found for [¹⁸F]DPA-C5yne alone, proving its selectivity for the TSPO and not for the CBR.

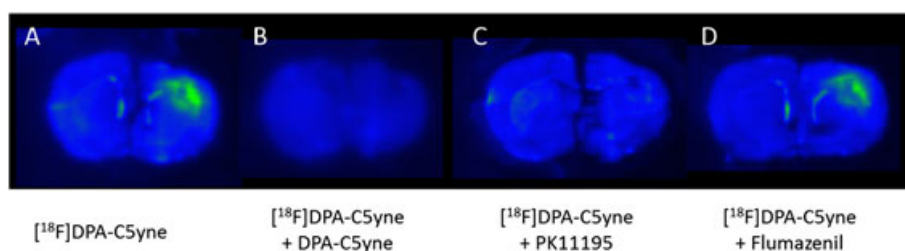


Figure 3. Autoradiography studies on slices of AMPA-lesioned rat brains incubated with [¹⁸F]DPA-C5yne ([¹⁸F]-**1**, 7.4 nM) alone (A) or with non-labelled DPA-C5yne (20 μM) (B), with PK11195 (20 μM) (C) and with Flumazenil (20 μM) (D), respectively.

Conclusions

The pyrazolo[1,5-*a*]pyrimidine-acetamide [^{18}F]DPA-C5yne is a novel, fluorine-18-labelled, radioligand targeting the TSPO with promising *in vitro* properties. PET imaging studies are currently being carried out in both acute and chronic animal models of neurodegeneration in order to evaluate the *in vivo* potential of this DPA-714 analogue.

Experimental

General

Chemicals

Chemicals were purchased from Aldrich, Fluka, Sigma or Cooper (France) and were used without further purification, unless otherwise stated.

Thin-layer chromatography analysis and flash chromatography

Thin-layer chromatography was run on pre-coated plates of silica gel 60F₂₅₄ (WVR, Fontenay-sous-Bois, France). The compounds were localized when possible at 254 nm using a UV-lamp and/or by dipping the TLC-plates in a 1% ethanolic ninhydrin solution, a basic KMnO_4 aqueous solution or a 1% $\text{MeOH}/\text{H}_2\text{O}$ (1/1, v:v) FeCl_3 solution and heating on a hot plate. Flash chromatographies were conducted on silica gel or alumina gel (0.63–0.200 mm, WVR) columns.

High-performance liquid chromatography analysis

[HPLC A]: Equipment: Waters (Guyancourt, France) system equipped with a 600E System Controller, a Prep LC 3000 pump, a 490E programmable multiwavelength UV-detector and a Kipp and Zonen (Emerainville, France) BD12E flatbed recorder; column: preparative Zorbax[®] RX-SIL, Hewlett Packard (Les Ulis, France) (250 × 21.2 mm); porosity: 5 μm ; conditions: eluent: $\text{CH}_2\text{Cl}_2/\text{MeOH}$: 98.5/1.5 (v:v); flow rate: 10 mL/min; temperature: room temperature (RT); UV detection at λ : 230 nm. [HPLC B]: Equipment: Waters system equipped with a 510 pump and a Shimadzu SPD-10A UV-multiwavelength detector. Column: semipreparative SymmetryPrep[®] C-18, Waters (300 × 7.8 mm); porosity: 7 μm ; conditions: eluent: $\text{CH}_3\text{CN}/\text{H}_2\text{O}/\text{TFA}$: 50/50/0.1 (v:v:v); flow rate: 5 mL/min; temperature: RT; UV detection at λ : 254 nm. [HPLC C]: Equipment: Waters system equipped with a 510 pump and a Shimadzu SPD-10A UV-multiwavelength detector. Column: semipreparative SymmetryPrep[®] C-18, Waters (300 × 7.8 mm); porosity: 7 μm ; conditions: eluent: $\text{CH}_3\text{CN}/\text{H}_2\text{O}/\text{TFA}$: 60/40/0.1 (v:v:v); flow rate: 5 mL/min; temperature: RT; UV detection at λ : 254 nm. [HPLC D]: Equipment: TRACERLab FX N Pro (GE Medical Systems, Germany) integrated system, equipped with a Sykam S1122 Solvent Delivery System (pump), a Knauer K-2501 UV-multiwavelength detector and a miniaturized gamma-radioactivity detector. Column: semipreparative SymmetryPrep[®] C-18, Waters (300 × 7.8 mm); porosity: 7 μm ; conditions: eluent: $\text{CH}_3\text{CN}/\text{H}_2\text{O}/\text{TFA}$: 60/40/0.1 (v:v:v); flow rate: 5 mL/min; temperature: RT; UV detection at λ : 254 nm. [HPLC E]: Equipment: Waters Alliance 2690 (or a Waters binary HPLC Pump 1525) equipped with a Waters 996 UV photodiode array detector and a Berthold LB509 radioactivity detector; column: analytical Symmetry-M[®] C-18, Waters (50 × 4.6 mm); porosity: 3.5 μm ; conditions: eluent: solvA/solvB: 20/80 (v:v) [solvA: H_2O containing Low-UV PIC[®] B7 reagent (Waters), 20 mL for 1000 mL; solvB: $\text{H}_2\text{O}/\text{CH}_3\text{CN}$: 30/70 (v:v) containing Low-UV PIC[®] B7 reagent (Waters), 20 mL for 1000 mL]; flow rate: 2.0 mL/min; temperature: 30°C (or RT); UV detection at λ : 280 nm.

Spectroscopies

Nuclear magnetic resonance spectra ($^1\text{H}/^{13}\text{C}$) were recorded on a Bruker (Wissembourg, France) Avance (400 MHz) apparatus using the hydrogenated residue of the deuterated solvent CDCl_3 ($\delta = 7.23$ ppm) as internal standard for ^1H -NMR as well as the deuterated solvent CDCl_3 ($\delta = 77.0$ ppm) as internal standard for ^{13}C -NMR. The chemical shifts are reported in parts per million, downfield from Tetramethylsilane (TMS)

(s, d, t, q, m, b for singlet, doublet, triplet, quadruplet, multiplet and broad, respectively). The MS were measured on a Thermo Scientific (Les Ulis, France) Ion Trap LCQ Deca XP + spectrometer (ESI+). The high resolution MS (HRMS) analyses were performed by Imagif (ICSN-CNRS, Gif-sur-Yvette, France) by electrospray with positive (ESI+) ionization mode on a Waters LCT Premier XE (Milford, MA, USA) spectrometer.

Radioisotope production

No-carrier-added fluorine-18 (half-life: 109.8 min) was produced via the [$^{18}\text{O}(\text{p},\text{n})^{18}\text{F}$] nuclear reaction by irradiation of a 2 mL [^{18}O]water (>97%-enriched, Rotem (CortecNet, Paris, France)) target on an IBA Cyclone-18/9 (IBA, Louvain-la-Neuve, Belgium) cyclotron (18 MeV proton beam), and the aqueous radioactive solution was then transferred to the appropriate hot cell. *Target hardware*: commercial, 2-mL, two-port, stainless steel target holder equipped with a domed-end niobium cylinder insert. *Target to hot cell liquid-transfer system*: 50 m Polytetrafluoroethylene (PTFE) line (0.8 mm internal diameter; 1/16 inch external diameter), 2.0 bar helium drive pressure and transfer time 2–3 min. Typical production of [^{18}F]fluoride at the end of bombardment for a 25 μA , 30 min (12.5 μAh) irradiation: 31.5–32.5 GBq.

Acute neuroinflammatory animal model

Striatal AMPA-mediated excitotoxicity and acute local neuroinflammation was induced in the brain of Wistar rats according to reported procedures.^{49–51} The protocol used includes a stereotaxic injection in the right striatum of 0.5 μL of AMPA ((*R,S*)- α -amino-3-hydroxy-5-methyl-4-isoxazolopropionique, 15 mM in phosphate buffered saline buffer) in anaesthetized and normothermally controlled animals followed by a resting period of 7 days.

Chemistry

N,N-diethyl-2-(2-(4-(4-hydroxypent-1-yn-1-yl)phenyl)-5,7-dimethylpyrazolo[1,5-*a*]pyrimidin-3-yl)acetamide (3)

Synthesized in five steps from commercially available methyl 4-iodobenzoate according to reference.⁴⁶ Rf ($\text{CH}_2\text{Cl}_2/\text{MeOH}$: 95/5 v:v): 0.21. ^1H -NMR (CDCl_3 , 400 MHz): δ 7.74 (d, 2H, $J = 8.0$ Hz, Ph), 7.46 (d, 2H, $J = 8.0$ Hz, Ph), 6.54 (s, 1H), 3.93 (s, 2H, CH_2), 3.81 (t, 2H, $J = 6.4$ Hz, CH_2OH), 3.49 (q, 2H, $J = 7.2$ Hz, NCH_2CH_3), 3.40 (q, 2H, $J = 7.2$ Hz, NCH_2CH_3), 2.74 (s, 3H, CH_3), 2.56 (s, 3H, CH_3), 2.55 (t, 2H, $J = 6.4$ Hz, CH_2), 1.86 (q⁵, 2H, $J = 6.4$ Hz, CH_2), 1.22 (t, 3H, $J = 7.2$ Hz, NCH_2CH_3), 1.10 (t, 3H, $J = 7.2$ Hz, NCH_2CH_3). ^{13}C -NMR (CDCl_3 , 400 MHz): δ 169.8 [C], 157.6 [C], 154.5 [C], 147.5 [C], 145.0 [C], 133.0 [C], 131.6 [2xCH], 128.4 [2xCH], 123.6 [C], 108.4 [CH], 101.3 [C], 90.2 [C], 81.1 [C], 61.7 [CH₂], 42.2 [CH₂], 40.6 [CH₂], 31.3 [CH₂], 28.0 [CH₂], 24.5 [CH₃], 16.8 [CH₃], 16.0 [CH₂], 14.3 [CH₃], 13.0 [CH₃]. MS (ESI+): m/z 419 (M + H)⁺.

N,N-diethyl-2-(2-(4-(3-fluoropent-1-yn-1-yl)phenyl)-5,7-dimethylpyrazolo[1,5-*a*]pyrimidin-3-yl)acetamide (1, DPA-C5yne)

To a solution of compound **3** (84 mg, 0.201 mmol) in dry CH_2Cl_2 (4 mL) was added a 50% Deoxofluor[®] solution in toluene (0.5 mL, excess). The reaction mixture was stirred for 3 days at RT, then diluted with MeOH (0.5 mL) and concentrated to dryness. Finally, the residue was purified by flash chromatography on silica gel (heptane/acetone: 4/1 (v:v)) to afford **1** (20 mg, 24%) as a yellow solid. For analytical purposes only, compound **1** was further purified using preparative HPLC [HPLC A] and obtained, after solvents removal, as a light yellow solid. Rf (heptane/acetone: 1/1 (v:v)): 0.35. t_{R} : 30 min [HPLC A], 10.5 min [HPLC B], 9.5 min [HPLC C], 9.5 min [HPLC D] and 2.20 min [HPLC E]. ^1H -NMR (CDCl_3 , 400 MHz): δ 7.76 (d, 2H, $J = 8.0$ Hz, Ph), 7.47 (d, 2H, $J = 8.0$ Hz, Ph), 6.54 (s, 1H), 4.62 (dt, 2H, $J_{\text{H-F}}^2 = 47.2$ Hz, $J_{\text{H-H}}^3 = 6.0$ Hz, CH_2F), 3.97 (s, 2H, CH_2), 3.50 (q, 2H, $J = 7.2$ Hz, NCH_2CH_3), 3.41 (q, 2H, $J = 7.2$ Hz, NCH_2CH_3), 2.76 (s, 3H, CH_3), 2.59 (t, 2H, $J = 7.2$ Hz, CH_2), 2.58 (s, 3H, CH_3), 2.01 (dq⁵, 2H, $J_{\text{H-F}}^3 = 25.6$ Hz, $J_{\text{H-H}}^3 = 6.0$ Hz, CH_2), 1.23 (t, 3H, $J = 7.2$ Hz, NCH_2CH_3), 1.12 (t, 3H, $J = 7.2$ Hz, NCH_2CH_3). ^{13}C -NMR (CDCl_3 , 400 MHz): δ 169.7 [C], 157.6 [C], 154.5 [C], 147.4 [C], 145.2 [C], 133.0 [C], 131.6 [2xCH], 128.4 [2xCH], 123.5 [C], 108.4 [CH], 101.3 [C], 89.3 [C], 82.5 [d, $J_{\text{C-F}}^1 = 164$ Hz, CH_2], 81.2 [C], 42.2 [CH₂], 40.6 [CH₂], 29.5 [d, $J_{\text{C-F}}^2 = 20$ Hz,

CH₂], 28.0 [CH₂], 24.3 [CH₃], 16.9 [CH₃], 15.4 [d, $J_{C-F}^3 = 4$ Hz, CH₂], 14.3 [CH₃], 13.0 [CH₃]. MS (ESI+): *m/z*: 421 (M+H)⁺. HRMS (*m/z*, ESI) calculated for C₂₅H₃₀FN₄O (M+1), 421.2404; found, 421.2404.

6-(4-(3-(2-(diethylamino)-2-oxoethyl)-5,7-dimethylpyrazolo[1,5-a]pyrimidin-2-yl)phenyl)pent-4-yn-1-yl)4-methylbenzenesulfonate (2)

To a solution of compound **3** (200 mg, 0.478 mmol) in dry CH₂Cl₂ (5 mL) was added Et₃N (80 μL, 0.578 mmol, 1.2 eq) and DMAP (6 mg, 0.049 mmol, 0.1 eq). The flask was degassed and flushed with argon (two cycles), then cooled to 0°C. 4-toluenesulfonic anhydride (170 mg, 0.521 mmol, 1.1 eq) was slowly added to the previous solution, and the reaction mixture stirred at 0°C for 15 min, then at RT overnight. 4-toluenesulfonic anhydride (50 mg, 0.153 mmol, 0.3 eq) and Et₃N (100 μL, 0.71 mmol, 1.5 eq) were added once again, and the mixture stirred another 2 days at RT. The reaction mixture was then evaporated under reduced pressure, and the resulting brownish oil was portioned between EtOAc (20 mL) and aq 0.05 M HCl (15 mL). The organic layer was separated, washed with water (10 mL), brine (10 mL), dried over Na₂SO₄, filtered and concentrated to dryness. Finally, the resulting residue was purified by flash chromatography on silica gel (pure CH₂Cl₂ to CH₂Cl₂/MeOH: 98/2 (v:v)) to afford **2** (145 mg, 54%) as a light yellow solid. Rf (CH₂Cl₂/MeOH: 93/7 v:v): 0.58. *t*_R: 21.5 min [HPLC B], 15.5 min [HPLC C], 15.3–15.9 min [HPLC D], 3.51 min [HPLC E]. ¹H-NMR (CDCl₃, 400 MHz): δ 7.80 (d, 2H, *J*=8.0 Hz, Ph), 7.76 (d, 2H, *J*=8.4 Hz, Ph), 7.36 (d, 2H, *J*=8.4 Hz), 7.31 (d, 2H, *J*=8.0 Hz, Ph), 6.53 (s, 1H), 4.21 (t, 2H, *J*=5.6 Hz, CH₂OTs), 3.94 (s, 2H, CH₂), 3.51 (q, 2H, *J*=7.2 Hz, NCH₂CH₃), 3.40 (q, 2H, *J*=7.2 Hz, NCH₂CH₃), 2.74 (s, 3H, CH₃), 2.55 (s, 3H, CH₃), 2.49 (t, 2H, *J*=6.8 Hz, CH₂), 2.39 (s, 3H, CH₃), 1.94 (q⁵, 2H, *J*=6.8 Hz, CH₂), 1.23 (t, 3H, *J*=7.2 Hz, NCH₂CH₃), 1.11 (t, 3H, *J*=7.2 Hz, NCH₂CH₃). ¹³C-NMR (CDCl₃, 400 MHz): δ 169.7 [C], 157.6 [C], 154.4 [C], 147.0 [C], 145.0 [C], 144.8 [C], 133.1 [C], 132.8 [C], 131.6 [2xCH], 129.8 [2xCH], 128.4 [2xCH], 127.8 [2xCH], 123.3 [C], 108.4 [CH], 101.3 [C], 88.4 [C], 81.7 [C], 68.9 [CH₂], 42.2 [CH₂], 40.6 [CH₂], 28.0 [CH₂], 27.9 [CH₂], 24.3 [CH₃], 21.6 [CH₃], 16.8 [CH₃], 15.7 [CH₂], 14.3 [CH₃], 13.0 [CH₃]. MS (ESI+): *m/z*: 573 (M+H)⁺. HRMS (*m/z*, ESI) calculated for C₃₂H₃₇N₄O₄S (M+1), 573.2536; found, 573.2524.

Radiochemistry

The TRACERLab FX N Pro synthesizer: description, configuration, preparation and sequences used

Synthesizer description and sequences used

Fluorine-18 labelling, purification with HPLC and formulation of [¹⁸F]DPA-C5yne ([¹⁸F]-**1**) as an *i.v.* injectable solution was performed using a commercially available TRACERLab FX N Pro synthesizer (GE Medical Systems, Germany), placed in a 5.0-cm-lead shielded and ventilated cell. The whole process was thus fully automated and used a dedicated method supported by three generic 'time list', written according to the programming mode of General Electric synthesis modules, and named, respectively, 'Time list 1: K[¹⁸F]F-K₂₂₂ preparation', 'Time list 2: radiofluorination and pre-purification' and 'Time list 3: purification and formulation'.¹² Before each [¹⁸F]DPA-C5yne ([¹⁸F]-**1**) batch production, the synthesizer was cleaned out (e.g. used-cartridge removal), purged from any residual chemicals or solvents left-over (reservoirs, reactors and tubings) from a previous radiotracer production and dried using another in-house programmed method, based on the use of two generic 'time list', named, respectively, 'Time list: clean' and 'Time list: clean and dry'.¹² The first cleaning procedure used deionized water to rinse both reactors [Reactor 1–2], the flask collecting the oxygen-18-enriched water [Water collect] and the tube dedicated to the HPLC injection [HPLC tube] and most of the connecting tubings. The second procedure used both

acetone and ethanol to further clean the synthesizer but also to dry all reservoirs [Reservoir 1–14], both reactors [Reactor 1–2], the tube dedicated to the HPLC injection [HPLC tube], the flask allowing the dilution of the HPLC-collected fraction prior to cartridge formulation [Dilution flask] and the flask required for receiving at last the batch of formulated product [Product vial] as well as all tubings connecting these elements.

Synthesizer configuration

Valves VZ1 and VZ2 were both turned in up-position for the preparation of [¹⁸F]DPA-C5yne ([¹⁸F]-**1**), therefore by-passing most of the added functionalities of the TRACERLab FX N Pro synthesizer when compared to the TRACERLab FX FN one (e.g. the second reactor [Reactor 2] and its connected reservoirs [Reservoir 7–11] and associated tubings). Note that valves VX3 and VX4 as well as the associated option of using an additional cartridge purification unit were also not requested for this process.

Synthesizer preparation

Prior to [¹⁸F]DPA-C5yne ([¹⁸F]-**1**) production, the following reservoirs and vessels were filled with the solutions described here: [Reservoir 1]: a mixture of deionized water and acetonitrile (30/70 v/v, 1 mL) containing 1.5 mg of K₂CO₃ and 12–15 mg of Kryptofix[®]222; [Reservoir 3]: a DMSO solution (0.7 mL) containing the tosylate **2** (4.0–5.0 mg, 7.0–8.7 μmol), as the labelling precursor; [Reservoir 4]: HPLC solvent (2 mL, see [HPLC D]); [Reservoir 5]: HPLC solvent (2 mL, see [HPLC D]); [Reservoir 12]: deionized water (10 mL); [Reservoir 13]: ethanol (1.5 mL); [Reservoir 14]: aq 0.9% NaCl (8.5 mL); [Dilution flask]: deionized water (20 mL). Note that [Reservoir 2], [Reservoir 6], [Reservoir 7–11], [Reactor 1], [Reactor 2], [Product vial], [HPLC tube], [¹⁸O] Water collect, [Water waste] and all other [WASTE] were left empty. Additionally, all cartridges requested for the preparation of [¹⁸F]DPA-C5yne ([¹⁸F]-**1**) were, before being mounted on the synthesizer, conditioned as described here: [QMA cartridge]: Sep-Pak[®] Light Accell[™] Plus QMA cartridge (Waters), hydroxide form, generated from the chloride form by washing with aq 1 M NaHCO₃ (2 mL) and rinsed with deionized water (20 mL) and CH₃CN (10 mL); [Alumina N cartridge]: Sep-Pak[®] Alumina N[™] cartridge (Waters), washed with deionized water (10 mL); [C-18 cartridge]: Sep-Pak[®] Plus C18 cartridge (Waters), washed with EtOH (2 mL) and then rinsed with deionized water (10 mL). Finally, the HPLC-column and system was also conditioned with the appropriate solvent (see [HPLC D]), and DPA-C5yne (**1**), as standard, was injected once.

Radiosynthesis, purification and formulation of [¹⁸F]DPA-C5yne ([¹⁸F]-**1**)

K[¹⁸F]F-K₂₂₂ preparation (Time list 1)

The target content (oxygen-18-enriched water containing [¹⁸F] fluorine-18) was transferred to the TRACERLab FX N Pro synthesizer using helium pressure (2 bars) and was first collected in the [¹⁸O]-water collect vial, then sucked through the [QMA cartridge]. At this stage, fluorine-18 was trapped, as [¹⁸F]fluoride, in the cartridge, and the oxygen-18-enriched water was collected in the [Water waste] vial. [¹⁸F]fluoride anions were then released from the cartridge using the solution stored in [Reservoir 1] and eluted into [Reactor 1]. The mixture was gently concentrated to dryness using the following two heating steps sequentially: (i) 60°C, 7 min at a pressure between 30 and

35 kPa, then (ii) 120°C, 5 min under vacuum. Additional dilution with CH₃CN followed by azeotropic distillation was not performed. The expected K[¹⁸F]F-K₂₂₂ complex, ready for the fluorination step, was obtained within 18 min.

Fluorine-18 incorporation and pre-purification (Time list 2)

The content of the [Reservoir 3] (e.g. 4–5 mg of **2** as precursor for labelling in solution in 700 µL of DMSO) was added to the [Reactor 1] (the latter containing the aforementioned K[¹⁸F]F-K₂₂₂ complex). The [Reactor 1] was then heated at 100°C for 10 min and then cooled down to 50°C. The content of [Reservoir 4] (HPLC solvent, 2 mL) was added to the [Reactor 1]. The diluted content of [Reactor 1] was then transferred under pressure through the [Alumina cartridge] and collected in the [HPLC tube]. The content of [Reservoir 5] (HPLC solvent, 2 mL) was further added to the [Reactor 1] and the novel content of [Reactor 1] was then analogously transferred (under pressure) through the [Alumina cartridge] and collected in the [HPLC tube] too. The part of the process described here lasted about 17 min.

High-performance liquid chromatography purification and formulation (Time list 3)

The cartridge-purified solution (about 4.7 mL) collected in the [HPLC tube] was transferred under pressure into the HPLC injection loop (5 mL). HPLC purification started at the signal given by the fluid detector, the latter switching the loop-valve from the 'load' position to the 'inject' position. HPLC elution was followed by both UV (254 nm) and radioactivity detection. The fraction containing [¹⁸F]DPA-C5yne ([¹⁸F]-**1**) was collected separately, on the operator's actions (clicking on the start-collect and end-collect icons), in the [Dilution flask], prefilled with water (20 mL). Final formulation of the radiotracer was performed automatically using a Sep-Pak® Plus C18-based system. For this, the content of the [Dilution flask] was first passed through the [C-18 cartridge] (trapping the radiotracer), the latter being then washed with water (10 mL, stored in the [Reservoir 12]). Elution of the cartridge with EtOH (1.5 mL, stored in the [Reservoir 13]) afforded [¹⁸F]DPA-C5yne ([¹⁸F]-**1**), which was recovered in the [Product flask]. Addition of 0.9% aq NaCl (8.5 mL, stored in the [Reservoir 14]) through the [C-18 cartridge] was performed at last to complete the formulation step. HPLC purification and formulation steps lasted about 20–25 min.

Quality control of formulated [¹⁸F]DPA-C5yne ([¹⁸F]-**1**)

Appearance test

The radiotracer preparation was visually inspected behind a lead-shielded glass window for clarity and absence of particulates.

pH test

The pH was determined using standard pH paper using an aliquot of the radiotracer preparation.

Identification and chemical and radiochemical purity test

Identification as well as chemical and radiochemical purity determinations were assessed by separate analytical-HPLC analysis, using a sample of authentic **1** as standard (particular attention was paid to the absence of non-radioactive precursor **2** (tosyloxy derivative)). For this, an aliquot of the radiotracer

preparation (5–20 µL) was injected onto HPLC [HPLC E]. The chemical identity was determined by UV-spectrometric analysis, by comparison of the UV-profile, λ_{max} and retention time recorded with those observed for the corresponding reference compound (**1**) in the same HPLC system and conditions. Chemical purity was also assessed on the UV-chromatogram based on the relative integration of the peak areas. Radiochemical identity was also confirmed by combined radioactive and UV-spectrometric analysis, by comparison of the retention time of the radioactive compound with the corresponding non-radioactive reference compound (**1**). Radiochemical purity was assessed on the radioactive chromatogram based on the relative integration of the peak area corresponding to the radiotracer.

Specific radioactivity determination

Specific radioactivity of the radiotracer was calculated from three consecutive HPLC analyses. For this, an aliquot of the radiotracer preparation (5–20 µL) was injected onto HPLC [HPLC E], and for each injection, the area of the UV absorbance peak corresponding to the product was measured (integrated) on the HPLC chromatogram and compared to a standard curve relating mass to UV absorbance, allowing the determination of the corresponding mass. The HPLC fraction corresponding to the peak was also collected in a vial, and its radioactivity measured in an ionization chamber (Capintec, Ramsey, NJ, USA). The specific radioactivity, as a mean of three independent experiments, was calculated by dividing the counted radioactivity by the found mass (triplicate).

On-shelf stability test

Chemical and radiochemical stability of the entire preparation was checked by HPLC. For this, aliquots of the radiotracer preparation (20 µL) were injected onto HPLC [HPLC E] at regular 15-min intervals during 120 min. For each injection, the chemical and radiochemical purity was determined (see in the preceding text). Moreover, for each injection, the mass associated to the peak corresponding to the product was calculated (using the standard curve relating mass to UV absorbance), and its radioactivity was also measured, before being then corrected for the decay of fluorine-18. Values of both mass and decay-corrected radioactivity per sample were plotted against time and fitted for linearity.

Lipophilicity determination

LogP (*n*-octanol/water partition coefficient)

[¹⁸F]DPA-C5yne ([¹⁸F]-**1**, 1–5 kBq in 50 µL of water) was added to a two-layer system of *n*-octanol (500 µL) and water (450 µL) in an Eppendorf cap (VWR, Fontenay-sous-Bois, France). The vessel was strongly vortexed for 3 min and then centrifuged at 3000 rpm for 2 min. An aliquot of each layer (100 µL) was assessed for radioactivity in a cross-calibrated Perkin-Elmer Cobra Quantum γ-counter (Les Ulis, France).

LogD (*n*-octanol/buffer pH 7.4 partition coefficient)

The procedure described earlier was repeated by replacing water by 0.1 M phosphate buffered saline pH 7.4 (450 µL). The partition coefficients (LogP and LogD) were calculated as the decimal logarithm of the ratio between the counted radioactivity in the *n*-octanol phase and the counted radioactivity in the aqueous phase.

CLogP (calculated LogP)

CLogP values were determined using CHEMBIODRAW ULTRA 11.0.1 software (Cambridge Soft., Perkin-Elmer, Waltham, MA, USA).

In vitro stability in rat plasma

Sample preparation

Rat plasma (4 mL, prepared from whole blood by centrifugation (5 min, 3000 g and at 4°C)) was spiked with 40 µL of a 10 mM DPA-C5yne (1) solution in CH₃CN (final concentration: 100 µM, maximum 1% of organic solvent). Two samples of 200 µL were first removed, and an equal volume of CH₃CN (200 µL) was added. For each sample, the mixture was centrifuged (4°C, 3500 rpm, 5 min) and the supernatant was collected. 20 µL of each extract were then injected onto the LC-MS system, and the peak area corresponding to DPA-C5yne was measured (time zero). The remainder of the spiked plasma was then incubated at 37°C for 5, 15, 30, 60 and 90 min. For each time point, two samples were removed and processed as indicated earlier.

LC-MS analyses

Liquid chromatography-mass spectrometry analyses were performed using an Ion Trap LCQ Deca XP+ mass spectrophotometer equipped with an electrospray source (Thermo Scientific, Les Ulis, France). Pressurized nitrogen was used as sheath gas with a flow rate of 25 units (arbitrary units for sheath gas pressure as defined by the manufacturer). The source voltage for ESI was 4.5 kV and the capillary voltage was 38 V. The capillary temperature was 275°C. The HPLC system (Thermo Scientific) interfaced with the mass spectrophotometer consisted of a Surveyor pump (54949 series), a Surveyor autosampler (55989 series), a photodiode array detector (56470 series) and an analytical Atlantis C18 (Waters) column (2.1 × 150 mm, porosity 5 µm). The mobile phase consisted of A: H₂O containing 0.05% formic acid and B: CH₃CN containing 0.05% formic acid. A linear gradient from 40 to 80% of B in 10 min was applied to the column at a flow rate of 200 µL/min and returns to the initial conditions within 5 min. The whole output of the LC column was passed through the photodiode array detector (190–600 nm) before ESI probe of the mass spectrometer (operated in the positive mode). In the full scan MS acquisition mode, the instrument method was set up to detect ions in the range of *m/z* 50–500. Data acquisition and processing were performed with XCALIBUR™ software (version 2.0, Thermo Scientific, Les Ulis, France). The peak area corresponding to DPA-C5yne (1) was measured as a function of the incubation time.

Brain autoradiography studies with [¹⁸F]DPA-C5yne ([¹⁸F]-1)

Brain slices of unilaterally AMPA-lesioned animals were prepared according to reported procedures.^{49–51} The protocol used includes the decapitation of the animals under terminal anaesthesia, quick brain removal and freezing in cold (–80°C, dry-ice) isopentane followed by coronally, 10 µm thick slicing of the brain at the level of the lesion. Then, adjacent brain slices (36 slices from the centre of the lesioned area) were taken and incubated for 20 min in Tris Buffer (TRIZMA pre-set Crystals, Sigma®, adjusted at pH 7.4 at 4°C, 50 mM with NaCl 120 mM) containing [¹⁸F]DPA-C5yne (111 MBq, 75 GBq/µmol, 555 MBq/L, 7.4 nM) alone, or [¹⁸F]DPA-C5yne and PK11195 (20 µM), [¹⁸F]

DPA-C5yne and DPA-C5yne (20 µM) as well as [¹⁸F]DPA-C5yne and Flumazenil (20 µM). Brain sections were then washed two times for 2 min and once for 10 s with cold (4°C) buffer, then exposed on a Phosphor-Imager (Storm 860, Molecular Dynamics, Pharmacia, GE Medical systems, Germany) screen overnight. Autoradiograms were scanned and then analysed using the IMAGEJ software (developed by the National Institutes of Health). A region of interest was manually drawn around the core of the lesion, and an identical area was copy-pasted symmetrically into the contralateral hemisphere. Binding in the region of interest was then expressed as the number of counts per surface unit. The TBR was calculated as the ratio of the binding in the lesioned versus the contralateral hemisphere.

Acknowledgements

The authors wish to thank the cyclotron operators Mr Daniel Gouel, Mr Christophe Lechène and Mr Tony Catarina for performing the irradiations. This work was supported by the CEA-I²BM intramural programmes, as well as the European Union's Seventh Framework Programme [FP7/2007–2013] INMiND (Grant agreement no HEALTH-F2-2011-278850). PhD students Vincent Médran-Navarrete and Nicholas Bernards were in part supported by a CEA Irtelis doctoral grant and the EU FP7 INMiND programme (see in the preceding text), respectively.

References

- [1] V. Papadopoulos, M. Baraldi, T. R. Guilarte, T. B. Knudsen, J. J. Lacapere, P. Lindemann, M. D. Norenberg, D. Nutt, A. Weizman, M. R. Zhang, M. Gavish, *Trends Pharmacol. Sci.* **2006**, *27*, 402–409.
- [2] R. Rupprecht, V. Papadopoulos, G. Rammes, T. C. Baghai, J. Fan, N. Akula, G. Groyer, D. Adams, M. Schumacher, *Nat. Rev. Drug Discovery* **2010**, *9*, 971.
- [3] A. M. Scarf, M. Kassiou, *J. Nucl. Med.* **2011**, *52*, 677.
- [4] F. Chauveau, H. Boutin, N. Van Camp, F. Dollé, B. Tavitian, *Eur. J. Nucl. Med. Mol. Imaging* **2008**, *35*, 2304.
- [5] F. Dollé, C. Luus, A. Reynolds, M. Kassiou, *Curr. Med. Chem.* **2009**, *16*, 2899.
- [6] C. Luus, R. Hanani, A. Reynolds, M. Kassiou, *J. Label. Compd. Radiopharm.* **2010**, *53*, 501.
- [7] D. Roeda, B. Kuhnast, A. Damont, F. Dollé, *J. Fluor. Chem.* **2012**, *134*, 107.
- [8] A. S. C. Ching, B. Kuhnast, A. Damont, D. Roeda, B. Tavitian, F. Dollé, *Insights into Imaging* **2012**, *3*, 111.
- [9] A. Damont, D. Roeda, F. Dollé, *J. Label. Compd. Radiopharm.* **2013**, *56*, 96.
- [10] M. L. James, R. R. Fulton, J. Vercouillie, D. J. Henderson, L. Garreau, S. Chalou, F. Dollé, B. Costa, D. Guilloteau, M. Kassiou, *J. Nucl. Med.* **2008**, *49*, 814.
- [11] A. Damont, F. Hinnen, B. Kuhnast, M.-A. Schöllhorn-Peyronneau, M. L. James, C. Luus, B. Tavitian, M. Kassiou, F. Dollé, *J. Label. Compd. Radiopharm.* **2008**, *51*, 286.
- [12] B. Kuhnast, A. Damont, F. Hinnen, T. Catarina, S. Demphel, S. Le Helleix, C. Coulon, S. Goutal, P. Gervais, F. Dollé, *Appl. Rad. Isot.* **2012**, *70*, 489.
- [13] C. Fookes, T. Pham, F. Mattner, I. Greguric, C. Loc'h, X. Liu, P. Berghofer, R. Shepherd, M.-C. Grégoire, A. Katsifis, *J. Med. Chem.* **2008**, *51*, 3700.
- [14] A. Martin, R. Boisgard, B. Thézé, N. Van Camp, B. Kuhnast, A. Damont, M. Kassiou, F. Dollé, B. Tavitian, *J. Cereb. Blood Flow Metab.* **2010**, *30*, 230.
- [15] A. Martin, R. Boisgard, M. Kassiou, F. Dollé, B. Tavitian, *Mol. Imag. Biol.* **2011**, *13*, 10.
- [16] J. Zheng, R. Boisgard, K. Siquier-Pernet, D. Decaudin, F. Dollé, B. Tavitian, *Mol. Pharmaceutics* **2011**, *8*, 823.
- [17] A. Winkler, R. Boisgard, A. R. Awde, A. Dubois, B. Thézé, J. Zheng, L. Ciobanu, F. Dollé, T. Viel, A. H. Jacobs, B. Tavitian, *Eur. J. Nucl. Med. Mol. Imaging* **2012**, *39*, 811.
- [18] D. Tang, M. R. Hight, E. T. McKinley, A. Fu, J. R. Buck, R. A. Smith, M. N. Tantawy, T. E. Peterson, D. C. Colvin, M. S. Ansari, M. Nickels, H. C. Manning, *J. Nucl. Med.* **2012**, *53*, 287.
- [19] N. Arlicot, J. Vercouillie, M.-J. Ribeiro, C. Tauber, Y. Venel, J.-L. Baulieu, S. Maia, P. Corcia, M. G. Stabin, A. Reynolds, M. Kassiou, D. Guilloteau, *Nucl. Med. Biol.* **2012**, *39*, 570.

- [20] G. Abourbeh, B. Thézé, R. Maroy, A. Dubois, V. Brulon, Y. Fontyn, F. Dollé, B. Tavitian, R. Boisgard, *J. Neurosci.* **2012**, *32*, 5728.
- [21] S. Lavis, M. Guillermier, A. S. Hérad, F. Petit, M. Delahaye, N. Van Camp, L. Ben Haim, V. Lebon, P. Remy, F. Dollé, T. Delzescaux, G. Bonvento, P. Hantraye, C. Escartin, *J. Neurosci.* **2012**, *32*, 10809.
- [22] P. Corcia, C. Tauber, J. Vercoullie, N. Arlicot, C. Prunier, J. Praline, G. Nicolas, Y. Venel, C. Hommet, J.-L. Baulieu, J. P. Cottier, C. Roussel, M. Kassiou, D. Guilloteau, M.-J. Ribeiro, *PLoS One* **2012**, *7*, e52941.
- [23] H. Boutin, C. Prenant, R. Maroy, J. Galea, A. D. Greenhalgh, A. Smigova, C. Cawthorne, P. Julyan, S. M. Wilkinson, S. D. Banister, G. Brown, K. Herholz, M. Kassiou, N. J. Rothwell, *PLoS One* **2013**, *8*, e56441.
- [24] R. Camsonne, C. Crouzel, D. Comar, M. Mazière, C. Prenant, J. Sastre, M. A. Moulin, A. Syrota, *J. Label. Compd. Radiopharm.* **1984**, *21*, 985.
- [25] R. B. Banati, J. Newcombe, R. N. Gunn, A. Cagnin, F. Turkheimer, F. Heppner, G. Price, F. Wegner, G. Giovannoni, D. H. Miller, D. G. Perkin, T. Smith, A. K. Hewson, G. Bydder, G. W. Kreutzberg, T. Jones, M. L. Czuzner, R. Myers, *Brain* **2000**, *123*, 2321.
- [26] E. Briard, J. L. Hong, J. L. Musachio, S. S. Zoghbi, M. Fujita, M. Imaizumi, V. Cropley, R. B. Innis, V. W. Pike, *J. Label. Compd. Radiopharm.* **2005**, *48*, S71.
- [27] M. Imaizumi, H. J. Kim, S. S. Zoghbi, E. Briard, J. Hong, J. L. Musachio, C. Ruetzler, D. M. Chuang, V. W. Pike, R. B. Innis, M. Fujita, *Neurosci. Lett.* **2007**, *411*, 200–205.
- [28] A. K. Brown, M. Fujita, Y. Fujimura, J.-S. Liow, M. Stabin, Y. H. Ryu, M. Imaizumi, J. Hong, V. W. Pike, R. B. Innis, *J. Nucl. Med.* **2007**, *48*, 2072–2079.
- [29] E. Briard, S. S. Zoghbi, M. Imaizumi, J. P. Gourley, H. U. Shetty, J. Hong, V. Cropley, M. Fujita, R. B. Innis, V. W. Pike, *J. Med. Chem.* **2008**, *51*, 17–30.
- [30] M. Imaizumi, E. Briard, S. S. Zoghbi, J. P. Gourley, J. Hong, I. Fujimura, V. W. Pike, R. B. Innis, M. Fujita, *Neuroimage* **2008**, *39*, 1289–1298.
- [31] M. Fujita, M. Imaizumi, S. S. Zoghbi, Y. Fujimura, A. G. Farris, T. Suhara, J. Hong, V. W. Pike, R. B. Innis, *Neuroimage* **2008**, *40*, 43–52.
- [32] W. C. Kreisl, M. Fujita, Y. Fujimura, N. Kimura, K. J. Jenko, P. Kannan, J. Hong, C. L. Morse, S. S. Zoghbi, R. L. Gladding, S. Jacobson, U. Oh, V. W. Pike, R. B. Innis, *Neuroimage* **2010**, *49*, 2924–2932.
- [33] A. A. Wilson, A. Garcia, J. Parkes, P. McCormick, K. A. Stephenson, S. Houle, N. Vasdev, *Nucl. Med. Biol.* **2008**, *35*, 305–314.
- [34] R. Mizrahi, P. M. Rusjan, I. Vitcu, A. Ng, A. A. Wilson, S. Houle, P. M. Bloomfield, *Mol. Imaging Biol.* **2013**, *15*, 353.
- [35] D. R. Owen, O. W. Howell, S. P. Tang, L. A. Wells, I. Bennacef, M. Bergström, R. N. Gunn, E. A. Rabiner, M. R. Wilkins, R. Reynolds, P. M. Matthews, C. A. Parker, *J. Cereb. Blood Flow Metab.* **2010**, *30*, 1608–1618.
- [36] D. R. Owen, R. N. Gunn, E. A. Rabiner, I. Bennacef, M. Fujita, W. C. Kreisl, R. B. Innis, V. W. Pike, R. Reynolds, P. M. Matthews, C. A. Parker, *J. Nucl. Med.* **2011**, *52*, 24–32.
- [37] D. R. Owen, A. J. Yeo, R. N. Gunn, K. Song, G. Wadsworth, A. Lewis, C. Rhodes, D. J. Pulford, I. Bennacef, C. A. Parker, P. L. StJean, L. R. Cardon, V. E. Mooser, P. M. Matthews, E. A. Rabiner, J. P. Rubio, *J. Cereb. Blood Flow Metab.* **2012**, *32*, 1–5.
- [38] M. A. Peyronneau, W. Saba, S. Goutal, A. Damont, F. Dollé, M. Kassiou, M. Bottlaender, H. Valette, *Drug Metab. Dispos.* **2013**, *41*, 122.
- [39] J. Marik, A. Ogasawara, B. Martin-McNulty, J. Ross, J. E. Flores, H. S. Gill, J. N. Tinianow, A. N. Vanderbilt, M. Nishimura, F. Peale, C. Pastuskovas, J. M. Greve, N. van Bruggen, S. P. Williams, *J. Nucl. Med.* **2009**, *50*, 982–990.
- [40] S. S. Zoghbi, H. U. Shetty, M. Ichise, M. Fujita, M. Imaizumi, J. S. Liow, J. Shah, J. L. Musachio, V. W. Pike, R. B. Innis, *J. Nucl. Med.* **2006**, *47*, 520–527.
- [41] M. A. Peyronneau, W. Saba, F. Dollé, S. Goutal, C. Coulon, M. Bottlaender, H. Valette, *Nucl. Med. Biol.* **2012**, *39*, 347–359. Difficulties in dopamine transporter radioligand PET analysis: the example of LBT-999 using [18F] and [11C] labelling: part II: Metabolism studies.
- [42] B. Teclé, J. E. Casida, *Chem. Res. Toxicol.* **1989**, *2*, 429–435.
- [43] D. E. Ponde, C. S. Dence, N. Oyama, J. Kim, Y. C. Tai, R. Laforest, B. A. Siegel, M. J. Welch, *J. Nucl. Med.* **2007**, *48*, 420–428.
- [44] R. Nishii, W. Tong, R. Wendt, S. Soghomonyan, U. Mukhopadhyay, J. Balatoni, O. Mawlawi, L. Bidaut, P. Tinkey, A. Borne, M. Alauddin, C. Gonzalez-Lepera, B. Yang, J. G. Gelovani, *Mol. Imaging Biol.* **2012**, *14*, 231–224.
- [45] V. W. Pike, *Trends Pharmacol. Sci.* **2009**, *30*, 431–440.
- [46] V. Médran-Navarrete, A. Damont, M.-A. Peyronneau, B. Kuhnast, N. Bernards, G. Pottier, F. Marguet, F. Puech, R. Boisgard, F. Dollé, *Bioorg. Med. Chem. Lett.* **2014**, *24*, 1550–1556.
- [47] H. H. Coenen, B. Klatter, A. Knoechel, M. Schueller, G. Stöcklin, *J. Label. Compd. Radiopharm.* **1986**, *23*, 455.
- [48] K. Hamacher, H. H. Coenen, G. Stöcklin, *J. Nucl. Med.* **1986**, *27*, 235.
- [49] H. Boutin, F. Chauveau, C. Thominaux, B. Kuhnast, M.-C. Grégoire, M. L. James, S. Jan, V. Brulon, Y. Fontyn, R. Trébossen, P. Hantraye, F. Dollé, B. Tavitian, M. Kassiou, *J. Nucl. Med.* **2007**, *48*, 573.
- [50] H. Boutin, F. Chauveau, C. Thominaux, B. Kuhnast, M.-C. Grégoire, S. Jan, V. Brulon, Y. Fontyn, R. Trébossen, P. Hantraye, F. Dollé, B. Tavitian, A. Katsifis, *Glia* **2007**, *55*, 1459.
- [51] F. Chauveau, N. Van Camp, F. Dollé, B. Kuhnast, F. Hinnen, A. Damont, H. Boutin, M. L. James, M. Kassiou, B. Tavitian, *J. Nucl. Med.* **2009**, *50*, 468.
- [52] N. Van Camp, R. Boisgard, B. Kuhnast, B. Thézé, T. Viel, M.-C. Grégoire, F. Chauveau, H. Boutin, A. Katsifis, F. Dollé, B. Tavitian, *Eur. J. Nucl. Med. Mol. Imaging* **2010**, *37*, 962.
- [53] F. Chauveau, H. Boutin, N. Van Camp, C. Thominaux, P. Hantraye, L. Rivron, F. Marguet, M.-N. Castel, T. Rooney, J. Benavides, F. Dollé, B. Tavitian, *J. Nucl. Med. Mol. Imag.* **2011**, *38*, 509.

RESEARCH ARTICLE

Open Access

[¹⁸F]DPA-714 as a biomarker for positron emission tomography imaging of rheumatoid arthritis in an animal model

Géraldine Pottier^{1,2}, Nicholas Bernards^{1,2}, Frédéric Dollé² and Raphael Boisgard^{1,2*}

Abstract

Introduction: Rheumatoid arthritis (RA) is a chronic disease, affecting 0.5 to 1% of adults in industrialized countries, in which systemic inflammation and synovitis drive joint destruction. [¹⁸F]DPA-714 is a specific tracer of the 18 kDa translocator protein (TSPO), which is overexpressed on activated macrophages, and proposed as a biomarker of neuroinflammation. Today, diagnosis of patients with early inflammatory arthritis is limited by poor sensitivity and specificity. The present study aims to investigate the potential of [¹⁸F]DPA-714 to monitor *in vivo* inflammatory processes at a preclinical stage via positron emission tomography (PET).

Methods: RA was induced in Dark Agouti rats by subcutaneous injection of inactivated *Mycobacterium tuberculosis*. Development of arthritis clinical signs was investigated daily and the severity of the disease evaluated. Animals were imaged at the peak of inflammation using [¹⁸F]DPA-714 and a small-animal PET-CT tomograph.

Results: The first clinical signs appeared at 10 days post-injection, with a peak of inflammation at 20 days. At this time, PET-analyses showed a clear uptake of [¹⁸F]DPA-714 in swollen ankles, with mean values of $0.52 \pm 0.18\%$ injected dose (ID/cc) for treated ($n = 11$) and 0.19 ± 0.09 for non-treated ($n = 6$) rats. A good correlation between [¹⁸F]DPA-714's uptake and swelling was also found. Immunohistochemistry showed an enhanced TSPO expression in hind paws, mainly co-localized with the macrophages specific antigen CD68 expressing cells.

Conclusion: These preliminary results demonstrate that the TSPO 18kDa specific radioligand [¹⁸F]DPA-714 is adapted for the study and follow-up of inflammation linked to RA in our experimental model, suggesting also a strong potential for clinical imaging of peripheral inflammation.

Introduction

Rheumatoid arthritis (RA) is a chronic inflammatory disorder that can affect many tissues and organs. This disease leads to progressive joint destruction principally due to synovial inflammation, but also to articular complications and functional disability. In addition to causing joint problems, RA can also affect the whole body with fevers and fatigue. RA is a systemic autoimmune disease that also leads to many disorders in organ systems and is associated with other diseases, including infections, malignancies and cardiovascular diseases. One percent of the world's population today is affected by

RA with a repartition much more common in women than in men with ages ranging from 40 to 60 years [1]. Smoking is the main environmental risk factor for developing RA. Other potential risks, including alcohol abuse, vitamin D status, contraception use and coffee intake, have been reported too [2].

The detection of RA is important in clinical strategies that include early treatments which may slow down the disease progression and improve the long-term clinical outcome. Criteria proposed in 1987 by the American College of Rheumatology (ACR) 1987 are rather limited by the poor sensitivity and specificity for the classification of patients with early RA [3]. These criteria include morning stiffness, arthritis of three or more areas, arthritis of hand joints (>1 swollen joint), rheumatoid nodules, serum rheumatoid factor, radiographic changes (erosions). However, early events failed to be detected by

* Correspondence: raphael.boisgard@cea.fr

¹Inserm, Unité 1023, Université Paris Sud, Orsay 91400, France

²Commissariat à l'Energie Atomique et aux Energies Alternatives, Direction des Sciences du Vivant, Institut d'Imagerie Biomédicale, Service Hospitalier Frédéric Joliot, Orsay 91400, France

those means. Until today, identification of bone changes in RA is traditionally the domain of plain radiography. In parallel to this, other techniques such as Magnetic Resonance Imaging and Ultrasound have demonstrated a superior sensitivity for the detection of erosive changes around the bone. Several teams have shown that sub-clinical arthritis can be detected by advanced imaging techniques such as sonography or power Doppler [4-6]. The development of non-invasive, highly sensitive and 3D-imaging-based methods for detecting early arthritis could also offer an opportunity to initiate treatments at very early stages to the patient.

Molecular- and nuclear-based imaging techniques offer a large scale opportunity for detection of diseases. These techniques are based on the use of tracers labeled with radioactive isotopes and allow non-invasive *in vivo* detection of different physiologic and pathologic phenomena with high sensitivity. Positron Emission Tomography (PET) is one of those that are increasingly used to diagnose and characterize disease activity in the setting of inflammatory disorders such as RA [7-10]. PET is even more sensitive than Single Photon Emission Computed Tomography (SPECT) and can also provide quantitative measurements. The low spatial resolution can make assigning the signal to specific anatomical structures difficult and can be partially compensated by combining PET with CT (X-ray Computed Tomography). [¹⁸F]Fluorodeoxyglucose ([¹⁸F]FDG), a radio-fluorinated analogue of glucose and the most widely used radiopharmaceutical worldwide today, was proposed for imaging RA [11,12]. Using this radiotracer, inflamed joints could be detected even though [¹⁸F]FDG is not a specific marker of inflammation. Macrophage infiltration has been identified in early stages of RA [13], and therefore a specific tracer of such a process would be more specific and possibly also enable an earlier detection of inflammation. Recently, expression of the folate receptor has been investigated in a rat model of RA using [¹⁸F]fluoro-PEG-folate [14] illustrating the interest for molecular imaging in this type of pathology.

The 18kDa translocator protein (TSPO), previously known as the peripheral benzodiazepine receptor (PBR), is located in the outer mitochondrial membrane [15]. This protein is up-regulated in inflammatory processes, making radiolabeled TSPO ligands attractive imaging probes in a multitude of pathologies. Different TSPO ligands have already been used as imaging probes in different animal models of human diseases such as cancer [16], cerebral ischemia [17], lung [18] and liver diseases [19].

Today, [¹¹C]PK11195 is still considered as the reference radioligand for imaging *in vivo* TSPO expression mainly in central nervous system disorders and rarely in the case of peripheral inflammatory diseases. Numerous publications in the recent literature have, however, highlighted the limitations of this radiotracer for quantitative *in vivo*

measurement of TSPO expression [20] and several novel TSPO radioligands have been developed today as alternatives to the use of [¹¹C]PK11195 [21-23]. Among them, the pyrazolo [1,5] pyrimidine acetamide DPA-714, labeled with fluorine-18 ([¹⁸F]DPA-714) is one of the most promising compounds. For the moment, [¹⁸F]DPA-714 is mainly used to image brain injury in various animal models [17,24-26] but also in the field of oncology with applications in breast cancer [27] and glioma [28]. Interest for the molecular imaging of peripheral inflammation has also been investigated recently in non-alcoholic fatty liver disease in rats [19] and lungs by the same team [18] using another radiolabelled TSPO ligand ([¹⁸F]FEDAC). Recently, [¹¹C]PK11195 has been shown to be of potential interest in imaging arthritis in humans [7,10,29]. The visualization of macrophages using [¹¹C]PK11195 PET seems to be useful for detecting early synovitis and for monitoring disease evolution during treatment.

The present study aims to investigate the potential of [¹⁸F]DPA-714 PET to image and quantify *in vivo* peripheral inflammation in an autoimmune adjuvant-induced RA rat model.

Methods

Animals

Male Dark Agouti rats (216.7 g ± 16.4 g) were purchased from Centre d'Élevage René Janvier (Saint Berthevin, France), housed and acclimatized for one week before treatment with free access to food and water. Animal studies were conducted in accordance with the French legislation and European directives (2010/63/UE) on the uses of animals in research. Experiments were done in the approved French laboratory D 91 471 105 from 2 August 2012, under the supervision of the institutional ethical committee (CETEA DSV, recorded in 6 June 2011 under No. 44 by CNREEA, National Committee for ethical reflection on animal experimentation).

Preparation of CFA (complete Freund's adjuvant)

Mycobacterium tuberculosis H37 Ra (Mtb) and incomplete Freund's adjuvant (IFA) were purchased from Difco Laboratories (USA). CFA was prepared as follows: IFA (20 mL) was drop-wise added, with continuous mixing, to finely crushed Mtb (100 mg). The resulting oily preparation (Mtb: 5 mg/mL) may be temporarily stored at -20°C if not readily used.

Induction of RA

Rats were anesthetized with an isoflurane/oxygen mixture (2 to 4%). Induction of RA was performed for each rat by intra-dermal injection at the base of the tail of 100 µL (single dose) of the above reported CFA.

Clinical evaluation of RA

Rats were observed daily. Animals were weighed and development of arthritis clinical signs investigated every two days. The clinical severity of RA was evaluated according to the following scale: 1 = detectable swelling in one joint; 2 = swelling in two joints; 3 = swelling in three joints; 4 = severe swelling of the entire paw. The maximum score per animal for the four paws was 16. Each observation was done under short anesthesia using an isoflurane/oxygen mixture (2 to 3%).

[¹⁸F]DPA-714 preparation

DPA-714 was labeled with fluorine-18 (half-life, 109.8 minutes) at its 2-fluoroethyl moiety using a tosyloxy-for-fluorine nucleophilic aliphatic substitution, according to slight modifications of procedures already reported [30,31], and using a commercially available GE TRACERLab FX-FN synthesizer [32]. Ready-to-inject, >99% radiochemically pure [¹⁸F]DPA-714 (formulated in physiological saline containing less than 10% of ethanol) was obtained with 15 to 20% non-decay-corrected yields and specific radioactivities at the end of the radiosynthesis ranging from 37 to 111 GBq/μmol. Injected doses (MBq and nmoles, mean ± SD) will be given within the text.

PET/CT imaging and data analysis

PET/CT scans were performed using small-animal INVEON (Siemens, Munich, Germany) tomography. This system combines both PET and CT modalities under the control of a unique workstation, including CT-based attenuation correction which allows for superior quality PET images. PET/CT scans were performed around the peak of the disease (20 days) following CFA-injection in all animals showing a clinical score ranging from 1 to 16 as well as in control animals (free of injection).

Animals were anesthetized with an isoflurane/oxygen mixture (2 to 4%) and maintained normothermically using a heating pad. Injections of [¹⁸F]DPA-714 were made in the caudal lateral vein using a 24-gauge catheter.

Dynamic acquisitions were done as follows: imaging started at the time of injection of [¹⁸F]DPA-714 (38.0 ± 3.1 MBq/rat corresponding to 2.2 ± 0.8 nmol by injection) and continued for 60 minutes (n = 5). Static acquisitions were obtained 45 minutes after injection of the radiotracer and lasted for a period of 15 minutes (n = 6). In displacement studies (n = 3) animals received, 30 minutes post [¹⁸F]DPA-714-injection, a solution of DPA-714 (5 mg/kg) intravenously. Data acquisition was continued for another 30 minutes.

All PET-measurements were performed with a time coincidence window of 3.432 ns and the energy levels of discrimination at 350 keV and 650 keV. The list mode data files were histogrammed into 3D-sinograms with a maximum ring difference of 79 and a span of 3. Images were

reconstructed using ASIPro (Siemens) with the FORE + OSEM2D algorithm (16 subsets and 4 iterations).

Image analysis and quantification of radioactivity in volumes of interest were performed using Brain-Visa/Anatomist version 3.1 [33]. Regions of interest (ROIs) were drawn on the ankle joints. These ROIs were then projected onto all dynamic frames, thereby creating time activity curves for each ROI. Radioactivity uptake values were quantified in Bq per cubic cm (cc) of tissue, corrected for fluorine-18-decay and converted into the percentage of injected dose per cubic cm (% ID/cc).

Histology

After rat euthanasia (lethal dose of pentobarbital 150 mg/kg), the paws were then collected and fixed in 10% (v/v) buffered formalin phosphate (Labonord, France) for 24 h to 48 h, before being decalcified using Immunocal (Decal Chemical Corporation, USA) for two weeks. After decalcification, the paws were frozen in liquid nitrogen and stored at -80°C before being sliced with a cryotome (Leica CM3050, Germany). Finally, the ankle joints were cut in a sagittal plane and sectioned at 5 μm.

Selected sections were stained with Mayer's hematoxylin solution (Sigma, USA) and eosin-y (Labonord, France) or directly used for immunohistochemistry.

Immunohistochemistry

Immunohistochemistry (IHC) was performed on 5 μm frozen sections of paw slices. Slices were placed for 15 minutes in fixative containing 4% paraformaldehyde in PBS (phosphate-buffered saline), then removed and placed in 50 mM aq. NH₄Cl for 5 minutes. Slices were then placed in PBS containing 5% BSA (bovine serum albumin) (Merck, Germany) and 0.5% Tween 20 (Sigma, USA) for five minutes at room temperature (RT). Finally, slices were incubated (1 h, RT) with the following primary antibodies in solution in the above mentioned buffer: mouse anti-CD68 (MRA341R, 1:100; Serotec, Germany), goat anti-Iba1 (ab5076, 1:100; Abcam, UK) and rabbit anti-TSPO (NBP1-95674, 1:1,000; Novus Biologicals, UK).

Slices were then washed three times with PBS and then incubated (30 minutes, RT) with Alexa Fluor-546 donkey anti-mouse (A10036, 1:1,000; Invitrogen, France), Alexa Fluor-647 donkey anti goat (A21447, 1:1,000; Invitrogen, France), Alexa Fluor-488 goat anti-rabbit (A11034; 1:1,000; Invitrogen, France), respectively, in a solution of PBS containing 5% BSA and 0.5% Tween 20.

Slices were again washed three times in PBS and then mounted with a DAPI Kit (P36931 Invitrogen, France).

The number of CD68-, TSPO- and Iba1-positive cells were counted under the ×20-objective of an Axio observer Z1 microscope (Zeiss, France) on seven fields of view taken from three adjacent sections per rat.

Statistical analysis

Statistical analyses were conducted using Microsoft Excel software. A significant difference between arthritic and control groups was determined at each point by the one-tailed Student's *t*-test. A *P*-value of less than 0.05 was deemed as significant.

Results

Rheumatoid arthritis model

An arthritic model was induced by a single dose injection of 0.5 mg of *Mycobacterium tuberculosis* H37 Ra (Mtb) in male Dark Agouti rats (DA rats). During the disease progression, two parameters were followed: the bodyweight and the joint swelling. These parameters are both reported as systemic RA symptoms. Figure 1A illustrates the typical clinical course of the RA in DA male rats after injection of Mtb. The initial signs of arthritis appeared around 10 to 13 days after the injection, mostly as swelling of the metatarsophalangeal or ankle joints of the hind paws. The inflammation progressed to the entire hind paw (Figure 1B) and at a later stage, the joints in the front paws also became inflamed. The inflammation's peak appeared at around 20 days after Mtb-injection; thereafter, the swelling progressively declined and disappeared by about 40 days after Mtb-injection. The body weight of treated animals started to decrease six to seven days post-Mtb-injection. A loss of weight of up to 18.5% could be observed. This loss of weight stopped with the decrease of the inflammation. No

apparent clinical symptoms occurred for the non-treated animals. As expected for this group, a regular weight gain was observed.

Histological evaluation of the RA model

The arthritic effects of the RA model were analyzed on histological joint sections stained with Hematoxylin and Eosin at 20 days post-Mtb-injection. Severe signs of inflammation could be detected in treated rats (Figure 2B) with an increased amount of infiltrated inflammatory cells (such as lymphocytes and macrophages) while only scarce proliferation was observed in non-treated rats (Figure 2A). Immunohistochemical staining on joint sections was also performed in order to characterize TSPO expressing cells. Specific antibodies directed against CD68 and Iba 1 confirmed the significant increase of activated macrophages in treated (RA) rats (Figure 3A, C) compared to non-treated rats (Figure 3B, D). TSPO-labeling on the RA rats' joints slides (Figure 3E) was mainly co-localized with CD68-labeling. Cell counting showed that 23% of the cells present in the ankle were CD68 positive. Among them, 95% expressed TSPO and only about 5% were TSPO negative. In the inflamed ankle, around 4% of the cells were visualized expressing only the TSPO (CD68-). In non-treated animals, these cell activations were not visible in joint slides and the proportion of CD68 positive cell was less than 1% (Figure 3F).

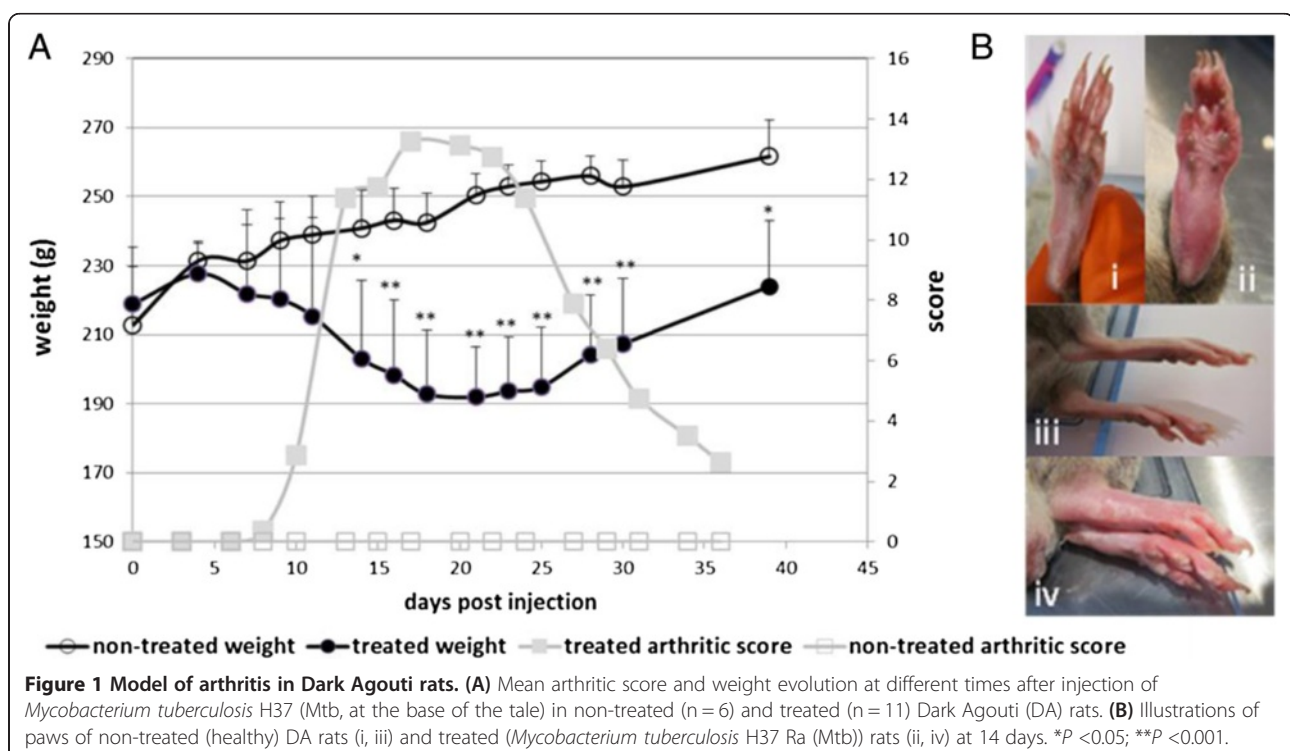


Figure 1 Model of arthritis in Dark Agouti rats. (A) Mean arthritic score and weight evolution at different times after injection of *Mycobacterium tuberculosis* H37 (Mtb, at the base of the tale) in non-treated (n = 6) and treated (n = 11) Dark Agouti (DA) rats. **(B)** Illustrations of paws of non-treated (healthy) DA rats (i, iii) and treated (*Mycobacterium tuberculosis* H37 Ra (Mtb)) rats (ii, iv) at 14 days. **P* < 0.05; ***P* < 0.001.

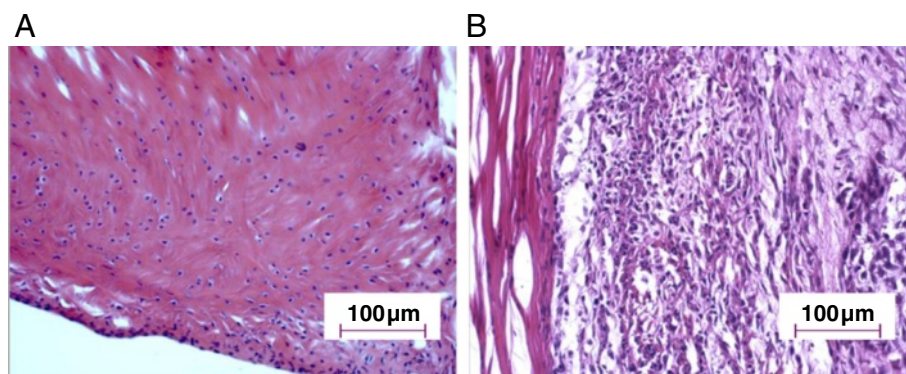


Figure 2 Histological characterization of the RA model in DA rats. Tissue slides from joints of non-treated rats (A) and joints from Mtb-treated rats (B) were analyzed at 20 days post-injection using Hematoxylin and Eosin stained sections from ankle joints (hind paw). The histological architecture shows synovial hyperplasia and infiltration of inflammatory cells. (Magnification x200).

Uptake of [^{18}F]DPA-714 in paws (ankles) of RA rats and non-treated rats

The capacity to detect and quantify peripheral inflammation lesions in the hind paw of rats *in vivo* was evaluated by microPET imaging using [^{18}F]DPA-714. Figure 4A shows an image of a coronal section in which increased uptake of [^{18}F]DPA-714 in ankles of Mtb-treated (RA) rat (4A, i) compared to non-treated (control) rat (4A, ii) at 20 days. Both images are represented using the same color scale. A sharp increase of the radiotracer's uptake in the ankles of the treated rat is clearly illustrated (indicated by white arrows). A typical time-activity curve observed in the hind paw of a treated rat at 20 days post-Mtb-induction, scored 4 (clinical severity grade) is represented in Figure 4B. As shown, the uptake of [^{18}F]DPA-714 rapidly reached a maximum and steady value, only a few minutes following the i.v. injection of the radiotracer and remained stable throughout the 60-minute acquisition. The mean [^{18}F]DPA-714 uptake value in treated animals was more than twice that of the non-treated animals. Values reaching 0.52 ± 0.18 and $0.19 \pm 0.09\%$ ID/cc were found for treated animals ($n = 11$ with a score ranging from 5 to 16) and non-treated animals ($n = 6$), respectively (Figure 4C). These results were statistically significant with a P -value of 0.00008 (t-test).

In vivo specificity

To eliminate the possibility that [^{18}F]DPA-714 uptake was driven by unspecific processes, and also to evaluate at the same time the specificity of this binding, animals were injected 30 minutes post-[^{18}F]DPA-714 administration, with a large excess (5 mg/kg of body weight) of DPA-714 (unlabeled). Figure 5A permits us to compare the same animal just before injection (5A, i) and 15 minutes after injection of unlabeled DPA-714 (5A, ii). An important decrease of the signal in the ankles as well as an increase of the background signal (illustrated by the

higher signal in the muscle) could be noticed following the intravenous injection of non-labeled DPA-714. This increase of background could mainly be explained by the release of [^{18}F]DPA-714 from the heart, lungs and spleen, three organs characterized by a high level of TSPO expression. Figure 5 illustrates the mean curve of displacement carried out on four different animals with similar grades of the disease. The mean radioactivity in this group of animals is around $0.46 \pm 0.06\%$ of ID/cc just before the displacement challenge and decreased to $0.27 \pm 0.03\%$ of ID/cc at 30 minutes after the injection of unlabeled DPA-714. This variation corresponds to a displacement around 45% of the initial signal present in the ankles. During the same time, the mean value in the muscle increased from $0.06 \pm 0.01\%$ ID/cc to $0.20 \pm 0.01\%$ ID/cc corresponding to a variation around 300%.

Correlation between the uptake of [^{18}F]DPA-714 and the severity of the disease

To analyze the relation between the uptake of the radiotracer and the inflammatory status, the ID/cc and the volume of the ankle were plotted as presented in Figure 6. A linear regression, using the least square method, gave a determination coefficient of R^2 equal to 0.65 illustrating a good relation between the uptake of this radiotracer and the severity (swelling) of the disease.

Discussion

The present study used a readily accessible, small molecular weight, fluorine-18-labeled compound, coded DPA-714, as the radiotracer for the inflammatory processes. This TSPO radioligand has been largely used to monitor neuroinflammation. The results published recently in various articles illustrate the potential of [^{18}F]DPA-714 to provide quantitative information about the expression of TSPO with correlation between the radioactive signal obtained by PET imaging and the molecular

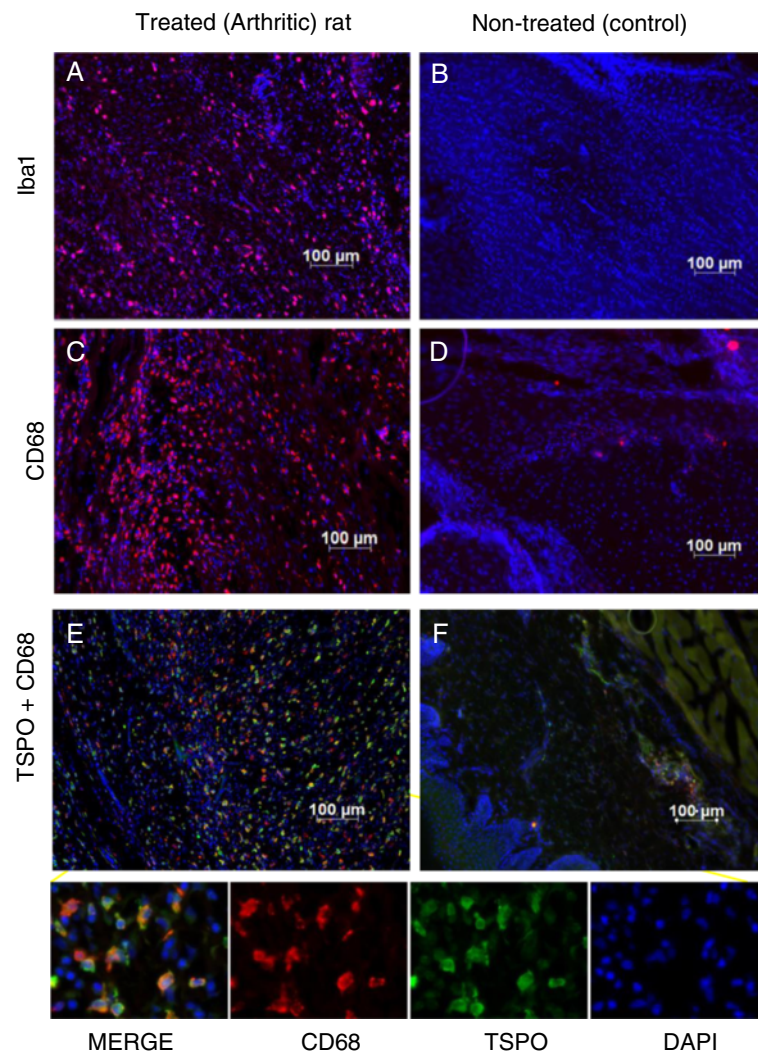
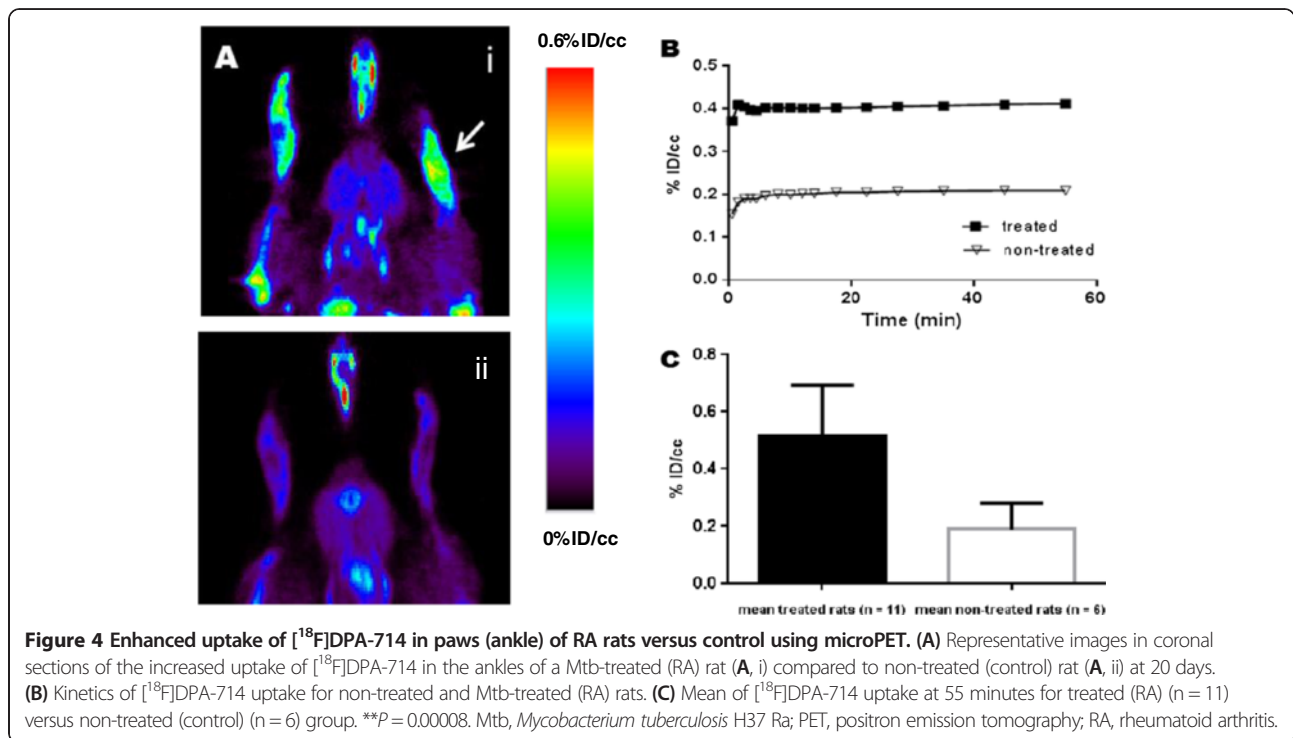


Figure 3 TSPO expression in hind paws of RA rats is associated with activated macrophages. Slide tissues of treated (RA) (A and C) and non-treated (control) rats (B and D) were stained with CD68 (red) or Iba1 (red) for activated macrophages. Nucleuses were colored with DAPI (blue). Representative IHC staining of TSPO positives cells (green) from treated (RA) rats (E) and non-treated (control) rats (F) and the colocalization with CD68 cells (red) are also shown. IHC, immunohistochemistry; RA, rheumatoid arthritis; TSPO, translocator protein.

expression of the target, at a cellular level, obtained by Western blot analysis [16,24]. In our inflammatory model, biochemical analysis could not be easily performed due to the presence of bones and cartilages. For this reason we chose to illustrate the increase of TSPO using IHC. This approach, done on fixed tissues, required a decalcification step to permit the slicing of the articular tissues. These analyses were done on control, mild and severe inflammatory grade permitting us to visualize an increasing number of CD68 and TSPO positive cells (data not shown). The combination of both [^{18}F]DPA-714 PET imaging and IHC clearly illustrated the increase of TSPO expression in the ankles of treated rats in comparison to non-treated animals. IHC using

CD68 showed the important infiltration of white blood cells, mainly macrophages, in the ankle. The CD68 positive cells represented around 25% of the cells counted on tissue samples from inflamed ankles. Co-labeling using a TSPO antibody showed that 95% of these CD68 marked cells were also TSPO positive. TSPO is expressed in mitochondria whereas CD68 is mainly localized in cytoplasmic granules. This non-overlap, adding to the counting error incertitude, does not permit us to affirm that some CD68 positives cells are really TSPO negatives. These types of cells (TSPO-; CD68+) represent less than one percent of total cells counted in the different fields of view for this quantitative approach. On the other hand, around 4% of total cells by field of view are TSPO + and CD68-. This cell

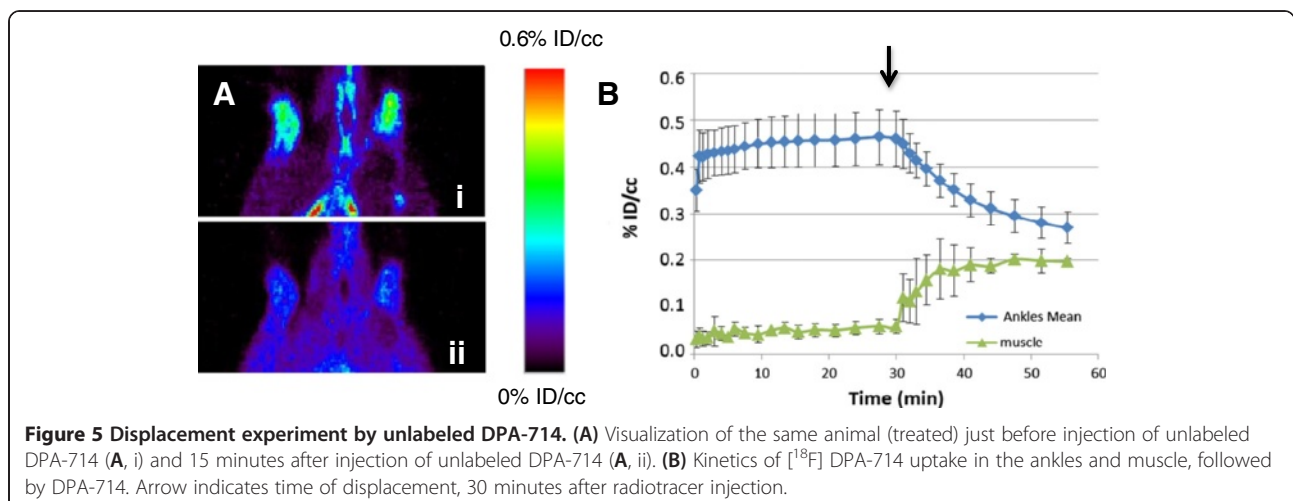


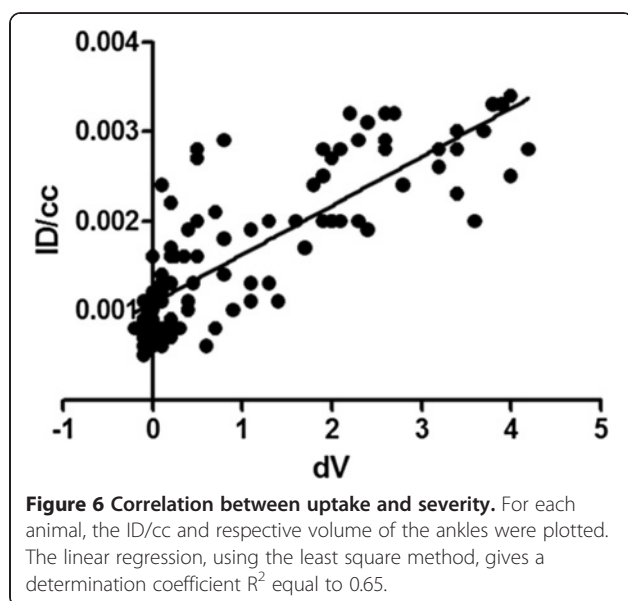
population could represent other immune cells, such as lymphocytes or macrophages as suggested by the presence of Iba1+/CD68- or MRP8+/CD68- cells.

Conventional radiography is nowadays considered as the gold standard in RA imaging for the evaluation of structural damages. The main limitation with this technique is that its sensitivity is considered to be low and also that it is not able to assess the disease activity.

Recently, an international group of expert rheumatologists, radiologists and methodologists published some recommendations for the use of imaging of the joints in the

clinical management of rheumatoid arthritis [34]. They compared the potential of different imaging techniques for diagnosis of RA, detecting inflammation and damage, predicting outcome and response to treatment, monitoring disease activity, progression and remission. These techniques, conventional radiography, MRI, CT, dual emission X-ray absorptiometry, digital X-ray radiogrammetry are anatomical images based mainly on density alteration of bones and cartilages. Two other techniques were included in this comparative study, SPECT and PET imaging. These two nuclear-based approaches mainly provide information





on biological functions (molecular imaging) as opposed to anatomical imaging. In arthritis, anatomical alterations of bone, cartilage or at least severe stage tendon swelling, represents a late stage of the disease with clinical symptoms illustrative of a long molecular process of inflammation. Concerning the diagnosis of RA, precocity has been described as an important point to implement appropriate therapeutics and thus limit structural alterations and delayed invalidity associated with this disease. Molecular imaging, such as TSPO PET imaging, represents a possibility of following early events in the physiopathology of RA. It has, therefore, been proposed that [^{11}C]PK11195 PET imaging could be used for detecting early synovitis and for monitoring the evolution of the disease during treatment [7,10]. The present work, performed in a rat RA model, demonstrates that [^{18}F]DPA-714 can be used to image inflammation of joints non-invasively. The specificity of the uptake was assessed here by intravenous injection of a large amount of unlabeled DPA-714. This injection displaced specific binding of [^{18}F]DPA-714 by saturation of TSPO binding site by a non-labelled compound. The phenomena took place in an inflamed area but also in every organ with a physiological high content of TSPO inducing plasma release of a large quantity of [^{18}F]DPA-714. This effect is illustrated by the huge increase in an unspecific signal quantified in the muscle with a variation from 0.06 to 0.20% of ID/cc (Figure 5B). In the inflamed ankles, the displacement leads a decrease of the signal around 45%. After administration of unlabeled DPA-714, the ankle-to-muscle ratio in these animals was around 1:4 while this ratio was 7:8 before administration. This value illustrates that the signal quantified in the ankle after displacement is largely due to background corresponding to

free [^{18}F]DPA-714 (not bound to the TSPO 18kDa). In the inflamed areas it has been shown that the vascular density is also increased. This high vascular density can increase the volume of blood in the considered area and participate in the higher signal in comparison to normal ankles or muscle use as the reference area. Local inflammation also induces edema. Edematous areas are well known to present high oncotic pressure inducing extravasation of macromolecules. This phenomenon was not described for small ligands, such as DPA-714, with a molecular weight around 400 g/mol. This hypothesis is certainly not the explanation concerning the remaining radioactivity present in the ankle after displacement. The level of radiotracer accumulation in the swollen hind paws correlates to the thickness of the ankles, and is chosen as macroscopic criteria for the severity of the disease (Figure 6). In this graph, uptake results were expressed as density by number of the receptors by volume unit here extrapolated as Becquerel/cc corrected by the ID/cc. The fact that the increase of ankle volume was linked to an increase of the TSPO density (for example, [^{18}F]DPA-714's uptake) underlines the relation between the severity of the disease and the level of TSPO expression. This functional information represents an important point concerning the ability of imaging techniques to evaluate disease activity, a parameter simply not accessible using conventional anatomical imaging approaches. Another criterion that represents a large interest for rheumatologists is the potential of such non-invasive imaging tools and techniques to predict the evolution of the disease.

Conclusion

The results of the present work demonstrates that the use of the TSPO-targeting PET-ligand [^{18}F]DPA-714 is well-adapted to the study of peripheral inflammation in an experimental rodent model of RA. [^{18}F]DPA-714 PET imaging may provide new objective parameters to evaluate the early stages of the disease and to determine disease activity, also suggesting a strong potential of this technique for clinical investigation of peripheral inflammation.

Abbreviations

[^{18}F]FDG: [^{18}F]Fluorodeoxyglucose; ACR: American College of Rheumatology; BSA: Bovine serum albumin; CFA: Complete Freund's adjuvant; CT: X-ray computed tomography; ID/cc: Injected dose; IFA: Incomplete Freund's adjuvant; IHC: Immunohistochemistry; Mtb: *Mycobacterium tuberculosis* H37 Ra; PBS: Phosphate-buffered saline; PET: Positron emission tomography; RA: Rheumatoid arthritis; ROIs: Regions of interest; RT: Room temperature; SPECT: Single photon emission computed tomography; TSPO: Translocator protein.

Competing interests

The authors declare that they have no competing interests.

Authors' contributions

GP helped to design the study, performed the experiments, analyzed and interpreted data and drafted the manuscript. NB participated in imaging acquisitions and critically reviewed the manuscript. FD participated in [^{18}F]DPA-714 syntheses and was involved in revising the manuscript. RB

designed the study, participated in data analysis and drafted the manuscript. All authors read and approved the final version of the manuscript.

Acknowledgments

The authors thank Dr. Serge DESARNAUD for stimulating discussions and for his help in writing this manuscript. This work was supported by CEA-I2BM intramural programs, as well as the European Union's Seventh Framework Programme [FP7/2007-2013] INMiND (Grant agreement number HEALTH-F2-2011-278850).

Received: 1 August 2013 Accepted: 17 February 2014

Published: 13 March 2014

References

1. Scott DL, Wolfe F, Huizinga TW: **Rheumatoid arthritis.** *Lancet* 2010, **376**:1094–1108.
2. Liao KP, Alfredsson L, Karlson EW: **Environmental influences on risk for rheumatoid arthritis.** *Curr Opin Rheumatol* 2009, **21**:279–283.
3. Banal F, Dougados M, Combescure C, Gossec L: **Sensitivity and specificity of the American College of Rheumatology 1987 criteria for the diagnosis of rheumatoid arthritis according to disease duration: a systematic literature review and meta-analysis.** *Ann Rheum Dis* 2009, **68**:1184–1191.
4. Wakefield RJ, Gibbon WW, Conaghan PG, O'Connor P, McGonagle D, Pease C, Green MJ, Veale DJ, Isaacs JD, Emery P: **The value of sonography in the detection of bone erosions in patients with rheumatoid arthritis: a comparison with conventional radiography.** *Arthritis Rheum* 2000, **43**:2762–2770.
5. Perić P, Laktasić-Zerjavić N: **The value of sonography and power Doppler in the detection of early arthritis.** *Reumatizam* 2011, **58**:94–104.
6. van de Stadt LA, Bos WH, Meursing Reynders M, Wieringa H, Turkstra F, van der Laken CJ, van Schaardenburg D: **The value of ultrasonography in predicting arthritis in auto-antibody positive arthralgia patients: a prospective cohort study.** *Arthritis Res Ther* 2010, **12**:R98.
7. Gent YY, Voskuyl AE, Kloet RW, van Schaardenburg D, Hoekstra OS, Dijkmans BA, Lammertsma AA, van der Laken CJ: **Macrophage positron emission tomography imaging as a biomarker for preclinical rheumatoid arthritis: findings of a prospective pilot study.** *Arthritis Rheum* 2012, **64**:62–66.
8. Okamura K, Yonemoto Y, Arisaka Y, Takeuchi K, Kobayashi T, Oriuchi N, Tsushima Y, Takagishi K: **The assessment of biologic treatment in patients with rheumatoid arthritis using FDG-PET/CT.** *Rheumatology (Oxford)* 2012, **51**:1484–1491.
9. Kubota K, Ito K, Morooka M, Minamimoto R, Miyata Y, Yamashita H, Takahashi Y, Mimori A: **FDG PET for rheumatoid arthritis: basic considerations and whole-body PET/CT.** *Ann N Y Acad Sci* 2011, **1228**:29–38.
10. van der Laken CJ, Elzinga EH, Kropholler MA, Molthoff CF, van der Heijden JW, Maruyama K, Boellaard R, Dijkmans BAC, Lammertsma AA, Voskuyl AE: **Noninvasive imaging of macrophages in rheumatoid synovitis using 11C-(R)-PK11195 and positron emission tomography.** *Arthritis Rheum* 2008, **58**:3350–3355.
11. Polisson RP, Schoenberg OI, Fischman A, Rubin R, Simon LS, Rosenthal D, Palmer WE: **Use of magnetic resonance imaging and positron emission tomography in the assessment of synovial volume and glucose metabolism in patients with rheumatoid arthritis.** *Arthritis Rheum* 1995, **38**:819–825.
12. Imler IM, Opfermann T, Gebhardt P, Gajda M, Brauer R, Saluz HP, Kamradt T: **In vivo molecular imaging of experimental joint inflammation by combined 18F-FDG positron emission tomography and computed tomography.** *Arthritis Res Ther* 2010, **12**:R203.
13. Kraan MC, Versendaal H, Jonker M, Bresnihan B, Post WJ, Hart BA, Breedveld FC, Tak PP: **Asymptomatic synovitis precedes clinically manifest arthritis.** *Arthritis Rheum* 1998, **41**:1481–1488.
14. Gent YY, Weijers K, Molthoff CF, Windhorst AD, Huisman MC, Smith DE, Kularatne SA, Jansen G, Low PS, Lammertsma AA, van der Laken J: **Evaluation of the novel folate receptor ligand [18F]fluoro-PEG-folate for macrophage targeting in a rat model of arthritis.** *Arthritis Res Ther* 2013, **15**:R37.
15. Casellas P, Galiege S, Basile S: **Peripheral benzodiazepine receptors and mitochondrial function.** *Neurochem Int* 2002, **40**:475–486.
16. Tang D, Hight MR, McKinley ET, Fu A, Buck JR, Smith RA, Tantawy MN, Peterson TE, Colvin DC, Ansari MS, Nickels M, Manning HC: **Quantitative preclinical imaging of TSPO expression in glioma using N, N-diethyl-2-(2-(4-(2-18F-fluoroethoxy)phenyl)-5,7-dimethylpyrazolo[1,5-a]pyrimidin-3-yl)acetamide.** *J Nucl Med* 2012, **53**:287–294.
17. Martín A, Boisgard R, Kassiou M, Dollé F, Tavitian B: **Reduced PBR/TSPO expression after minocycline treatment in a rat model of focal cerebral ischemia: a PET study using [18F]DPA-714.** *Mol Imaging Biol* 2011, **13**:10–15.
18. Hatori A, Yui J, Yamasaki T, Xie L, Kumata K, Fujinaga M, Yoshida Y, Ogawa M, Nengaki N, Kawamura K, Fukumura T, Zhang M-R: **PET imaging of lung inflammation with [18F]FEDAC, a radioligand for translocator protein (18kDa).** *PLoS One* 2012, **7**:e45065.
19. Xie L, Yui J, Hatori A, Yamasaki T, Kumata K, Wakizaka H, Yoshida Y, Fujinaga M, Kawamura K, Zhang M-R: **Translocator protein (18kDa), a potential molecular imaging biomarker for non-invasively distinguishing non-alcoholic fatty liver disease.** *J Hepatol* 2012, **57**:1076–1082.
20. Chauveau F, Boutin H, Van Camp N, Dollé F, Tavitian B: **Nuclear imaging of neuroinflammation: a comprehensive review of [11C]PK11195 challengers.** *Eur J Nucl Med Mol Imaging* 2008, **35**:2304–2319.
21. Dollé F, Luus C, Reynolds A, Kassiou M: **Radiolabelled molecules for imaging the translocator protein (18kDa) using positron emission tomography.** *Curr Med Chem* 2009, **16**:2899–2923.
22. Roeda D, Kuhnast B, Damont A, Dollé F: **Synthesis of fluorine-18-labelled TSPO ligands for imaging neuroinflammation with positron emission tomography.** *J Fluor Chem* 2012, **134**:107–114.
23. Damont A, Roeda D, Dollé F: **The potential of carbon-11 and fluorine-18 chemistry: illustration through the development of positron emission tomography radioligands targeting the translocator protein 18 kDa.** *J Labelled Comp Radiopharm* 2013, **56**:96–104.
24. Abourbeh G, Thézé B, Maroy R, Dubois A, Brulon V, Fontyn Y, Dollé F, Tavitian B, Boisgard R: **Imaging microglial/macrophage activation in spinal cords of experimental autoimmune encephalomyelitis rats by positron emission tomography using the mitochondrial 18kDa translocator protein radioligand [18F]DPA-714.** *J Neurosci* 2012, **32**:5728–5736.
25. Winkeler A, Boisgard R, Martin A, Tavitian B: **Radioisotopic imaging of neuroinflammation.** *J Nucl Med* 2010, **51**:1–4.
26. Chauveau F, Van Camp N, Dollé F, Kuhnast B, Hinnen F, Damont A, Boutin H, James M, Kassiou M, Tavitian B: **Comparative evaluation of the translocator protein radioligands 11C-DPA-713, 18F-DPA-714, and 11C-PK11195 in a rat model of acute neuroinflammation.** *J Nucl Med* 2009, **50**:468–476.
27. Zheng J, Boisgard R, Siquier-Pernet K, Decaudin D, Dollé F, Tavitian B: **Differential expression of the 18kDa translocator protein (TSPO) by neoplastic and inflammatory cells in mouse tumors of breast cancer.** *Mol Pharm* 2011, **8**:823–832.
28. Winkeler A, Boisgard R, Awde AR, Dubois A, Thézé B, Zheng J, Ciobanu L, Dollé F, Viel T, Jacobs AH, Tavitian B: **The translocator protein ligand [18F]DPA-714 images glioma and activated microglia in vivo.** *Eur J Nucl Med Mol Imaging* 2012, **39**:811–823.
29. Kropholler M, Boellaard R, Elzinga E, van der Laken C, Maruyama K, Kloet R, Voskuyl A, Dijkmans B, Lammertsma A: **Quantification of (R)-[11C]PK11195 binding in rheumatoid arthritis.** *Eur J Nucl Med Mol Imaging* 2009, **36**:624–631.
30. James ML, Fulton RR, Vercoullie J, Henderson DJ, Garreau L, Chalon S, Dolle F, Costa B, Selleri S, Guilloteau D, Kassiou M: **DPA-714, a new translocator protein-specific ligand: synthesis, radiofluorination, and pharmacologic characterization.** *J Nucl Med* 2008, **49**:814–822.
31. Damont A, Hinnen F, Kuhnast B, Schöllhorn-Peyronneau M-A, James M, Luus C, Tavitian B, Kassiou M, Dollé F: **Radiosynthesis of [18F]DPA-714, a selective radioligand for imaging the translocator protein (18kDa) with PET.** *J Labelled Comp Radiopharm* 2008, **51**:286–292.
32. Kuhnast B, Damont A, Hinnen F, Catarina T, Demphel S, Le Helleix S, Coulon C, Goutal S, Gervais P, Dollé F: **[18F]DPA-714, [18F]PBR111 and [18F]FEDAA1106-selective radioligands for imaging TSPO 18kDa with PET: automated radiosynthesis on a TRACERLab FX-FN synthesizer and quality controls.** *Appl Radiat Isot* 2012, **70**:489–497.
33. Cointepas Y, Mangin J-F, Garnero L, Poline J-B, Benali H: **BrainVISA: Software platform for visualization and analysis of multi-modality brain data.** *Neuroimage* 2001, **13**:S98.

34. Colebatch AN, Edwards CJ, Østergaard M, van der Heijde D, Balint PV, D'Agostino M-A, Forslind K, Grassi W, Haavardsholm EA, Haugeberg G, Jurik A-G, Landewé RB, Naredo E, O'Connor PJ, Ostendorf B, Potočki K, Schmidt WA, Smolen JS, Sokolovic S, Watt I, Conaghan PG: **EULAR recommendations for the use of imaging of the joints in the clinical management of rheumatoid arthritis.** *Ann Rheum Dis* 2013, **72**:804–814.

doi:10.1186/ar4508

Cite this article as: Pottier et al.: [^{18}F]DPA-714 as a biomarker for positron emission tomography imaging of rheumatoid arthritis in an animal model. *Arthritis Research & Therapy* 2014 **16**:R69.

**Submit your next manuscript to BioMed Central
and take full advantage of:**

- Convenient online submission
- Thorough peer review
- No space constraints or color figure charges
- Immediate publication on acceptance
- Inclusion in PubMed, CAS, Scopus and Google Scholar
- Research which is freely available for redistribution

Submit your manuscript at
www.biomedcentral.com/submit





Contents lists available at ScienceDirect

Bioorganic & Medicinal Chemistry Letters

journal homepage: www.elsevier.com/locate/bmcl

Preparation and evaluation of novel pyrazolo[1,5-*a*]pyrimidine acetamides, closely related to DPA-714, as potent ligands for imaging the TSPO 18 kDa with PET



Vincent Médran-Navarrete^a, Annelaure Damont^{a,*}, Marie-Anne Peyronneau^a, Bertrand Kuhnast^a, Nicholas Bernards^{a,b}, Géraldine Pottier^{a,b}, Frank Marguet^c, Frédéric Puech^c, Raphaël Boisgard^{a,b}, Frédéric Dollé^a

^aCEA, I2BM, Service Hospitalier Frédéric Joliot, Orsay, France

^bInserm, U1023, Université Paris Sud, Orsay, France

^cExploratory Unit, Sanofi, Chilly-Mazarin, France

ARTICLE INFO

Article history:

Received 29 August 2013

Revised 24 January 2014

Accepted 27 January 2014

Available online 7 February 2014

Keywords:

DPA-714 analogues

TSPO 18 kDa

Fluorinated ligands

Metabolism

PET imaging

ABSTRACT

A series of four novel analogues of DPA-714, bearing a fluoroalkynyl side chain (with a length ranging from three to six carbon atoms) in replacement of the fluoroethoxy motif, have been synthesized in six steps from commercially available methyl 4-iodobenzoate. The synthetic strategy for the preparation of these *N,N*-diethyl-2-(2-(4-(ω -fluoroalk-1-ynyl)phenyl)-5,7-dimethylpyrazolo[1,5-*a*]pyrimidin-3-yl)acetamides (**7a–d**) consisted in derivatizing a key iodinated building block featuring the pyrazolopyrimidine acetamide backbone of DPA-714, by Sonogashira couplings with various alkynyl reagents. The resulting alkynols were subsequently fluorinated, yielding the expected target derivatives. All four analogues exhibited slightly higher affinity and selectivity towards the TSPO 18 kDa (K_i vs [³H]PK11195: 0.35–0.79 nM; K_i vs [³H]flunitrazepam: >1000 nM) when compared to DPA-714 (K_i vs [³H]PK11195: 0.91 nM; K_i vs [³H]flunitrazepam: >1000 nM). Lipophilicities (HPLC, $\log D_{7.4}$) increased with the chain length (from 3.6 to 4.3) and were significantly higher than the one determined for DPA-714 (2.9). Preliminary in vitro metabolism evaluation using rat microsomal incubations and LC–MS analyses showed, for all four novel analogues, the absence of defluorinated metabolites. Among them, the fluoropentynyl compound, DPA-C5yne (**7c**), was selected, labelled in one single step with fluorine-18 from the corresponding tosylate and in vivo evaluated with PET on our in-house-developed rat model of acute local neuroinflammation.

© 2014 Elsevier Ltd. All rights reserved.

The translocator protein (TSPO 18 kDa), formerly known as the peripheral benzodiazepine receptor (PBR), is a highly lipophilic tryptophan-rich protein comprising 169 amino acids.^{1–3} It is located in the outer mitochondrial membrane of cells where it combines with a 32 kDa voltage-dependent anion channel (VDAC) and a 30 kDa adenine nucleotide carrier (ANC).^{3,4} This trimeric complex, involved in the mitochondrial permeability transition pore (MPTP), plays an important role in certain transport processes. For example, it is well-established that TSPO controls the translocation of cholesterol from the outer to inner mitochondrial membrane, where it is converted to pregnenolone, a key intermediate for the biosynthesis of steroids.⁵ While it is minimally produced in the healthy brain,⁶ the translocator protein is

overexpressed in inflamed brains.^{7–9} As a result, TSPO has become over the years an attractive biological target for imaging neuroinflammatory disorders, for example in Alzheimer's or Parkinson's disease, using PET.¹⁰

Regarding TSPO tracers, the first PET-radioligand synthesized, the isoquinoline carboxamide [¹¹C]PK11195 (Fig. 1), has been used clinically since 1984.¹¹ Even though it is still considered as a standard, [¹¹C]PK11195 presents serious limitations for PET imaging such as a poor signal-to-noise ratio and low brain penetration as well as the short radioactive half-life of carbon-11 ($t_{1/2}$ = 20.4 min).¹² These drawbacks have encouraged the design of improved radiotracers.^{13–18} For instance, in the phenoxyphenyl acetamide class, [¹¹C]DAA1106 was found to exhibit a higher specificity^{19–21} and its fluorinated analogue, FEDAA1106, labelled with the longer half-lived positron-emitter fluorine-18 ($t_{1/2}$ = 109.8 min), turned out to be also a better radioligand, with a better signal-to-noise ratio

* Corresponding author.

E-mail address: annelaure.damont@cea.fr (A. Damont).

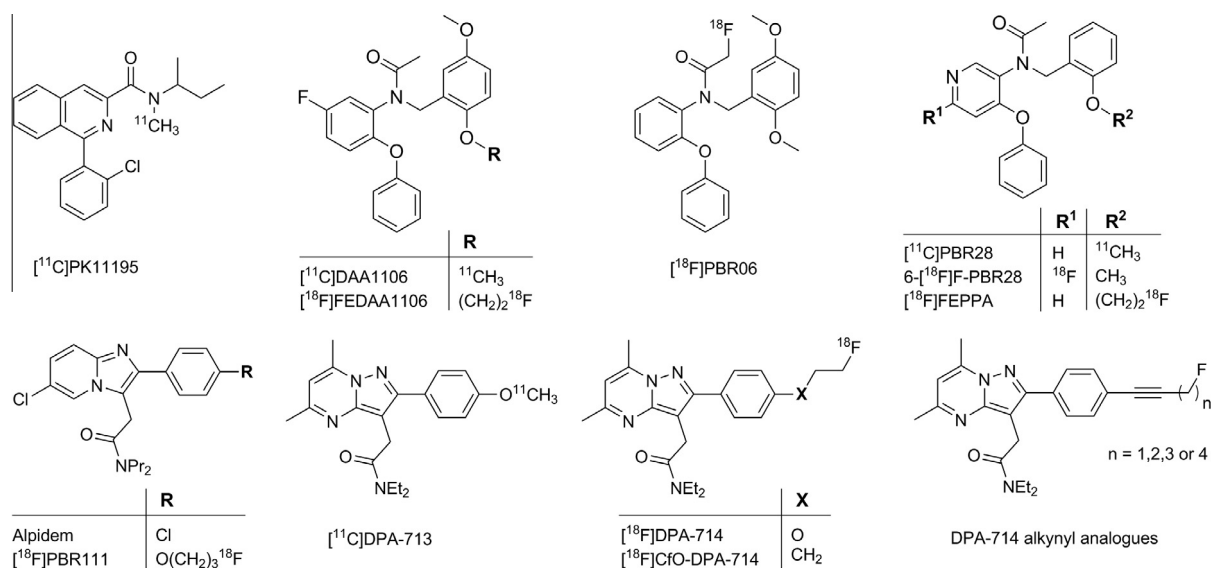


Figure 1. Selected TSPO ligands, including, at the right bottom corner, the general structure of the DPA-714 alkynyl analogues synthesized in the present work.

compared to [¹¹C]PK11195.^{22,23} [¹⁸F]PBR06 is another representative of this series that has been labelled with introduction of the fluorine-18 at the *N*-acyl function.^{24,25} Concomitantly, carbon-11 or fluorine-18-labelled compounds featuring a pyridine motif were developed. Among them, [¹¹C]PBR28, a ligand displaying encouraging in vivo imaging properties,^{26–32} and the fluorinated analogues 6-[¹⁸F]fluoro-PBR28 and [¹⁸F]FEPPA, were reported in the literature.^{33–35}

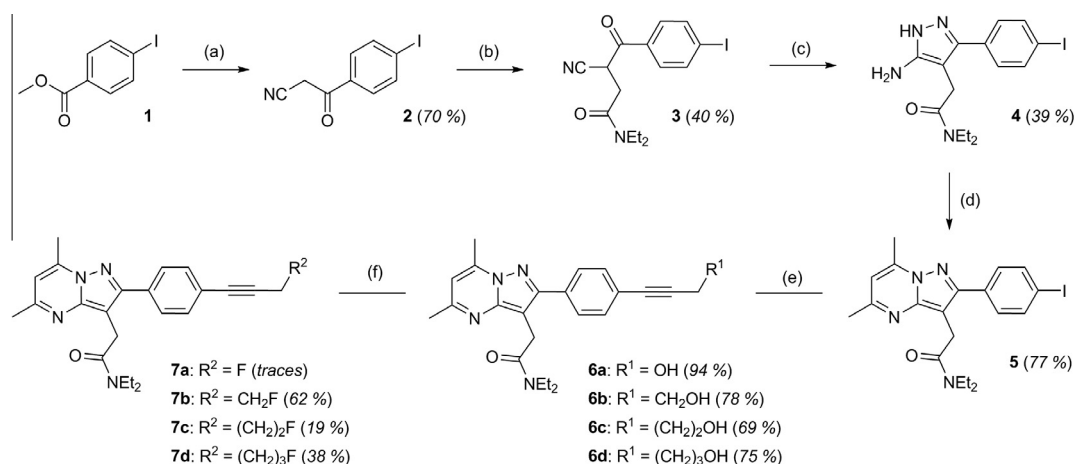
Another class of high affinity TSPO ligands gathers compounds related to the imidazopyridine alpidem³⁶ (Fig. 1). A well-known fluorine-18-labelled example of this class is [¹⁸F]PBR111.^{37,38} Bioisosteric derivatives such as pyrazolopyrimidine acetamides have also been developed to target the TSPO. Within this sub-class, the best known compounds are [¹¹C]DPA-713^{39–45} and [¹⁸F]DPA-714^{42,43,46–59} (Fig. 1), both already in vivo evaluated at the preclinical and clinical stage. Even though [¹⁸F]DPA-714 has a slightly higher lipophilicity than [¹¹C]DPA-713, which could lead to an increased non-specific binding, this radioactive compound allows longer imaging protocols and therefore can be considered as a more suitable radiotracer. The use of radioligands belonging to this class may also facilitate accurate quantitative interpretation of the PET data. Indeed, pyrazolopyrimidine acetamides show a relatively low difference in affinity (~4 fold) between the high- (HABs) and the low- or the mixed-affinity binders (LABs/MABs), when compared to the *N*-benzyl-*N*-(2-phenoxyaryl) acetamides PBR06 (~17 fold) or PBR28 (~50 fold).^{60–62} Thus, the impact of inter-individual variations which are linked to the expression of different TSPO binding sites encoded by the rs6971 polymorphism at the gene level could be reduced, and may not require subject genotyping.

Recent studies clearly demonstrated [¹⁸F]DPA-714 that rapidly and extensively undergoes in vivo metabolism in both rodents (rats) and non-human primates (baboons). In particular, the observed fluoroethoxy side chain cleavage leads to the formation of small radiometabolites entering the brain and lowering PET imaging quality and restraining quantitative analysis.^{63,64} Regarding this metabolic pathway, we intended to improve DPA-714 stability by replacing the oxygen atom bridging the phenyl group and the fluoroethyl motif by a methylene unit. Such a modification gave rise to a new compound named CfO-DPA-714 whose corresponding fluorine-18-labelled version ([¹⁸F]CfO-DPA-714, Fig. 1) has recently been prepared and is currently evaluated in vivo.⁶⁵

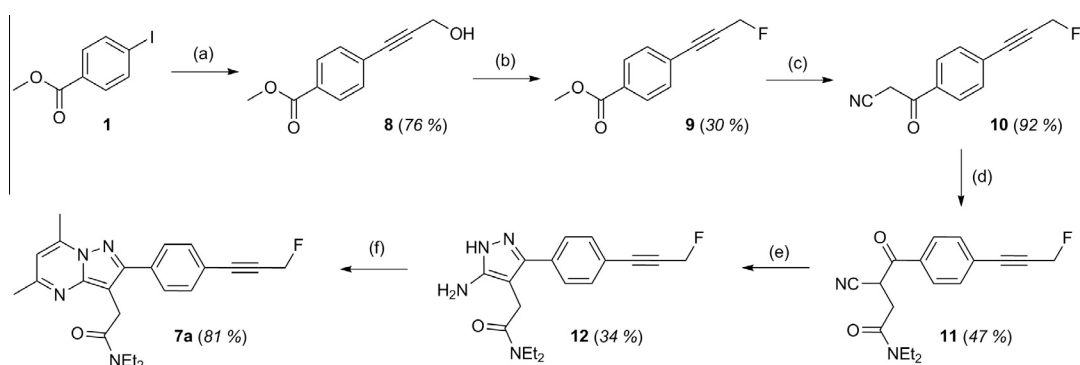
In this article, we report the chemical synthesis (Schemes 1 and 2) of a new subclass of DPA-714 analogues featuring an alkyne triple bond and a short alkane spacer linking the pyrazolopyrimidine scaffold and the fluorine atom (Fig. 1). The series includes four compounds with a side chain ranging from three to six carbon atoms (7a–d). Preliminary evaluation of some of their physical and in vitro biological properties (log *D*_{7.4}, *K*_i against [³H]PK11195 and [³H]flunitrazepam) as well as in vitro metabolism studies for all four compounds are described. In addition, fluorine-18-labelling and first in vivo PET-imaging of one of them is also presented herein.

The synthesis of DPA-714 alkynyl analogues 7a–d was envisaged from the key iodopyrazolopyrimidine 5 using the pathway depicted in Scheme 1.

Thus, the synthesis of compounds 7a–d started with a nucleophilic addition of acetonitrile carbanion on the commercially available methyl 4-iodobenzoate 1, leading to 3-oxopropanenitrile 2 upon the loss of the methoxide moiety. The reaction, initially performed with NaOMe in boiling acetonitrile,³⁹ was improved by using *n*-BuLi as a base at low temperature.⁶⁶ This strategy allowed to decrease ester hydrolysis and resulted in an improved reaction yield of 70% compared to maximum 45% when using NaOMe. The resulting β-ketonitrile 2 was then C-alkylated with *N,N*-diethylchloroacetamide in presence of NaI in ethanolic sodium hydroxide. This reaction usually took a few days to reach completion and resulted in the formation of the expected *N,N*-diethylamide 3 with a modest yield of 40%. In the next step, compound 3 was subjected to a first cyclization using monohydrated hydrazine in refluxing acetic acid to lead to the aminopyrazole 4 which was isolated in a moderate yield of 39%. Finally, reaction of compound 4 with acetylacetone in boiling ethanol for 5 h allowed the pyrazolopyrimidine ring formation in 77% yield, and moreover in a clean and easy way since no side-product formation was observed. While cooling down the reaction mixture, the iodopyrazolopyrimidine 5 often crystallized in a pure form (shiny white solid) that did not require additional purification. In our synthesis strategy, compound 5 was a key intermediate since it could give access to a wide range of fluorinated alkynyl compounds in a straightforward (two steps) and versatile way. To generate the analogues 7a–d, first Sonogashira couplings between 5 and the appropriate alkynyl alcohols were carried out to give the alkynols 6a–d in good to excellent yields (69–94%). Then, compounds 6a–d were submitted to fluoro-deoxygenation using Deoxofluor[®] in methylene chloride to yield



Scheme 1. Synthesis of the DPA-714 alkynyl analogues **7a–d**. Reagents and conditions: (a) *n*-BuLi, CH₃CN, THF, 30 min, –65 °C then methyl 4-iodobenzoate (**1**), 2 h, –65 °C to –45 °C; (b) NaOH, EtOH, 15 min then ClCH₂C(O)NEt₂, NaI, 4 days, rt; (c) N₂H₄·H₂O, AcOH, EtOH, 5–8 h, 80 °C; (d) acetylacetone, EtOH, 5 h, 80 °C; (e) alkynyl alcohol, CuI, Pd(PPh₃)₂Cl₂, Et₂NH, 24 h, rt; (f) Deoxofluor[®], CH₂Cl₂, 2–4 days, rt.



Scheme 2. Synthesis of the DPA-714 alkynyl analogue **7a**. Reagents and conditions: (a) 2-propyn-1-ol, CuI, Pd(PPh₃)₂Cl₂, Et₂NH, 24 h, rt; (b) deoxofluor[®], CH₂Cl₂, 2 days, rt; (c) *n*-BuLi, CH₃CN, THF, 30 min, –60 °C then compound **9**, 2 h, –60 °C; (d) NaOH, EtOH, 15 min then ClCH₂C(O)NEt₂, NaI, 4 days, rt; (e) N₂H₄·H₂O, AcOH, EtOH, 5 h, 80 °C; (f) acetylacetone, EtOH, 8 h, 80 °C.

7b–d with variable efficiency (19–62%). Typically, the reaction mixture was worked up after 48 h. For analogue **7b**, it is important not to run the reaction for too long otherwise a side-product involving allene formation is produced.

Finally, analogues **7b–d** were produced in six steps with chemical purities higher than 95% (¹H NMR). Their structures were confirmed by ¹H NMR, ¹³C NMR and MS (Table 1).⁶⁷

Regarding the analogue **7a**, since the fluorodeoxygenation turned out to be only partially successful when applied to alcohol **6a**, a different pathway was considered (Scheme 2). For the preparation of this compound (**7a**), the major improvement was made by performing the fluorination at the very beginning of the synthesis as depicted below (Scheme 2).

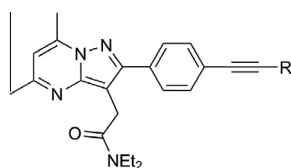
Thus, starting with the iodoester **1**, a Sonogashira coupling using 2-propyn-1-ol was first carried out to yield the propargyl alcohol **8** in 76% yield. Then, **8** was submitted to fluorodeoxygenation using Deoxofluor[®] at room temperature in methylene chloride. Although this reaction was not clean (several by-products were observed on TLC), the fluoroester **9** was successfully isolated with a good purity in 30% yield. The oxopropanenitrile **10** was then obtained in good to excellent yields (92%) using similar conditions to those previously described. Analogously, C-alkylation with *N*, *N*-diethylchloroacetamide gave the amide **11** in a moderate 47% yield. Cyclisation with hydrazine led to the aminopyrazole **12** in a moderate yield of 34%, and was further converted to the pyrazolopyrimidine **7a** (81% yield). Finally, the target fluoropropynyl

compound **7a** was also obtained in six steps with a high purity and its structure was confirmed by ¹H NMR, ¹³C NMR and MS (Table 1).⁶⁷

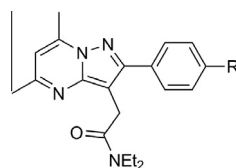
The log_{D7.4} (*n*-octanol/buffer pH 7.4 partition coefficient) of compounds **7a–d** were evaluated on the basis of their HPLC retention times⁶⁸ and were also calculated using the ACD 11.0 software (Table 2). As expected, both measured and calculated log_{D7.4} values were higher than those calculated for DPA-714, and increased as the fluorinated side chain R lengthened. Additionally, while analogues **7a** and **7b** exhibited comparable experimental log_{D7.4} values, 3.61 and 3.67 respectively, **7c** and **7d** were found to be significantly more lipophilic with values slightly above 4.0.

The in vitro binding affinities of compounds **7a–d** for the TSPO 18 kDa were determined by competition with [³H]PK11195 using membrane homogenates from rat heart. All four analogues exhibited high affinities for the protein with subnanomolar K_i values—all lower than the one measured for DPA-714 in the same assays—ranging from 0.35 nM (**7c**) to 0.79 nM (**7d**), as well as high specificity since no affinity for the central benzodiazepine receptor (CBR) was observed (Table 2).

The metabolism of the four novel DPA-714 fluoroalkynyl analogues (**7a–d**) was also studied in vitro in rat liver microsomes.⁶⁴ Liquid chromatography–mass spectrometry (LC–MS and MS–MS) analyses, after 30 minutes of incubation, allowed the detection of the main metabolites formed for each analogue. The formation of two to four metabolites (M1–M4) was observed as summarized

Table 1
Analytical characterization (MS, ¹H NMR and ¹³C NMR data) of DPA-714 fluoroalkynyl analogues **7a–d**

Compd	R	MW	m/z ^{a,b}	Fluoroalkynyl side chain ¹ H NMR chemical shifts (δ, ppm, CDCl ₃) ^{c,d}	Fluoroalkynyl side chain ¹³ C NMR chemical shifts (δ, ppm, CDCl ₃) ^{c,d}
7a	CH ₂ -F	392	393	5.20 (d, 2H, <i>J</i> _{HF} ² = 47.6 Hz)	89.5 [d, <i>J</i> _{CF} ³ = 12 Hz, C], 83.2 [d, <i>J</i> _{CF} ² = 22 Hz, C], 71.1 [d, <i>J</i> _{CF} ¹ = 164 Hz, CH ₂]
7b	(CH ₂) ₂ -F	406	407	4.60 (dt, 2H, <i>J</i> _{HF} ² = 46.8 Hz, <i>J</i> _{HH} ³ = 6.8 Hz), 2.86 (dt, 2H, <i>J</i> _{HF} ² = 19.2 Hz, <i>J</i> _{HH} ³ = 6.8 Hz)	89.4 [C], 85.1 [C], 81.3 [d, <i>J</i> _{CF} ¹ = 171 Hz, CH ₂], 21.6 [d, <i>J</i> _{CF} ² = 24 Hz, CH ₂]
7c	(CH ₂) ₃ -F	420	421	4.62 (dt, 2H, <i>J</i> _{HF} ² = 47.2 Hz, <i>J</i> _{HH} ³ = 6.0 Hz), 2.59 (t, 2H, <i>J</i> = 7.2 Hz), 2.01 (dq ⁵ , 2H, <i>J</i> _{HF} ² = 25.6 Hz, <i>J</i> _{HH} ³ = 6.0 Hz)	89.3 [C], 82.5 [d, <i>J</i> _{CF} ¹ = 164 Hz, CH ₂], 81.2 [C], 29.5 [d, <i>J</i> _{CF} ² = 20 Hz, CH ₂], 15.4 [d, <i>J</i> _{CF} ³ = 4 Hz, CH ₂]
7d	(CH ₂) ₄ -F	434	435	4.52 (dt, 2H, <i>J</i> _{HF} ² = 47.2 Hz, <i>J</i> _{HH} ³ = 6.0 Hz), 2.50 (t, 2H, <i>J</i> = 7.2 Hz), 1.89 (m, 2H), 1.75 (q ⁵ , 2H, <i>J</i> = 7.2 Hz)	90.3 [C], 83.6 [d, <i>J</i> _{CF} ¹ = 164 Hz, CH ₂], 81.1 [C], 29.5 [d, <i>J</i> _{CF} ² = 20 Hz, CH ₂], 24.4 [d, <i>J</i> _{CF} ³ = 5 Hz, CH ₂], 19.1 [CH ₂]

^a ESI+ ionization.^b Value corresponding to the [M+H]⁺ peak.^c Recorded on a 400 MHz Bruker avance.^d See note⁶⁷ in the 'references and notes' section for a complete NMR description of compounds **7a–d**.**Table 2**
Lipophilicities and binding affinities of the DPA-714 fluoroalkynyl analogues **7a–d**

Compd	R	HPLC t _R (min) ^a	Log D _{7.4} ^b	cLog D _{7.4} ^c	K _i (TSPO) ^d (nM)	K _i (CBR) ^e (nM)
DPA-714	O-(CH ₂) ₂ -F	1.10	2.89	3.21	0.91	>1000
7a	C≡C-CH ₂ -F	1.19	3.61	3.81	0.54	>1000
7b	C≡C-(CH ₂) ₂ -F	1.20	3.67	4.19	0.74	>1000
7c	C≡C-(CH ₂) ₃ -F	1.30	4.06	4.58	0.35	>1000
7d	C≡C-(CH ₂) ₄ -F	1.33	4.35	5.03	0.79	>1000

^a HPLC conditions: UPLC/SQD Acquity BEH C18 column, 2.1 × 50 mm, 1.7 μm, mobile phase: H₂O (A)/CH₃CN + 0.1% formic acid (B), gradient: 2–100% (B) in 3 min, 1.0 mL/min.^b See note⁶⁸ in the 'references and notes' section for description of the log D_{7.4} determination method using HPLC.^c Calculated with ACD 11.0 software.^d K_i values were determined using membrane homogenates from rat heart and screened against [³H]PK11195 (K_d = 1.8 nM, C = 0.2 nM).^e K_i values were determined using membrane homogenates from rat cerebral cortex and screened against [³H]flunitrazepam (K_d = 2.1 nM, C = 0.4 nM).

in **Table 3**. For all four analogues **7a–d**, no metabolites resulting from the loss of the fluorine atom by cleavage of the fluoroalkynyl side chain was observed by LC–MS. The predominant metabolites, detected by HPLC at 275 nm and characterised by ESI–MS–MS analyses according to their fragmentation profiles, resulted from N-deethylation (M1, –28 Da) at the diethylacetamide position and also from hydroxylation (M2 and M3, +16 Da) or dihydroxylation (M4, +32 Da) most probably on the methyl groups of the pyrazolo-pyrimidine part of the molecule as already observed for DPA-714.⁶⁴

The fluoropentynyl analogue **7c** (coded DPA-C5yne), displaying the highest TSPO binding affinity and a favourable in vitro metabolic profile, was chosen for radiofluorination^{69,70} and first in vivo evaluation as potential PET imaging tool. Indeed, despite the good in vitro profile of the fluoropropynyl analogue **7a** that features an improved TSPO affinity in comparison to DPA-714, a better lipophilicity value than **7c** and only two main in vitro

metabolites after 30 min microsomal incubation, compound **7c** was preferred based on (i) the difficulties encountered to generate the corresponding precursor for labelling (tosyloxy derivative of **6a**) and (ii) our past experience with compounds bearing comparable motif, e.g. the predicted issues to get efficient radiolabelling.

Thus, the tosylate **13** was prepared from the alkynol **6c** by treatment with *p*-toluenesulfonic anhydride in dichloromethane in the presence of TEA at room temperature for 2–3 days, and obtained in 54% yield. Fluorine-18-labelling was then performed in a single-step procedure by nucleophilic aliphatic substitution using the activated K[¹⁸F]F-Kryptofix K₂₂₂ complex as the fluorinating reactant, in DMSO and heating at 100 °C for 10 min⁷¹ on a TRACER-Lab FX N Pro synthesizer (GEMS). Ready-to-inject [¹⁸F]-**7c** (>99% chemically and radiochemically pure, 55–110 GBq/μmol) was obtained in 20–25% decay-corrected yields (based on starting [¹⁸F]fluoride) and within 50–60 min, semi-preparative HPLC purification and SepPak® Plus-based formulation included (**Scheme 3**).

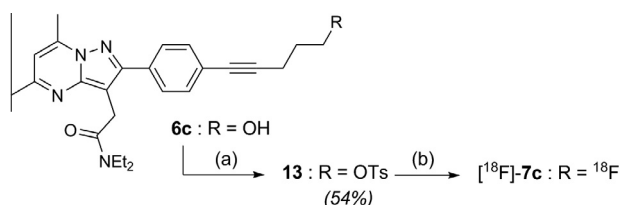
Table 3
Microsomal metabolites of the DPA-714 fluoroalkynyl analogues **7a–d** (LC–MS and MS–MS analyses)

 7a (m/z 392)				 7b (m/z 406)			
Compds	t_R^a (min)	[M+H] ⁺	Fragments ^b	t_R^a (min)	[M+H] ⁺	Fragments ^b	
Parent	15.66	393	375, 346, 320, 292	15.81	407	389, 360, 334, 306	
M1	11.41	365 (–28)	347, 320, 292	11.68	379 (–28)	361, 334, 306	
M2	11.0	409 (+16)	391, 362, 336, 308	11.19	423 (+16)	405, 376, 350, 322	
M3	–	–	–	10.01	423 (+16)	405, 376, 350, 322	
M4	–	–	–	5.89	439 (+32)	421, 392, 366, 338	

 7c (m/z 420)				 7d (m/z 434)			
Compds	t_R^a (min)	[M+H] ⁺	Fragments ^b	t_R^a (min)	[M+H] ⁺	Fragments ^b	
Parent	17.05	421	403, 348, 320	15.81	435	417, 362, 334	
M1	12.08	393 (–28)	375, 348, 320	11.68	407 (–28)	362, 334, 306	
M2	11.37	437 (+16)	419, 364, 336	11.19	451 (+16)	433, 404, 378, 350	
M3	8.92	437 (+16)	419, 364, 336	10.01	451 (+16)	433, 404, 378, 350	
M4	3.43	453 (+32)	435, 380, 353	5.89	467 (+32)	449, 420, 394, 366	

^a HPLC conditions: Atlantis C18 column, 2.1 × 150 mm, 5 μm, mobile phase: H₂O + 0.05% formic acid (A)/CH₃CN + 0.05% formic acid (B), gradient (A/B): 60:40–20:80 (20 min), 200 μL/min, detection at 275 nm.

^b See Ref. 64 in the 'references and notes' section for a complete description of the materials and methods used for ESI–MS–MS analyses.



Scheme 3. Synthesis of the labelling precursor **13** and radioligand [¹⁸F]-**7c**. Reagents and conditions: (a) Ts₂O, CH₂Cl₂, TEA, rt, 3 h; (b) (i) K[¹⁸F]F-K₂₂₂, K₂CO₃, DMSO, 100 °C, 10 min, (ii) cartridge purification (SepPak® Alumina N™), (iii) HPLC purification (Waters Symmetry® C-18).

First imaging properties of [¹⁸F]DPA-C5yne ([¹⁸F]-**7c**) were investigated in vivo with PET (INVEON PET/CT and PET only tomographs, Siemens) and compared to [¹⁸F]DPA-714 on our in-house-developed rat model of acute local neuroinflammation. MicroPET studies were performed on anesthetized brain-lesioned Wistar rats 7 days after AMPA injection in their right striatum.⁴³ As shown in Figure 2A, the lesion (indicated by the white cross-cursor) could clearly be identified within the rat's brain from 5 minutes post-iv-injection of [¹⁸F]-**7c** until the end of the PET acquisition. A relatively high contrast between the lesioned area and the corresponding area in the intact contralateral hemisphere was also observed. Uptake of [¹⁸F]-**7c** in the lesioned striatum was high (0.24 percent of injected dose per milliliter (% ID/mL) at 60 min, Fig. 2B) but slightly lower than the one routinely observed for [¹⁸F]DPA-714 (0.30% ID/mL, same time). Uptake of [¹⁸F]-**7c** in the contralateral side was also significantly lower

(0.05% ID/mL at 60 min) than the one reported for [¹⁸F]DPA-714 (0.08% ID/mL at 60 min, respectively). Thus, an in vivo ipsilateral-to-contralateral ratio of 4.62 ± 0.4 (*p* < 0.0001), calculated as the bound tracer in the lesion versus the bound tracer in the contralateral side at 60 min post-injection, was found for [¹⁸F]-**7c**, a notably higher value than the one measured for [¹⁸F]DPA-714 (3.71 ± 0.4 (*p* < 0.001) or [¹¹C]PK11195 (1.65 ± 0.2 (*p* < 0.001), data not shown).

Four novel closely related analogues of DPA-714 (**7a–d**) featuring a fluoroalkynyl side chain in replacement of the fluoroethoxy motif, have been synthesized in six steps from commercially available methyl 4-iodobenzoate. All target derivatives showed a high affinity and specificity toward the TSPO 18 kDa (as the parent molecule DPA-714). These compounds (**7a–d**) exhibited rather high lipophilicities compared to DPA-714, which nevertheless, keeps in the range favored for good passive cerebral penetration. Preliminary in vitro metabolism evaluation using rat microsomal incubations and LC–MS analyses have confirmed, for all derivatives, the stability of the chosen fluorination position, that is the alkynyl side chain. This results portend, in contrast to [¹⁸F]DPA-714, the absence in vivo of small interfering radiofluorinated metabolites formation. Among the four analogues prepared, the fluoropentynyl compound **7c** was successfully labelled with fluorine-18 and its subsequent first PET in vivo evaluation has demonstrated its potential to image the TSPO 18 kDa. Additional studies, including in vivo metabolism analysis, in acute and chronic models of neurodegeneration will be performed in order to further evaluate the potential of this radioligand as a biomarker of neuroinflammation in neuropathological conditions.

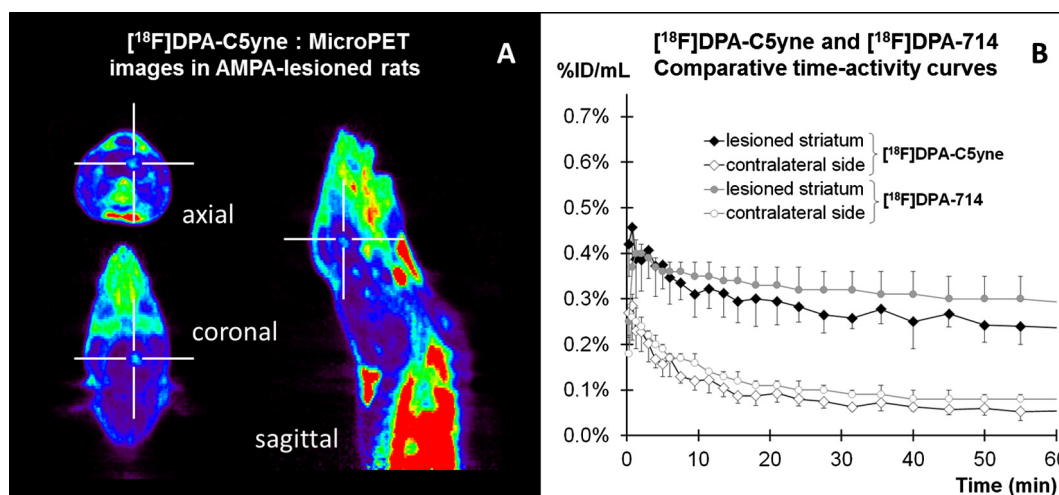


Figure 2. (A) MicroPET axial, coronal and sagittal summed images (5–60 min) following iv injection of [^{18}F]DPA-C5yne ([^{18}F]7c) in AMPA-lesioned rat. A cross-cursor indicates in each section the visible right-side lesion. (B) Comparative time-activity curves expressed in between [^{18}F]DPA-C5yne ([^{18}F]7c) and [^{18}F]DPA-714. Data are expressed in percent of injected dose per milliliter (% ID/mL) versus minutes (min).

Acknowledgments

The authors wish to thank LGCR Analytical Sciences (Sanofi, Chilly Mazarin) for logD measurements, Cyrielle Letaillandier for her technical assistance as well as Dr. Dirk Roeda for proof reading the manuscript and suggesting linguistic corrections. This work was supported by CEA- ^{12}C intramural programs, as well as the European Union's Seventh Framework Programme [FP7/2007–2013] INMiND (Grant agreement n° HEALTH-F2-2011-278850). PhD students Vincent Médran-Navarrete and Nicholas Bernards were in part supported by a CEA Irtelis doctoral grant and the EU FP7 INMiND program (see above), respectively.

References and notes

- Beurdeley-Thomas, A.; Miccoli, L.; Oudard, S.; Dutrillaux, B.; Poupon, M. F. *J. Neurooncol.* **2000**, *46*, 45.
- Joseph-Liauzun, E.; Delmas, P.; Shire, D.; Ferrara, P. *J. Biol. Chem.* **1998**, *273*, 2146.
- Papadopoulos, V.; Baraldi, M.; Guilarte, T. R.; Knudsen, T. B.; Lacapere, J.-J.; Lindemann, P.; Norenberg, M. D.; Nutt, D.; Weizman, A.; Zhang, M.-R.; Gavish, M. *Trends Pharmacol. Sci.* **2006**, *27*, 402.
- Casellas, P.; Galiegue, S.; Basile, A. S. *Neurochem. Int.* **2002**, *40*, 475.
- Papadopoulos, V.; Brown, A. S. *J. Steroid Biochem. Mol. Biol.* **1995**, *53*, 103.
- Gavish, M.; Bachman, I.; Shoukrun, R.; Katz, Y.; Veenman, L.; Weisinger, G.; Weizman, A. *Pharmacol. Rev.* **1999**, *51*, 629.
- Bourguignon, J. J. In *Endogenous and Synthetic Ligands of Mitochondrial Benzodiazepine Receptors: Structure-Affinity Relationships, Peripheral Benzodiazepine Receptors*; Giensen-Crouse, E., Ed.; Academic Press: London, 1993; pp 59–85.
- Kettenmann, H.; Burton, G. A.; Moening, U. J. In *Neuroinflammation—from Bench to Bedside*; Ernst Schering Research Foundation, Ed.; Springer: Berlin, Heidelberg, 2002; pp 1–234.
- Raghavendra Rao, V. L.; Dogan, A.; Bowen, K. K.; Dempsey, R. *J. Exp. Neurol.* **2000**, *161*, 102.
- Rupprecht, R.; Papadopoulos, V.; Rammes, G.; Baghai, T. C.; Fan, J.; Akula, N.; Groyer, G.; Adams, D.; Schumacher, M. *Nat. Rev. Drug Disc.* **2010**, *9*, 971.
- Camsonne, R.; Crouzel, C.; Comar, D.; Mazière, M.; Prenant, C.; Sastre, J.; Moulin, M. A.; Syrota, A. *J. Labelled Compd. Radiopharm.* **1984**, *21*, 985.
- Banati, R. B.; Newcombe, J.; Gunn, R. N.; Cagnin, A.; Turkheimer, F.; Heppner, F.; Price, G.; Wegner, F.; Giovannoni, G.; Miller, D. H.; Perkin, D. G.; Smith, T.; Hewson, A. K.; Bydder, G.; Kreutzberg, G. W.; Jones, T.; Cuzner, M. L.; Myers, R. *Brain* **2000**, *123*, 2321.
- Chauveau, F.; Boutin, H.; Van Camp, N.; Dollé, F.; Tavitian, B. *Eur. J. Nucl. Med. Mol. Imaging* **2008**, *35*, 2304.
- Dollé, F.; Luus, C.; Reynolds, A.; Kassiou, M. *Curr. Med. Chem.* **2009**, *16*, 2899.
- Luus, C.; Hanani, R.; Reynolds, A.; Kassiou, M. *J. Labelled Compd. Radiopharm.* **2010**, *53*, 501.
- Scarf, A. M.; Kassiou, M. *J. Nucl. Med.* **2011**, *52*, 677.
- Roeda, D.; Kuhnast, B.; Damont, A.; Dollé, F. *J. Fluorine Chem.* **2012**, *134*, 107.
- Ching, A. S. C.; Kuhnast, B.; Damont, A.; Roeda, D.; Tavitian, B.; Dollé, F. *Insights Imaging* **2012**, *3*, 111.
- Maeda, J.; Sahara, T.; Zhang, M. R.; Okauki, T.; Yasuno, F.; Ikoma, Y.; Inaji, M.; Nagai, Y.; Takano, A.; Obayashi, S.; Suzuki, K. *Synapse* **2004**, *52*, 283.
- Chaki, S.; Funakoshi, T.; Yoshikawa, R.; Okuyama, S.; Okubo, T.; Nakazato, A.; Nagamine, M.; Tomisawa, K. *Eur. J. Pharmacol.* **1999**, *371*, 197.
- Zhang, M. R.; Kida, T.; Noguchi, J.; Furutsuka, K.; Maeda, J.; Sahara, T.; Suzuki, K. *Nucl. Med. Biol.* **2003**, *30*, 513.
- Fujimura, Y.; Ikoma, Y.; Yasuno, F.; Sahara, T.; Ota, M.; Matsumoto, R.; Nozaki, S.; Takano, A.; Kosaka, J.; Zhang, M. R.; Nakao, R.; Suzuki, K.; Kato, N.; Ito, H. *J. Nucl. Med.* **2006**, *47*, 43.
- Zhang, M. R.; Maeda, J.; Ogawa, M.; Noguchi, J.; Ito, T.; Yoshida, Y.; Okauchi, T.; Obayashi, S.; Sahara, T.; Suzuki, K. *J. Med. Chem.* **2004**, *47*, 228.
- Briard, E.; Shah, J.; Musachio, J. L.; Zoghbi, S. S.; Fujita, M.; Imaizumi, M.; Cropley, V.; Innis, R. B.; Pike, V. W. *J. Labelled Compd. Radiopharm.* **2005**, *48*, S4.
- Briard, E.; Zoghbi, S. S.; Simeon, F. G.; Imaizumi, M.; Gourley, J. P.; Shetty, H. U.; Lu, S. Y.; Fujita, M.; Innis, R. B.; Pike, V. W. *J. Med. Chem.* **2009**, *52*, 688.
- Briard, E.; Hong, J.; Musachio, J. L.; Zoghbi, S. S.; Fujita, M.; Imaizumi, M.; Cropley, V.; Innis, R. B.; Pike, V. W. *J. Labelled Compd. Radiopharm.* **2005**, *48*, S71.
- Imaizumi, M.; Kim, H.-J.; Zoghbi, S. S.; Briard, E.; Hong, J.; Musachio, J. L.; Ruetzler, C.; Chuang, D. M.; Pike, V. W.; Innis, R. B.; Fujita, M. *Neurosci. Lett.* **2007**, *411*, 200.
- Brown, A. K.; Fujita, M.; Fujimura, Y.; Liow, J.-S.; Stabin, M.; Ryu, Y. H.; Imaizumi, M.; Hong, J.; Pike, V. W.; Innis, R. B. *J. Nucl. Med.* **2007**, *48*, 2072.
- Briard, E.; Zoghbi, S. S.; Imaizumi, M.; Gourley, J. P.; Hong, J.; Fujimura, Y.; Pike, V. W.; Innis, R. B.; Fujita, M. *NeuroImage* **2008**, *39*, 1289.
- Fujita, M.; Imaizumi, M.; Zoghbi, S. S.; Fujimura, Y.; Farris, A. G.; Sahara, T.; Hong, J.; Pike, V. W.; Innis, R. B. *NeuroImage* **2008**, *40*, 43.
- Kreisl, W. C.; Fujita, M.; Fujimura, Y.; Kimura, N.; Jenko, K. J.; Kannan, P.; Hong, J.; Morse, C. L.; Zoghbi, S. S.; Gladding, R. L.; Jacobson, S.; Oh, U.; Pike, V. W.; Innis, R. B. *NeuroImage* **2010**, *49*, 2924.
- Damont, A.; Boisgard, R.; Kuhnast, B.; Lemée, F.; Raggiri, G.; Scarf, A. M.; Da Pozzo, E.; Selli, S.; Martini, C.; Tavitian, B.; Kassiou, M.; Dollé, F. *Bioorg. Med. Chem. Lett.* **2011**, *21*, 4819.
- Wilson, A. A.; Garcia, A.; Parkes, J.; McCormick, P.; Stephenson, K. A.; Houle, S.; Vasdev, N. *Nucl. Med. Biol.* **2008**, *35*, 305.
- Mizrahi, R.; Rusjan, P. M.; Vitcu, I.; Ng, A.; Wilson, A. A.; Houle, S.; Bloomfield, P. M. *Mol. Imag. Biol.* **2013**, *15*, 353.
- Selli, S.; Bruni, F.; Costagli, C.; Costanzo, A.; Guerrini, G.; Ciciani, G.; Costa, B.; Martini, C. *Bioorg. Med. Chem.* **2001**, *9*, 2661.
- Fookes, C. J. R.; Pham, T. Q.; Mattner, F.; Gregoric, I.; Loc'h, C.; Liu, X.; Berghofer, P.; Shepherd, R.; Grégoire, M.-C.; Katsifis, A. *J. Med. Chem.* **2008**, *51*, 3700.
- Dollé, F.; Hinnen, F.; Damont, A.; Kuhnast, B.; Fookes, C.; Pham, T.; Tavitian, B.; Katsifis, A. *J. Labelled Compd. Radiopharm.* **2008**, *51*, 435.
- James, M. L.; Fulton, R. R.; Henderson, D. J.; Eberl, S.; Meikle, S. R.; Thomson, R.; Allan, D.; Dollé, F.; Fulhama, M. J.; Kassiou, M. *Bioorg. Med. Chem.* **2005**, *13*, 6188.
- Thominiaux, C.; Dollé, F.; James, M.; Bramoullé, Y.; Boutin, H.; Besret, L.; Grégoire, M.-C.; Valette, H.; Bottlaender, M.; Tavitian, B.; Hantraye, P.; Selli, S.; Kassiou, M. *Appl. Radiat. Isot.* **2006**, *64*, 570.
- Boutin, H.; Chauveau, F.; Thominiaux, C.; Kuhnast, B.; Grégoire, M.-C.; James, M.; Jan, S.; Brulon, V.; Fontyn, Y.; Selli, S.; Trébassen, R.; Hantraye, P.; Dollé, F.; Tavitian, B.; Kassiou, M. *J. Nucl. Med.* **2007**, *48*, 573.

42. Doorduyn, J.; Klein, H. C.; Dierckx, R. A.; James, M.; Kassiou, M.; de Vries, E. F. *J. Mol. Imag. Biol.* **2009**, *11*, 386.
43. Chauveau, F.; Van Camp, N.; Dollé, F.; Kuhnast, B.; Hinnen, F.; Damont, A.; Boutin, H.; James, M. L.; Kassiou, M.; Tavitian, B. *J. Nucl. Med.* **2009**, *50*, 468.
44. Leaver, K. R.; Reynolds, A.; Bodard, S.; Guilloteau, D.; Chalon, S.; Kassiou, M. *ACS Chem. Neurosci.* **2012**, *3*, 114.
45. Endres, C. J.; Coughlin, J. M.; Gage, K. L.; Watkins, C. C.; Kassiou, M.; Pomper, M. G. *J. Nucl. Med.* **2012**, *53*, 330.
46. James, M. L.; Fulton, R. R.; Vercoullie, J.; Henderson, D. J.; Garreau, L.; Chalon, S.; Dollé, F.; Costa, B.; Guilloteau, D.; Kassiou, M. *J. Nucl. Med.* **2008**, *49*, 814.
47. Damont, A.; Hinnen, F.; Kuhnast, B.; Schollhorn-Peyronneau, M. A.; James, M. L.; Luus, C.; Tavitian, B.; Kassiou, M.; Dollé, F. *J. Labelled Compd. Radiopharm.* **2008**, *51*, 286.
48. Fookes, C.; Pham, T.; Mattner, F.; Greguric, I.; Loc'h, C.; Liu, X.; Berghofer, P.; Shepherd, R.; Grégoire, M. C.; Katsifis, A. *J. Med. Chem.* **2008**, *51*, 3700.
49. Martin, A.; Boisgard, R.; Theze, B.; Van Camp, N.; Kuhnast, B.; Damont, A.; Kassiou, M.; Dollé, F.; Tavitian, B. *J. Cereb. Blood Flow Metab.* **2010**, *30*, 230.
50. Martin, A.; Boisgard, R.; Kassiou, M.; Dollé, F.; Tavitian, B. *Mol. Imag. Biol.* **2011**, *13*, 10.
51. Zheng, J.; Boisgard, R.; Siquier-Pernet, K.; Decaudin, D.; Dollé, F.; Tavitian, B. *Mol. Pharm.* **2011**, *8*, 823.
52. Winkeler, A.; Boisgard, R.; Awde, A. R.; Dubois, A.; Thézé, B.; Zheng, J.; Ciobanu, L.; Dollé, F.; Viel, T.; Jacobs, A. H.; Tavitian, B. *Eur. J. Nucl. Med. Mol. Imaging* **2012**, *39*, 811.
53. Tang, D.; Hight, M. R.; McKinley, E. T.; Fu, A.; Buck, J. R.; Smith, R. A.; Tantawy, M. N.; Peterson, T. E.; Colvin, D. C.; Ansari, M. S.; Nickels, M.; Manning, H. C. *J. Nucl. Med.* **2012**, *53*, 287.
54. Arlicot, N.; Vercoullie, J.; Ribeiro, M. J.; Tauber, C.; Venel, Y.; Baulieu, J. L.; Maia, S.; Corcia, P.; Stabin, M. G.; Reynolds, A.; Kassiou, M.; Guilloteau, D. *Nucl. Med. Biol.* **2012**, *39*, 570.
55. Abourbeh, G.; Thézé, B.; Maroy, R.; Dubois, A.; Brulon, V.; Fontyn, F.; Dollé, F.; Tavitian, B.; Boisgard, R. *J. Neurosci.* **2012**, *32*, 5728.
56. Lavis, S.; Guillermier, M.; Hérard, A. S.; Petit, F.; Delahaye, M.; Van Camp, N.; Ben Haim, L.; Lebon, V.; Remy, P.; Dollé, F.; Delzescaux, T.; Bonvento, G.; Hantraye, P.; Escartin, C. *J. Neurosci.* **2012**, *32*, 10809.
57. Kuhnast, B.; Damont, A.; Hinnen, F.; Catarina, T.; Dempfel, S.; Le Helleix, S.; Coulon, C.; Goutal, S.; Gervais, P.; Dollé, F. *Appl. Radiat. Isot.* **2012**, *70*, 489.
58. Corcia, P.; Tauber, C.; Vercoullie, J.; Arlicot, N.; Prunier, C.; Praline, J.; Nicolas, G.; Venel, Y.; Hommet, C.; Baulieu, J. L.; Cottier, J. P.; Roussel, C.; Kassiou, M.; Guilloteau, D.; Ribeiro, M. J. *PLoS ONE* **2012**, *7*, e52941.
59. Boutin, H.; Prenant, C.; Maroy, R.; Galea, J.; Greenhalgh, A. D.; Smigova, A.; Cawthorne, C.; Julian, P.; Wilkinson, S. M.; Banister, S. D.; Brown, G.; Herholz, K.; Kassiou, M.; Rothwell, N. J. *PLoS ONE* **2013**, *8*, e56441.
60. Owen, D. R.; Howell, O. W.; Tang, S. P.; Wells, L. A.; Bennacef, I.; Bergström, M.; Gunn, R. N.; Rabiner, E. A.; Wilkins, M. R.; Reynolds, R.; Matthews, P. M.; Parker, C. A. *J. Cereb. Blood Flow Metab.* **2010**, *30*, 1608.
61. Owen, D. R.; Gunn, R. N.; Rabiner, E. A.; Bennacef, I.; Fujita, M.; Kreisl, W. C.; Innis, R. B.; Pike, V. W.; Reynolds, R.; Matthews, P. M.; Parker, C. A. *J. Nucl. Med.* **2011**, *52*, 24.
62. Owen, D. R.; Yeo, A. J.; Gunn, R. N.; Song, K.; Wadsworth, G.; Lewis, A.; Rhodes, C.; Pulford, D. J.; Bennacef, I.; Parker, C. A.; StJean, P. L.; Cardon, L. R.; Mooser, V. E.; Matthews, P. M.; Rabiner, E. A.; Rubio, J. P. *J. Cereb. Blood Flow Metab.* **2012**, *32*, 1.
63. Peyronneau, M. A.; Damont, A.; Valette, H.; Saba, W.; Delforge, J.; Goutal, S.; Bourgeois, S.; Hinnen, F.; Dollé, F.; Bottlaender, M. *J. Labelled Compd. Radiopharm.* **2009**, *52*, S385.
64. Peyronneau, M. A.; Saba, W.; Goutal, S.; Damont, A.; Dollé, F.; Kassiou, M.; Bottlaender, M.; Valette, H. *Drug Metab. Dispos.* **2013**, *41*, 122.
65. Damont, A.; Ching, A. S. C.; Médran-Navarrete, V.; Kuhnast, B.; Gaudy, H.; Dollé, F. *J. Labelled Compd. Radiopharm.* **2011**, *54*, S461.
66. Fernandez, M.-C.; Castaño, A.; Dominguez, E.; Escribano, A.; Jiang, D.; Jimenez, A.; Hong, E.; Hornback, W. J.; Nisenbaum, E. S.; Rankl, N.; Tromiczak, E.; Vaught, G.; Zarrinmayeh, H.; Zimmerman, D. M. *Bioorg. Med. Chem. Lett.* **2006**, *16*, 5057.
67. **Spectroscopic data:** Compound **7a**: $^1\text{H NMR}$ (CDCl_3): δ 7.83 (d, 2H, $J = 8.0$ Hz), 7.55 (d, 2H, $J = 8.0$ Hz), 6.55 (s, 1H), 5.20 (d, 2H, $J_{\text{HF}}^2 = 47.6$ Hz), 3.95 (s, 2H), 3.52 (q, 2H, $J = 7.2$ Hz), 3.40 (q, 2H, $J = 7.2$ Hz), 2.75 (s, 3H), 2.56 (s, 3H), 1.23 (t, 3H, $J = 7.2$ Hz), 1.11 (t, 3H, $J = 7.2$ Hz). $^{13}\text{C NMR}$ (CDCl_3): δ 169.7 [C], 157.7 [C], 154.2 [C], 147.5 [C], 145.0 [C], 134.4 [C], 131.9 [2 \times CH], 128.5 [2 \times CH], 121.5 [d, $J_{\text{CF}}^4 = 4$ Hz, C], 108.5 [CH], 101.4 [C], 89.5 [d, $J_{\text{CF}}^2 = 12$ Hz, C], 83.2 [d, $J_{\text{CF}}^2 = 22$ Hz, C], 71.1 [d, $J_{\text{CF}}^1 = 164$ Hz, CH_2], 42.3 [CH₂], 40.6 [CH₂], 27.9 [CH₂], 24.4 [CH₃], 16.8 [CH₃], 14.3 [CH₃], 13.0 [CH₃]. Compound **7b**: $^1\text{H NMR}$ (CDCl_3): δ 7.77 (d, 2H, $J = 8.0$ Hz), 7.48 (d, 2H, $J = 8.0$ Hz), 6.52 (s, 1H), 4.60 (dt, 2H, $J_{\text{HF}}^2 = 46.8$ Hz, $J_{\text{HH}}^3 = 6.8$ Hz), 3.94 (s, 2H), 3.50 (q, 2H, $J = 7.2$ Hz), 3.40 (q, 2H, $J = 7.2$ Hz), 2.86 (dt, 2H, $J_{\text{HF}}^3 = 19.2$ Hz, $J_{\text{HH}}^3 = 6.8$ Hz), 2.73 (s, 3H), 2.55 (s, 3H), 1.24 (t, 3H, $J = 7.2$ Hz), 1.11 (t, 3H, $J = 7.2$ Hz). $^{13}\text{C NMR}$ (CDCl_3): δ 169.6 [C], 157.6 [C], 154.0 [C], 147.5 [C], 145.1 [C], 133.2 [C], 131.7 [2 \times CH], 128.5 [2 \times CH], 123.1 [C], 108.3 [CH], 101.3 [C], 89.4 [C], 85.1 [d, $J_{\text{CF}}^3 = 6$ Hz, C], 81.3 [d, $J_{\text{CF}}^1 = 171$ Hz, CH_2], 42.2 [CH₂], 40.6 [CH₂], 28.0 [CH₂], 24.1 [CH₃], 21.6 [d, $J_{\text{CF}}^2 = 24$ Hz, CH_2], 16.9 [CH₃], 14.3 [CH₃], 13.0 [CH₃]. Compound **7c**: $^1\text{H NMR}$ (CDCl_3): δ 7.76 (d, 2H, $J = 8.0$ Hz), 7.47 (d, 2H, $J = 8.0$ Hz), 6.54 (s, 1H), 4.62 (dt, 2H, $J_{\text{HF}}^2 = 47.2$ Hz, $J_{\text{HH}}^3 = 6.0$ Hz), 3.97 (s, 2H), 3.50 (q, 2H, $J = 7.2$ Hz), 3.41 (q, 2H, $J = 7.2$ Hz), 2.76 (s, 3H), 2.59 (t, 2H, $J = 7.2$ Hz), 2.58 (s, 3H), 2.01 (dq⁵, 2H, $J_{\text{HF}}^2 = 25.6$ Hz, $J_{\text{HH}}^3 = 6.0$ Hz), 1.23 (t, 3H, $J = 7.2$ Hz), 1.12 (t, 3H, $J = 7.2$ Hz). $^{13}\text{C NMR}$ (CDCl_3): δ 169.7 [C], 157.6 [C], 154.5 [C], 147.4 [C], 145.2 [C], 133.0 [C], 131.6 [2 \times CH], 128.4 [2 \times CH], 123.5 [C], 108.4 [CH], 101.3 [C], 89.3 [C], 82.5 [d, $J_{\text{CF}}^1 = 164$ Hz, CH_2], 81.2 [C], 42.2 [CH₂], 40.6 [CH₂], 29.5 [d, $J_{\text{CF}}^2 = 20$ Hz, CH_2], 28.0 [CH₂], 24.3 [CH₃], 16.9 [CH₃], 15.4 [d, $J_{\text{CF}}^3 = 4$ Hz, CH_2], 14.3 [CH₃], 13.0 [CH₃]. Compound **7d**: $^1\text{H NMR}$ (CDCl_3): δ 7.76 (d, 2H, $J = 8.0$ Hz), 7.46 (d, 2H, $J = 8.0$ Hz), 6.54 (s, 1H), 4.52 (dt, 2H, $J_{\text{HF}}^2 = 47.2$ Hz, $J_{\text{HH}}^3 = 6.0$ Hz), 3.96 (s, 2H), 3.50 (q, 2H, $J = 7.2$ Hz), 3.42 (q, 2H, $J = 7.2$ Hz), 2.75 (s, 3H), 2.58 (s, 3H), 2.50 (t, 2H, $J = 7.2$ Hz), 1.89 (m, 2H), 1.75 (q⁵, 2H, $J = 7.2$ Hz), 1.20 (t, 3H, $J = 7.2$ Hz), 1.10 (t, 3H, $J = 7.2$ Hz). $^{13}\text{C NMR}$ (CDCl_3): δ 169.6 [C], 157.6 [C], 154.9 [C], 147.5 [C], 146.0 [C], 132.7 [C], 131.6 [2 \times CH], 128.4 [2 \times CH], 123.8 [C], 108.3 [CH], 101.3 [C], 90.3 [C], 83.6 [d, $J_{\text{CF}}^1 = 164$ Hz, CH_2], 81.1 [C], 42.2 [CH₂], 40.6 [CH₂], 29.5 [d, $J_{\text{CF}}^2 = 20$ Hz, CH_2], 28.0 [CH₂], 24.4 [d, $J_{\text{CF}}^3 = 5$ Hz, CH_2], 23.9 [CH₃], 19.1 [CH₂], 16.9 [CH₃], 14.2 [CH₃], 13.0 [CH₃].
68. **Determination of $\log D_{7.4}$ (HPLC):** The retention time recorded for the tested compound was converted into its $\log D_{7.4}$ value using a validated, standardized HPLC method (correlation between retention times and known $\log D$ values of similar compounds). HPLC conditions: Alliance 2695—PDA Waters, X-Terra MS C18 (4.6 \times 20 mm, 3.5 μm) column; mobile phase 5 mM MOPS/(CH₃)₄NOH pH 7.4 (A), 5% MOPS/(CH₃)₄NOH (100 mM, pH 7.4)/95% CH₃CN (B); gradient (A/B): 98:2 (0.5 min), 0:100 (4.8 min), 98:2 (1.6 min); 1.2 mL/min; 25 °C; detection at 254 nm.
69. Dollé, F. *J. Labelled Compd. Radiopharm.* **2013**, *56*, 63.
70. Damont, A.; Roeda, D.; Dollé, F. *J. Labelled Compd. Radiopharm.* **2013**, *56*, 96.
71. Dollé, F.; Roeda, D.; Kuhnast, B.; Lasne, M.-C. In *Fluorine and Health: Molecular Imaging, Biomedical Materials and Pharmaceuticals*; Tressaud, A., Haufe, G., Eds.; Elsevier: Amsterdam, 2008; pp 3–65.

Compact tridentate ligands for enhanced aqueous stability of quantum dots and *in vivo* imaging†

Cite this: *Chem. Sci.*, 2013, 4, 411

Edmond Gravel,^a Chloé Tanguy,^a Elsa Cassette,^b Thomas Pons,^b Fabien Knittel,^a Nicholas Bernards,^c Anikitos Garofalakis,^c Frédéric Ducongé,^c Benoît Dubertret^{*b} and Eric Doris^{*a}

We describe here a simple and versatile route for the preparation of a tridentate ligand that not only provides stable interactions with colloidal semiconductor nanocrystals (quantum dots, QDs) but also makes them water soluble. The designed ligand incorporates a biocompatible solubilizing polyethylene glycol (PEG) chain connected to a tridentate thiol motif with improved affinity towards the QDs surface. Stability experiments revealed better resistance to various drastic conditions compared to classical dihydrolipoic-based ligands. The enhanced stability of the assembly also enabled *in vivo* imaging experiments using near infrared-emitting QDs.

Received 30th July 2012
Accepted 10th October 2012

DOI: 10.1039/c2sc21113k

www.rsc.org/chemicalscience

Introduction

Since their discovery in the 1980s, semiconductor nanocrystals, also known as quantum dots (QDs), have drawn a great deal of attention for various types of applications, including biomedical imaging. Quantum dots display size-dependent fluorescence emission, high quantum yield, and improved resistance to photobleaching compared to classical organic dyes.^{1–4} In addition, recent developments led to the synthesis of nanocrystals emitting in the most appropriate optical window for *in vivo* applications that is in the near infrared (NIR) region.^{5–13}

QDs are classically synthesized using the pyrolysis technique which produces nanocrystals coated with hydrophobic ligands.¹⁴ However, for biomedical applications hydrophilic QDs are required and various strategies have been developed to convert hydrophobic nanoparticles into hydrophilic QDs. For example, one can either (i) use micellar surfactants to encapsulate the nanocrystals (Fig. 1a),^{15–20} (ii) perform cap exchange with precursors to grow an inorganic hydrophilic shell around the crystals (*e.g.* silica coating) (Fig. 1b),^{21–23} or (iii) exchange the primary lipophilic ligands with hydrophilic moieties (Fig. 1c).^{24,25} In the latter case, and if biological applications are foreseen, the new ligands must, in addition, provide biocompatibility to the QDs through suitable solubilizing units such as

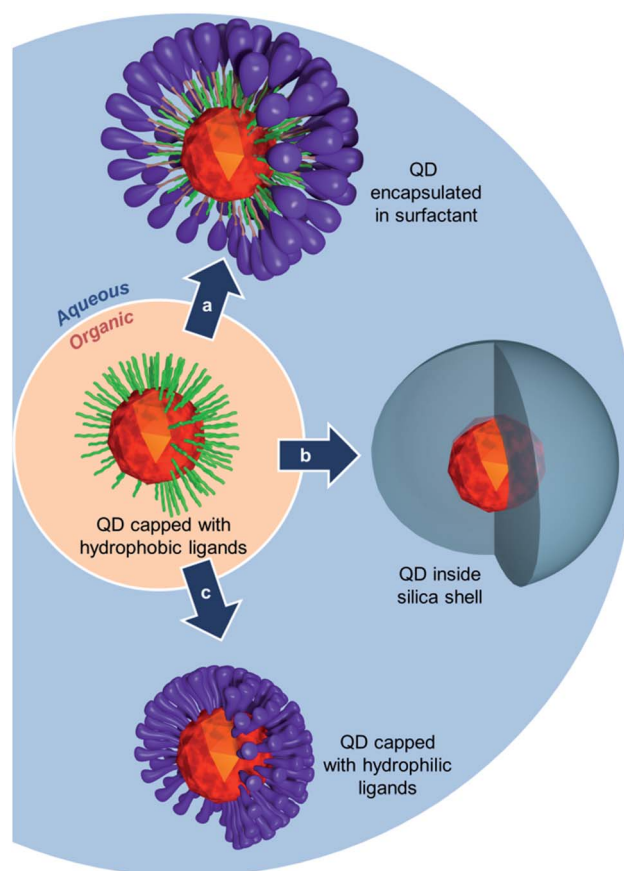


Fig. 1 Schematic representation of different possible routes to transfer QDs from organic to aqueous medium.

^aCEA, iBiTecS, Service de Chimie Bioorganique et de Marquage, 91191 Gif-sur-Yvette, France. E-mail: eric.doris@cea.fr; Fax: +33 169 08 79 91; Tel: +33 169 08 80 71

^bLaboratoire de Physique et d'Etude des Matériaux, UMR8213 du CNRS, ESPCI, 10 rue Vauquelin, 75005 Paris, France. E-mail: benoit.dubertret@espci.fr; Tel: +33 140 79 45 92

^cCEA, I2BM, Service Hospitalier Frédéric Joliot, INSERM U1023, Laboratoire d'Imagerie Moléculaire Expérimentale, Université Paris Sud, 4 place du général Leclerc, 91401 Orsay, France

† Electronic supplementary information (ESI) available: Experimental procedures and supplementary figures. See DOI: 10.1039/c2sc21113k

polyethylene glycol chains (PEG).²⁶ For improved stability, anchoring of the ligands to the nanocrystals must be robust and stand various stress conditions that are likely to be encountered in biological medium. Amongst the various ligands developed in the literature, thiols have emerged as the most widespread group of ligands since thiolate groups ($-S^-$) are highly affine toward the surface of the QDs.^{27–29} However, the interaction can be disrupted under oxidative conditions³⁰ that induce the formation of disulfide bridges and release of the ligands from the QD surface. Simple thiol groups are also readily displaced from the QD's surface by competing sulphur-containing molecules which are abundant species in biological media. However, this stability issue can be partly circumvented using bidentate dihydrolipoic acid (DHLA) ligands that were originally developed by Mattoussi and Bawendi.^{31–35}

DHLA-based ligands were shown to exhibit stronger anchoring properties compared to their monothiol equivalents due to the chelating effect of the bidentate group (two thiol units). Recent development also focused on multidentate ligands^{36–38} including poly-DHLA^{39–41} and poly-thiols⁴² whose increased coordination units gave access to more stable nanocrystals.

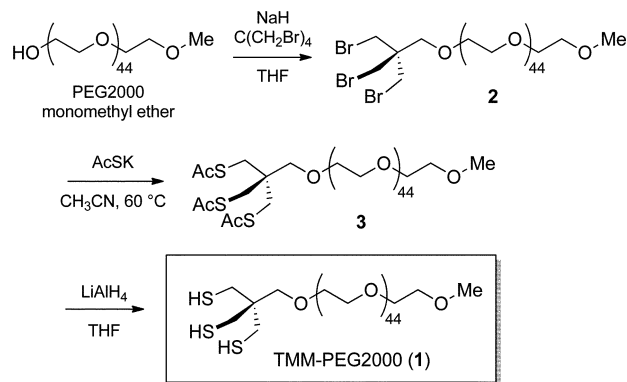
We describe here the synthesis and evaluation of a novel family of QD ligands made of a compact tris(mercaptomethyl) head group (three thiol units) and a PEG chain. The tris(mercaptomethyl) chelating group (TMM) has already been shown to bind strongly to metal surfaces while maintaining dense coverage. Previous studies on gold surfaces⁴³ and nanoparticles⁴⁴ demonstrated that tris(mercaptomethyl) groups are stronger chelators than their dithiol counterparts while providing comparable ligand density. A TMM-based ligand was therefore synthesized and used in the capping of QDs before the nanoparticles were evaluated as regards their overall colloidal stability and *in vivo* behavior.

Results and discussion

Design and synthesis of the tridentate ligands

For *in vivo* applications, the ideal QD ligands should, (i) be robustly attached to the nanocrystal surface, (ii) provide stable colloidal dispersion, and (iii) confer high biocompatibility to the nanoparticle. These properties could be respectively attained by combining multiple coordinating groups in the same structure to reinforce surface interactions, attaching a highly solubilizing group, and using a non-toxic stealth ligand. With these prerequisites in mind, the compact tris(mercaptomethyl) head was selected as an anchoring group because of its improved chelating properties.^{41,42} The latter was connected to a solubilizing PEG chain that classically promotes extended blood residence time while being non-toxic.²⁶ A simple and efficient route to the pegylated tridentate ligand was thus developed.

We conceived that connection of the TMM chelating unit to the polyethylene glycol solubilizing chain using an ether linkage could improve the overall robustness of the ligand as the bridging C–O–C bond is non-hydrolysable. To this end, the hydroxyl group of PEG2000–monomethyl ether was first deprotonated by treatment with sodium hydride in refluxing



Scheme 1 Synthesis of the TMM-PEG2000 ligand (1).

THF before tetrakis(bromomethyl) methane in excess was added. Nucleophilic substitution of one of the bromine atoms permitted to anchor the PEG chain to the trithiol precursor unit. In this step, the addition of over-stoichiometric amounts of the bromomethyl electrophile enabled us to substantially minimize the formation of poly-substituted adducts (multiple addition of PEG chains to the same tetrakis(bromomethyl) methane molecule) and recover, as the main product, the expected mono-pegylated tribromide compound **2**. The latter was thereafter converted into the corresponding trithioacetate **3** by nucleophilic displacement of the three remaining bromine atoms by potassium thioacetate. Compound **3**, which corresponds to the masked form of our target ligand, was finally converted to the corresponding free trithiol **1** by lithium aluminum hydride deprotection of the thiol groups (Scheme 1). This simple route thus permitted the multigram scale synthesis of the tridentate ligand. It is to be noted that the resulting trithiol **1** was stable over time and could be stored for more than a year at $-20\text{ }^\circ\text{C}$ with neither noticeable oxidation of the SH groups nor degradation.

Preparation of PEG-capped hydrophilic CdSe/CdS/ZnS core-shell QDs

To make fluorescent nanocrystals water soluble, the native capping oleic acid and oleylamine ligands were replaced by our newly designed TMM-PEG ligand (Fig. 2). Evaluation of the performances of the tridentate TMM-PEG as a colloidal stabilizer of QDs was then assessed by comparison with those of the thoroughly investigated bidentate DHLA-PEG ligands.³² Toward this goal, multilayered CdSe/CdS/ZnS QDs were synthesized using the high temperature pyrolysis process, as described elsewhere.⁴⁵ The resulting oleic acid/oleylamine capped nanocrystals were then precipitated in ethanol and transferred to chloroform to perform the ligand exchange reaction.

The native organic layer was replaced by thiol-based ligands by overnight stirring of the QD suspension in refluxing chloroform and in the presence of an excess of either TMM-PEG2000 (**1**) or DHLA-PEG2000 (**4**). The ligand excess was then removed by precipitation of the QDs in a mixture of chloroform-ethanol-hexane, followed by centrifugation. The supernatant was discarded and the precipitate (containing the QDs)

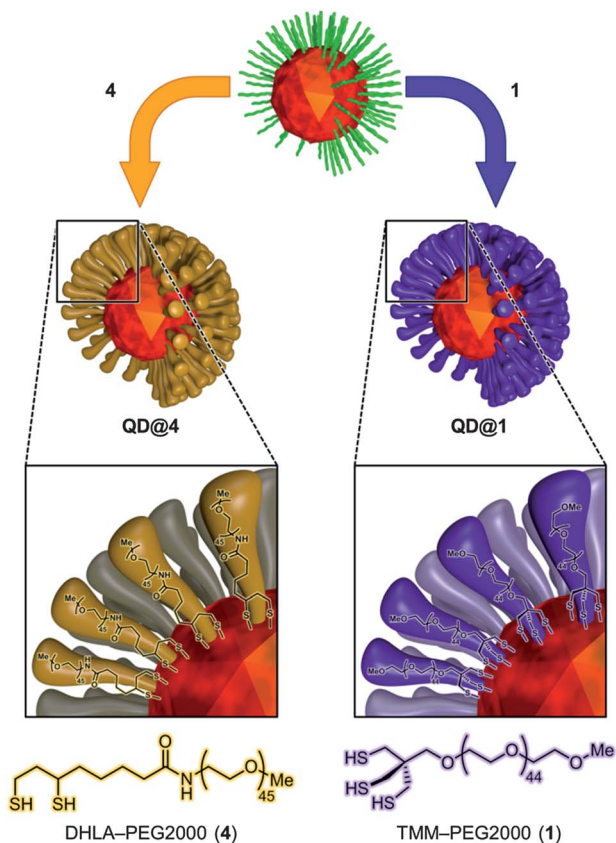


Fig. 2 Schematic representation of ligand exchange and interaction with the crystal surface.

was suspended in water. Further purification by ultracentrifugation finally afforded a clear and homogeneous QD colloidal suspension. Both TMM and DHLA hence provided access to aggregate-free aqueous dispersions of the fluorescent nanoparticles that were stable for several months at 4 °C. The hydrodynamic radii of QDs encapsulated with TMM-PEG2000 or DHLA-PEG2000 were measured by dynamic light scattering (DLS) and values of 11.2 ± 0.5 nm and 9.3 ± 0.5 nm were obtained, respectively (see Fig. S1 in the ESI†). These values are consistent with those previously reported in the literature for shorter PEG-chain ligands.^{13,46}

Optical characterization of the QDs capped with multidentate ligands

Absorption and fluorescence spectra were recorded in hexane for QDs capped with the original oleic acid/oleylamine ligands and in pure water for the two hydrophilic QDs (Fig. 3). The aqueous QD dispersions that were produced by ligand exchange with TMM-PEG (QD@1) or DHLA-PEG (QD@4) exhibited absorption and emission profiles that were nearly identical to those of the starting QDs. As the optical properties of the QD are retained after the exchange step, one can speculate that the replacement of the original organic layer by the pegylated multidentate ligands did not alter the inorganic core of the nanocrystals. It is noteworthy, that while the

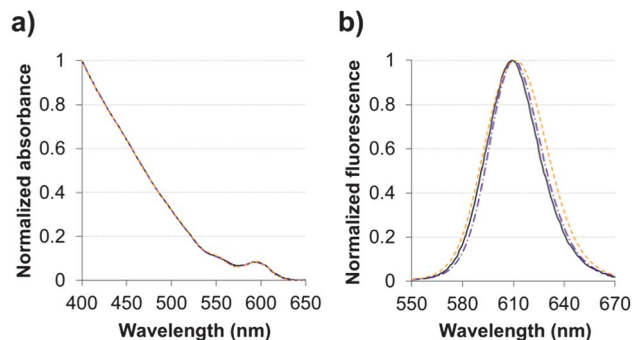


Fig. 3 (a) Absorbance and (b) fluorescence spectra of CdSe/CdS/ZnS QDs capped with organic ligands (—) in hexane or with either DHLA-PEG2000 (---) or TMM-PEG2000 (---) in water.

photoluminescence quantum yield of the organic grown QDs was 44%, those of the aqueous colloidal QDs dropped to *ca.* 25%. This feature of QDs that were transferred into aqueous medium has already been observed and commented on by others.³¹

Evaluation of the stability of the QDs capped with multidentate ligands

Colloidal stability of the aqueous dispersions of TMM-PEG2000-capped nanocrystals was evaluated under various conditions including a broad pH range, oxidizing conditions, and in the presence of the competing ligand dithiothreitol (DTT). The performances of our newly designed ligand under diverse conditions were compared to those of the well-established DHLA-PEG ligands.

First, colloidal stability of the two coated QDs was assessed by measuring their fluorescence intensities (excitation at 400 nm) after incubation in buffered solutions of pH values ranging from 1.5 to 12. Fig. 4 shows the fluorescence intensities of TMM-PEG- and DHLA-PEG-coated QDs at various pH values. The first observation was that under acidic conditions and the fluorescence of QD@1 remained steady until pH 3 was reached. Conversely, we observed a drop in the fluorescence intensity of QD@4 which started from pH 6 as a 20% loss of the initial fluorescence was detected at this value. This effect was even

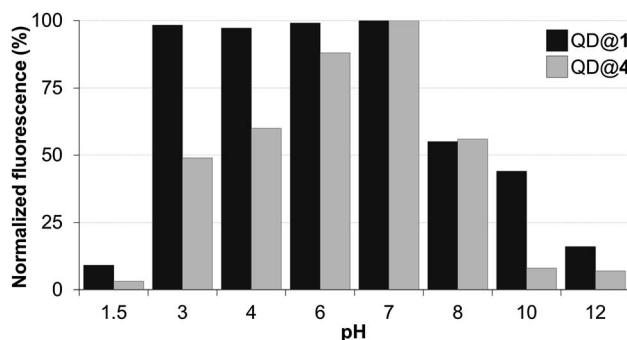


Fig. 4 Fluorescence intensity of QDs capped with DHLA-PEG2000 (QD@4) or TMM-PEG2000 (QD@1) at different pH values.

more accentuated at lower pH values with a decrease of fluorescence of *ca.* 40% and 50% at pH 4 and pH 3, respectively. These results underline the higher stability of the TMM ligand over DHLA under mildly acidic conditions. However, it should be noted that fluorescence of both samples was nearly extinguished under extreme acidic conditions (*i.e.* pH 1.5). The same trend, that is higher stability of TMM-PEG ligand, was observed under basic conditions, although fewer differences were evidenced at mildly basic pH 8 where both samples lost approximately 45% of their initial fluorescence. At higher pH values (*e.g.* pH 10), a more significant benefit of the TMM-PEG coating was detected with 45% of the initial fluorescence remaining. Under the same conditions, DHLA-PEG QDs lost 90% of their photoluminescence. At extreme basic pH values (above 12), virtually all fluorescence had vanished from the two QD samples.

The stability of the colloidal QDs was also assessed under oxidizing conditions by monitoring fluorescence intensity variations in the presence of molecular iodine. In fact, iodine is a well-established reagent for the mild oxidation of thiols into the corresponding disulfides.^{47,48} If this reaction were to occur with the thiolated QD-capping ligands (TMM-PEG or DHLA-PEG), they would detach from the QD surface and lead to aggregation of the nanocrystals and loss of the fluorescence properties. Accordingly, a 0.25 μM colloidal solution of QD capped with either TMM-PEG or DHLA-PEG was stirred with increasing concentrations of molecular iodine ranging from 33 to 300 μM before fluorescence emission (excitation at 400 nm) was recorded. The performances of the TMM-PEG QDs under the oxidizing conditions were obviously superior to those of the DHLA-PEG QDs since lower fluorescence extinction was observed at all of the studied iodine concentrations. The emission of the DHLA QDs sample decreased rapidly and steadily at the same time as the local concentration of iodine increased and less than 15% of the initial fluorescence was detected at 300 μM of I_2 . In contrast, under the highest iodine concentrations (*i.e.* 300 μM), TMM-PEG QDs retained nearly 60% of their fluorescence (Fig. 5). These observations demonstrate the higher resistance of the newly synthesized TMM-based ligands (compared to DHLA ligands) regarding their

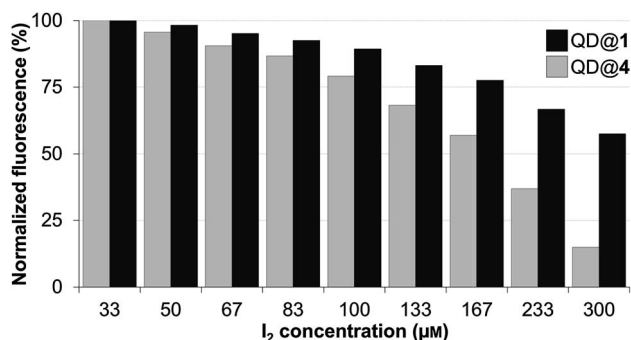


Fig. 5 Fluorescence intensity of QDs capped with DHLA-PEG2000 (QD@4) or TMM-PEG2000 (QD@1) when exposed to increasing concentrations of molecular iodine.

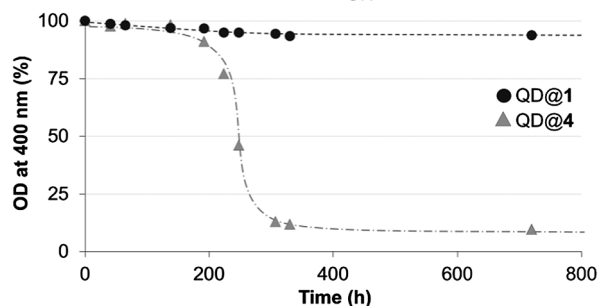
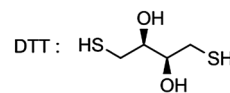


Fig. 6 Time dependant evolution of the optical density at 400 nm measured for QDs capped with DHLA-PEG2000 (QD@4) or TMM-PEG2000 (QD@1) incubated with DTT (structure shown).

susceptibility to oxidation which is often challenging when working with thiol derivatives.

Finally, stability of the colloidal QDs was evaluated in the presence of a competing ligand.⁴⁰ Considering that QDs coated with TMM-PEG ligands are intended to be used *in vivo*, it appeared important to investigate their stability upon exposure to other thiol groups which are abundant species in biological environments. Dithiothreitol (DTT), a dithiol derivative of threose, was chosen as a test competitor. DTT is made of two thiol units that are able to bind to the surface of the QDs. However, DTT cannot confer aqueous solubility to the QD which will therefore precipitate. QDs capped with either DHLA-PEG or TMM-PEG were diluted in 1.5 M aqueous DTT and aggregation kinetics were evaluated by measuring the absorption spectra of each sample at different time frames, after mild centrifugation to eliminate QD aggregates. Concentration of the non-aggregated QDs (those which were unaffected by DTT) was evaluated by optical density (OD) measurement at 400 nm. While we observed no changes for the TMM-PEG QDs throughout the duration of the experiment (720 h), DHLA-PEG QDs precipitated after 200 hours of exposure to DTT to reach a plateau at *ca.* 10% of the original

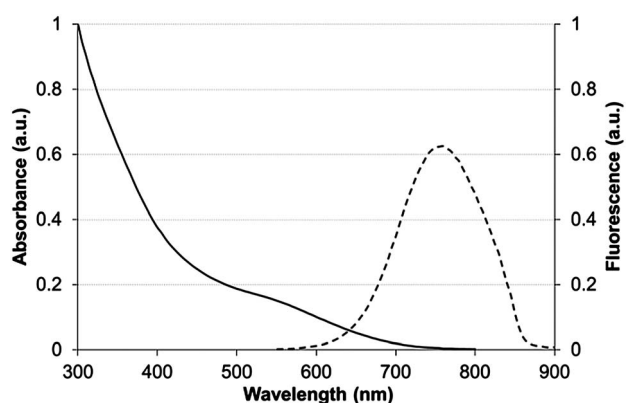


Fig. 7 Absorbance (solid line) and fluorescence (dashed line) spectra of CuInS₂/ZnS QDs capped with TMM-PEG2000 in water.

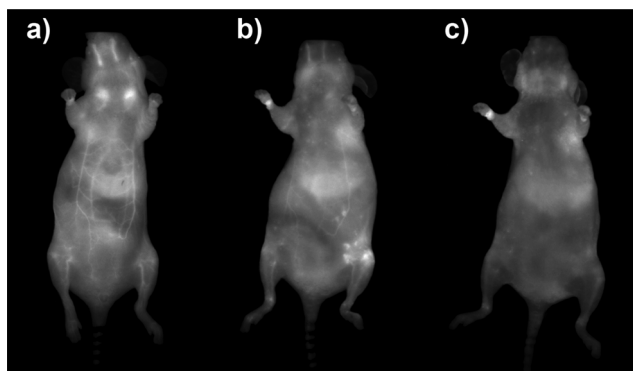


Fig. 8 Whole body fluorescence images recorded (a) 2 h, (b) 4 h, and (c) 24 h after intravenous injection of TMM-PEG2000-capped NIR-QDs to nude mice (ventral side of the animal).

absorbance (Fig. 6). These experiments highlight the higher stability of QDs capped with TMM ligands when exposed to competing species.

In vivo imaging studies

With encouraging results from the *in vitro* stability tests, the next step was to evaluate the *in vivo* behavior of TMM-PEG-capped QDs. For optimal *in vivo* imaging applications, the QD emission wavelength should ideally be set in a region of the spectrum where blood and other tissues have low absorption which corresponds to the near-infrared domain (NIR). Thus, cadmium-free near infrared-emitting CuInS₂/ZnS quantum dots (NIR-QDs) were synthesized and subsequently capped with our newly developed tridentate-PEG ligand **1**. Absorption and emission spectra of the TMM-PEG coated nanoparticles are depicted in Fig. 7 which shows that the absorption spectrum of the TMM-PEG NIR-QDs is continuous up to ca. 700 nm and that the maximum emission is detected at 760 nm. It

is to be noted that the hydrodynamic diameter of the NIR-emitting QDs could not be measured because of the strong absorption of the quantum dots at 633 nm, which is the operating wavelength of the DLS laser beam. Since the inorganic core-shell diameter of NIR-QDs is only slightly smaller (typically 3–4 nm) than that of visible-emitting CdSe/CdS/ZnS QDs (typically 6–7 nm), one can assume that their final (PEG-coated) hydrodynamic diameter is in the same range, that is approximately 20 nm.

Prior to *in vivo* experiments, preliminary toxicity studies were undertaken. No harmful effect of the TMM-PEG NIR-QDs was detected at the QD-concentration (ca. 100 nM) used for the *in vivo* experiments and cell proliferation assays on MDA-MB-231 cells indicated an IC₅₀ value of 12.2 ± 1.1 μM (see Fig. S2 in the ESI†). The water soluble TMM-PEG NIR-QDs were thereafter injected intravenously to female nude mice (*n* = 3) at a dose of 10 nmol kg⁻¹ (ca. 200 pmol per animal) and their bio-distribution was monitored in real-time using whole body planar fluorescence imaging (Fig. 8). The first observation is that the TMM-PEG coated QDs produced a clear *in vivo* image contrast which demonstrated their effectiveness as NIR optical probes. During the first two hours after injection, a high contrast of the blood vessels was observed, suggesting that most of the injected QDs remained in the bloodstream. As time elapsed, the fluorescence distribution in the mice became more diffuse but the vessels were still clearly visible 4 h after injection. However, nearly all fluorescence had vanished from the bloodstream 24 h after injection. A comparable overall *in vivo* behavior was observed for DHLA-PEG2000-coated NIR-QDs (see Fig. S3 in the ESI†).

The biodistribution of a nanoparticulate system is classically governed by its size and surface coating. In our case, the slow clearance from the bloodstream is not only due to the minimization of the nanoparticles opsonization thanks to the PEGs but also to the stability of the tridentate QD-complexing unit. Consequently, QD uptake by macrophages is delayed and

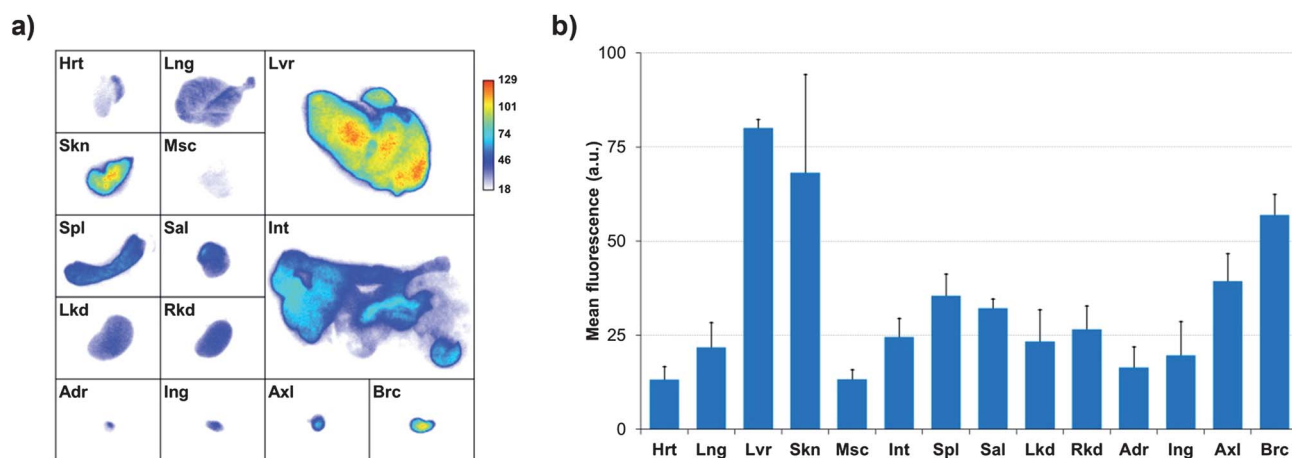


Fig. 9 (a) Planar NIR fluorescence images of different organs of nude mice 24 h after injection of TMM-PEG2000-capped NIR-QDs and (b) quantification of the mean fluorescence adjusted by subtracting the autofluorescence of the same organs measured on a non-injected control mouse (Hrt = heart; Lng = lung; Lvr = liver; Skn = skin; Msc = muscle; Int = intestine; Spl = spleen; Sal = salivary gland; Lkd = left kidney; Rkd = right kidney; Adr = adrenal gland; Ing = inguinal lymph node; Axl = axillary lymph node; Brc = brachial lymph node).

higher blood residence time is observed. Quantification of fluorescence by *in vivo* planar imaging is usually difficult to achieve because of the absorption and scattering of photons when migrating through tissues. To have a clearer picture of the TMM-PEG-QD tissue distribution, animals were euthanized 24 h after injection and organ resection permitted *ex vivo* quantification of mean fluorescence (Fig. 9). Analysis of the different mice groups showed distribution of the QDs in the main organs (Fig. 9a) with a slightly higher uptake (Fig. 9b) in the liver, lymph nodes (especially in brachial lymph nodes), and skin. The uptake of the QDs by the skin was unexpected, although such a phenomenon has already been observed with PEG-coated fluorescent gadolinium oxide nanoparticles.⁴⁹ On the other hand, the preferential accumulation in the liver and lymph nodes can be ascribed to QD-uptake by local phagocytes that act as nanoparticles traps.⁹ Interestingly, we did not observe any increase of the uptake in the spleen, although this organ is also rich in phagocytes. Besides, only weak fluorescence was detected in the kidneys or bladder, suggesting low renal excretion. In fact, the hydrodynamic diameter of the TMM-PEG2000-encapsulated QDs is likely above the renal filtration threshold.⁵⁰ This behavior is in line with previous reports where QDs coated with short polyethylene glycol chains (up to PEG400) were mainly excreted through the urines, while QDs with larger PEG coatings were detected in intestines and lymph nodes.¹³ Our study thus corroborates the influence of the PEG chain length on the biodistribution and clearance of nanoparticulate systems.

Conclusions

A new family of ligands incorporating a tris(mercaptomethyl) chelating head and a polyethylene glycol chain has been synthesized and evaluated for the stabilization of quantum dots in aqueous media. Comparison with well-known DHLA-based ligands demonstrated that colloids obtained from the new ligand were more resistant to pH variations, oxidizing conditions, and against an excess of a competing ligand. Colloids of NIR-emitting QDs capped with TMM-PEG2000 ligands were prepared and injected into nude mice. The acquired images demonstrated that these nanoparticles could be used as NIR optical imaging probes for *in vivo* imaging and permit the assessment of their *in vivo* distribution which was confirmed *ex vivo*, after organ resection. Overall, the TMM-PEG ligands described herein appear well suited for the biocompatibilization of QDs for biomedical applications and compare favorably with previously reported systems in terms of overall stability.

Acknowledgements

The “Service de Chimie Bioorganique et de Marquage” belongs to the Laboratory of Excellence in Research on Medication and Innovative Therapeutics (LabEx LERMIT). The “Agence Nationale de la Recherche” (ANR) (Dot Imager and IVF-proteomic projects) is acknowledged for financial support.

Notes and references

- 1 X. Michalet, F. F. Pinaud, L. A. Bentolila, J. M. Tsay, S. Doose, J. J. Li, G. Sundaresan, A. M. Wu, S. S. Gambhir and S. Weiss, *Science*, 2005, **307**, 538.
- 2 R. Gill, M. Zayats and I. Willner, *Angew. Chem., Int. Ed.*, 2008, **47**, 7602.
- 3 A. Rogach, N. Gaponik, J. Lupton, C. Bertoni, D. Gallardo, S. Dunn, N. Li Pira, M. Paderi, P. Repetto, S. G. Romanov, C. O'Dwyer, C. M. Sotomayor Torres and A. Eychmüller, *Angew. Chem., Int. Ed.*, 2008, **47**, 6538.
- 4 T. Jamieson, R. Bakhshi, D. Petrova, R. Pocock, M. Imani and A. M. Seifalian, *Biomaterials*, 2007, **28**, 4717.
- 5 Y. He, Y. L. Zhong, Y. Y. Su, Y. M. Lu, Z. Y. Jiang, F. Peng, T. Xu, S. Su, Q. Huang, C. Fan and S. T. Lee, *Angew. Chem., Int. Ed.*, 2011, **50**, 5694.
- 6 P. M. Allen, W. Liu, V. P. Chauhan, J. Lee, A. Y. Ting, D. Fukumura, R. K. Jain and M. G. Bawendi, *J. Am. Chem. Soc.*, 2010, **132**, 470.
- 7 L. Li, T. J. Daou, I. Texier, T. K. C. Tran, Q. L. Nguyen and P. Reiss, *Chem. Mater.*, 2009, **21**, 2422.
- 8 T. Pons, E. Pic, N. Lequeux, E. Cassette, L. Bezdetnaya, F. Guillemin, F. Marchal and B. Dubertret, *ACS Nano*, 2010, **4**, 2531.
- 9 E. Cassette, T. Pons, C. Bouet, M. Helle, L. Bezdetnaya, F. Marchal and B. Dubertret, *Chem. Mater.*, 2010, **22**, 6117.
- 10 Y. Y. Su, F. Peng, Z. Y. Jiang, Y. L. Zhong, Y. M. Lu, X. Jiang, Q. Huang, C. Fan, S.-T. Lee and Y. He, *Biomaterials*, 2011, **32**, 5855.
- 11 M. Praetner, M. Rehberg, P. Bihari, M. Lerchenberger, B. Uhl, M. Holzer, M. E. Eichhorn, R. Fürst, T. Perisic, C. A. Reichel, U. Welsch and F. Krombach, *Biomaterials*, 2010, **31**, 6692.
- 12 H. Yukawa, M. Watanabe, N. Kaji, Y. Okamoto, M. Tokeshi, Y. Miyamoto, H. Noguchi, Y. Baba and S. Hayashi, *Biomaterials*, 2012, **33**, 2177.
- 13 H. S. Choi, B. I. Ipe, P. Misra, J. H. Lee, M. G. Bawendi and J. V. Frangioni, *Nano Lett.*, 2009, **9**, 2354.
- 14 C. B. Murray, D. J. Norris and M. G. Bawendi, *J. Am. Chem. Soc.*, 1993, **115**, 8706.
- 15 B. Dubertret, P. Skourides, D. J. Norris, V. Noireaux, A. H. Brivanlou and A. Libchaber, *Science*, 2002, **298**, 1759.
- 16 X. Y. Wu, H. J. Liu, J. Q. Liu, K. N. Haley, J. A. Treadway, J. P. Larson, N. Ge, F. Peale and M. P. Bruchez, *Nat. Biotechnol.*, 2003, **21**, 41.
- 17 T. Pellegrino, L. Manna, S. Kudera, T. Liedl, D. Koktysh, A. L. Rogach, S. Keller, J. Rädler, G. Natile and W. J. Parak, *Nano Lett.*, 2004, **4**, 703.
- 18 N. Travert-Branger, F. Dubois, O. Carion, G. Carrot, B. Mahler, B. Dubertret, E. Doris and C. Mioskowski, *Langmuir*, 2008, **24**, 3016.
- 19 N. Travert-Branger, F. Dubois, J. P. Renault, S. Pin, B. Mahler, E. Gravel, B. Dubertret and E. Doris, *Langmuir*, 2011, **27**, 4358.
- 20 E. Genin, O. Carion, B. Mahler, B. Dubertret, N. Arhel, P. Charneau, E. Doris and C. Mioskowski, *J. Am. Chem. Soc.*, 2008, **130**, 8596.

- 21 D. Gerion, F. Pinaud, S. C. Williams, W. J. Parak, D. Zanchet, S. Weiss and A. P. Alivisatos, *J. Phys. Chem. B*, 2001, **105**, 8861.
- 22 S. Selvan, T. Tan and J. Ying, *Adv. Mater.*, 2005, **17**, 1620.
- 23 M. Darbandi, G. Urban and M. Krüger, *J. Colloid Interface Sci.*, 2012, **365**, 41.
- 24 W. C. W. Chan and S. Nie, *Science*, 1998, **281**, 2016.
- 25 F. Dubois, B. Mahler, B. Dubertret, E. Doris and C. Mioskowski, *J. Am. Chem. Soc.*, 2007, **129**, 482.
- 26 K. Knop, R. Hoogenboom, D. Fischer and U. S. Schubert, *Angew. Chem., Int. Ed.*, 2010, **49**, 6288.
- 27 W. Liu, H. S. Choi, J. P. Zimmer, E. Tanaka, J. V. Frangioni and M. G. Bawendi, *J. Am. Chem. Soc.*, 2007, **129**, 14530.
- 28 V. V. Breus, C. D. Heyes, K. Tron and G. U. Nienhaus, *ACS Nano*, 2009, **3**, 2573.
- 29 R. Gill, L. Bahshi, R. Freeman and I. Willner, *Angew. Chem.*, 2008, **120**, 1700.
- 30 J. Aldana, N. Lavelle, Y. J. Wang and X. G. Peng, *J. Am. Chem. Soc.*, 2005, **127**, 2496.
- 31 H. Mattoussi, J. M. Mauro, E. R. Goldman, G. P. Anderson, V. C. Sundar, F. V. Mikulec and M. G. Bawendi, *J. Am. Chem. Soc.*, 2000, **122**, 12142.
- 32 H. T. Uyeda, I. L. Medintz, J. K. Jaiswal, S. M. Simon and H. Mattoussi, *J. Am. Chem. Soc.*, 2005, **127**, 3870.
- 33 W. Liu, M. Howarth, A. B. Greytak, Y. Zheng, D. G. Nocera, A. Y. Ting and M. G. Bawendi, *J. Am. Chem. Soc.*, 2008, **130**, 1275.
- 34 E. Muro, T. Pons, N. Lequeux, A. Fragola, N. Sanson, Z. Lenkei and B. Dubertret, *J. Am. Chem. Soc.*, 2010, **132**, 4556.
- 35 K. Susumu, E. Oh, J. B. Delehanty, J. B. Blanco-Canosa, B. J. Johnson, V. Jain, W. J. Hervey, W. R. Algar, K. Boeneman, P. E. Dawson and I. L. Medintz, *J. Am. Chem. Soc.*, 2011, **133**, 9480.
- 36 A. M. Smith and S. Nie, *J. Am. Chem. Soc.*, 2008, **130**, 11278.
- 37 W. Liu, A. B. Greytak, J. Lee, C. R. Wong, J. Park, L. F. Marshall, W. Jiang, P. N. Curtin, A. Y. Ting, D. G. Nocera, D. Fukumura, R. K. Jain and M. G. Bawendi, *J. Am. Chem. Soc.*, 2010, **132**, 472.
- 38 P. F. Zhang, S. H. Liu, D. Y. Gao, D. H. Hu, P. Gong, Z. H. Sheng, J. Z. Deng, Y. F. Ma and L. T. Cai, *J. Am. Chem. Soc.*, 2012, **134**, 8388.
- 39 I. Yildiz, E. Deniz, B. McCaughan, S. F. Cruickshank, J. F. Callan and F. M. Raymo, *Langmuir*, 2010, **26**, 11503.
- 40 M. H. Stewart, K. Susumu, B. C. Mei, I. L. Medintz, J. B. Delehanty, J. B. Blanco-Canosa, P. E. Dawson and H. Mattoussi, *J. Am. Chem. Soc.*, 2010, **132**, 9804.
- 41 G. Palui, H. B. Na and H. Mattoussi, *Langmuir*, 2012, **28**, 2761.
- 42 M. Thiry, K. Boldt, M. S. Nikolic, F. Schulz, M. Ijeh, A. Panicker, T. Vossmeier and H. Weller, *ACS Nano*, 2011, **5**, 4965.
- 43 J. S. Park, A. Nguyen Vo, D. Barriet, Y. S. Shon and T. R. Lee, *Langmuir*, 2005, **21**, 2902.
- 44 K. Wojczykowski, D. Meißner, P. Jutzi, I. Ennen, A. Hütten, M. Fricke and D. Volkmer, *Chem. Commun.*, 2006, 3693.
- 45 L. Qu, Z. A. Peng and X. Peng, *Nano Lett.*, 2001, **1**, 333.
- 46 T. Pons, H. T. Uyeda, I. L. Medintz and H. Mattoussi, *J. Phys. Chem. B*, 2006, **110**, 20308.
- 47 H. Fraenkel-Conrat, *J. Biol. Chem.*, 1955, **217**, 373.
- 48 J. P. Danehy and M. Y. Oester, *J. Org. Chem.*, 1967, **32**, 1491.
- 49 A. C. Faure, S. Dufort, V. Josserand, P. Perriat, J. L. Coll, S. Roux and O. Tillement, *Small*, 2009, **5**, 2565.
- 50 H. S. Choi, W. Liu, P. Misra, E. Tanaka, J. P. Zimmer, B. I. Ipe, M. G. Bawendi and J. V. Frangioni, *Nat. Biotechnol.*, 2007, **25**, 1165.

Bibliography

- [Aalto 11] Kristiina Aalto, Anu Autio, Elina A Kiss, Kati Elima, Yvonne Nymalm, Tibor Z Veres, Fumiko Marttila-Ichihara, Heli Elovaara, Tiina Saanijoki, Paul R Crocker *et al.* *Siglec-9 is a novel leukocyte ligand for vascular adhesion protein-1 and can be used in PET imaging of inflammation and cancer.* *Blood*, vol. 118, no. 13, pages 3725–3733, 2011.
- [Aguzzi 13] Adriano Aguzzi, Ben A Barres & Mariko L Bennett. *Microglia: scapegoat, saboteur, or something else?* *Science*, vol. 339, no. 6116, pages 156–161, 2013.
- [Antonov 11] Alexander S Antonov, Galina N Antonova, David H Munn, Nahid Mivechi, Rudolf Lucas, John D Catravas & Alexander D Verin. *alpha-V-beta3 integrin regulates macrophage inflammatory responses via PI3 kinase/Akt-dependent NF-kappa B activation.* *Journal of Cellular Physiology*, vol. 226, no. 2, pages 469–476, 2011.
- [Arlicot 12] Nicolas Arlicot, Johnny Vercouillie, Maria-João Ribeiro, Clovis Tauber, Yann Venel, Jean-Louis Baulieu, Serge Maia, Philippe Corcia, Michael G Stabin, Aaron Reynolds *et al.* *Initial evaluation in healthy humans of [18F] DPA-714, a potential PET biomarker for neuroinflammation.* *Nuclear Medicine and Biology*, vol. 39, no. 4, pages 570–578, 2012.
- [Austin 13] Christopher JD Austin, Jan Kahlert, Michael Kassiou & Louis M Rendina. *The translocator protein (TSPO): a novel target for cancer chemotherapy.* *The International Journal of Biochemistry and Cell Biology*, vol. 45, no. 7, pages 1212–1216, 2013.

BIBLIOGRAPHY

- [Autio 11] Anu Autio, Tiina Henttinen, Henri J Sipilä, Sirpa Jalkanen & Anne Roivainen. *Mini-PEG spacing of VAP-1-targeting 68Ga-DOTAVAP-P1 peptide improves PET imaging of inflammation*. EJNMMI Research, vol. 1, no. 1, pages 1–7, 2011.
- [Basu 09] Sandip Basu, Hongming Zhuang, Drew A Torigian, Joshua Rosenbaum, Wengen Chen & Abass Alavi. *Functional Imaging Of Inflammatory Diseases Using Nuclear Medicine Techniques*. In *Seminars In Nuclear Medicine*, volume 39, pages 124–145. Elsevier, 2009.
- [Batarseh 10] Amani Batarseh & Vassilios Papadopoulos. *Regulation of translocator protein 18kDa (TSPO) expression in health and disease states*. *Molecular and cellular endocrinology*, vol. 327, no. 1, pages 1–12, 2010.
- [Benaroyo 94] L Benaroyo. *[How do we define inflammation?]*. *Praxis*, vol. 83, no. 48, pages 1343–1347, 1994.
- [Benavides 83] J Benavides, D Quarteronet, F Imbault, C Malgouris, A Uzan, C Renault, MC Dubroeuq, C Guerey & G Le Fur. *Labelling of “Peripheral-Type” Benzodiazepine Binding Sites in the Rat Brain By Using [3H] PK 11195, an Isoquinoline Carboxamide Derivative: Kinetic Studies and Autoradiographic Localization*. *Journal of Neurochemistry*, vol. 41, no. 6, pages 1744–1750, 1983.
- [Bettenworth 13] Dominik Bettenworth, Stefan Reuter, Sven Hermann, Matthias Weckesser, Linda Kerstiens, Athanasios Stratis, Tobias Max Nowacki, Matthias Ross, Frank Lenze, Bayram Edemire *et al.* *Translational 18F-FDG PET/CT imaging to monitor lesion activity in intestinal inflammation*. *Journal of Nuclear Medicine*, vol. 54, no. 5, pages 748–755, 2013.
- [Bird 10] JLE Bird, D Izquierdo-Garcia, JR Davies, JHF Rudd, KC Probst, N Figg, JC Clark, PL Weissberg, AP Davenport & EA Warburton. *Evaluation of translocator protein quantification as a tool for characterising macrophage burden in human carotid atherosclerosis*. *Atherosclerosis*, vol. 210, no. 2, pages 388–391, 2010.

BIBLIOGRAPHY

- [Boutin 07a] Hervé Boutin, Fabien Chauveau, Cyrille Thominiaux, Marie-Claude Grégoire, Michelle L James, Régine Trebossen, Philippe Hantraye, Frédéric Dollé, Bertrand Tavitian & Michael Kassiou. *11C-DPA-713: a novel peripheral benzodiazepine receptor PET ligand for in vivo imaging of neuroinflammation*. *Journal of Nuclear Medicine*, vol. 48, no. 4, pages 573–581, 2007.
- [Boutin 07b] Hervé Boutin, Fabien Chauveau, Cyrille Thominiaux, Bertrand Kuhnast, Marie-Claude Grégoire, Sébastien Jan, Régine Trebossen, Frédéric Dollé, Bertrand Tavitian, Filomena Mattner *et al.* *In vivo imaging of brain lesions with [11C] CLINME, a new PET radioligand of peripheral benzodiazepine receptors*. *Glia*, vol. 55, no. 14, pages 1459–1468, 2007.
- [Bronstein 95] DM Bronstein, I Perez-Otano, V Sun, SB Mullis Sawin, J Chan, G-C Wu, PM Hudson, L-Y Kong, J-S Hong & MK McMillian. *Glia-dependent neurotoxicity and neuroprotection in mesencephalic cultures*. *Brain Research*, vol. 704, no. 1, pages 112–116, 1995.
- [Buck 11] Jason R Buck, Eliot T McKinley, Matthew R Hight, Allie Fu, Dewei Tang, Ralph Adam Smith, Mohammed Noor Tantawy, Todd E Peterson, Daniel Colvin, Mohammed Sib Ansari *et al.* *Quantitative, preclinical PET of translocator protein expression in glioma using 18F-N-fluoroacetyl-N-(2, 5-dimethoxybenzyl)-2-phenoxyaniline*. *Journal of Nuclear Medicine*, vol. 52, no. 1, pages 107–114, 2011.
- [Buscombe 03] J. Buscombe & A. Signore. *FDG-PET in Infectious and Inflammatory Disease*. *European Journal of Nuclear Medicine and Molecular Imaging*, vol. 30, no. 11, pages 1571–1573, 2003.
- [Cabral 08] GA Cabral, ES Raborn, L Griffin, J Dennis & F Marciano-Cabral. *CB2 receptors in the brain: role in central immune function*. *British Journal of Pharmacology*, vol. 153, no. 2, pages 240–251, 2008.
- [Chauveau 08] Fabien Chauveau, Hervé Boutin, Nadja Van Camp, Frédéric Dollé & Bertrand Tavitian. *Nuclear imag-*

BIBLIOGRAPHY

- ing of neuroinflammation: a comprehensive review of [11C] PK11195 challengers*. European journal of nuclear medicine and molecular imaging, vol. 35, no. 12, pages 2304–2319, 2008.
- [Chauveau 09] Fabien Chauveau, Nadja Van Camp, Frédéric Dollé, Bertrand Kuhnast, Françoise Hinnen, Annelaure Damont, Hervé Boutin, Michelle James, Michael Kassiou & Bertrand Tavitian. *Comparative evaluation of the translocator protein radioligands 11C-DPA-713, 18F-DPA-714, and 11C-PK11195 in a rat model of acute neuroinflammation*. Journal of Nuclear Medicine, vol. 50, no. 3, pages 468–476, 2009.
- [Citraro 06] Rita Citraro, Emilio Russo, Santo Gratteri, Eugenio Donato Di Paola, Guido Ferreri Ibbadu, Carmela Curinga, Rosaria Gitto, Alba Chimirri, Giuseppe Donato & Giovambattista De Sarro. *Effects of non-competitive AMPA receptor antagonists injected into some brain areas of WAG/Rij rats, an animal model of generalized absence epilepsy*. Neuropharmacology, vol. 51, no. 6, pages 1058–1067, 2006.
- [Cobbold 07] Richard SC Cobbold. Foundations of Biomedical Ultrasound. Oxford University Press, USA, 2007.
- [CORNELIUS 90] PETER CORNELIUS, MELISSA MARLOWE & PHILLIP H PEKALA. *Regulation of Glucose Transport by Tumor Necrosis Factor-[alpha] in Cultured Murine 3T3-L1 Fibroblasts*. Journal of Trauma-Injury, Infection, and Critical Care, vol. 30, pages 15–19, 1990.
- [Damont 08] Annelaure Damont, Françoise Hinnen, Bertrand Kuhnast, Marie-Anne Schöllhorn-Peyronneau, Michelle James, Christopher Luus, Bertrand Tavitian, Michael Kassiou & Frédéric Dollé. *Radiosynthesis of [18F] DPA-714, a selective radioligand for imaging the translocator protein (18 kDa) with PET*. Journal of Labelled Compounds and Radiopharmaceuticals, vol. 51, no. 7, pages 286–292, 2008.
- [Danese 06] Silvio Danese, Miquel Sans, Carol de la Motte, Cristina Graziani, Gail West, Manijeh H Phillips, Roberto Pola,

BIBLIOGRAPHY

- Sergio Rutella, Joe Willis, Antonio Gasbarrini *et al.* *Angiogenesis as a novel component of inflammatory bowel disease pathogenesis*. *Gastroenterology*, vol. 130, no. 7, pages 2060–2073, 2006.
- [de Vries 03] Erik FJ de Vries, Aren van Waarde, Anne Rixt Bursma & Willem Vaalburg. *Synthesis and in vivo evaluation of ^{18}F -desbromo-DuP-697 as a PET tracer for cyclooxygenase-2 expression*. *Journal of Nuclear Medicine*, vol. 44, no. 10, pages 1700–1706, 2003.
- [de Vries 08] Erik FJ de Vries, Janine Doorduyn, Rudi A Dierckx & Aren van Waarde. *Evaluation of ^{11}C rofecoxib as PET tracer for cyclooxygenase 2 overexpression in rat models of inflammation*. *Nuclear Medicine and Biology*, vol. 35, no. 1, pages 35–42, 2008.
- [Dedeurwaerdere 12] Stefanie Dedeurwaerdere, Paul D Callaghan, Tien Pham, Gita L Rahardjo, Halima Amhaoul, Paula Berghofer, Mitchell Quinlivan, Filomena Mattner, Christian Loc'h, Andrew Katsifiset *et al.* *PET imaging of brain inflammation during early epileptogenesis in a rat model of temporal lobe epilepsy*. *EJNMMI Res*, vol. 2, no. 1, page 60, 2012.
- [Desgrosellier 10] Jay S Desgrosellier & David A Cheresch. *Integrins in cancer: biological implications and therapeutic opportunities*. *Nature Reviews Cancer*, vol. 10, no. 1, pages 9–22, 2010.
- [Di Gialleonardo 12] Valentina Di Gialleonardo, Alberto Signore, Antoon TM Willemsen, Jurgen WA Sijbesma, Rudi AJO Dierckx & Erik FJ de Vries. *Pharmacokinetic modelling of N -(4- ^{18}F fluorobenzoyl) interleukin-2 binding to activated lymphocytes in an xenograft model of inflammation*. *European journal of nuclear medicine and molecular imaging*, vol. 39, no. 10, pages 1551–1560, 2012.
- [Edison 08] Paul Edison, Hilary A Archer, Alexander Gerhard, Rainer Hinz, Nicola Pavese, Federico E Turkheimer, Alexander Hammers, Yen Fong Tai, Nick Fox, Angus Kennedy *et al.* *Microglia, amyloid, and cognition in Alzheimer's disease: An ^{11}C (R) PK11195-PET and*

BIBLIOGRAPHY

- [11C] *PIB-PET study*. *Neurobiology of Disease*, vol. 32, no. 3, pages 412–419, 2008.
- [Evens 11] Nele Evens, Caroline Vandeputte, Giulio G Muccioli, Didier M Lambert, Veerle Baekelandt, Alfons M Verbruggen, Zeger Debyser, Koen Van Laere & Guy M Bormans. *Synthesis, in vitro and in vivo evaluation of fluorine-18 labelled FE-GW405833 as a PET tracer for type 2 cannabinoid receptor imaging*. *Bioorganic and Medicinal Chemistry*, vol. 19, no. 15, pages 4499–4505, 2011.
- [Evens 12] Nele Evens, Caroline Vandeputte, Charlotte Coolen, Peter Janssen, Raf Sciot, Veerle Baekelandt, Alfons M Verbruggen, Zeger Debyser, Koen Van Laere & Guy M Bormans. *Preclinical evaluation of [11C] NE40, a type 2 cannabinoid receptor PET tracer*. *Nuclear Medicine and Biology*, vol. 39, no. 3, pages 389–399, 2012.
- [Fenster 01] Aaron Fenster, Dóal B Downey & H Neale Cardinal. *Three-dimensional ultrasound imaging*. *Physics in Medicine and Biology*, vol. 46, no. 5, page R67, 2001.
- [Foley 13] John F Foley. *Focus issue: understanding mechanisms of inflammation*. *Science Signaling*, vol. 6, no. 258, page eg2, 2013.
- [Fotiadou 11] Anastasia Fotiadou, Arpit Patel, Tony Morgan & Apostolos H. Karantanas. *Wrist injuries in young adults: The diagnostic impact of {CT} and {MRI}*. *European Journal of Radiology*, vol. 77, no. 2, pages 235–239, 2011. *Imaging of the Hand*.
- [Gaemperli 12] Oliver Gaemperli, Joseph Shalhoub, David RJ Owen, Frederic Lamare, Saga Johansson, Naghmeh Fouladi, Alun H Davies, Ornella E Rimoldi & Paolo G Camici. *Imaging intraplaque inflammation in carotid atherosclerosis with 11C-PK11195 positron emission tomography/computed tomography*. *European Heart Journal*, vol. 33, no. 15, pages 1902–1910, 2012.
- [Gaertner 12] FC Gaertner, H Kessler, H-J Wester, M Schwaiger & AJ Beer. *Radiolabelled RGD peptides for imaging and*

BIBLIOGRAPHY

- therapy*. European Journal of Nuclear Medicine and Molecular Imaging, vol. 39, no. 1, pages 126–138, 2012.
- [Gao 11] Mingzhang Gao, Min Wang, Kathy D Miller & Qi-Huang Zheng. *Synthesis and preliminary in vitro biological evaluation of new carbon-11-labeled celecoxib derivatives as candidate PET tracers for imaging of COX-2 expression in cancer*. European journal of medicinal chemistry, vol. 46, no. 9, pages 4760–4767, 2011.
- [Gaudio 99] Eugenio Gaudio, Gennaro Taddei, Antonella Vetuschi, Roberta Sferra, Giuseppe Frieri, Giuseppe Ricciardi & Renzo Caprilli. *Dextran Sulfate Sodium (DSS) Colitis in Rats (Clinical, Structural, and Ultrastructural Aspects)*. Digestive Diseases and Sciences, vol. 44, no. 7, pages 1458–1475, 1999.
- [Gismera 08] Cristina Saro Gismera & Beatriz Sicilia Aladrén. *Inflammatory bowel diseases: a disease (s) of modern times? Is incidence still increasing?* World journal of gastroenterology: WJG, vol. 14, no. 36, page 5491, 2008.
- [Haberkorn 11] U Haberkorn, A Markert, W Mier, V Askoxylakis & A Altmann. *Molecular imaging of tumor metabolism and apoptosis*. Oncogene, vol. 30, no. 40, pages 4141–4151, 2011.
- [Hannestad 12] Jonas Hannestad, Jean-Dominique Gallezot, Thomas Schafbauer, Keunpoong Lim, Tracy Kloczynski, Evan D Morris, Richard E Carson, Yu-Shin Ding & Kelly P Cosgrove. *Endotoxin-induced systemic inflammation activates microglia:[11C] PBR28 positron emission tomography in nonhuman primates*. Neuroimage, vol. 63, no. 1, pages 232–239, 2012.
- [Hartung 07] Dagmar Hartung, Michael Schäfers, Shinichiro Fujimoto, Bodo Levkau, Navneet Narula, Klaus Kopka, Renu Virmani, Chris Reutelingsperger, Leo Hofstra, Frank D Kolodgie *et al.* *Targeting of matrix metalloproteinase activation for noninvasive detection of vulnerable atherosclerotic lesions*. European journal of nuclear medicine and molecular imaging, vol. 34, no. 1, pages 1–8, 2007.

BIBLIOGRAPHY

- [Hawkey 99] CJ Hawkey. *COX-2 inhibitors*. The Lancet, vol. 353, no. 9149, pages 307–314, 1999.
- [Hermann 12] Sven Hermann, Andrea Starsichova, Bianca Waschkau, Michael Kuhlmann, Christian Wenning, Otmar Schober & Michael Schäfers. *Non-FDG imaging of atherosclerosis: Will imaging of MMPs assess plaque vulnerability?* Journal of Nuclear Cardiology, vol. 19, no. 3, pages 609–617, 2012.
- [Hibi 02] Toshifumi Hibi, Haruhiko Ogata & Atsushi Sakuraba. *Animal models of inflammatory bowel disease*. Journal of Gastroenterology, vol. 37, no. 6, pages 409–417, 2002.
- [Hirsch 89] JAMES D Hirsch, CARL F Beyer, LORRAINE Malkowitz, BERNARD Beer & ARTHUR J Blume. *Mitochondrial benzodiazepine receptors mediate inhibition of mitochondrial respiratory control*. Molecular pharmacology, vol. 35, no. 1, pages 157–163, 1989.
- [Hodivala-Dilke 08] Kairbaan Hodivala-Dilke. *Alpha-v-beta 3 integrin and angiogenesis: a moody integrin in a changing environment*. Current opinion in Cell Biology, vol. 20, no. 5, pages 514–519, 2008.
- [Horti 10] Andrew G Horti, Yongjun Gao, Hayden T Ravert, Paige Finley, Heather Valentine, Dean F Wong, Christopher J Endres, Alena V Savonenko & Robert F Dannals. *Synthesis and biodistribution of [11C] A-836339, a new potential radioligand for PET imaging of cannabinoid type 2 receptors (CB2)*. Bioorganic and Med Chem, vol. 18, no. 14, pages 5202–5207, 2010.
- [Jacobs 12] Andreas H Jacobs & Bertrand Tavitian. *Noninvasive molecular imaging of neuroinflammation*. Journal of Cerebral Blood Flow and Metabolism, vol. 32, no. 7, pages 1393–1415, 2012.
- [James 06] Michelle L James, Silvia Selleri & Michael Kassiou. *Development of ligands for the peripheral benzodiazepine receptor*. Current Medicinal Chemistry, vol. 13, no. 17, pages 1991–2001, 2006.

BIBLIOGRAPHY

- [Kadrmas 05] Dan J Kadrmas & Thomas C Rust. *Feasibility of rapid multitracer PET tumor imaging*. Nuclear Science, IEEE Transactions on, vol. 52, no. 5, pages 1341–1347, 2005.
- [Katori 00] M Katori & M Majima. *Cyclooxygenase-2: its rich diversity of roles and possible application of its selective inhibitors*. Inflammation Research, vol. 49, no. 8, pages 367–392, 2000.
- [Kintscher 08] Ulrich Kintscher, Martin Hartge, Katharina Hess, Anna Foryst-Ludwig, Markus Clemenz, Martin Wabitsch, Pamela Fischer-Posovszky, Thomas FE Barth, Duska Dragun, Thomas Skurket *al.* *T-lymphocyte Infiltration in Visceral Adipose Tissue A Primary Event in Adipose Tissue Inflammation and the Development of Obesity-Mediated Insulin Resistance*. Arteriosclerosis, thrombosis, and vascular biology, vol. 28, no. 7, pages 1304–1310, 2008.
- [Korkhov 10] Vladimir M Korkhov, Carsten Sachse, Judith M Short & Christopher G Tate. *Three-dimensional structure of TspO by electron cryomicroscopy of helical crystals*. Structure, vol. 18, no. 6, pages 677–687, 2010.
- [Kreisl 10] William C Kreisl, Masahiro Fujita, Yota Fujimura, Nobuyo Kimura, Kimberly J Jenko, Pavitra Kannan, Jinsoo Hong, Cheryl L Morse, Sami S Zoghbi, Robert L Gladding *et al.* *Comparison of [11C]-(R)-PK 11195 and [11C] PBR28, two radioligands for translocator protein (18 kDa) in human and monkey: Implications for positron emission tomographic imaging of this inflammation biomarker*. Neuroimage, vol. 49, no. 4, pages 2924–2932, 2010.
- [Kuge 10] Yuji Kuge, Nozomi Takai, Yuki Ogawa, Takashi Temma, Yan Zhao, Kantaro Nishigori, Seigo Ishino, Junko Kamihashi, Yasushi Kiyono, Masashi Shiomi *et al.* *Imaging with radiolabelled anti-membrane type 1 matrix metalloproteinase (MT1-MMP) antibody: potentials for characterizing atherosclerotic plaques*. European journal of nuclear medicine and molecular imaging, vol. 37, no. 11, pages 2093–2104, 2010.

BIBLIOGRAPHY

- [Kuhnast 12] Bertrand Kuhnast, Annelaure Damont, Françoise Hinnen, Tony Catarina, Stéphane Demphel, Stéphane Le Helleix, Christine Coulon, Sébastien Goutal, Philippe Gervais & Frédéric Dollé. *[18F] DPA-714, [18F] PBR111 and [18F] FEDAA1106-selective radioligands for imaging TSPO 18 kDa with PET: automated radiosynthesis on a TRACERLab FX-FN synthesizer and quality controls*. Applied radiation and isotopes: including data, instrumentation and methods for use in agriculture, industry and medicine, vol. 70, no. 3, pages 489–497, 2012.
- [Lankinen 08] Petteri Lankinen, Tatu J Mäkinen, Tiina A Pöyhönen, Pauliina Virsu, Satu Salomäki, Antti J Hakanen, Sirpa Jalkanen, Hannu T Aro & Anne Roivainen. *68Ga-DOTAVAP-P1 PET imaging capable of demonstrating the phase of inflammation in healing bones and the progress of infection in osteomyelitic bones*. European Journal of Nuclear Medicine and Molecular Imaging, vol. 35, no. 2, pages 352–364, 2008.
- [Leijser 10] LaraM. Leijser, FranciscaT. de Bruïne, Jeroen van der Grond, SylkeJ. Steggerda, FransJ. Walther & Gerda van Wezel-Meijler. *Is sequential cranial ultrasound reliable for detection of white matter injury in very preterm infants?* Neuroradiology, vol. 52, no. 5, pages 397–406, 2010.
- [Ley 01] Klaus Ley, Yuqing Huo *et al.* *VCAM-1 is critical in atherosclerosis*. Journal of Clinical Investigation, vol. 107, no. 10, pages 1209–1210, 2001.
- [Locke 09] Landon W Locke, Mahendra D Chordia, Yi Zhang, Bijoy Kundu, Dylan Kennedy, Jessica Landseadel, Li Xiao, Karen D Fairchild, Stuart S Berr, Joel Linden *et al.* *A novel neutrophil-specific PET imaging agent: cFLFLFK-PEG-64Cu*. Journal of Nuclear Medicine, vol. 50, no. 5, pages 790–797, 2009.
- [Mäki-Petäjä 06] Kaisa M Mäki-Petäjä, Frances C Hall, Anthony D Booth, Sharon ML Wallace, Philip WP Bearcroft, Srinivasan Harish, Anita Furlong, Carmel M McEniery, John Brown, Ian B Wilkinson *et al.* *Rheumatoid arthritis is associated with increased aortic pulse-wave velocity, which*

BIBLIOGRAPHY

- is reduced by anti-tumor necrosis factor- α therapy.* *Circulation*, vol. 114, no. 11, pages 1185–1192, 2006.
- [Mäkinen 05] Tatu J Mäkinen, Petteri Lankinen, Tiina Pöyhönen, Jari Jalava, Hannu T Aro & Anne Roivainen. *Comparison of ^{18}F -FDG and ^{68}Ga PET imaging in the assessment of experimental osteomyelitis due to *Staphylococcus aureus*.* *European Journal of Nuclear Medicine and Molecular Imaging*, vol. 32, no. 11, pages 1259–1268, 2005.
- [Mankoff 07] David A Mankoff. *A definition of Molecular Imaging.* *Journal of Nuclear Medicine*, vol. 48, no. 6, pages 18N–21N, 2007.
- [Maroy 08] Renaud Maroy, Raphaël Boisgard, Claude Comtat, Vincent Frouin, Pascal Cathier, Edouard Duchesnay, Frédéric Dollé, Peter E Nielsen, Régine Trébossen & Bertrand Tavitian. *Segmentation of rodent whole-body dynamic PET images: an unsupervised method based on voxel dynamics.* *Medical Imaging, IEEE Transactions on*, vol. 27, no. 3, pages 342–354, 2008.
- [Matter 06] Christian M Matter, Matthias T Wyss, Patricia Meier, Nicolas Späth, Tobias von Lukowicz, Christine Lohmann, Bruno Weber, Ana Ramirez de Molina, Juan Carlos Lacal, Simon M Ametamey *et al.* *^{18}F -choline images murine atherosclerotic plaques ex vivo.* *Arteriosclerosis, Thrombosis, and Vascular Biology*, vol. 26, no. 3, pages 584–589, 2006.
- [McCarthy 02] Timothy J McCarthy, Ahmed U Sheriff, Matthew J Graneto, John J Talley & Michael J Welch. *Radiosynthesis, in vitro validation, and in vivo evaluation of ^{18}F -labeled COX-1 and COX-2 inhibitors.* *Journal of Nuclear Medicine*, vol. 43, no. 1, pages 117–124, 2002.
- [Médran-Navarrete 14] Vincent Médran-Navarrete, Annelaure Damont, Marie-Anne Peyronneau, Bertrand Kuhnast, Nicholas Bernards, Géraldine Pottier, Frank Marguet, Frédéric Puech, Raphaël Boisgard & Frédéric Dollé. *Preparation and evaluation of novel pyrazolo [1, 5- α] pyrimidine acetamides, closely related to DPA-714, as potent ligands for imaging the TSPO 18kDa with PET.* *Bioorganic*

BIBLIOGRAPHY

- and Medicinal Chemistry Letters, vol. 24, no. 6, pages 1550–1556, 2014.
- [Minghetti 04] Luisa Minghetti. *Cyclooxygenase-2 (COX-2) in inflammatory and degenerative brain diseases*. Journal of Neuropathology & Experimental Neurology, vol. 63, no. 9, pages 901–910, 2004.
- [Mueller 13] Kristen Mueller. *Inflammation's Yin-Yang*. Science, vol. 339, no. 6116, pages 155–155, 2013.
- [Nahrendorf 09] Matthias Nahrendorf, Edmund Keliher, Peter Panizzi, Hanwen Zhang, Sheena Hembrador, Jose-Luiz Figueiredo, Elena Aikawa, Kimberly Kelly, Peter Libby & Ralph Weissleder. *18F-4V for PET-CT Imaging of VCAM-1 Expression in Atherosclerosis*. JACC: Cardiovascular Imaging, vol. 2, no. 10, pages 1213–1222, 2009.
- [Okayasu 90] Isao Okayasu, Shigeru Hatakeyama, Masahiro Yamada, TOSHIFUMI Ohkusa, Yoshio Inagaki, Rintaro Nakaya *et al.* *A novel method in the induction of reliable experimental acute and chronic ulcerative colitis in mice*. Gastroenterology, vol. 98, no. 3, pages 694–702, 1990.
- [Ostuni 07] Mariano A Ostuni, Robert Ducroc, Gabriel Peranzi, Marie-Christine Tonon, Vassilios Papadopoulos & Jean-Jacques Lacapere. *Translocator protein (18 kDa) ligand PK 11195 induces transient mitochondrial Ca²⁺ release leading to transepithelial Cl⁻ secretion in HT-29 human colon cancer cells*. Biology of the Cell, vol. 99, no. 11, pages 639–647, 2007.
- [Ostuni 10] Mariano A Ostuni, Leeyah Issop, Gabriel Péranzi, Francine Walker, Magali Fasseu, Carole Elbim, Vassilios Papadopoulos & Jean-Jacques Lacapere. *Overexpression of translocator protein in inflammatory bowel disease: Potential diagnostic and treatment value*. Inflammatory Bowel Diseases, vol. 16, no. 9, pages 1476–1487, 2010.
- [Owen 10] David R Owen, Owain W Howell, Sac-Pham Tang, Lisa A Wells, Idriss Bennacef, Mats Bergstrom, Roger N

BIBLIOGRAPHY

- Gunn, Eugenii A Rabiner, Martin R Wilkins, Richard Reynoldset *al.* *Two binding sites for [3H]PBR28 in human brain: implications for TSPO PET imaging of neuroinflammation.* *Journal of Cerebral Blood Flow and Metabolism*, vol. 30, no. 9, pages 1608–1618, 2010.
- [Owen 11] David R Owen, Astrid J Yeo, Roger N Gunn, Ki-joung Song, Graham Wadsworth, Andrew Lewis, Chris Rhodes, David J Pulford, Idriss Bennacef, Christine A Parker *et al.* *An 18-kDa translocator protein (TSPO) polymorphism explains differences in binding affinity of the PET radioligand PBR28.* *Journal of Cerebral Blood Flow and Metabolism*, vol. 32, no. 1, pages 1–5, 2011.
- [Pålsson-McDermott 04] Eva M Pålsson-McDermott & Luke AJ O’Neill. *Signal transduction by the lipopolysaccharide receptor, Toll-like receptor-4.* *Immunology*, vol. 113, no. 2, pages 153–162, 2004.
- [Papadopoulos 06] Vassilios Papadopoulos, Mario Baraldi, Tomás R Guilarte, Thomas B Knudsen, Jean-Jacques Lacapère, Peter Lindemann, Michael D Norenberg, David Nutt, Abraham Weizman, Ming-Rong Zhanget *al.* *Translocator protein (18kDa): new nomenclature for the peripheral-type benzodiazepine receptor based on its structure and molecular function.* *Trends in Pharmacological Sciences*, vol. 27, no. 8, pages 402–409, 2006.
- [Peyronneau 13] Marie-Anne Peyronneau, Wadad Saba, Sébastien Goutal, Annelaure Damont, Frédéric Dollé, Michael Kassiou, Michel Bottlaender & Héric Valette. *Metabolism and Quantification of [18F] DPA-714, a New TSPO Positron Emission Tomography Radioligand.* *Drug Metabolism and Disposition*, vol. 41, no. 1, pages 122–131, 2013.
- [Pichler 05] Bernd J Pichler, Manfred Kneilling, Roland Haubner, Heidi Braumüller, Markus Schwaiger, Martin Röcken & Wolfgang A Weber. *Imaging of delayed-type hypersensitivity reaction by PET and 18F-galacto-RGD.* *Journal of Nuclear Medicine*, vol. 46, no. 1, pages 184–189, 2005.

BIBLIOGRAPHY

- [Pickhardt 05] Perry J Pickhardt, Richard B Halberg, Andrew J Taylor, Ben Y Durkee, Jason Fine, Fred T Lee & Jamey P Weichert. *Microcomputed tomography colonography for polyp detection in an in vivo mouse tumor model*. Proceedings of the National Academy of Sciences of the United States of America, vol. 102, no. 9, pages 3419–3422, 2005.
- [Pottier 14] Géraldine Pottier, Nicholas Bernards, Frédéric Dollé & Raphaël Boisgard. *[18F]DPA-714 as a biomarker for positron emission tomography imaging of rheumatoid arthritis in an animal model*. Arthritis Research and Therapy, page 16:R69, 2014.
- [Prabhakaran 05] Jaya Prabhakaran, Vattoly J Majo, Norman R Simpson, Ronald L Van Heertum, J John Mann & JS Kumar. *Synthesis of [11C] celecoxib: a potential PET probe for imaging COX-2 expression*. Journal of Labelled Compounds and Radiopharmaceuticals, vol. 48, no. 12, pages 887–895, 2005.
- [Pugliese 10] Francesca Pugliese, Oliver Gaemperli, Anne R Kinderlerer, Frederic Lamare, Joseph Shalhoub, Alun Huw Davies, Ornella E Rimoldi, Justin C Mason & Paolo G Camici. *Imaging of vascular inflammation with [11C]-PK11195 and positron emission tomography/computed tomography angiography*. Journal of the American College of Cardiology, vol. 56, no. 8, pages 653–661, 2010.
- [Rahmim 08] Arman Rahmim & Habib Zaidi. *PET versus SPECT: strengths, limitations and challenges*. Nuclear Medicine Communications, vol. 29, no. 3, pages 193–207, 2008.
- [Reader 07] Andrew J Reader & Habib Zaidi. *Advances in PET Image Reconstruction*. PET Clinics, vol. 2, no. 2, pages 173–190, 2007.
- [Rocha e Silva 78] M Rocha e Silva. *A brief survey of the history of inflammation*. Inflammation Research, vol. 8, no. 1, pages 45–49, 1978.
- [Roivainen 06] Anne Roivainen & Timo Yli-Kerttula. *Whole-body distribution of [11C]choline and uptake in knee synovitis*.

BIBLIOGRAPHY

- European Journal of Nuclear Medicine and Molecular Imaging, vol. 33, no. 11, pages 1372–1373, 2006.
- [Rosenbaum 06] Sandra J Rosenbaum, Thomas Lind, Gerald Antoch & Andreas Bockisch. *False-positive FDG PET uptake- the role of PET/CT*. European Radiology, vol. 16, no. 5, pages 1054–1065, 2006.
- [Rust 06] TC Rust & DJ Kadrmas. *Rapid dual-tracer PTSM+ ATSM PET imaging of tumour blood flow and hypoxia: a simulation study*. Physics in Medicine and Biology, vol. 51, no. 1, page 61, 2006.
- [Ryu 12] Ju Hee Ryu, Aeju Lee, Myung Sook Huh, Junuk Chu, Kwangmeyung Kim, Byung-Soo Kim, Kuiwon Choi, Ick Chan Kwon, Jong Woong Park & Inchan Youn. *Measurement of MMP activity in synovial fluid in cases of osteoarthritis and acute inflammatory conditions of the knee joints using a fluorogenic peptide probe-immobilized diagnostic kit*. Theranostics, vol. 2, no. 2, pages 198–206, 2012.
- [Sakai 10] Mônica Sakai, Viviane Ferraz-de Paula, ML Pinheiro, A Ribeiro, Wanderley Moreno Quinteiro-Filho, MB Rone, DB Martinez-Arguelles, Maria Lúcia Zaidan Dagli, Vassilios Papadopoulos & João Palermo-Neto. *Translocator protein (18kDa) mediates the pro-growth effects of diazepam on Ehrlich tumor cells in vivo*. European Journal of Pharmacology, vol. 626, no. 2, pages 131–138, 2010.
- [Salmi 01] Marko Salmi & Sirpa Jalkanen. *VAP-1: an adhesin and an enzyme*. Trends in Immunology, vol. 22, no. 4, pages 211–216, 2001.
- [Scarf 09] Alana M Scarf, Lars M Ittner & Michael Kassiou. *The translocator protein (18 kDa): central nervous system disease and drug design*. Journal of Medicinal Chemistry, vol. 52, no. 3, pages 581–592, 2009.
- [Scarf 11] Alana M Scarf & Michael Kassiou. *The translocator protein*. Journal of Nuclear Medicine, vol. 52, no. 5, pages 677–680, 2011.

BIBLIOGRAPHY

- [Schäfers 04] Michael Schäfers, Burkhard Riemann, Klaus Kopka, Hans-Jörg Breyholz, Stefan Wagner, Klaus P Schäfers, Marilyn P Law, Otmar Schober & Bodo Levkau. *Scintigraphic imaging of matrix metalloproteinase activity in the arterial wall in vivo*. *Circulation*, vol. 109, no. 21, pages 2554–2559, 2004.
- [Schwartz 13] Michal Schwartz, Jonathan Kipnis, Serge Rivest & Alexandre Prat. *How do immune cells support and shape the brain in health, disease, and aging?* *The Journal of Neuroscience*, vol. 33, no. 45, pages 17587–17596, 2013.
- [Schwarzenböck 12] S Schwarzenböck, M Souvatzoglou & BJ Krause. *Choline PET and PET/CT in primary diagnosis and staging of prostate cancer*. *Theranostics*, vol. 2, no. 3, page 318, 2012.
- [Seibel 09] Jan Seibel, Almut F Molzberger, Torsten Hertrampf, Ute Laudenschach-Leschowski & Patrick Diel. *Oral treatment with genistein reduces the expression of molecular and biochemical markers of inflammation in a rat model of chronic TNBS-induced colitis*. *European Journal of Nutrition*, vol. 48, no. 4, pages 213–220, 2009.
- [Shoda 07] H Shoda, Y Kakugawa, D Saito, T Kozu, T Terauchi, H Daisaki, C Hamashima, Y Muramatsu, N Moriyama & H Saito. *Evaluation of 18F-2-deoxy-2-fluoro-glucose positron emission tomography for gastric cancer screening in asymptomatic individuals undergoing endoscopy*. *British Journal of Cancer*, vol. 97, no. 11, pages 1493–1498, 2007.
- [Shukuri 11] Miho Shukuri, Misato Takashima-Hirano, Keiko Tokuda, Tadayuki Takashima, Kiyoshi Matsumura, Osamu Inoue, Hisashi Doi, Masaaki Suzuki, Yasuyoshi Watanabe & Hirotaka Onoe. *In vivo expression of cyclooxygenase-1 in activated microglia and macrophages during neuroinflammation visualized by PET with 11C-ketoprofen methyl ester*. *Journal of Nuclear Medicine*, vol. 52, no. 7, pages 1094–1101, 2011.
- [Signore 02] Alberto Signore, Calogero D’alessandria, Alessio Annovazzi & Francesco Scopinaro. *Radiolabelled cytokines for*

BIBLIOGRAPHY

- imaging chronic inflammation*. Brazilian Archives of Biology and Technology, vol. 45, no. SPE, pages 15–23, 2002.
- [Silvola 11] Johanna MU Silvola, Iina Laitinen, Henri J Sipilä, V Jukka O Laine, Pia Leppänen, Seppo Ylä-Herttuala, Juhani Knuuti & Anne Roivainen. *Uptake of ^{68}Ga in atherosclerotic plaques in LDLR $^{-/-}$ ApoB100/100 mice*. EJNMMI research, vol. 1, no. 1, pages 1–8, 2011.
- [Solomon 11] Metasebya Solomon, Yang Liu, Mikhail Y Berezin & Samuel Achilefu. *Optical imaging in cancer research: basic principles, tumor detection, and therapeutic monitoring*. Medical Principles and Practice, vol. 20, no. 5, pages 397–415, 2011.
- [Stasiuk 13] Graeme J Stasiuk, Helen Smith, Marzena Wylezinska-Arridge, Jordi L Tremoleda, William Trigg, Sajinder Kaur Luthra, Veronique Morisson Iveson, Felicity NE Gavins & Nicholas J Long. *Gd $^{3+}$ cFLFLFK conjugate for MRI: a targeted contrast agent for FPR1 in inflammation*. Chemical Communications, vol. 49, no. 6, pages 564–566, 2013.
- [Tabas 13] Ira Tabas & Christopher K Glass. *Anti-inflammatory therapy in chronic disease: challenges and opportunities*. Science, vol. 339, no. 6116, pages 166–172, 2013.
- [Thiel 10] Alexander Thiel, Basia A Radlinska, Caroline Paquette, Michael Sidel, Jean-Paul Soucy, Ralf Schirmacher & Jeffrey Minuk. *The Temporal Dynamics of Poststroke Neuroinflammation: A Longitudinal Diffusion Tensor Imaging-Guided PET Study with ^{11}C -PK11195 in Acute Subcortical Stroke*. Journal of Nuclear Medicine, vol. 51, no. 9, pages 1404–1412, 2010.
- [Tsan 85] Min-Fu Tsan. *Mechanism of gallium-67 accumulation in inflammatory lesions*. Journal of Nuclear Medicine, vol. 26, no. 1, pages 88–92, 1985.
- [Uddin 11] Md Jashim Uddin, Brenda C Crews, Kebreab Ghebreselasie, Imran Huda, Philip J Kingsley, Mohammad Sib Ansari, Mohammed N Tantawy, Jeffery Reese

- & Lawrence J Marnett. *Fluorinated COX-2 inhibitors as agents in PET imaging of inflammation and cancer*. Cancer Prevention Research, vol. 4, no. 10, pages 1536–1545, 2011.
- [Ujula 09] Tiina Ujula, Satu Salomäki, Pauliina Virsu, Petteri Lankinen, Tatu J Mäkinen, Anu Autio, Gennady G Yegutkin, Juhani Knuuti, Sirpa Jalkanen & Anne Roivainen. *Synthesis, 68 Ga labeling and preliminary evaluation of DOTA peptide binding vascular adhesion protein-1: a potential PET imaging agent for diagnosing osteomyelitis*. Nuclear Medicine and Biology, vol. 36, no. 6, pages 631–641, 2009.
- [Vandeputte 11] Caroline Vandeputte, Nele Evens, Jaan Toelen, Christophe M Deroose, Barbara Bosier, Abdelilah Ibrahimi, Anke Van der Perren, Rik Gijssbers, Peter Janssen, Didier M Lambert *et al.* *A PET brain reporter gene system based on type 2 cannabinoid receptors*. Journal of Nuclear Medicine, vol. 52, no. 7, pages 1102–1109, 2011.
- [Veenman 07] Leo Veenman, Vassilios Papadopoulos & Moshe Gavish. *Channel-like functions of the 18-kDa translocator protein (TSPO): regulation of apoptosis and steroidogenesis as part of the host-defense response*. Current Pharmaceutical Design, vol. 13, no. 23, pages 2385–2405, 2007.
- [Venneti 06] Sriram Venneti, Brian J Lopresti & Clayton A Wiley. *The peripheral benzodiazepine receptor (Translocator protein 18kDa) in microglia: from pathology to imaging*. Progress in Neurobiology, vol. 80, no. 6, pages 308–322, 2006.
- [Venneti 08] Sriram Venneti, Guoji Wang, Jason Nguyen & Clayton A Wiley. *The positron emission tomography ligand DAA1106 binds with high affinity to activated microglia in human neurological disorders*. Journal of Neuropathology and Experimental Neurology, vol. 67, no. 10, page 1001, 2008.
- [Verma 87] Ajay Verma, Jeffrey S Nye & Solomon H Snyder. *Porphyrins are endogenous ligands for the mitochondrial*

BIBLIOGRAPHY

- (*peripheral-type*) benzodiazepine receptor. Proceedings of the National Academy of Sciences, vol. 84, no. 8, pages 2256–2260, 1987.
- [Wagner 9] Stefan Wagner, Hans-Joerg Breyholz, Carsten Hoeltke, Andreas Faust, Otmar Schober, Michael Schaefer & Klaus Kopka. *A new (18)F-labelled derivative of the MMP inhibitor CGS 27023A for PET: Radiosynthesis and initial small-animal PET studies*. Applied Radiation And Isotopes, vol. 67, pages 606–610, 2009.
- [Weissleder 99] Ralph Weissleder. *Molecular Imaging: Exploring the Next Frontier*. Radiology, vol. 212, no. 3, pages 609–614, 1999. PMID: 10478223.
- [Wilder 02] RL Wilder. *Integrin alpha V beta 3 as a target for treatment of rheumatoid arthritis and related rheumatic diseases*. Annals of the Rheumatic Diseases, vol. 61, no. suppl 2, pages ii96–ii99, 2002.
- [Wimo 10] Anders Wimo & Martin James Prince. World Alzheimer Report 2010: the global economic impact of dementia. Alzheimer’s Disease International, 2010.
- [Witney 12] Timothy H Witney, Israt S Alam, David R Turton, Graham Smith, Laurence Carroll, Diana Brickute, Frazer J Twyman, Quang-Dé Nguyen, Giampaolo Tomasi, Ramla O Awaiset *al*. *Evaluation of deuterated 18F- and 11C-labeled choline analogs for cancer detection by positron emission tomography*. Clinical Cancer Research, vol. 18, no. 4, pages 1063–1072, 2012.
- [Wu 13] Chenxi Wu, Fang Li, Gang Niu & Xiaoyuan Chen. *PET Imaging Of Inflammation Biomarkers*. Theranostics, vol. 3, no. 7, pages 448–466, 2013.
- [Wyatt 10] Shelby K Wyatt, H Charles Manning, Mingfeng Bai, Stephanie N Bailey, Pascal Gallant, Guobin Ma, Laura McIntosh & Darryl J Bornhop. *Molecular imaging of the translocator protein (TSPO) in a pre-clinical model of breast cancer*. Molecular Imaging and Biology, vol. 12, no. 3, pages 349–358, 2010.

BIBLIOGRAPHY

- [Xiao 10] Li Xiao, Yi Zhang, Zhongqiu Liu, Min Yang, Lin Pu & Dongfeng Pan. *Synthesis of the Cyanine 7 labeled neutrophil-specific agents for noninvasive near infrared fluorescence imaging*. Bioorg. Med Chemistry Letters, vol. 20, no. 12, pages 3515–3517, 2010.
- [Zhang 10] Yi Zhang, Li Xiao, Mahendra D Chordia, Landon W Locke, Mark B Williams, Stuart S Berr & Dongfeng Pan. *Neutrophil targeting heterobivalent SPECT imaging probe: cFLFLF-PEG-TKPPR-99mTc*. Bioconjugate Chemistry, vol. 21, no. 10, pages 1788–1793, 2010.
- [Zheng 02] Qi-Huang Zheng, Xiangshu Fei, Xuan Liu, Ji-Quan Wang, Hui Bin Sun, Bruce H Mock, K Lee Stone, Tanya D Martinez, Kathy D Miller, George W Sledge *et al.* *Synthesis and preliminary biological evaluation of MMP inhibitor radiotracers [¹¹C] methyl-halo-CGS 27023A analogs, new potential PET breast cancer imaging agents*. Nuclear Medicine and Biology, vol. 29, no. 7, pages 761–770, 2002.
- [Zhu 11] Lei Zhu, Huiling Wang, Lin Wang, Ye Wang, Kun Jiang, Cheng Li, Qingjie Ma, Shi Gao, Liping Wang, Wei Liet *et al.* *High-affinity peptide against MT1-MMP for in vivo tumor imaging*. Journal Of Controlled Release, vol. 150, no. 3, pages 248–255, 2011.